CSIC
Consejo Superior de Investigaciones Científicas

eman ta zabal zazu
Universidad del País Vasco
Euskal Herriko Unibertsitatea

CFM
Materials Physics Center
Centro de Física de Materiales

Electronic structure, dynamics and spectroscopy of metallic nanosized systems: Pb thin overlayers and Na nanocontacts

Doctoral thesis submitted by

Asier Zugarramurdi Camino

for the degree of Doctor of Philosophy in Physics

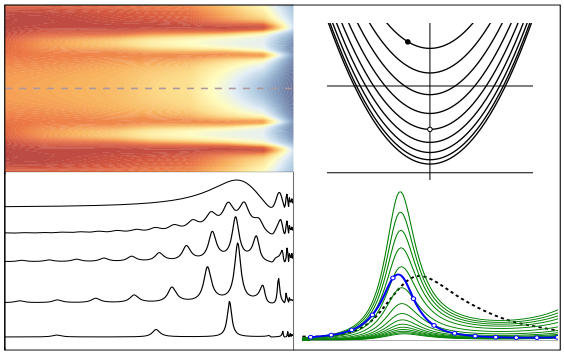

Supervisors:

Nerea Zabala & Eugene Chulkov

December 2011

Acknowledgments in a nutshell

First, I want to thank Nerea Zabala and Eugene Chulkov, my supervisors, for proposing an interesting research field and for providing the possibility to write this thesis. I also thank you both for your time, patience, encouragement and confidence put at the start and at the end of this long way and for providing the freedom and flexibility as required by the circumstances. The final effort has been worthwhile, eskerrik asko eta спасибо!

Of course, this endeavor would not be possible without the financial support from Donostia International Physics Center (DIPC), during the first year, and that of Consejo Superior de Investigaciones Científicas (CSIC) through the Centro de Física de Materiales (CFM) during the following four years, as well as the continuous support from various projects, and the support from the University of the Basque Country, at the Elektronika eta Elektrizitea Department.

This thesis is also indebted, to many collaborators that, directly and indirectly, have contributed to the development of the present thesis from the very beginning until the very last moment: Sharing codes, opinions, ideas, figures, advices, revising notes, papers, rewriting papers, reading drafts of the thesis ...

I start with Edu Ogando who always friendly shared his time to teach me the first basic tricks to deal with electronic structure calculations, and introducing me to the world of scripting ... but not only that, he also has been, together with Txema Mercero, helping me continuously with the calculations in the Arina Cluster.

Then, Slava Silkin, for explaining the GW code and for helping me with Eugene's notes. I have learned a lot of useful tricks from these vintage FORTRAN 77 subroutines!

A special place is reserved to Andrei Borisov. I had the pleasure to meet him in Donostia and to be invited to the Institut des Sciences Moléculaires d'Orsay (ISMO)

laboratory (and former LCAM) in Orsay several times, which eventually led me to meet Serena. Only for that, I could write an entire page of acknowledgments! I will be brief. Thank you for these special years of close collaboration and friendship, from which I have learned a lot of physics and boosted my curiosity, particularly on the magic WPP method. As well as for sharing codes, tricks, time, and in general, for teaching physics, history, diplomacy, and helping me climbing cloudy peaks. Спасибо!

I also thank M. J. Puska for his collaboration in the posters and in the paper concerning the study of the conductance of Na nanocontacts.

Below I continue with the people I have shared these thesis years. Espero dut jende gutxi ahaztea!

Adriantxo doktore judoka dotorearekin hasiko naiz, gure hizketaldiekin mundua mila bider konpondu dugulako. Ondoren departamentuko jendearekin (eta ohiak): Olalla, Edu, Axpe, Ane, Eneko, Javi, Zipi ta Zape, David de Cos, eta abar eta abar, eta ahaztu gabe, departamentuko txokoan dauden bi gaztetxoei Aitziber eta Nerea ;-)

Donostia aldean Xabi, batez ere azkeneko urteetan berraurkitutako laguna, mila esker zure laguntzarengatik eta bazkalondoko kafeengatik, laster zuri datorkizu idazten hasteko eguna! Eta hemen CFM-n, besteak beste, Peter, Ludo, eta eskerrak Iñigori Matplotlib eta Python erabiltzeko emandako aholkuengatik.

A special salut! goes to the students, postdocs (Sergio!) and professors from ISMO in Orsay, specially to Pierre, for the evenings in the K-fet and for introducing me to Serena and Antonella.

Urte hauetan eduki ditudan hainbat pixukide ezin ditut ahaztu: SanFranen, a la salada de Reme, Juantxu, Aritz el melenas eta Aska, besteak beste, zuen bixita Oreretara ahaztezina da. Deustoko urteak Mikel, Txema eta Malake-rekin, eta Miribillan Joven Davidson-ekin, y el Zohan de Jordi!

Eta Oreretako kuadrila osoari beti hor egoteagatik (eta ez naiz Lokalaz hitz egiten ari!). Alde batetik Nomisekoak : Txouza, Urkijo, Huizi, Ruiz, Iosu, Oiertxo, Galdos, Urtzi. Eta Asper: Mazon, Ionko, Otaño, Indio, Xabi, Judas, Ander, Eneko eta Asier.

Azkenik, nire familiari eskerrak eman nahi nieke, Leiretxu (eta Jose), amatxo, aitatxo, amona Xole, izeba Ainara (eta Isi), osaba Ricardo (eta Alma), beraien laguntza gabe bide hau egitea ezinezkoa izango bait litzateke. Baina bereziki, amoña Rosarioren larunbateko bazkariei eta bidean geratutako gure aitona Ricardo-ri. Eta bihotz bihotzez Serenari, grazie per tutto!

Donostia, December 2011.

Contents

Chapter 1

Overview and aims of the thesis

Introduction

The understanding and control of **quantum size effects** (QSEs), i.e., variations of the properties of a physical system as a function of its size, due to the discretization of the electronic states resulting from the quantum confinement, is one of the central issues in **nanoscience**. This area of physics covers a broad range of (mesoscopic) systems having reduced dimensionality [1], frequently in the nanoscale (1–1000 nm), such as thin films confined in one-dimension (2D systems), nanowires and nanotubes confined in two dimensions (1D systems) and quantum dots confined in three dimensions (0D systems).

The miniaturization of the electronic components has been the natural pathway for the progress in computer chips technology. On the one hand, when entering the nanoscale it is found that the "rules" governing the behavior of the systems are not scalable, due to the electronic confinement mentioned above, giving rise to quantum phenomena. On the other hand, **nanotechnology** holds a promise of taking advantage of these new phenomena, which in a long term future might lead to the development of solid state quantum computers [2, 3].

In particular, the study of **electron transport** properties in metallic nanowires is important because they represent the ultimate limit of the wires for the realization of electronic **nanocontacts** between electronic devices [4]. However, not only is the nanowire a natural component of (molecular) electronic devices, but it can also serve as an efficient chemical and biological sensor [5].

Special attention has been paid to confined electron systems in semiconductor thin layers in heterostructures, where the quantization of the electronic states in the direction perpendicular to the film interface provides observable QSEs, which have enabled technological achievements such as the development of quantum well lasers [6]. On the other hand, **metallic thin overlayers** are of great interest in **surface science**, as they belong to the class of nanostructures showing electron confinement at metal surfaces. One of the aims in this field is to engineer surfaces with desirable electronic and magnetic properties. It has diverse perspectives, such as the development of nanoelectronics based on surface states, in analogy with plasmon nanophotonics [7].

Many of the systems showing confined electronic states at surfaces, such as quantum corrals, vacancy islands and atomic chains, are (directly) accessible only using the scanning tunneling microscopy (STM). At variance, the electronic states formed by electron confinement in thin metal overlayers, called **quantum well states** (QWSs), can be studied with photoemission and inverse photoemission techniques, so they are a subject of intense research activity already for decades [8, 9].

In this thesis we have focused on some theoretical aspects of the electronic structure, dynamics and spectroscopy of two nanosized metallic systems: Pb thin overlayers on Cu(111) surfaces and the nanocontacts formed during the stretching process of a Na nanowire. The former is one of the most studied metal-overlayer/metal systems and its characteristic feature is that stationary states, i.e., QWSs are formed in the direction perpendicular to the surface, due to the confinement barriers provided by the vacuum and the projected band gap of Cu in the (111) crystallographic direction [10, 11]. The latter system is one of the first metallic nanocontacts in which the conductance quantization has been demonstrated [12, 13]. In this case the confinement takes place in the two directions perpendicular to the wire axis. Both systems are interesting due to the relative simplicity of their configurations, and the possibility of describing them by simple models, which allows us to perform a transparent physical analysis of their fundamental properties. Furthermore, it is an encouraging task to study theoretically systems characterized by low-dimensional electron gases, which are relatively easy to prepare and to probe by different experimental means.

Our studies are based on a variety of complementary theoretical tools which involve many-body and one-electron, stationary and time-dependent treatments of the electron systems. These are:

- The density functional theory (DFT) within the local density approximation (LDA), which has been used to obtain the electronic (and geometrical) structure of metallic systems and the one-electron effective potentials. (Chapter 2).

- Many-body perturbation theory within the GW approximation has been used for the study of the finite lifetimes of electron (hole) excitations originated in the inelastic electron-electron scattering. (Chapter 3).
- The wave packet propagation method (WPP) has been used to calculate diverse properties of the systems described with the one-electron effective potentials. This versatile method allows to obtain the density of states, the one-electron decay rates and wave functions of resonant states, as well as the one-electron transmission probability through various (tunneling) junctions. (Chapter 4).

The problems studied in this thesis have required a significant dedication to the detailed study of the theoretical methods mentioned above. Thus, we provide extended presentations to describe them. The corresponding chapters are based on the experience acquired at different levels of scientific computing, i.e., use, modification and implementation of numerical codes and eventual interpretation of the results. In this respect, much of the details can be skipped through a quick reading of the present manuscript. Nevertheless, the particular equations used in present studies are collected in specific sections which are referred recurrently through the thesis work.

Among the above methods, the WPP method has been addressed in much more detail. This is reflected in the diverse applications found for this particular method in our studies. The corresponding Chapter 4 is indebted to the close collaboration with the group in Orsay (France), which has developed this approach in the present form. This presentation might serve as a bridge between the general textbook [14] and highly condensed reviews [15] in the considered fields.

Pb thin overlayers

Despite the number of works, both theoretical and experimental, dedicated to the study of Pb thin overlayers (or extended Pb nanoislands) on different substrates, such as Cu(111) [10,11,16–20], Si(111) [21–24] and Ag(111) [25], as well as for free standing Pb thin slabs [26–28] and bulk [29], there are still open questions concerning the electronic structure, dynamics and spectroscopy of the electronic states in Pb thin overlayers.

With respect to the electronic structure, whereas for energies close to the Fermi level QWSs are formed inside the Pb overlayers on Cu(111), when the energies of the confined states are close to the vacuum level, QWSs hybridize with **image states** (ISs). As far as we know, this fundamental effect has not been studied in detail except for Ref. [30], where confined states in Au thin overlayers on Pd(111) are studied. Furthermore, this

is a previously uncovered energy region in Pb/Cu(111), which is studied in the present thesis. (Chapter 6, Section 6.5).

The *lifetime* is a fundamental property of electrons in a metal system. Under an external perturbation of a many-electron system (for example by a laser pulse), an electron can be excited to a higher energy state. However, this situation is unstable due to the inelastic scattering with other (quasi-) particles. Then, the electron only remains for a finite time τ (the lifetime) in this state before it decays to a low lying state. The fundamental study of the electron dynamics is important for different fields. For example, excited electrons at surfaces play an important role in surface reactivity [15, 31, 32]. The lifetime of electrons also affects the linewidth in experimental spectra (photoemission, STS, ...) of electron systems.

The *GW* approximation has been previously used for the study of surface state and image state lifetimes in noble metals [31] and also for the lifetime of the QWS formed in Na/Cu(111) for the coverage of one monolayer [33]. Up to our knowledge, we provide in the present thesis the first theoretical systematic study of the electron-electron decay rate (or inverse lifetime) of QWSs and of hybrid QWS-ISs, discussing the effect of the overlayer thickness. (Chapter 6, Section 6.3).

Apart from the QWSs, when the reflectivity of the confinement barriers is not perfect, an electron can be trapped in a quasi-stationary state. An electron in this state can decay resonantly through an energy conserving process. In Pb/Cu(111) overlayers **quantum well resonances** (QWRs) can exist [19] below the Cu gap. Resonant decay rates of QWRs have been studied previously by Crampin *et al.* [34] in the Ag/Fe(001) system. However, it has not been discussed what is the most important decay channel for the QWRs: the elastic resonant decay or the inelastic electron-electron decay. This question, important from the point of view of the resolvability of the states in experiments, is addressed in our study of QWRs in Pb/Cu(111). (Chapter 6, Section 6.4).

One of the aims of this thesis is to try to interpret some of the diverse available experimental data on the systems mentioned above or in similar systems. For this purpose, one has to understand the **spectroscopy** of these electronic states. In general, spectroscopic studies are of great interest for two reasons: (i) There is additional physics involved in the probing process, because any measurement requires interaction with the system, and (ii) this interaction is reflected in the spectra. Thus, a detailed knowledge of the spectroscopic process provides the means for interpreting correctly the experimental results and allows a reliable characterization of the probed system.

We have performed simulations of STM constant current spectroscopy studies, from which we extract dZ/dV characteristics in Pb/Cu(111). This work has been motivated

by recent experimental results on Pb/Cu(111) [20] and Pb/Ag(111) [25]. We have used a flat-tip approximation to model the STM probe and for describing the STM junction we have included the electric field induced by the STM in front of the surface. This electric field provides a linear barrier for the electronic states at the surface, leading to the formation of **field emission resonances** (FERs), which are hybridized with QWSs above the vacuum level of the bare sample. We have studied the electronic structure, dynamics and spectral properties of these states. (Chapter 7).

Sodium nanocontacts

Concerning the breakage of metallic nanowires, much attention has been paid to the last stage of the breakage, where a monatomic chain is formed [35–37]. In principle, this is because of the simpler configuration of the break junction, that allows faster calculations and also because the interpretation of the results appears easier than, for example, the study of the formation of embedded clusters during the breaking process [38–45].

Thus, in several works, the effect of cluster-like structure formations on the conductance has been overlooked. The study of this phenomenon can serve to understand the different patterns of the *conductance curves*, apart from the typical conductance plateaus obtained during the breaking of metallic nanowires. Eventually, one can try to find out fingerprints in the conductance curves that can lead to the identification of the different structures formed in the break junction.

This is the main motivation for the study of Chapter 8, where we focus on the conductance during the elongation and breakage of Na nanowires described with the ultimate jellium model. A combined approach is used where the nanowire breakage is simulated self-consistently within the DFT, and the WPP technique is applied for ballistic electron transport. This method allows us to calculate quantum mechanically exact transmission probabilities beyond the semi-classical WKB (Wentzel-Kramers-Brillouin) approach, previously implemented by E. Ogando *et al.* in their earlier work [41].

For certain conditions, the breakage of the nanowire is preceded by the formation of clusters of magic size in the break junction. This affects the conductance G, in particular the shape of the $G = 3G_0$ to $G = G_0(= 2e2/h)$ step upon elongation. The observed trends can be explained as due to the transient trapping of ballistic electrons inside the cluster, leading to a resonant character of the electron transport through

the break junction. According to our results, the cluster-derived resonances appear as peak structures in the differential conductance.

Overview

With respect to the results presented in this thesis, we would like to underline below some contributions, because of their particular relevance for the considered fields, and specially for experimentalists:

(i) In general, for energies within a few eV around the Fermi level, no quantum size effect is found in the energy dependence of the inelastic electron-electron lifetime of the QWSs in Pb/Cu(111) at the high symmetry point in reciprocal space, $\bar{\Gamma}$. Only some deviations from the general behavior have been found for the thinnest overlayers (1–3 monolayers) considered. (Fig. 6.4).

(ii) However, we predict a noticeable quantum size effect in the electron-electron lifetime of quantum well states when they acquire an image state character in Pb/Cu(111). This effect takes its origin in the strong thickness dependence of the charge spilling into the vacuum for the electronic states with energies close to the vacuum level. (Fig. 6.10).

(iii) With our calculations we provide a theoretical justification for the possibility to extract the dispersion of electronic bands in metals from STS studies of the energies of QWSs (and hybrid QWS-FERs) formed in overlayers of the same material. (Fig. 7.8a).

(iv) Based on the realistic electronic band structure of bulk Pb metal, we provide a physically sound explanation for the spectral peak energies observed in a recent experimental STM study probing the QWSs in Pb/Cu(111) [20, 46, 47]. (Fig. 7.8b).

(v) We theoretically support that, in the ballistic regime, the cluster-derived resonances of Na nanocontacts are resolvable in the differential conductance spectra. (Fig. 8.8).

The rest of the thesis manuscript is organized as follows:

The following three chapters present the theoretical methods used in our work. Chapter 2 is devoted to the electronic structure calculations and effective one-electron potentials within simple models. Chapter 3 presents the many-body theory used for the calculations of the electron-electron inelastic decay rate within the *GW* approxima-

tion. Chapter 4 provides a detailed description of the WPP method. As mentioned above, these three chapters are extended with the aim of providing a self-contained presentation.

Chapter 5 provides an overview of the different surface-localized states, confined in the direction perpendicular to the surface. The properties of these states are illustrated within the simplest one-dimensional models. Then, these concepts are used in the subsequent chapters where the main results of this thesis, including the lifetimes (Chapter 6) and constant current STM spectroscopy (Chapter 7) of the QWSs, QWRs, ISs and FERs found in the Pb/Cu(111) system are discussed. In Chapter 8, which can be read independently, we provide the results of the conductance of the different nanocontacts formed during the stretching process of a Na nanowire.

Last Chapter 9, is devoted to the summary of the original results obtained in this thesis. Appendices collect some additional results, mathematical details and supplementary figures.

Unless otherwise stated, we shall use atomic units throughout this thesis (i.e., $e^2 = \hbar = m_e = 4\pi\epsilon_0 = 1$).

Chapter 2

Theoretical methods I: Electronic structure

2.1. Introduction

The original density functional theory (DFT) is a reformulation of the many-body problem of an interacting electron system in terms of the electronic density, which is exact for the ground state. It is one of the most successful theoretical frameworks for understanding the electronic structure of atoms, molecules and condensed phases. But the DFT is not only a theory, it also comprises a well developed calculation methodology.

The widespreadly used Kohn-Sham (KS) approach to the DFT replaces the interacting many-body problem by an effective noninteracting one. In practice, the KS equations are solved under non-rigorous approximations and assumptions, basically due to the lack of knowledge of the exact density functional of the exchange-correlation energy. The validity of the method is established by its ability to reproduce experimental results.

In this chapter we start from the very first principles describing a general (nanosized) metallic system in order to explain the different assumptions and approximations taken through the path that leads to the (Kohn-Sham) equations determining the electronic structure (and shape) of the systems considered in this thesis.

Then, in Sections 2.3 and 2.4 we explain the different jellium models we have used and we write the corresponding form of the KS equations solved within those models for one-dimensional and cylindrical symmetries.

The modeling of the one-dimensional self-consistent effective potential for the description of thin Pb overlayers supported on Cu(111) surfaces and the inclusion of the image potential correction are explained in Section 2.5.

Additional jellium-like model potentials describing the interaction between a metallic flat tip and a metallic surface are provided in Section 7.2 of Chapter 7. Further details on the numerical approaches used for solving the one-dimensional Schrödinger equation are given in Appendix B.

2.2. The many-body problem

2.2.1. The fundamental Hamiltonian

In principle, ordinary matter can be understood by a simple structure: it is composed of different nuclei and electrons, where the positively charged nuclei essentially provide the mass and the electrons, carrying the negative electric charge, work as a glue of matter. Furthermore, we know the fundamental quantum mechanical equation describing such a system, i.e., the (non-relativistic) many-particle Schrödinger equation

$$i\partial_t \Psi(\{\mathbf{r}\},\{\mathbf{R}\},t) = \hat{H}\Psi(\{\mathbf{r}\},\{\mathbf{R}\},t), \tag{2.1}$$

with Hamiltonian operator given by

$$\begin{aligned}\sum_i \frac{1}{2m_e}\nabla_i^2 + \sum_j \frac{1}{2M_j}\nabla_j^2 + \frac{1}{2}\sum_j^{N_{\mathrm{nuc}}}\sum_{j'\neq j}^{N_{\mathrm{nuc}}} \frac{Z_j Z_{j'}}{|\mathbf{R}_j - \mathbf{R}_{j'}|} \\ + \frac{1}{2}\sum_i^{N_e}\sum_{i'\neq i}^{N_e} \frac{1}{|\mathbf{r}_i - \mathbf{r}_{i'}|} - \sum_j^{N_{\mathrm{nuc}}}\sum_i^{N_e} \frac{Z_j}{|\mathbf{R}_j - \mathbf{r}_i|}.\end{aligned} \tag{2.2}$$

where m_e is the electron mass and N_e is the number of electrons in the solid and N_{nuc} is the number of nuclei with charge and mass Z and M respectively. We use the short-notation $\{\mathbf{r}\} \equiv (\mathbf{r}_1, \sigma_1, \mathbf{r}_2, \sigma_2, \ldots, \mathbf{r}_{N_e}, \sigma_{N_e})$ to refer to the electron spatial coordinates and spins, and similarly, $\{\mathbf{R}\} \equiv (\mathbf{R}_1, \tilde{\sigma}_1, \mathbf{R}_2, \tilde{\sigma}_2, \ldots, \mathbf{R}_{N_{\mathrm{nuc}}}, \tilde{\sigma}_{N_{\mathrm{nuc}}})$ for the nuclei. Provided Eq. (2.1) with the initial condition $\Psi(\{\mathbf{r}\},\{\mathbf{R}\}, t = t_0)$, the state of the system is determined for all future times. Usually, for electronic structure studies the time-independent Schrödinger equation is considered

$$\hat{H}\Psi(\{\mathbf{r}\},\{\mathbf{R}\}) = E\Psi(\{\mathbf{r}\},\{\mathbf{R}\}). \tag{2.3}$$

In principle, all the information about the system is coded in this equation, however, it is not directly accessible in this form. The solution to Eq. (2.3) is not a numerically tractable problem above a given number of particles. Then, an alternative approach is needed in order to extract the properties of the system.

The first step in simplifying the problem is to decouple the electronic and ionic motion. Intuitively one can expect that nuclear motion in crystals is very slow with respect to the electronic motion, so that it might be assumed that the electrons reach the ground state energy instantaneously for a given configuration of the underlaying ions. This is known as the Born-Oppenheimer approximation, named after Max Born and J. Robert Oppenheimer, and it was already proposed in 1927. Formally, for a given nuclei configuration, we can always consider the solutions [48],

$$\Psi_s(\{\mathbf{r}\},\{\mathbf{R}\}) = \sum_i \chi_{si}(\{\mathbf{R}\})\psi_i(\{\mathbf{r}\};\{\mathbf{R}\}), \tag{2.4}$$

where χ are the linear coefficients and the ψ_i form a complete set, called the adiabatic solutions of the following Schrödinger equation:

$$H_e\psi_i(\{\mathbf{r}\};\{\mathbf{R}\}) = \epsilon_i\psi_i(\{\mathbf{r}\};\{\mathbf{R}\}), \tag{2.5}$$

with ϵ_i being the corresponding eigenenergies of the electronic system. The electronic Hamiltonian H_e is defined for a fixed configuration of the ions as:

$$\hat{H}_e = \hat{T}_e + \hat{V}_{ee}(\mathbf{r}) + \hat{V}_{ne}(\{\mathbf{r}\};\{\mathbf{R}\}), \tag{2.6}$$

where $\hat{T}_e$, $\hat{V}_{ee}$ and $\hat{V}_{ne}$ denote the kinetic and the corresponding electron-electron and electron-nuclei interaction terms in Eq. (2.2).

In general, the different adiabatic solutions (different i) in Eq. (2.5) are coupled during the motion of the ions. Neglect of this coupling is known as the adiabatic approximation and it is justified by the fact that $M \gg m_e$. Under this approximation, the ψ_i are considered as stationary states of the many-body *frozen* system. Furthermore, when the energy corrections to ϵ_i due to the dependence of the electronic wave function on the nuclear coordinates are also neglected, it is called the Born-Oppenheimer approximation [49]. Thus, the contribution to the total energy due to the nuclei is usually set as the zero energy reference.

At this point, we assume that the original *molecular* quantum mechanical problem can be approximated by the *interacting electronic* system under the influence of an external potential due to the nuclei, described by the Hamiltonian given in Eq. (2.6).

2.2.2. Kohn-Sham equations

Still the many-body electronic system is an extremely difficult problem, even to be solved numerically. A big step was taken toward the feasibility of the numerical treatment when the reformulation of the many-body ground state problem was settled with the theorems by Hohenberg and Kohn [50],

1. If two systems of electrons, one trapped in a potential $v_1(\mathbf{r})$ and the other in $v_2(\mathbf{r})$ have the same ground state density $n(\mathbf{r})$, then, necessarily, $v_1(\mathbf{r}) - v_2(\mathbf{r})$ is a constant. Corollary: the ground state density uniquely determines the potential and thus all properties of the system, including the many-body wave function.

2. For any positive integer N and potential $v(\mathbf{r})$ the energy density functional $E_{(v,N)}[n] = F[n] + \int v(\mathbf{r})n(\mathbf{r})d\mathbf{r}$ obtains its minimal value at the ground-state density of N electrons in the potential $v(\mathbf{r})$. The minimal value of $E_{(v,N)}[n]$ is then the ground state energy of this system.

From the above statements, the KS approach consists in replacing the original problem by that of a noninteracting electron system with the same ground state electron density. Then, we can formally rewrite the many-body ground state energy as

$$E[n] = T[n] + \int d\mathbf{r}\, n(\mathbf{r})V_{\text{ext}} + \frac{1}{2}\int d\mathbf{r} \int d\mathbf{r}' \frac{n(\mathbf{r})n(\mathbf{r}')}{|\mathbf{r}-\mathbf{r}'|} + E_{xc}[n], \tag{2.7}$$

where T contains the kinetic energy of a noninteracting electron system with the same n ground state density of the many-body system. The second term is the energy due to the Coulomb interaction between the nuclei and electrons (or might contain any other external field acting on the electrons). The third term is the Hartree energy, and the last one, E_{xc}, is the exchange-correlation energy containing all the rest many-body contributions, including part of the true many-body kinetic energy not taken into account in $T[n]$. Applying the minimization principle, the following KS equations are obtained, which have the mathematical structure of the one-electron Schrödinger equation:

$$\left\{-\frac{1}{2}\nabla^2 + V_{\text{eff}}(\mathbf{r})\right\}\psi_i(\mathbf{r}) = E_i\psi_i(\mathbf{r}), \tag{2.8}$$

but with a density dependent effective potential given by:

$$V_{\text{eff}}(\mathbf{r}) = V_{\text{ext}}(\mathbf{r}) + \underbrace{\int \frac{n(\mathbf{r}')}{|\mathbf{r}-\mathbf{r}'|}d\mathbf{r}'}_{V_H} + \underbrace{\frac{\delta E_{xc}[n]}{\delta n(\mathbf{r})}}_{V_{xc}}. \tag{2.9}$$

The density is calculated by summing the electronic charge density for all the occupied states up to the Fermi level,

$$n(\mathbf{r}) = \sum_{i}^{\text{occ}} |\psi_i(\mathbf{r})|^2, \tag{2.10}$$

where the Fermi level E_F is determined by the total number of electrons in the system

$$N = \int n(\mathbf{r}) d\mathbf{r}. \tag{2.11}$$

The above equations are solved self-consistently. The important point here is that the many-body problem of an electron gas at the ground state under an external potential, in terms of the one-electron Schrödinger equation picture, has been rigorously reformulated. This is the framework behind the theories which will be used in the present studies.

Concerning the excitation energies in the above scheme, the unoccupied KS orbitals do not enter the self-consistent cycle and thus play a limited role in the theory. In principle, KS eigenvalues are not designed to have a direct physical interpretation, except for the ones associated with the highest occupied molecular orbital (HOMO) [51]. Nevertheless, according to the Görling-Levy perturbation theory, quoted from Ref. [52]:

> "... KS [Kohn-Sham] orbital eigenvalues are not just auxiliary quantities without physical meaning; their difference is a well-defined approximation to excitation energies of zeroth order in the electron-electron interaction ...".

Since in the following treatment of the different problems we assume more dramatic approximations in V_{xc}, and also in the modeling of systems included in V_{ext}, the usual justification for considering the KS eigenvalues as approximate excitation energies lies on the standard and pragmatic procedure: to check *a posteriori* the reliability of the calculations when comparing to experimental data [53].

2.2.3. Local density approximation

DFT establishes the existence of E_{xc} as a functional of density, but does not provide the functional itself or a prescription of how to approximate it. The local density approximation (LDA) is one of the simplest approximations to E_{xc} and V_{xc} in order to provide a practical use of the DFT theory. Basically, it substitutes the unknown

real exchange-correlation function at each point by the corresponding value of the homogeneous noninteracting electron system at the corresponding density:

$$E_{xc} = \int \epsilon_{xc}[n(\mathbf{r})]n(\mathbf{r})d\mathbf{r}, \tag{2.12}$$

where ϵ_{xc} is the exchange-correlation energy per electron, which is well known from Monte-Carlo calculations [54], and several parameterizations for practical use can be found in the literature. For example, the parametrization due to Perdew and Zunger is given by

$$\epsilon_{xc}(n) = \underbrace{\frac{0.458}{r_s}}_{\epsilon_x} - \underbrace{\frac{\gamma}{1+\beta_1\sqrt{r_s}+\beta_2 r_s}}_{\epsilon_c} \tag{2.13}$$

$$V_{xc} = -\frac{0.611}{r_s} - \frac{\gamma(1+\frac{7}{6}\beta_1\sqrt{r_s}+\frac{4}{3}\beta_2 r_s)}{(1+\beta_1\sqrt{r_s}+\beta_2 r_s)^2}, \tag{2.14}$$

where the parameters $\gamma = 0.1423$, $\beta_1 = 1.0529$ and $\beta_2 = 0.3334$ are given in atomic units [55]. The first term in Eq. (2.13) represents the exact exchange energy, as obtained from Hartree-Fock calculations [56].

The LDA combined with DFT gives very good results for a large set of weakly correlated systems. However, there are special cases where the DFT-LDA approach is known to describe incorrectly certain features, such as the band gaps in semiconductors, which need special consideration.

Concerning the metallic surfaces, for a correct description of electronic states close to the vacuum level, a proper non-local exchange-correlation would be needed to correctly reproduce the interaction between an electron and the charge induced in the metal surface. The approximate DFT-LDA approach results in an incorrect exponential decay of the potential. Thus, in Section 2.5 we explain how to correct the self-consistent potential in order to correctly account for the *image potential* tail.

2.3. Metallic slabs and the stabilized jellium model

A system with translational invariance in a plane perpendicular to the z-axis is described by an only z-dependent effective potential $V_{\text{eff}}(\mathbf{r}) \equiv V_{\text{eff}}(z)$. The solutions to Eq. (2.8) are then written as

$$\psi_{n\mathbf{k}_\parallel}(\mathbf{r}) = \frac{1}{L}\phi_n(z)e^{i\mathbf{k}_\parallel\cdot\mathbf{r}_\parallel}, \tag{2.15}$$

where L is a normalization length, $\mathbf{r}_\parallel = (x, y)$ and $\mathbf{k}_\parallel = (k_x, k_y)$. By plugging the solution above in Eq. (2.8) the following 1D KS equation is obtained

$$\left\{ -\frac{1}{2}\frac{d^2}{dz^2} + V_{\text{eff}}(z) \right\} \phi_n(z) = E_n \phi_n(z), \tag{2.16}$$

with

$$V_{\text{eff}} = V_{\text{ext}} + \int \frac{n_-(z')}{|\mathbf{r} - \mathbf{r}'|} d\mathbf{r}' + V_{xc}, \tag{2.17}$$

and the total energy is given by

$$E_{n\mathbf{k}_\parallel} = E_n + \frac{k_\parallel^2}{2m_n^*}, \tag{2.18}$$

where for each n-band, we have introduced a phenomenological effective mass m_n^* accounting for the effects of the underlaying crystal lattice on the parallel motion. For example, this can account for the surface corrugation effects or more pragmatically, it might be fitted to the realistic band structure. The electronic structure calculations in this thesis have been obtained by assuming $m^* = 1$, both in perpendicular and parallel direction.

The V_{eff} potential is enormously simplified in the *simple* jellium model approach, where the crystal ions are substituted by a constant positively charged background n_+, corresponding to the charge density of the metal. Then, by manipulating the electrostatic term (see Appendix B.1) the simple jellium effective potential is finally written as:

$$V_{\text{eff}}(z) = -2\pi \int_{-\infty}^{\infty} \left[n_-(z') - n_+(z') \right] |z - z'| dz' + V_{xc}[n_-(z)]. \tag{2.19}$$

where the electron charge density is given by n_-. The crude jellium approximation is justified for the simple metals by their rather weak ionic pseudopotentials.

The next step in the crystal lattice description beyond the simple jellium model, is to add a structureless pseudopotential, i.e., to correct the positive background by a constant shift. This correction, known as the stabilized jellium model, was proposed by Perdew, and, Shore and Rose, with different approaches but similar results. The constant shift can be considered as an averaged pseudopotential over the bulk Wigner-Seitz cell. A mechanically stable metal ($dE/dr_s = 0$) is also demanded, which provides qualitative correct values of properties such as the cohesive energy, surface energy and bulk modulus. This is an important issue when the study of metallic surfaces is addressed. In particular, a realistic work function is an important ingredient when

the energies of calculated electronic states localized at the surface are to be compared with experiments. Thus, in this thesis (Chapters 6 and 7) we have used the following effective potential form

$$V_{\rm eff}(z) = -2\pi \int_{-\infty}^{\infty} \left[n_-(z') - n_+(z')\right] |z - z'| dz' + V_{xc}[n_-(z)] + V_{ps}(z), \qquad (2.20)$$

with $V_{ps} =< \delta v >$ only for z inside the crystal, where the following expression has been used

$$< \delta v >= -\frac{1}{5}\left[\frac{9\pi}{4}\right]^{2/3} r_s^{-2} + \frac{1}{4\pi}\left[\frac{9\pi}{4}\right]^{1/3} r_s^{-1} + \frac{1}{3} r_s \frac{d\epsilon_c}{dr_s}, \qquad (2.21)$$

for describing the metallic slabs [57]. For example, for flat Pb metal the corresponding values is $< \delta v >= -1.8$ eV. Further details on the construction of the pseudopotentials for the Pb/Cu(111) are discussed in Section 2.5.

A more sophisticated stabilized jellium model has been proposed [58] (not considered in this thesis) that takes into account the relaxation in the interlayer spacing in a metallic slab, and so, accounts for the self-compression. This model can improve the description for Pb overlayers on Cu(111), at least, for small number of monolayers. Indeed, introducing self-compression effects by hand [11, 17] has improved slightly the agreement between theoretical predictions and experimental observation of the most abundant island heights reported for Pb extended islands grown on Cu(111) surfaces.

Among simple schemes allowing to take into account the relaxation, the *ultimate jellium* model can be used. This model is introduced in the following section.

2.4. The ultimate jellium model in axial symmetric systems

The ultimate jellium model (UJ) is an approach to obtain ground state geometries within a jellium picture. Once the number of electrons is fixed and the spatial constrictions are set (for example, symmetry constrictions), the ground state geometry is obtained self-consistently. The background positive charge density is fully relaxed in shape and density so that it equals at every point to the electron density. In this way, the Coulomb term in the potential always vanishes. Thus, the shape and energy of the system result from the interplay between the exchange-correlation and kinetic energies.

One characteristic of this model is that there is only one equilibrium charge density at $r_s \approx 4.18\, a_0$, being $n = 3/(4\pi r_s^3)$, which is close to that of Na with $r_s = 3.93\, a_0$ [59].

The UJ has been shown to reproduce qualitatively *ab initio* geometries in sodium clusters [60]. Futhermore, this model has been used also for addressing the study of the breaking of nanocontacts and the corresponding resonances appearing in the process [41].

In Chapter 8 we present an electronic transport study of the breaking of Na nanocontacts formed during the stretching of a Na nanowire. This kind of processes in real experiments have a stochastic nature and the thinest contacts are expected to present a quasi-cylindrical symmetry. Thus, a natural approach to the study of nanowires is to consider the perfectly axial symmetric case in order to reduce the complexity of the analysis, and also because the properties of the system can be calculated easier taking advantage of the reduced dimensionality of the computational problem. In the rest of the section below we describe the calculation method based on the DFT-LDA and UJ model to obtain the one-electron effective potentials developed by E. Ogando *et al.* in Ref. [41] within the MIKA package (Appendix B).

We assume a system with axial symmetry along the z direction, so the cylindrical coordinates (ρ, φ, z) are used. Then, demanding periodic boundary conditions in z direction, the wave functions are sought in the form

$$\psi_{mnk_z}(\rho, z, \varphi) = e^{im\varphi} U_{mnk_z}(\rho, z), \tag{2.22}$$

where $U_{mnk_z}(\rho, z)$ are Bloch functions,

$$U_{mnk_z}(\rho, z + L_{\text{cell}}) = e^{ik_z L_{\text{cell}}} U_{mnk_z}(\rho, z), \tag{2.23}$$

with L_{cell} corresponding to the computational cell size, which is taken large enough to avoid interaction between the adjacent periodic systems. Then, the KS equations are transformed to

$$-\frac{1}{2}\left(\frac{1}{\rho}\frac{\partial}{\partial\rho} + \frac{\partial^2}{\partial\rho^2} - \frac{m^2}{\rho^2} + \frac{\partial^2}{\partial z^2} + 2V_{\text{eff}}(\rho, z)\right) U_{mnk_z}(\rho, z) = \epsilon_{mnk_z} U_{mnk_z}(\rho, z), \tag{2.24}$$

with electronic density given by

$$n_-(\mathbf{r}) = 2\sum_{mnk_z} (2 - \delta_{0m}) f_{mnk_z} |U_{mnk_z}(\mathbf{r})|^2. \tag{2.25}$$

The $2(2-\delta_{0m})$ factor accounts for the spin and m-subspace degeneracy. The occupation numbers obey the Fermi-Dirac statistics through the Fermi-Dirac distribution function f, with the Fermi level determined by the number of electrons in the system. The use

of the ultimate jellium model means that the Coulomb term is set equal to zero, then only the exchange-correlation potential defines the KS potential:

$$V_{\text{eff}} = V_{xc}[n_-(\rho, z)], \tag{2.26}$$

which is evaluated within the LDA given by Eq. (2.14). In addition, a finite temperature of 1200 K [through f in Eq. (2.25)] is considered to stabilize the solution.

When considering the uniform infinite UJ nanowires of Na, there are radii for which the energy is at a minimum. They correspond to most stable wires. The first magic radii here are taken as $R = 4.3a_0$, $7.7a_0$, $10.7a_0$ ..., which slightly differ from the previously reported values [41]. These "magic radii" are analogous to the well-known "magic numbers" of abundance in metal clusters of different sizes.

More details on the simulation of the breaking of a Na nanowire modeled by UJ are given in Chapter 8 (Section 8.2).

2.5. 1D description of the Pb/Cu(111) system

2.5.1. Pb nanoislands

The Pb/Cu(111) system is described in this thesis with a 1D model potential derived from self-consistent calculations using the DFT within the LDA (Subsection 2.2). The potential only depends on the z coordinate perpendicular to the surface. A free-electron motion parallel to the surface is assumed with effective mass $m^* = 1$.

The above model is justified in the study of Pb nanoislands when the lateral dimensions are substantially larger than the mean free path of the electron. In some of the experiments considered in this thesis, for example in Refs. [20] and [25], the lateral dimensions of the Pb islands (see Fig. 2.1) are around 500–1000a_0 (25–50 nm). This value is larger than the mean free path L of the electron, in particular, at energies close to the Fermi level. Indeed, at this energy, the electron is essentially scattered by the phonons, where at temperatures as low as 5 K, the electron-phonon decay rate is $\gamma_{e-\text{ph}} \approx 20$ meV [61]. Then, the lifetime is given by $\tau = \gamma_{e-\text{ph}}^{-1} = 32.9$ fs and $L \sim v_F \cdot \tau \approx 100a_0$ (5 nm), where the Fermi velocity is $v_F = \frac{\hbar}{m_e} k_F = \sqrt{2(E_F - U_0)} \sim 1a_0$ with $U_0 \sim -13.5$ eV being the inner potential (with respect to the vacuum level).

The method to obtain one-dimensional effective potentials for describing metallic overlayer-substrates was developed by E. Ogando *et al.* [17–19] and applied to the study of systems such as Pb/Cu(111), Na/Al(111) and Na/Al(100). In the following

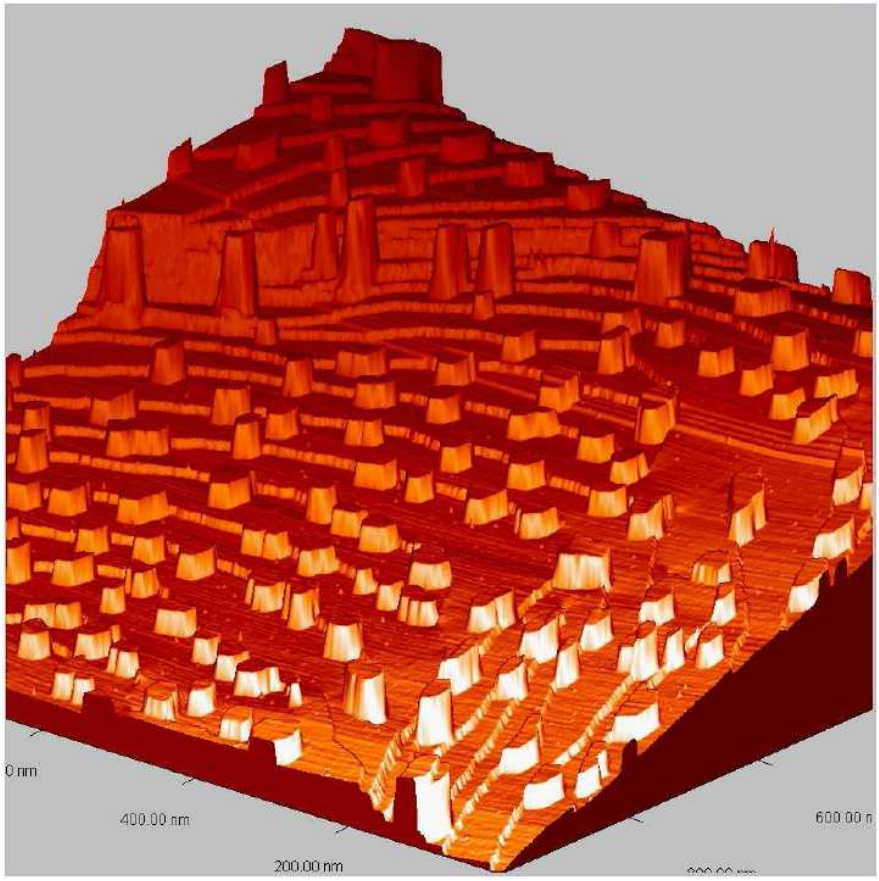

Figure 2.1.: An example of a topographic scanning tunneling microscopy image of Pb islands grown on Cu(111) (Courtesy of Rodolfo Miranda).

section we describe the steps involving the construction of these potentials for the Pb/Cu(111) system.

2.5.2. Bulk pseudopotential

The Cu(111) substrate is represented with an unscreened pseudopotential derived from the model potential proposed by Chulkov *et al.* [64], in which an atomic plane structure in z direction is accounted for by a periodic function. As the Cu surface is covered by several Pb layers, only the bulk part of the model potential is considered. The bulk function of the 1D-model potential is given by

$$V_{\mathrm{Cu}}(z) = A_{10} + A_1 \cos\left(\tfrac{2\pi}{d} z\right), \quad -\tfrac{d}{2} < z < \tfrac{d}{2} \tag{2.27}$$

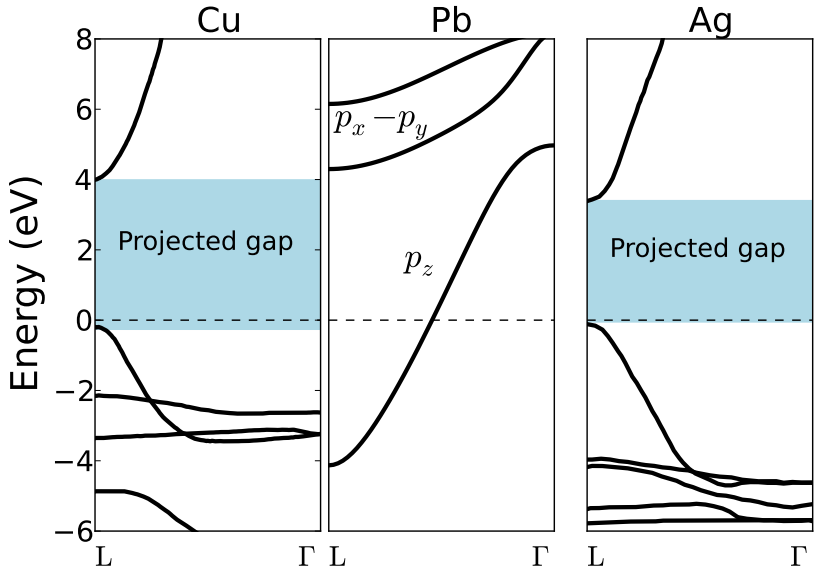

Figure 2.2.: Electronic band structure of bulk Cu [62], Pb [29,61,63] and Ag [62] along the Γ−L direction. Energies are given with respect to the Fermi level denoted by horizontal dashed lines. The shaded areas in Cu and Ag represent the projected band gap providing the confinement barrier in the substrate for the QWSs in Pb overlayers. The orbital character of the Pb bands is indicated.

where $d = 3.943\,a_0$ is the Cu interlayer distance in the (111) direction and A_{10} and A_1 are fitting parameters, optimized in such a way that the experimental Cu(111) work function, (4.94 eV [64]), as well as the projected band structure at the $\overline{\Gamma}$ point (see Fig. 2.2), are reproduced by the DFT-LDA calculation for the pristine Cu(111) surface.

Using periodic boundary conditions at $\pm d/2$ the KS equations are solved for the fixed $V_{\text{eff}}(z) = V_{\text{Cu}}(z)$ potential. Then, from the calculated eigenfunctions and experimental work function, a mean density parameter $r_s = 2.55\ a_0$ is recovered, comparable to the experimental value $r_s = 2.67\ a_0$. From the density, we can also easily obtain the exchange-correlation $V_{xc}^{\text{Cu}}(z)$ potential [Eq. (2.14)].

The Hartree term, however, needs special care because, in the periodic treatment above, due to the absence of the vacuum, the height of the surface dipole-barrier is not known as the energy origin of the Hartree term inside the bulk is not defined. This is fixed provisionally by setting the Hartree potential to zero at the boundaries of the periodic cell. After adding a homogeneous neutralizing positive background of the previously obtained $r_s = 2.55\,a_0$, the Hartree potential is retrieved. The periodic

unscreened pseudopotential, then, is evaluated as

$$V_{\text{unsc}}^{\text{Cu}} = V_{\text{eff}}^{\text{Cu}} - V_H^{\text{Cu}} - V_{xc}^{\text{Cu}}. \tag{2.28}$$

In order to use the above pseudopotential in slab calculations the correct Hartree potential must be found. For this purpose, we construct a semi-infinite slab (15 ML) by repeating the previously obtained periodic one and we add enough vacuum space. Here the Cu(111) edge is defined as one half ML above the last atom plane.

Then, the potential is shifted iteratively by a constant until the proper work function of the Cu(111) surface (4.94 eV) is retrieved in self-consistent calculations with $r_s = 2.55\, a_0$. The resulting screened pseudopotential is similar to the bulk part of the original model potential [Eq. (2.27)], but with different parameters.

2.5.3. Pb overlayers on Cu(111)

The Pb overlayer is described by the stabilized jellium model, where addition of a constant attractive potential inside the metal allows to retrieve the Pb work function value ($\Phi = 4.08$ eV) consistent with *ab initio* calculations and experimental data. The jellium description should hold in the energy range where the p_z band of the parent bulk-electronic structure along Γ-L can be approximated by a free-electron parabola (see Fig. 2.2).

For each Pb overlayer thickness, the semi-infinite Pb/Cu(111) potential is obtained by solving self-consistently the 1D KS equations within the LDA. It is convenient to perform the calculations in a symmetric system as considered in Fig. 2.3. In this way, the electronic states confined in the Pb overlayer can be easily identified from the eigenvalues, as they appear as doubly quasi-degenerate. This configuration is also considered in the numerical method for the many-body calculations of the electronic state lifetimes, to be presented in the following Chapter 3.

Within the wave packet propagation method (Chapter 4), a very large substrate is necessary to include outgoing boundary conditions inside the bulk, which is a characteristic technicality of the method. In this particular case, we have built a proper one-electron effective potential based on the self-consistent one: We have removed one of the surfaces, and starting from the fifth Cu atomic layer, we have extended the periodic Cu substrate up to 70 MLs. In this way, the spurious effects due to the quantization of the continuum states in the supercell geometry are removed.

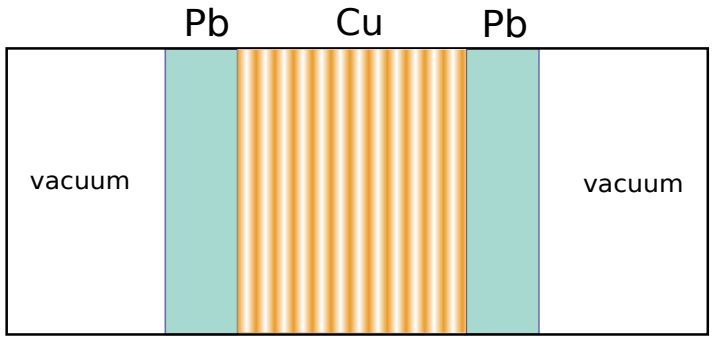

Figure 2.3.: Scheme of the metal slab considered in the calculation of the Pb/Cu(111) electronic structure.

2.5.4. Image potential

The effective one-electron potential V_{eff} obtained by the DFT-LDA scheme does not reproduce the long-range image charge interaction V_{im} for an electron being on the vacuum side above a metallic surface. Nevertheless, for the present study of the states close to the vacuum level it is of essential importance to account for V_{im}. We then modify the V_{eff} potential to include the image potential for an electron in front of a metallic surface. This is done by considering the following form for the model potential:

$$V_s(z) = \begin{cases} \frac{A\exp[-\lambda(z-z_0)]-1}{4(z-z_{\text{im}})} & z \geq z_0 \\ V_{\text{eff}}(z) & z < z_0, \end{cases} \tag{2.29}$$

where z_{im} is the image plane position and z_0 is an auxiliary parameter. We take $z_{\text{im}} = 1.23\,a_0$ in front of the Pb jellium edge from Ref. [65], and z_0 is set to $z_0 = z_{\text{im}} + 0.5\,a_0$, which has been checked to give a smooth final potential. The rest of the parameters, A and λ, are fixed by the continuity of $V_s(z)$ and its derivative $V_s'(z)$ at z_0:

$$\begin{aligned} A =& 4(z_0 - z_{\text{im}})V_{\text{eff}}(z_0) + 1 \\ \lambda =& \frac{1}{(z_0 - z_{\text{im}})}\left(\frac{\left[1 - 4(z_0 - z_{\text{im}})V_{\text{eff}}'(z_0)\right]}{A} - 1\right). \end{aligned} \tag{2.30}$$

Chapter 3

Theoretical methods II: Excitation lifetimes in the GW approximation

3.1. Introduction: Electron and hole excitation lifetimes

3.1.1. Decay rate contributions

Excited electrons can be viewed as electrons being promoted from an occupied state below the Fermi level to a higher energy unoccupied state. On the other hand, an electron being removed from the Fermi sea creates a hole, which behaves as an electron with opposite charge. These excitations are screened "instantaneously" in metals ($\tau_{\text{screen}} < 1$ fs) so that the mutual interaction (excitonic effects) can be neglected.

These screened excited particles are the electron (hole) quasiparticles, which decay in time. In the case of metallic quantum wells, there are several quasi-particles in the material which can scatter inelastically an electron excited into a QWS, leading to its decay. We focus on the contribution of phonons (collective excitations of the underlaying atomic lattice), other electronic (hole) excitations and scattering by defects.

In general, it is a good approximation to consider that the scattering events contribute additively to the decay rate Γ of the excited states as [15]:

$$\Gamma = \gamma_{1e} + \gamma_{e-e} + \gamma_{e-\text{ph}} + \gamma_{\text{def}}. \tag{3.1}$$

The first term represents the contribution from the energy-conserving resonant electron transfer mechanism. The second term, γ_{e-e}, is the inelastic electron-electron scattering to lower energies and $\gamma_{e-\mathrm{ph}}$ is the corresponding electron-phonon decay rate. The effect of the defects is accounted for by the last term γ_{def}. In certain cases Eq. (3.1) is not fulfilled, as has been shown in the study of image state resonances [66], where the resonant and inelastic decays do not contribute additively to the total decay rate.

The lifetime of the state is determined by the Heisenberg uncertainty principle ($\Delta E \Delta t = \hbar$) as $\hbar\tau^{-1} = \Gamma$. Usually, for electronic decay processes at surfaces, the decay rate is given in meV and the lifetime is measured in femtoseconds [1 femtosecond (fs) = 10^{-15} seconds]. The two quantities are related by

$$\tau\,[\mathrm{fs}] \approx \frac{658}{\Gamma\,[\mathrm{meV}]}. \tag{3.2}$$

A central issue is to identify which of the broadening mechanisms in Eq. (3.1) is the main one in determining the lifetime of the electronic (hole) states. With this knowledge one can attempt to design systems with desired surface electronic properties (within the physically possible). For example, excited electrons at surfaces play an important role in surface reactivity. Chemical reactions in ad-atoms and ad-molecules, induced by photons or electrons injected by the STM tip, involve an excited electronic state as an intermediary step. Then, the lifetime of the excited state determines the efficiency of the given reaction channel [32].

On the other hand, the existence of "simple" electronic states at surfaces challenges the precision of state-of-the-art photoemission and scanning tunneling microscope experiments. Together with the theoretical tools for interpreting the results, these states are also used for the experimental setup calibration. In this case, the lifetime is also a central quantity in experiments. A short lifetime, for example, might prevent the state from being probed experimentally.

3.1.2. The electron-electron decay rate

The decay rate of excited electrons and holes in a homogeneous electron gas, in the high electron density n limit, with energies close to the Fermi level, E_F, and low temperature, is given by the Quinn-Ferrell (QF) formula [67]:

$$\Gamma_{QF} \approx 2.5019\, r_s^{5/2} (E - E_F)^2, \tag{3.3}$$

where r_s is the density parameter given by $r_s = [3/(4\pi n)]^{1/3}$. A quadratic dependence of the decay rate on energy, as in Eq. (3.3), is usually referred to as a 3D Fermi liquid

behavior. It has been found that this model, although in principle only valid for the high density limit, does a good job in estimating the $e-e$ decay rates in metals with realistic densities. Then, an important issue to address when studying lifetimes of electron (hole) states is to ask to what extent are the actual lifetimes different from the 3D Fermi liquid behavior.

Another important issue to be addressed is the dimensionality of the system. In a 2D-gas, similar results to that of Eq. (3.3) are obtained [68], but the energy dependent part of the solution in this case includes a logarithmic factor $\sim (E-E_F)^2 \ln|E-E_F|^{-1}$ instead of the simpler $\sim (E-E_F)^2$.

Then, the question arises: what is the character (2D or 3D) of the quantum well state lifetimes, in our case of Pb overlayers? And consequently, what behavior might be expected for energies close to the Fermi level? The electronic structure for Pb overlayers grown in (111) direction is clearly quantized at $\overline{\Gamma}$ (see for example the band structure of a Pb slab in Fig. D.2). However, as it has been shown in photoemission experiments, the lifetimes of QWSs close to the Fermi level, even for small overlayer thicknesses, follow a 3D Fermi liquid behavior in Pb/Si(111) [24], which has been also seen in STM studies [25,61]. In principle, the finite size of the overlayer could affect the screening of the excitations in the metal, which is a central property determining the electron-electron decay. The screening spatial range in bulk metals can be characterized by the 3D Thomas-Fermi screening length [24, 68], which for Pb ($r_s = 2.3a_0$) is:

$$\lambda_s = \frac{1}{2}\left(\frac{\pi}{3n}\right)^{1/6} = \frac{1}{2}\sqrt{\pi(4/9\pi)^{1/3} r_s} = 0.97a_0. \tag{3.4}$$

This value is smaller than 1 ML thickness ($5.41a_0$), which is consistent with the observed 3D character of the lifetimes. Our results to be presented in next chapter are also consistent with the 3D character reported above. The similarity between the 3D density of states of a free electron gas and the 2D density of states in an infinite potential well which coincide at $\overline{\Gamma}$ can also provide an insight of why the lifetimes at $\overline{\Gamma}$ show a 3D Fermi liquid character (see also the brief discussion of Fig. D.1 in Appendix D).

Finally, it might happen that the states are not totally localized inside the metal where the $e-e$ scattering takes place. Then, the decay rate of the state is reduced. In this case, the decay rate might be estimated (neglecting the non-locality of the many-body decay and assuming that the inelastic scattering only takes place inside the metal) by multiplying the bulk metal decay rate value by the penetration of the wave function inside the metal. This issue is behind the quantum size effects on the lifetimes reported at the end of next Chapter 6.

3.2. Hedin's equations and GW approximation

The density functional theory (DFT) presented in previous Chapter 2 provides the ground state properties of a many-electron system, however, the many-body lifetime of the electronic excitations is not directly accessible with this formalism. Then, one should go beyond ground state DFT theories. For example, the time-dependent DFT [69, 70] allows, in principle, an exact description of neutral excitations (such as those involved in absorption of photons) [71].

In this thesis we use the Green's function theory to address the lifetime of electron excitations. Whereas the DFT contains a formalism based on the electronic density $n(\mathbf{r})$, the central quantity in the formalism studying the many-body excitations considered in this thesis is the Green's function G (to be defined below). Indeed, G is directly related to photoemission spectra in the limit of large kinetic energy ("sudden approximation") [72,73]. In Fig. 3.1 a direct photoemission and the inverse photoemission process are represented. In direct photoemission, a hole is created, i.e., a $(N-1)$ system is formed from the N-body electron system. On the other hand, in inverse photoemission the system acquires an additional electron so that a $(N+1)$ electron system is created.

The photoemission spectra are usually considered as a faithful map of the density of occupied or unoccupied states of the probed sample. This is linked to the picture of independent electrons which occupy some well-defined energy levels in the system. However the electrons in the sample are not independent, but they form a many-body system. An electron that leaves the sample will lead the remaining electrons to relax [71]. This process will affect the photoemission spectra, by renormalizing the single-particle energy levels and inducing a linewidth broadening. Indeed, the population decay of electronic states (leading to linewidth broadenings) can be directly measured in time-resolved two-photon photoemission experiments. One can still retain the one-electron picture, but dealing with "fictitious" particles called quasielectrons and quasiholes that derive from the many-body theory to be presented below.

In an interacting N-electron system, the probability amplitude of an additional electron to be propagated from $(\mathbf{r}', t')$ to $(\mathbf{r}, t)$ for $t > t'$ is given by the one-electron Green's function:

$$G(\mathbf{r}, \mathbf{r}', t, t') = -i\langle N|\mathcal{T}[\hat{\psi}(\mathbf{r}, t)\hat{\psi}^{\dagger}(\mathbf{r}', t')]|N\rangle, \tag{3.5}$$

where $\mathcal{T}$ is the time-ordering operator defined by

$$\mathcal{T}\left(\hat{A}(t_1)\hat{B}(t_2)\right) = \begin{cases} \hat{A}(t_1)\hat{B}(t_2) & \text{if} \quad t_1 > t_2 \\ \hat{B}(t_2)\hat{A}(t_1) & \text{if} \quad t_2 > t_1, \end{cases} \tag{3.6}$$

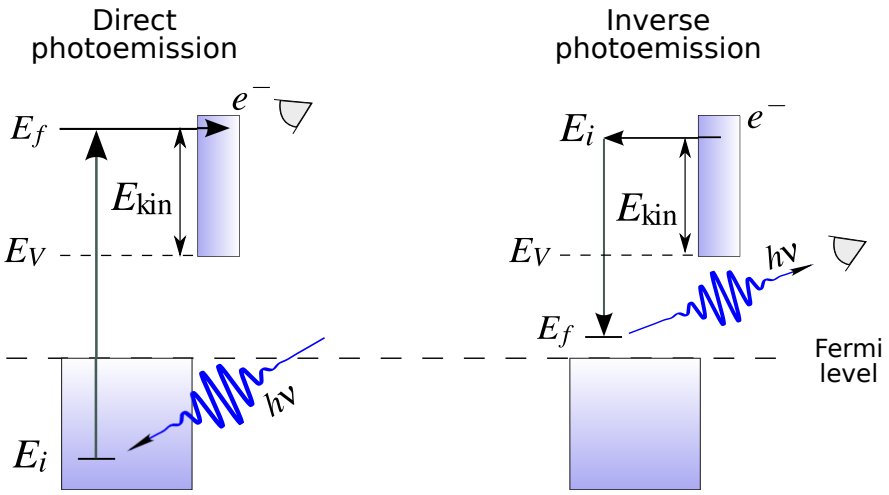

Figure 3.1.: Schematic representation of an electron (e^-) ejection by a photon of energy $h\nu$ in direct photoemission and electron injection in inverse photoemission spectroscopic experiments for probing electronic and structural properties as well as the electron dynamics in bulk and nanostructured surfaces. E_i and E_f refer to the initial and final electron states, respectively. The kinetic energy of the electron E_{kin} is measured with respect to the vacuum level (E_V). Adapted from Ref. [71].

with $\hat{\psi}$ being the electron annihilation field operator in the Heisenberg picture and $|N\rangle$ is the many-body N-electron ground state [72]. When $t < t'$, Eq. (3.5) describes the probability amplitude of a hole created in the N-electron system at $(\mathbf{r}, t)$ to be propagated to $(\mathbf{r}', t')$.

The formulation of the many-body fundamental equation [Eq. (2.1)] in terms of the Green's functions, allowed Hedin [74] to develop a perturbative approach to the many-body problem. This further gives the possibility to reformulate the exact many-body mathematical problem as a set of integro-differential equations, known as Hedin's equations, to be solved self-consistently [72]:

$$\begin{aligned}
W(12) =& v(12) + \int v(13)P(34)W(42)\,\mathrm{d}3\mathrm{d}4, \\
\Sigma(12) =& i\int\int G(13^+)W(1,4)\Gamma(324)\,\mathrm{d}3\mathrm{d}4, \\
G(12) =& G_0(12) + \int\int G_0(13)\Sigma(34)G(42)\,\mathrm{d}3\mathrm{d}4, \\
\Gamma(123) =& \delta(1-2)\delta(1-3) - \int\int\int \frac{\delta\Sigma(12)}{\delta G(45)} G(46)\Gamma(673)G(75)\,\mathrm{d}4\mathrm{d}5\mathrm{d}6\mathrm{d}7, \\
P(12) =& -i\int\int G(13)\Gamma(342)G(41^+)\,\mathrm{d}3\mathrm{d}4
\end{aligned} \tag{3.7}$$

In the notation above $(1) \equiv (\mathbf{r}, t)$ refers to the standard spatial and temporal compact notation and 1^+ refers to the $t \to t + i\eta^+$ substitution, η^+ being a positive infinitesimal number. P is the time-ordered polarization operator, v is the bare Coulomb interaction, W is the dynamical screened interaction, and Γ is the vertex function.

The functional derivative in the expression for Γ prevents these equations to be solved in a straightforward way. Thus, approximations are necessary. The zero order perturbation term of Γ in terms of W is

$$\Gamma^0(123) = \delta(12)\delta(23), \tag{3.8}$$

from which a set of four equations is obtained

$$\Sigma(12) = iG(12)W(12), \tag{3.9a}$$

$$G(12) = G_0(12) + \int\int G_0(13)\Sigma(34)G(42)\mathrm{d}3\mathrm{d}4, \tag{3.9b}$$

$$P(12) = -iG(12)G(21), \tag{3.9c}$$

$$W(12) = v(12) + \int\int v(13)P(34)W(42)\mathrm{d}3\mathrm{d}4. \tag{3.9d}$$

The approximation in the self-energy given in Eq. (3.9a) is the so-called GW approximation. Since the functional term is not present, these equations might be solved iteratively until self-consistency is obtained. However, these calculations are still computationally hard, and usually different approximations or levels of self-consistency are further employed.

It is not a trivial task to go beyond the GW approximation and to still maintain good predictive power. Furthermore, in practice it has been found that for band structure calculations, the fully self-consistent GW calculations perform worse than the simple G_0W_0 scheme. For the latter, the band-gap error of DFT-LDA in semiconductors appears corrected [72].

In this thesis the evaluation of the quantities of Eqs. (3.9)[a-d] have been addressed in a non self-consistent way and under further approximations. In the formalism outlined in following sections we use the density response function χ [see Eq. (3.33)], which is related to the polarizability P [72] appearing in Hedin's equations by:

$$\chi(12) = P(12) + \int\int P(13)v(34)\chi(42)\mathrm{d}3\mathrm{d}4. \tag{3.10}$$

In the literature the formulation of the quantities above can be found in terms of the inverse dielectric function ϵ^{-1}:

$$\epsilon^{-1}(\mathbf{r}, \mathbf{r}', \omega) = \delta(\mathbf{r} - \mathbf{r}') + \int d\mathbf{r}'' v(\mathbf{r} - \mathbf{r}'')\chi(\mathbf{r}'', \mathbf{r}', \omega). \tag{3.11}$$

In the rest of the sections we provide the basic equations describing the lifetimes of electron and hole excitations. Then, we provide the particular set of equations adapted to one-dimensional potentials.

3.3. The quasiparticle lifetime

Within an intuitive picture, when an electron moves through the many-electron system in a metal, it pushes or pulls on its neighbors and, as a consequence, it becomes screened by a cloud of positively charged holes. The real particle plus its cloud is called the quasiparticle (see Fig. 3.2). It turns out that an electron quasiparticle, to some extent, behaves as its parent electron, except that the interaction with other quasiparticles becomes weak in comparison to the electron-electron Coulomb interaction. This weak interaction is the dynamically screened interaction W.

Quasiparticles can be rigorously defined as excitations appearing in the many-body system. Indeed, the Green's function can be written [72] in the spectral representation as:

$$G(\mathbf{r}, \mathbf{r}', \omega) = \sum_j \frac{\tilde{\psi}_j(\mathbf{r}, \omega)\tilde{\psi}_j{}^{\dagger}(\mathbf{r}', \omega)}{\omega - E_j(\omega)}, \tag{3.12}$$

where $\tilde{\psi}_j$ are solutions to the quasiparticle equation:

$$\hat{H}_0\tilde{\psi}_j(\mathbf{r}) + \int \Sigma(\mathbf{r}, \mathbf{r}'; E_j)\tilde{\psi}_j(\mathbf{r}')d\mathbf{r}' = E_j\tilde{\psi}_j(\mathbf{r}). \tag{3.13}$$

$\hat{H}_0$ is the one-electron Hamiltonian

$$\hat{H}_0(\mathbf{r}) = -\frac{1}{2}\nabla^2 + V_{\text{ext}}(\mathbf{r}) + \int \frac{n(\mathbf{r}')}{|\mathbf{r} - \mathbf{r}'|}d\mathbf{r}', \tag{3.14}$$

where V_{ext} is the external (mean field) potential and n is the electron density.

The structure of the quasiparticle equation looks similar to other mean-field single-particle equations (for example the Kohn-Sham equations in Eqs. (2.8) and (2.9)).

There are important differences, however, between Kohn-Sham orbitals $\psi(\mathbf{r})$ and those of the quasiparticles $\tilde{\psi}(\mathbf{r})$. The latter orbitals, for example, are not required to be orthogonal. Furthermore, the quasiparticle eigenergies are not necessarily real numbers. However, empirically it is found that Kohn-Sham and quasiparticles eigenfunctions are very similar (when the calculation of both on the same system is possible) [75]. Thus, it is plausible to consider the quasiparticle equation as a perturbation to the Kohn-Sham equation. Then, assuming $\tilde{\psi} \approx \psi$ and expanding the quasiparticle energy in a Taylor series about the Kohn-Sham (mean-field) energy E_j^{KS} (assuming small differences between E_i and E_i^{KS}), we obtain:

$$E_j \approx E_j^{KS} + \int\int d\mathbf{r}d\mathbf{r}'\psi_j^*(\mathbf{r})\psi_j(\mathbf{r}')\left[\Sigma(\mathbf{r},\mathbf{r}';E_j) - V_{xc}(\mathbf{r}')\delta(\mathbf{r}-\mathbf{r}')\right]. \tag{3.15}$$

The self-energy, depending on the quasiparticle energy, is similarly expanded about E_i^{KS}:

$$\Sigma(\mathbf{r},\mathbf{r}';E_j) \approx \Sigma(\mathbf{r},\mathbf{r}';E_j^{KS}) + (E_j - E_j^{KS})\left.\frac{\partial\Sigma(\mathbf{r},\mathbf{r}';\omega)}{\partial\omega}\right|_{\omega=E_j^{KS}}. \tag{3.16}$$

Note that the approximate energy is given in general by a complex number, thus we can split the real and imaginary part:

$$E_j = E_j^{\mathrm{Re}} + iE_j^{\mathrm{Im}}. \tag{3.17}$$

Then, the probability to find a quasiparticle excited at $t = 0$ in the jth state at $\mathbf{r}$ position will decay in time:

$$|\psi_j(\mathbf{r},t)|^2 \propto e^{2E_j^{\mathrm{Im}}t}, \tag{3.18}$$

from which the inverse lifetime (or decay rate) of the quasiparticle is identified as

$$1/\tau = \Gamma = -2E_j^{\mathrm{Im}}. \tag{3.19}$$

If the imaginary part of the quasiparticle energy is evaluated in on-shell approximation ($E_j = E_j^{KS}$), the electron-electron inelastic decay rate of the ψ_j excited state with energy E_j^{KS} can be calculated by the following expression:

$$\Gamma_j = -2\,\mathrm{Im}\left[\int\int d\mathbf{r}\,d\mathbf{r}'\psi_j^*(\mathbf{r})\Sigma(\mathbf{r},\mathbf{r}',E_j^{KS})\psi_j(\mathbf{r}')\right]. \tag{3.20}$$

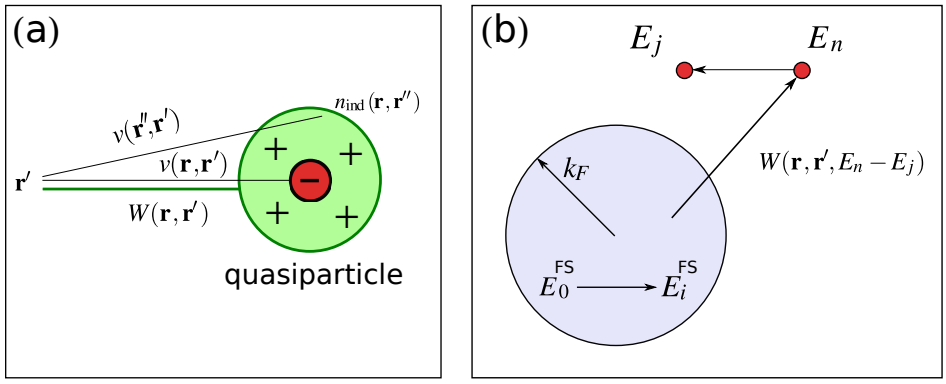

Figure 3.2.: (a) Screening of the Coulomb potential $v(\mathbf{r},\mathbf{r}')$ by the induced n_{ind} positive hole around the electron (adapted from Ref [75]). (b) Schematic representation (adapted from Ref. [76]) of the scattering of an external hot electron with a Fermi system (FS) of N interacting electrons at $T = 0$. The external electron, in an initial state of energy $E_n > E_j$, is scattered into an available state of energy E_j ($E_n > E_j > E_F$) by exciting the cold Fermi system from its many-body ground state of energy E_0^{FS} to some many-body excited state of energy E_i^{FS} ($E_i^{FS} - E_0^{FS} = E_n - E_j$).

3.4. Electron-electron decay rate in metallic slabs

3.4.1. Equations

In this section we derive the equations used in Chapter 6 for calculating the electron-electron inelastic decay rate of quantum well states formed in Pb thin overlayers supported on Cu(111). The Pb/Cu(111) system is described by a z-dependent one-electron effective potentials derived from DFT calculations. Thus, we consider slabs characterized by translational invariance, i.e., a homogeneous free-electron gas, along the surface ($\mathbf{r}_\parallel = (x, y)$ plane). In this picture a single-particle wave function with two-dimensional (2D) wave vector $\mathbf{k}_\parallel$ parallel to the slab surface and quantum number j is represented in the form

$$\Psi_{j\mathbf{k}_\parallel}(\mathbf{r}) = \frac{1}{L} e^{i\mathbf{k}_\parallel \cdot \mathbf{r}_\parallel} \phi_j(z), \tag{3.21}$$

where L is a normalization length, and the energies are given by

$$E_{j\mathbf{k}_\parallel} = E_j + \frac{\mathbf{k}_\parallel^2}{2m_j^*}, \tag{3.22}$$

where we have introduced the effective mass in parallel direction for each j band. Within the considered translational symmetry, the mathematical description is simplified by taking the 2D Fourier transforms of the quantities involved in the calculation

of the lifetime presented above [77]. The 2D Fourier series expansion of the self-energy is defined here as

$$\Sigma(\mathbf{r},\mathbf{r}',\omega)=\frac{1}{L^2}\sum_{\mathbf{q}_\parallel} e^{i\mathbf{q}_\parallel\cdot(\mathbf{r}_\parallel-\mathbf{r}'_\parallel)}\Sigma(z,z';\mathbf{q}_\parallel,\omega), \tag{3.23}$$

where the sum in $\mathbf{q}_\parallel$ is performed in the (auxiliary) superlattice Brillouin zone in the parallel plane to the surface. By inserting this expression into Eq. (3.20), and using the wave functions of Eq. (3.21), we write:

$$\begin{aligned}\Gamma_{j\mathbf{k}_\parallel} = -2\mathrm{Im}\Bigg[&\int_{-d/2}^{d/2}\int_{-d/2}^{d/2} dz\,dz'\phi_j^*(z)\Sigma(z,z';\mathbf{q}_\parallel,\omega)\phi_j(z') \\ &\int_{L^2} d\mathbf{r}_\parallel \frac{1}{L^4}\sum_{\mathbf{q}_\parallel} e^{i(\mathbf{q}_\parallel-\mathbf{k}_\parallel)\cdot\mathbf{r}_\parallel}\int_{L^2} d\mathbf{r}'_\parallel e^{i(\mathbf{k}_\parallel-\mathbf{q}_\parallel)\cdot\mathbf{r}'_\parallel}\Bigg],\end{aligned} \tag{3.24}$$

where the integration order has been rearranged in a convenient way. Then, by noting that the integral in $\mathbf{r}'$ gives a kronecker delta factor $\delta_{\mathbf{k}_\parallel,\mathbf{q}_\parallel}$, finally we obtain the expression of the decay rate for an electronic state with j quantum number and $\mathbf{k}_\parallel$ parallel vector as

$$\Gamma_{j\mathbf{k}_\parallel} = -2\int_{-d/2}^{d/2}\int_{-d/2}^{d/2} dz\,dz'\phi_j^*(z)\mathrm{Im}\Sigma(z,z';\mathbf{k}_\parallel,\omega)\phi_j(z'). \tag{3.25}$$

As follows from previous section, within the GW approximation of Eq. (3.9a), the time-to-energy Fourier transform of the self-energy is written

$$\Sigma(\mathbf{r},\mathbf{r}';\omega)=\int d\omega' iG(\mathbf{r},\mathbf{r}';\omega-\omega')W(\mathbf{r},\mathbf{r}';\omega'), \tag{3.26}$$

which for the symmetry considered above gives

$$\Sigma(z,z';\mathbf{k}_\parallel,\omega)=\int_{-\infty}^{\infty}\frac{d\omega'}{2\pi}\int\frac{d\mathbf{q}_\parallel}{(2\pi)^2}W(z,z';\mathbf{k}_\parallel-\mathbf{q}_\parallel,\omega')iG(z,z';\mathbf{q}_\parallel,\omega-\omega'), \tag{3.27}$$

where we have used the standard substitution

$$\frac{1}{L^2}\sum_{\mathbf{q}_\parallel}\longrightarrow\frac{1}{(2\pi)^2}\int_{-\infty}^{\infty} d\mathbf{q}_\parallel. \tag{3.28}$$

The next step for simplifying the calculations is to replace the full one-electron Green's function G by the noninteracting (time-ordered) Green's function G^0 given by:

$$G^0(z,z';\mathbf{q}_\parallel,\omega) = 2\sum_j \left(\frac{\phi_j(z)\phi_j^*(z')}{\omega - E_j - \frac{\mathbf{q}_\parallel^2}{2m_j^*} - i\eta}\theta\left(E_F - E_j - \frac{\mathbf{q}_\parallel^2}{2m_j^*}\right) + \frac{\phi_j(z)\phi_j^*(z')}{\omega - E_j - \frac{\mathbf{q}_\parallel^2}{2m_j^*} + i\eta}\theta\left(E_j + \frac{\mathbf{q}_\parallel^2}{2m_j^*} - E_F\right)\right), \tag{3.29}$$

where j runs over the one-dimensional Kohn-Sham eigenfunctions, and θ is the Heaviside step function. The two factor in front of the sum accounts for the spin degeneracy, and $i\eta$ is a small imaginary number. Since we assume that states of different spins are not coupled, we drop the two factor in the following expressions . Finally, the 2D Fourier transform of the imaginary part of the self-energy is given by

$$\mathrm{Im}\Sigma(z,z';\mathbf{k}_\parallel,E_j) = \frac{1}{(2\pi)^2}\sum_{j'}^{0\le\pm(E_j-E_{j'})\le\pm(E_j-E_F)} \phi_{j'}(z)\phi_{j'}^*(z') \times \int_{\mathcal{D}} \mathrm{Im}W\left(z,z';\mathbf{k}_\parallel-\mathbf{q}_\parallel,\left|E_j - E_{j'} + \frac{\mathbf{k}_\parallel^2}{2m_j^*} - \frac{\mathbf{q}_\parallel^2}{2m_{j'}^*}\right|\right) d\mathbf{q}_\parallel, \tag{3.30}$$

and the integral in $\mathbf{q}_\parallel$ for each j' is performed in the momentum space area $\mathcal{D}$ defined by

$$0 < \pm\left(E_j + \mathbf{k}_\parallel^2/(2m_j^*) - E_{j'} - \mathbf{q}_\parallel^2/(2m_{j'}^*)\right) < \pm\left(E_j + \mathbf{k}_\parallel^2/(2m_j^*) - E_F\right), \tag{3.31}$$

where "+" ("−") stands for electron (holes) in both equations above. Then, the decay rate is given as

$$\Gamma_{j\mathbf{k}_\parallel} = \frac{-2}{(2\pi)^2}\sum_{j'}^{0\le\pm(E_j-E_{j'})\le\pm(E_j-E_F)} \int\int dz dz' \phi_j^*(z)\phi_{j'}(z) \times \left[\int_{\mathcal{D}} \mathrm{Im}W\left(z,z';\mathbf{k}_\parallel-\mathbf{q}_\parallel,\left|E_j - E_{j'} + \frac{\mathbf{k}_\parallel^2}{2m_j^*} - \frac{\mathbf{q}_\parallel^2}{2m_{j'}^*}\right|\right) d\mathbf{q}_\parallel\right] \phi_j(z')\phi_{j'}^*(z'). \tag{3.32}$$

The 2D Fourier transform of the imaginary part of the screened interaction, $\mathrm{Im}W$, satisfies the following integral equation:

$$\mathrm{Im}W(z,z';\mathbf{q}_\parallel,\omega) = \int\int dz_1 dz_2\, v(z,z_1;\mathbf{q}_\parallel)\mathrm{Im}\chi(z_1,z_2;\mathbf{q}_\parallel,\omega)v(z_2,z';\mathbf{q}_\parallel). \tag{3.33}$$

Here $v(z, z', \mathbf{q}_\parallel)$ is the 2D Fourier transform of the bare Coulomb interaction (with $q = |\mathbf{q}_\parallel|$)

$$v(z, z'; \mathbf{q}_\parallel) = \frac{2\pi}{q} e^{-q|z-z'|}, \tag{3.34}$$

and $\chi(z, z'; \mathbf{q}_\parallel, \omega)$ is the corresponding 2D transform of the density response function of the interacting electron system. Within the random phase approximation (RPA), $\chi(z, z'; \mathbf{q}_\parallel, \omega)$ obeys the integral equation,

$$\begin{aligned}\chi(z, z'; \mathbf{q}_\parallel, \omega) =& \chi^0(z, z'; \mathbf{q}_\parallel, \omega) \\ &+ \int\int \chi^0(z, z_1; \mathbf{q}_\parallel, \omega) v(z_1, z_2; \mathbf{q}_\parallel) \chi(z_2, z'; \mathbf{q}_\parallel, \omega) dz_1 dz_2.\end{aligned} \tag{3.35}$$

Here, χ^0 is the density response function for the noninteracting electron system. It can be calculated in terms of eigenfunctions $\phi_j(z)$ and eigenvalues E_j considered in Eq. (3.22). We use the expression derived by Eguiluz [78] for χ^0. Unless otherwise stated, in the calculations free-electron motion with effective mass $m_j^* = 1$ for all j is assumed in the plane parallel to the surface. The details on the calculation of χ^0 are given in the following section and in Appendix C.

3.4.2. Numerical implementation

The numerical implementation of the previous equations is based on a symmetry of the slab system with respect to the $z = 0$ mirror-plane, as sketched in Fig. 2.3. The calculation box size, here denoted by d, includes the Cu substrate, the two Pb overlayers and vacuum spaces at both sides. That means that the physical quantities are invariant with respect to the $z \to -z$ transformation. Because of this invariance, it follows from Eq. (3.25) that the double-Fourier series of the imaginary part of the screened interaction W only contains the following terms:

$$\begin{aligned}\mathrm{Im}W(z, z'; \mathbf{q}, \omega) =& \sum_{n,n'}^{\infty} \mathrm{Im}W^+_{n,n'}(\mathbf{q}_\parallel, \omega) \cos\left(\frac{2\pi n}{d} z\right) \cos\left(\frac{2\pi n'}{d} z'\right) \\ &+ \sum_{n,n' \neq 0}^{\infty} \mathrm{Im}W^-_{n,n'}(\mathbf{q}_\parallel, \omega) \sin\left(\frac{2\pi n}{d} z\right) \sin\left(\frac{2\pi n'}{d} z'\right).\end{aligned} \tag{3.36}$$

Then the decay rate of the state ϕ_j can be split, depending on the state parity as:

$$\Gamma_{j\mathbf{k}_\parallel} = \begin{cases} \Gamma^{++}_{j\mathbf{k}_\parallel} + \Gamma^{+-}_{j\mathbf{k}_\parallel} & \text{for even } \phi_j \\ \Gamma^{--}_{j\mathbf{k}_\parallel} + \Gamma^{-+}_{j\mathbf{k}_\parallel} & \text{for odd } \phi_j, \end{cases} \tag{3.37}$$

with

$$\Gamma^{++}_{j\mathbf{k}_\parallel} = -\frac{2}{(2\pi)^2} \sum_{j'_{even}}^{0\le\pm(E_j-E_{j'})\le\pm(E_j-E_F)} \sum_{n,n'}^{\infty} \mathrm{Im}W^{+}_{n,n'}(\mathbf{k},\omega) \times \int_{-d/2}^{d/2} \phi^*_j(z)\phi_{j'}(z)\cos\left(\frac{2\pi n}{d}z\right)dz \int_{-d/2}^{d/2} \phi_j(z')\phi^*_{j'}(z')\cos\left(\frac{2\pi n'}{d}z'\right)dz', \tag{3.38}$$

$$\Gamma^{+-}_{j\mathbf{k}_\parallel} = -\frac{2}{(2\pi)^2} \sum_{j'_{odd}}^{0\le\pm(E_j-E_{j'})\le\pm(E_j-E_F)} \sum_{n,n'\neq 0}^{\infty} \mathrm{Im}W^{-}_{n,n'}(\mathbf{k},\omega) \times \int_{-d/2}^{d/2} \phi^*_j(z)\phi_{j'}(z)\sin\left(\frac{2\pi n}{d}z\right)dz \int_{-d/2}^{d/2} \phi(z')\phi^*_{j'}(z')\sin\left(\frac{2\pi n'}{d}z'\right)dz', \tag{3.39}$$

$$\Gamma^{--}_{j\mathbf{k}_\parallel} = -\frac{2}{(2\pi)^2} \sum_{j'_{odd}}^{0\le\pm(E_j-E_{j'})\le\pm(E_j-E_F)} \sum_{n,n'}^{\infty} \mathrm{Im}W^{+}_{n,n'}(\mathbf{k},\omega) \times \int_{-d/2}^{d/2} \phi^*_j(z)\phi_{j'}(z)\cos\left(\frac{2\pi n}{d}z\right)dz \int_{-d/2}^{d/2} \phi(z')\phi^*_{j'}(z')\cos\left(\frac{2\pi n'}{d}z'\right)dz', \tag{3.40}$$

and

$$\Gamma^{-+}_{j\mathbf{k}_\parallel} = -\frac{2}{(2\pi)^2} \sum_{j'_{even}}^{0\le\pm(E_j-E_{j'})\le\pm(E_j-E_F)} \sum_{n,n'\neq 0}^{\infty} \mathrm{Im}W^{-}_{n,n'}(\mathbf{k},\omega) \times \int_{-d/2}^{d/2} \phi^*_j(z)\phi_{j'}(z)\sin\left(\frac{2\pi n}{d}z\right)dz \int_{-d/2}^{d/2} \phi(z')\phi^*_{j'}(z')\sin\left(\frac{2\pi n'}{d}z'\right)dz'. \tag{3.41}$$

For lifetime calculations involving states at the surface (or in an overlayer) we have seen that $\Gamma^{++} \approx \Gamma^{+-}$ and $\Gamma^{--} \approx \Gamma^{-+}$. On the other hand, within the assumed symmetry of the calculation box, for a given energy, the QWSs of Chapter 6 localized in the overlayer, appear as doubly quasidegenerate and with opposite parity. That means that for the calculations of the lifetimes of a given QWS, we have two states: ϕ_j and ϕ_{j+1}, with even and odd parity, respectively, and energies $E_j \approx E_{j+1}$. Then the lifetime of a QWS with energy $E_0 = \frac{1}{2}(E_{j+1} + E_j)$ has been calculated as:

$$\Gamma \approx \Gamma^{++}_{j\mathbf{k}_\parallel} + \Gamma^{--}_{j+1\mathbf{k}_\parallel}. \tag{3.42}$$

In particular, for the calculation of the electron excitation decay rates shown in Fig. 6.10, we have used 31 MLs of Cu substrate and $100a_0$ of vacuum space in each side. With these parameters, the differences between quasidegerenate energies are smaller than 1 meV, and the differences between their linewidths is typically of the order of 1 meV, with an energy cuttoff of 120 meV.

The integrals over z and z' appearing in above equations, can be solved analytically (not shown here) by developing the states ϕ_j in their Fourier series in the periodic cell d. Following the notation by Silkin *et al.* in Ref. [79],

$$\phi_j(z) = \frac{1}{\sqrt{d}} c^+_{j,0} + \sqrt{\frac{2}{d}} \sum_{l=1}^{l_{\max}} \left[c^+_{j,l} \cos\left(\frac{2\pi}{d} z\right) + c^-_{j,l} \sin\left(\frac{2\pi}{d} z\right) \right]. \tag{3.43}$$

The energy cuttoff determines the $l_{\max}$ used in the truncation of the infinite sum of Eq. (3.43). As mentioned before, we consider the case of a system with symmetry with respect to the $z = 0$ mirror-plane. Then, states with different parity appear, the odd ($c^+_{j,l} = 0$) and even ($c^-_{j,l} = 0$) ones.

Similar double-Fourier series expansion, as in Eq. (3.36), of the rest of the quantities allows one to calculate the decay rates by matrix multiplications. The equation for calculating the imaginary part of the screened interaction in Eq. (3.33) is written then

$$\mathrm{Im}W^{\pm}_{n,n'}(\mathbf{k},\omega) = \sum_{n'',n'''} \frac{d^2}{\mu_{n''}\mu_{n'''}} v^{\pm}_{n,n''}(\mathbf{k}) \mathrm{Im}\chi^{\pm}_{n'',n'''}(\mathbf{k},\omega) v^{\pm}_{n''',n'}(\mathbf{k}), \tag{3.44}$$

where

$$\mu_n = \begin{cases} 1 & \text{for } n = 0 \\ 2 & \text{for } n \geq 1, \end{cases} \tag{3.45}$$

and $n'', n''' \neq 0$ for the "$-$" case. The coefficients $v_{n,n'}$ of the bare Coulomb potential can be calculated analytically [78]. The obtention of the $\chi_{n,n'}$ coefficients of the interacting density response function is more involved, because the solution of Eq. (3.35) is required. In the following we explain how this equation is solved.

The noninteracting density-response function at zero Kelvin temperature [79] is given by

$$\begin{aligned} \chi^0(z,z';\mathbf{q}_\parallel,\omega) =& \frac{2}{L^2} \sum_{j,j'} \phi_j(z)\phi^*_{j'}(z)\phi^*_j(z')\phi_{j'}(z') \\ & \times \sum_{\mathbf{k}_\parallel} \frac{f_{j\mathbf{k}_\parallel} - f_{j'\mathbf{k}_\parallel+\mathbf{q}_\parallel}}{E_{j\mathbf{k}_\parallel} - E_{j'\mathbf{k}_\parallel+\mathbf{q}_\parallel} + \omega + i\eta}, \end{aligned} \tag{3.46}$$

where $f_{j\mathbf{k}}$ is used to denote the Heaviside step function $\theta(E_F - E_{n\mathbf{k}_\parallel})$, with E_F being the Fermi level and $E_{n\mathbf{k}_\parallel}$ energies are given by Eq. (3.22). The Fourier representation of Eq. (3.46) is

$$\begin{aligned}\chi^0(z,z;\mathbf{q}_\parallel,\omega) = &\sum_{n=0}^{\infty}\sum_{n'=0}^{\infty}\chi^{0,+}_{n,n'}(q,\omega)\cos\left(\frac{2\pi n}{d}z\right)\cos\left(\frac{2\pi n'}{d}z\right)\\ &+\sum_{n=1}^{\infty}\sum_{n'=1}^{\infty}\chi^{0,-}_{n,n'}(q,\omega)\sin\left(\frac{2\pi n}{d}z\right)\sin\left(\frac{2\pi n'}{d}z'\right),\end{aligned} \tag{3.47}$$

and noting that similar equations hold for χ and v, the interacting density response equation is reformulated as

$$\chi^{\pm}_{n,n'}(q,\omega) = \chi^{0,\pm}_{n,n'} + \sum_{n'',n'''}\chi^{0,\pm}_{n,n''}(q,\omega)v^{\pm}_{n'',n'''}(q)\chi^{\pm}_{n''',n'}(q,\omega), \tag{3.48}$$

which can be expressed in matrix form, $\chi = \chi^0 + \chi^0 v\chi$, so that the solution can be formally written as:

$$\chi = (1+\chi^0 v)^{-1}\chi^0. \tag{3.49}$$

At the end, problem is reduced to that of finding the inverse of the $(1+\chi^0 v)$ matrix.

Chapter 4

Theoretical methods III: Wave packet propagation

4.1. Introduction

The wave packet propagation (WPP) method is a powerful theoretical tool widely applied both in quantum chemistry and physics. It allows to address on equal footing the characterization of the static properties of a molecular or mesoscopic system, and the solution of explicitly dynamical problems such as, e.g., response of the system to a time-dependent perturbation. It also allows an efficient and simultaneous treatment of both bound and continuum states, which otherwise is a challenge for numerical algorithms.

In the case of the (effective) one-electron problem, which is dealt with in this thesis, the idea underlying the method is the following: The time-dependent Schrödinger equation for the "active" electron is directly solved on a mesh of spatial points. Thus, one gets *a priori* the exact evolution of the electron wave function from the given initial state. For stationary Hamiltonians the "active" electron serves as a virtual probe. The proper choice of the initial state allows an efficient extraction of the energy-resolved scattering matrix, energies of bound states, energies and lifetimes of quasi-stationary states (resonances), projected density of electronic states, etc. Thus, a rather complete information on the system can be obtained. It should be emphasized that in contrast to frequency-domain techniques, where the stationary Schrödinger equation is solved for each energy, the present time-domain approach allows extraction of the energy-

resolved quantities from the single time propagation. In the case of time-dependent Hamiltonians the WPP is widely used to obtain the transition probabilities, including bound-to-continuum transitions.

It is worth noting that the numerical implementation of the state-of-the-art *ab initio* treatment of the dynamics of the many-body systems, the time-dependent density functional theory (TDDFT), borrows many of the aspects of the WPP technique as used here. Indeed, within TDDFT one considers the time-evolution of several (or even many) Kohn-Sham orbitals, each of which is analogous to the one-electron wave packet [80].

The review devoted to the electronic excitations in metals and metal surfaces in Ref. [15] contains a section reporting the state-of-the-art of the WPP method, as applied in surface science problems by the group in Orsay (France). Since our implementation of the WPP technique borrows a lot from above developments, certain overlap between the material covered in this chapter and that presented in Ref. [15] including references therein is inevitable. Further details are based on private communications during the fruitful collaboration stages with the group at Orsay. Thus, the aim of this chapter is also to provide a useful self-contained resource of the most important concepts related to the WPP, as considered here. Naturally, the presentation is biased to the specific problems solved in this thesis and it will be necessarily incomplete. In particular, we have explored the applicability of the WPP method to electron quantum well state (QWS) problems and to the study of electron transport properties in metallic nanocontacts.

We limit the presentation to the one-electron propagation driven by a general time-independent local potential $V(\mathbf{r})$ that effectively accounts for the electron interaction with crystal ions and other electrons (see Chapter 2). Section 4.2 presents the general equations and most common techniques for solving them numerically. Section 4.3 is devoted to the absorbing potentials used for implementing the outgoing wave boundary conditions and to mimic electron population decay of excited states. Section 4.4 explains the extraction of information about the system from the scattered wave packet, and the prescriptions for constructing a proper initial wave packet configuration. Sections 4.5 and 4.6 are devoted to the specific propagation schemes applied to the study of the electronic properties of the Pb/Cu(111) system and Na nanocontacts, respectively. The last Section 4.7 contains the equations relating the measurable macroscopic ballistic transport quantities with the mesoscopic scattering properties of nanosized systems. Care must be taken with notations because the same symbol might be used through the chapter for different quantities. Thus, in general, the scope of the symbol is limited to the corresponding subsection.

4.2. Solving the time-dependent Schrödinger equation (TDSE)

4.2.1. TDSE

The quantum mechanical evolution of the electron wave function $\psi(\mathbf{r},t)$ is described by the (non-relativistic) time-dependent Schrödinger equation (TDSE)

$$i\partial_t\psi = \hat{H}\psi, \tag{4.1}$$

with Hamiltonian

$$\hat{H} = -\frac{1}{2}\nabla^2 + \hat{V}(\mathbf{r},t). \tag{4.2}$$

Provided the initial condition $\psi(\mathbf{r},t=t_0)\equiv\psi_0$ the formal solution to Eq. (4.1) can be written as

$$\psi(\mathbf{r},t) = \hat{U}(t-t_0)\psi_0, \tag{4.3}$$

with the evolution operator $\hat{U}(t-t_0)$ given by

$$\hat{U}(t-t_0) = \mathcal{T}\exp[-i\int_{t_0}^{t}\hat{H}(t')dt'], \tag{4.4}$$

where $\mathcal{T}$ is the time-ordering operator defined by Eq. (3.6). For a conservative quantum system, i.e., $\partial V/\partial t$=0, which is assumed through the rest of the chapter, the Hamiltonian is time-independent and the evolution operator is given by

$$\hat{U}(t-t_0) = \exp[-i\hat{H}(t-t_0)]. \tag{4.5}$$

Without lost of generality, we set $t_0 = 0$.

The simplest form of the time-propagation is obtained when the eigenspectrum of the Hamiltonian is known. The eigenspectrum of the Hamiltonian operator is obtained by solving the time-independent Schrödinger equation (TISE)

$$\hat{H}\phi_n(\mathbf{r}) = E_n\phi_n(\mathbf{r}). \tag{4.6}$$

The eigenstates $\{\phi_n\}$ form a complete basis set (we use a discrete set notation but results are generalizable to a continuous set, i.e., the summation might imply an integration in the continuous spectrum part). Then, we can expand the solution of the TDSE in the eigenstate basis. Indeed,

$$\psi_0 = \sum_n a_n\phi_n(\mathbf{r}), \tag{4.7}$$

where $a_n =< \phi_n|\psi_0 >$, i.e., it is a projection of the initial state on the eigenstate. Then, from Eqs. (4.3) and (4.5) we find that the solution of the TDSE can be expressed as:

$$\psi(\mathbf{r},t) = \sum_n a_n \phi_n(\mathbf{r}) e^{-iE_n t}. \tag{4.8}$$

4.2.2. Gaussian wave packets

A textbook example of the solutions to the TDSE is the propagation in time of a Gaussian wave packet (GWP) in one-dimensional (1D) free space. GWPs play an important role as initial states in the WPP calculations presented in this thesis. Therefore, we find it useful to recall the analytical properties of the free GWP propagation. A GWP centered at $z = 0$ and characterized by the width Δz and average momentum k_0 is represented here as

$$\psi(z) = Ae^{-z^2/\Delta z^2} e^{ik_0 z}, \tag{4.9}$$

where A is the normalization constant given by

$$A = \left(\frac{2}{\pi}\right)^{1/4} \frac{1}{\sqrt{\Delta z}}. \tag{4.10}$$

An important feature of the GWP is that its Fourier transform is also a GWP in the reciprocal space:

$$\tilde{\psi}(k) \equiv \int \frac{1}{\sqrt{2\pi}} e^{-ikz} \psi(z) dz = A\frac{\sqrt{2}}{\Delta k} e^{-(k-k_0)^2/\Delta k^2}. \tag{4.11}$$

Thus, the wave packet is localized both in direct and reciprocal space. The widths in both spaces are related as:

$$\Delta z = \frac{2}{\Delta k}. \tag{4.12}$$

The time evolution of a GWP can be explicitly calculated (see Ref. [14] for a detailed derivation). It is useful to consider first the inverse Fourier transform of $\tilde{\psi}(k)$, which can be interpreted as an expansion in terms of the plane wave basis. Since plane waves are eigenstates of the free particle Hamiltonian, it follows from Eq. (4.8) that the time evolution of the GWP can be represented by

$$\psi(z,t) = \int \tilde{\psi}(k) \frac{1}{\sqrt{2\pi}} e^{ikz} e^{-i\omega(k)t} dk, \tag{4.13}$$

where obviously $\omega(k) = k^2/2$. Performing the integral we obtain [81]:,

$$\psi(z,t) = A(t)e^{-(z-k_0t)^2/|\Delta z(t)|^2}e^{ik_0z}e^{i\varphi(t)}e^{-i\frac{k_0^2}{2}t}, \tag{4.14}$$

with the phase φ given by

$$\varphi(t) = 2\frac{t}{\Delta z^2}\frac{(z-k_0t)^2}{|\Delta z(t)|^2} - \frac{1}{2}\arg\Delta z(t), \tag{4.15}$$

where the arg function returns the argument of a complex number. Here $A(t)$ is the normalization constant depending on time

$$A(t) = \left(\frac{2}{\pi}\right)^{1/4}\frac{1}{\sqrt{|\Delta z(t)|}}, \tag{4.16}$$

with the time-dependent width given by the norm of the following complex quantity

$$\Delta z(t) = \Delta z + 2i\frac{t}{\Delta z}. \tag{4.17}$$

From the above expressions it follows that a GWP maintains its Gaussian shape, as given by the general expression in Eq. (4.14), during the free propagation. Furthermore, the center of the wave packet always advances with a constant group velocity $v_g = \partial\omega/\partial k|_{k=k_0} = k_0$. However, the width of the wave packet in direct space increases in time as $|\Delta z(t)| = \sqrt{\Delta z^2 + 4t^2/\Delta z^2}$. This is a consequence of the different phase velocities of the plane waves composing the wave packet. On the other hand, the width of the GWP in k-space is always the same, because the momentum probability distribution $|\tilde{\psi}(k)|^2$ does not depend on time.

Then, for constructing an ingoing GWP, it is not enough to set a non-zero group velocity k_0 towards the direction of incidence. The broadening velocity of the wave packet $\frac{d}{dt}|\Delta z(t)|$ (which in the limit $t \to \infty$ reaches Δk) should be much slower than its group velocity. When this is not fulfilled, in overall the wave packet is also propagated in the opposite direction (it contains outgoing components). We will return to a detailed discussion in Subsection (4.4.4).

4.2.3. Grid representation

Here we consider the issue of the wave function representation. It is clear that due to the limited memory resources of computers, it is impossible to represent a general

wave function exactly. We can, however, represent the solution approximately by an expansion in a finite basis $\{\varphi_n\}$,

$$|\psi_0 > \approx \sum_{n=1}^{N} a_n |\varphi_n >, \tag{4.18}$$

where $a_n =< \varphi_n|\psi_0 >$. In other words, we have projected the wave function on a finite Hilbert space. The above representation requires a desired finite set N of complex numbers (furthermore, these numbers are also *finite* in the sense that they are represented by a truncated arithmetic, which leads to the numerical noise). In the Galerkin approximation, where the coupling with the non-projected space is neglected, the truncated solution in Eq. (4.18) still fulfills the time-dependent equation, provided that the Hamiltonian is replaced by the one projected on the space defined by the truncated basis. We will consider first the eigenfunctions of the original Hamiltonian as the basis to be truncated. Then, the solution can be represented as

$$\psi^{(N)}(z,t) = \sum_{n=1}^{N} a_n \varphi_n(z) e^{-iE_n t}, \tag{4.19}$$

which is the truncated counterpart of the solution given in Eq. (4.8). In general, however, the solution is expanded by a general basis. In this case, the diagonalization of the projected Hamiltonian does not retrieve the original eigenvalues and eigenfunctions but approximated ones ($\tilde{E}_n$,$\tilde{\varphi}_n$). Then the propagation above is approximated by

$$\psi^{(N)}(z,t) \approx \sum_{n=1}^{N} \tilde{a}_n \tilde{\varphi}_n(z) e^{-i\tilde{E}_n t}, \tag{4.20}$$

where $\tilde{a}_n =< \tilde{\varphi}_n|\psi_0 >$. This solution is said to be a spectral propagation [14].

Returning to the issue of representing approximately the solution, both in electronic structure calculations via the TISE and in time-dependent propagations, the discretization in a real-space grid is one of the most common representations. In this case, we also deal with a finite number of complex numbers describing the solution, as in the truncated spectral representation of Eq. (4.18). The intermediate values of the solution can be always approximated by common local interpolation schemes [82], where the derivatives entering the operators are naturally approximated by finite difference schemes.

On the other hand, one can use global interpolation schemes. This approach is based on a family of global functions spanning the physical space of the problem at hand with

the appropriate boundary conditions. The use of this global approach for interpolating the solution is known as the collocation method [83]. A closely related concept is the pseudo-spectral representation.

In brief, a grid representation can be loosely considered as a projection of the solution onto a finite set of Dirac's delta functions. On the other hand, if we consider the expansion of the solution within a (orthogonal) finite basis set, the Dirac's delta functions expanded in this basis are expected to be broadened around their grid point. The functions of the pseudo-spectral basis are characterized also by this local character. The requirement of a global interpolation of the solution (by the collocation method) by using a finite orthogonal basis set, defines a set of grid-points and weights at each grid-point that determines the precise relation between the pseudo-spectral basis and the above mentioned broadened Dirac's delta functions. The remarkable feature of the pseudo-spectral functions is that their value is one at their own grid-point and vanish at the other grid-points, thus simplifying function evaluations and integrals in real space. Indeed, the matrix elements of a local potential in a pseudo-spectral basis are represented as $V(\hat{z})_{ij} = V(z_j)\delta_{ij}$.

As an example, the band-limited ($-K < k < K$) Fourier spectral basis set composed of exponential functions $\{\exp(ikz)/\sqrt{2\pi}\}$ (which is at the core of the Fourier Method explained in appendix B) determines a pseudo-spectral basis in a uniform mesh (with equal weight at each grid-point z_j and Δz step) composed of sinc functions $\theta_j(z) = \mathrm{sinc}[K(z - z_j)]$ with $K = \pi/Dz$. These functions are one at their corresponding z_j and zero in the rest of the grid-points. These pseudo-spectral functions are also known as a *discrete variable representation* basis [84], although in Ref. [14] this denomination is reserved to the pseudo-spectral functions derived from classical polynomials.

4.2.4. Time propagation

Except for a few limited number of simple cases, like the one of the GWP propagation, in general it is not possible to obtain (even approximate) analytical solutions to the TDSE. Thus, we are forced to use numerical methods. A convenient starting point is the formal solution given in Eq. (4.3). Then, the numerical strategy is based on finding an appropriate method for evaluating the evolution operator given by Eq. (4.5). The choice of the specific approach is closely related to the issue of the wave function representation addressed before. The development in a finite basis set or discretization on a mesh of spatial points determines the way one calculates the action of the Hamiltonian or the exponential of the Hamiltonian on the wave function. There are two different approaches: the short-time propagation and the global propagation. In

the short-time propagation approach, the time evolution of the wave packet is obtained by several consecutive small time steps Δt_i propagations, i.e., the evolution operator is represented as

$$\hat{U}(t) = e^{-i\hat{H}t} = \prod_N e^{-i\hat{H}\Delta t_i} \tag{4.21}$$

where obviously $t = \sum_{i=1}^{N} \Delta t_i$. The advantage of the decomposition in Eq. (4.21) is that we can evaluate the action of the short-time evolution operator $\psi(t + \Delta t_i) = \hat{U}(\Delta t_i)\psi(t)$ with approximate methods, which are not applicable to the global propagation scheme. However, the error in the numerical evaluation of the short-evolution operator $\hat{U}(\Delta t)$ is accumulated during the entire propagation.

Projection of the initial state on the eigenbasis of the Hamiltonian allows one to obtain directly the solution at any time, as follows from Eq. (4.8). In this respect this is a way of performing a global time propagation. However, finding eigenstates of the Hamiltonian can be an extremely time-consuming numerical task. This is precisely the reason for the development of the WPP techniques (see the schematic diagram of Fig. 4.1) allowing to avoid the eigenstate calculation. Presently, the Chebyshev method is considered as the method of choice for the global time propagation. In this method the evolution operator is approximated by a truncated Chebyshev complex polynomial expansion [14]. Due to the optimal representation associated with this expansion, an exponential convergence with the number of polynomials is obtained. That is why this method is considered as a benchmark for other methods.

For short-time propagation, several methods have been developed in the literature. We quote here the most commonly used ones. The detailed discussion of the specific techniques used in this thesis work is presented later. (i) In the Lanczos method the evolution operator is projected on the finite basis covering the Krylov subspace. The latter is formed by the repeated actions of the Hamiltonian $\hat{H}$ on $\psi(t)$. (ii) The second order difference method (SOD), also known as leap-frog method, is another common method for WPP. (iii) An implicit method related to the SOD is the Crank-Nicholson propagation scheme. On the other hand, (iv) the dynamic Fourier method [85] combined with the split-operator technique [86] is one of the most popular among pseudo-spectral methods [14].

When the WPP method is applied to the propagation of electronic states (instead of heavy particles, as it is usual for molecular dynamics studies in quantum chemistry) one has to take care of the possible rapid variation of the wave function. The Coulomb cusp close to the charged core is one of the examples illustrating this effect. The representation of the system, in this case, results in an effective basis or grid-projected Hamiltonian with very large eigenvalues. On the other hand, the SOD method, being

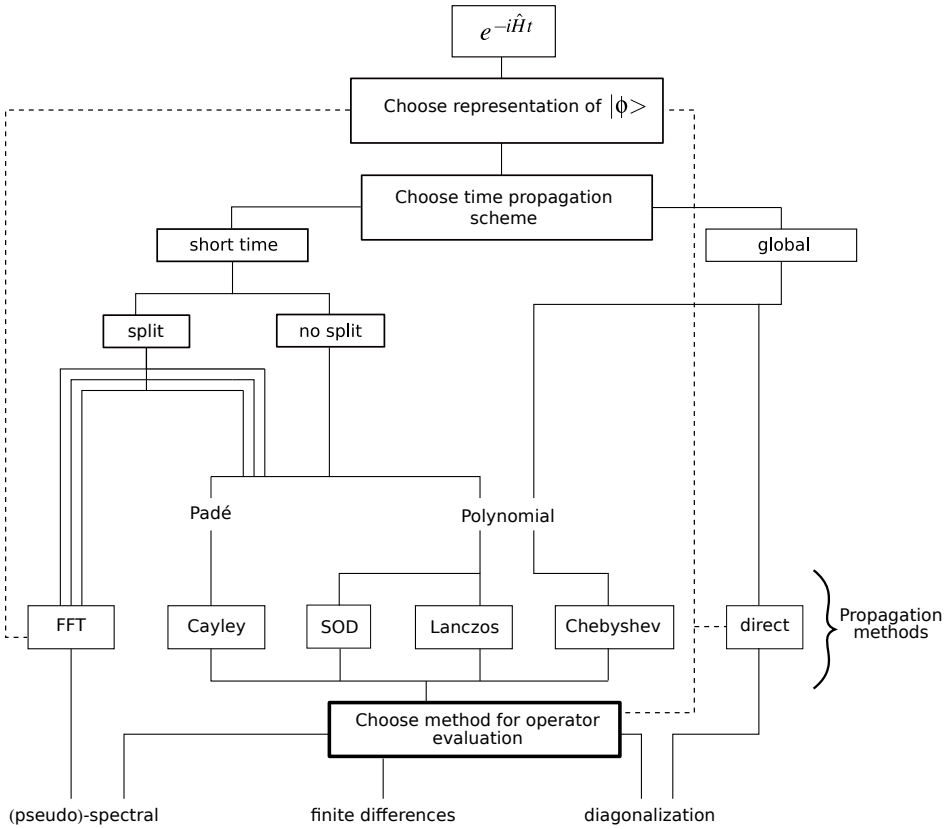

Figure 4.1.: Schematic diagram showing most common methods for WPP. The dashed line represents the influence of the grid representation on the evaluation of the action of an operator onto the wave function. The direct propagation method refers to the propagation through the representation of the solution in terms of the eigenfunctions, which requires the diagonalization of the Hamiltonian. Note also that the inclusion of absorbing potentials (thus the Hermiticity of the Hamiltonian) also determines the suitability of a method for a given problem.

conditionally stable, requires a time step $\Delta t < 1/|E|_{\max}$, where $|E|_{\max}$ is the largest in absolute value eigenvalue of the effective Hamiltonian matrix. Thus, for the case of the electronic WPP, the SOD method can appear completely inefficient because of the too small time step needed for stable propagation. Similarly, although the Lanczos technique is unconditionally stable, the technical aspects of the method result in a comparable constraint on the time step. In the global propagation with the Chebyshev method, the number of polynomials grows as $|E|_{\max}$. This also makes the method inefficient in many applications concerning the propagation of electronic wave packets. The dynamic Fourier method and the Crank-Nicholson method, together with the split-operator technique, appear to be free from these difficulties [15]. In what follows, we describe in detail these convenient propagation schemes used in our calculations.

4.2.5. Crank-Nicholson propagation scheme

One of the simplest approximations for the short-time evolution operator is obtained by expanding $\hat{U}(\Delta t)$ in Fourier series and keeping only a limited number of terms:

$$|\psi(t+\Delta t)> = \sum_{n=0}^{\infty} \frac{1}{n!} \left(-i\hat{H}\Delta t\right)^n |\psi(t)> = \sum_{n=0}^{N} \frac{1}{n!} \left(-i\hat{H}\Delta t\right)^n |\psi(t)> + O(\Delta t^{N+1}). \tag{4.22}$$

The approximate evolution operators obtained in this way are not unitary. The evolution in time does not conserve the norm and therefore, the convergence of the propagated solution is not guaranteed. For the particular case in which $N = 1$, one obtains

$$|\psi(t+\Delta t)> = (1 - i\hat{H}\Delta t)|\psi(t)> + O(\Delta t^2). \tag{4.23}$$

This propagation scheme can be interpreted as the Euler method: a first-order explicit numerical method for integrating a partial differential equation.

An improvement to the above approximation is obtained by considering a second order central difference (SOD) for the time-derivative. It can be derived from the following expression [87],

$$|\psi(t+\Delta t)> - |\psi(t-\Delta t)> = \left(\exp[-i\hat{H}\Delta t] - \exp[i\hat{H}\Delta t]\right)|\psi> . \tag{4.24}$$

Expanding the exponentials one obtains the third-order time propagation scheme:

$$|\psi(t+\Delta t)> = |\psi(t-\Delta t)> - 2i\Delta t\hat{H}|\psi(t)> + O(\Delta t^3). \tag{4.25}$$

From the known $|\psi(t-\Delta t)>$ and $|\psi(t)>$ one gets $|\psi(t+\Delta t)>$. Initialization of the propagation requires two time-points, for which the Euler method can be used at the first step. As previously mentioned, the SOD method is conditionally stable with stability condition $\Delta t < 1/|E|_{\max}$. To avoid the instability problem, the following exact expression is taken as a starting point:

$$\exp\left(i\hat{H}\frac{\Delta t}{2}\right)|\psi(t+\Delta t)> = \exp\left(-i\hat{H}\frac{\Delta t}{2}\right)|\psi(t)> . \tag{4.26}$$

Expanding in Taylor series both sides and considering the terms up to first order, we reach the implicit expression

$$(1 + i\hat{H}\frac{\Delta t}{2})|\psi(t+\Delta t)> = (1 - i\hat{H}\frac{\Delta t}{2})|\psi(t)> + O(\Delta t^3), \tag{4.27}$$

which is called Crank-Nicholson or Cayley approximation [88]. From Eq. (4.27) a unitary approximation to the evolution operator is straightforward to obtain as:

$$\hat{U}(t+\Delta t,t)=\frac{(1-i\hat{H}\frac{\Delta t}{2})}{(1+i\hat{H}\frac{\Delta t}{2})}+O(\Delta t^3). \tag{4.28}$$

This approximation is of third order accuracy in Δt, as can be immediately seen by comparing the Taylor series expansion of the denominator in Eq. (4.28) and the series given by Eq. (4.22). In mathematics Eq. (4.28) is known as a Caley transform of the skew-Hermitian operator $i\hat{H}\frac{\Delta t}{2}$.

In practice we will work with the expression given by Eq. (4.27) to calculate an intermediate step of the effect of the evolution operator (see Section 4.6). For the three-point finite differences used for the spatial derivatives entering the Hamiltonian, a system of linear equations connecting the wave function values at the mesh points can be derived. These equations can be efficiently solved with standard numerical linear algebra packages.

4.2.6. Split-operator technique

The split-operator technique is a powerful tool for evaluating the action of the short-time propagation operator $\exp(-i\hat{H}\Delta t)$ onto a wave function in a convenient way. It consists in splitting the action of each term inside the Hamiltonian $\hat{H}$ by factorizing the exponential operator. This allows us to conveniently pick up one of the short-time propagation schemes found in Table 4.I. In practice, the first order split formula [88] can be used,

$$e^{(\hat{A}+\hat{B})\Delta t}=e^{\hat{A}\Delta t}e^{\hat{B}\Delta t}+[\hat{A},\hat{B}]O(\Delta^2), \tag{4.29}$$

or the more accurate second order split

$$e^{(\hat{A}+\hat{B})\Delta t}=e^{\hat{A}\frac{\Delta t}{2}}e^{\hat{B}\Delta t}e^{\hat{A}\frac{\Delta t}{2}}+O(\Delta t^3). \tag{4.30}$$

The latter is the choice in this thesis. This technique is accurate up to Δt^3, although accuracy also depends on the commutation relation between the $\hat{A}$ and $\hat{B}$ operators.

4.2.7. Dynamic Fourier method

The dynamic Fourier method, also known as fast Fourier method [14], is a pseudo-spectral method for propagating the wave function in a real space grid. Like in the

Table 4.I.: Comparison of time propagation methods. Note that although the SPO is usually utilized with the FFT-technique, it can be used in combination with the rest of the short-time propagation schemes. N stands for the dimension of the Krylov space in the Lanczos method. Although the Chebyshev method, in principle, is conditionally stable, the characteristic exponential convergence with the number of polynomials makes the method accurate up to the machine precision. (Adapted from Table II of Ref. [87]).

Method	SPO	Cayley	SOD	Lanczos	Chebyshev
Norm	Conserved	Cons.	Cons.	Cons.	Not Cons.
Stability	Stable	Stable	Cond. stable	Stable	Exp. convergence
Error	Δt^3	Δt^3	Δt^3	Δt^N	Exp. convergence

Fourier grid Hamiltonian (FGH) method (see Section B.3 of Appendix B), the aim of the method is to calculate locally the effect of the Hamiltonian $\hat{H} = \hat{T} + \hat{V}$, where the effect of the local potential V is calculated in direct space and that of the kinetic energy operator in the k-space (where $\hat{T}$ is diagonal). It is used in combination with the split-operator technique to factorize

$$e^{-i\hat{H}\Delta t} \approx e^{-iV\Delta t/2} e^{-i\hat{T}\Delta t} e^{-iV\Delta t/2}, \tag{4.31}$$

where V, instead of T, is split for convenience (assuming that we start with the initial wave function in direct space representation). The fast Fourier transform (FFT) algorithm provides an efficient way for changing the wave representation between direct and k-space for a large mesh of points. The numerical effort of a FFT scales semilinearly as $O(N \log N)$, whereas a straightforward evaluation of the discrete Fourier transform scales as $O(N^2)$. Another advantage is that no extra memory for any Hamiltonian matrix allocation is needed (in contrast with the FGH method), because the solution is updated dynamically. This method has been used in the 1D propagation explained in Section 4.5, and also in the 2D propagation in cylindrical coordinates for calculating the action of the kinetic energy operator in the axial-symmetric direction, as explained in Section 4.6.

4.3. Absorbing potentials

4.3.1. Absorption at grid boundaries

In scattering problems outgoing wave boundary conditions appear naturally. A straightforward, but not practical way, to treat the outgoing asymptotic propagation of a scattered wave packet in numerical simulations is to set a large calculation box, keeping enough space for the wave packet to be propagated during the finite calculation time. However, this approach would require a huge computer memory to allocate the entire grid. It would be desirable to apply a method that allows us to suppress the effect of the boundaries arising from the finite size of the calculation grid. The goal is to obtain the same time evolution as in the infinite space, while performing the WPP calculations in the finite region comprising scatterer and perhaps, a small amount of the asymptotic region. One would like to let the outgoing wave packet to exit the calculation grid, without reflection from its boundary. The quest for the most efficient approach has been and continues to be a subject of active research [89–91].

Among different methods to treat open boundary conditions, we have chosen complex absorbing potentials (CAPs) placed at the boundaries of the calculation grid [85,92,93]. The advantage of this method is the straightforward implementation and compatibility with the dynamic Fourier method. The CAPs have to be tuned to the problem at hand, since the absorption is only optimal within a given energy range. For example, at the left boundary of the grid along z-axis, denoted here as $z_{\min}$, we might have a negative imaginary absorbing potential of the form:

$$\begin{cases} V_{\text{abs}} = -i\frac{C_1}{C_2^{\alpha}}\left[C_2 - (z - z_{\min})\right]^{\alpha} & \text{if } (z - z_{\min}) \leq C_2 \\ V_{\text{abs}} = 0 & \text{otherwise,} \end{cases} \tag{4.32}$$

where C_1 and C_2 are positive constants. We have used $\alpha = 2$ in all the calculations along this thesis. The strength of the potential C_1 and its range C_2 are adjusted to have desirable low reflection within the energy range of interest. It is worth noting that the range of the potential C_2 has to be several times larger than the largest electron wavelength to be absorbed. To give specific examples: In the study of the Pb/Cu(111) system in Chapters 6 and 7, we have used $C_1 \sim 0.01 \div 0.1\, a_0$ and $C_2 \sim 100 \div 1000\, a_0$ whereas in the study of Na nanocontacts, in Chapter 8, $C_1 = 0.16\, a_0$ and $C_2 = 100\, a_0$ have been used.

When absorbing potentials are introduced as explained above, the Hamiltonian of the system becomes non-Hermitian, with the consequent loss of the norm of the wave packet. However this loss mimics the sought effect of the departure of the particles

from the region of space limited by the finite size computation box. Along with their pure technical role in imposing the outgoing wave boundary conditions, CAPs can be used in the WPP scheme to represent "physical" loss of number of particles due to many-body inelastic effects, as discussed below.

4.3.2. Effective many-body absorbing potential

Since the WPP used in this work is a one-electron approach, scattering with quasiparticles in the system is not taken into account. In principle, the WPP only considers the elastic population decay of the quasi-stationary states (resonances). The main effect of the quasiparticles in the electron propagation is the state population decay via inelastic scattering. Usually, this effect is reflected in the density of states as an additional broadening of the bound or resonant states. However, this is not always true for resonant states. A discussion can be found in Ref. [66], where a WPP study of the lifetimes of the image state resonances is addressed.

The many-body effects can be simulated by absorbing potentials, similar to the procedure used in low energy electron diffraction calculations [94]. In metals one can effectively account for the inelastic decay, by including the following absorbing potential in the Hamiltonian, only active in the spatial region $\mathcal{R}$ where the inelastic scattering is assumed to take place:

$$V_{\rm mb}(\mathbf{r}) = -\frac{i}{2}\left(\gamma_{e-e} + \gamma_{e-{\rm ph}}\right) \qquad \text{for } \mathbf{r} \in \mathcal{R}. \tag{4.33}$$

So, inelastic effects are included through γ_{e-e} and $\gamma_{e-{\rm ph}}$ (metal dependent constants), which are the electron-electron and electron-phonon scattering decay rates, respectively.

Then, it is easy to see the suitability of the above many-body potential for simulating the decay rate of bound states. The first-order perturbation energy of the ϕ_n bound state with energy E_n is

$$E_n^{'} = E_n + < \phi_n | V_{\rm mb} | \phi_n >, \tag{4.34}$$

and, since $V_{\rm mb}$ is as a complex quantity, the bound state will decay in time as

$$\phi_n e^{-E_n t} \longrightarrow e^{-\gamma_{\rm mb}^{(n)} t/2} \phi_n e^{-E_n t}, \tag{4.35}$$

where $\gamma_{\rm mb}^{(n)} = 2i < \phi_n | V_{\rm mb} | \phi_n >$ is the many-body induced decay rate of the state. It should be noted that, in general, the bound state does not overlap with the region $\mathcal{R}$

where the scattering events are effectively accounted. Then, the decay rate, induced by the absorbing potential, can be estimated as

$$-i\frac{\gamma_{\rm mb}^{(n)}}{2} =< \phi_n|V_{\rm mb}|\phi_n >= -i\frac{w_n}{2}(\gamma_{e-{\rm ph}} + \gamma_{e-e}), \tag{4.36}$$

where w_n is the weight of the wave function in $\mathcal{R}$:

$$w_n = \int_{\mathcal{R}} \phi_n^* \phi_n \, d\mathbf{r}. \tag{4.37}$$

In the particular case of states confined in Pb overlayers considered in Chapter 6, γ_{e-e} strongly depends on the energy, whereas $\gamma_{e-{\rm ph}}$ can be considered as a constant. In fact, at 5 Kelvin temperature the many-body decay rates in Pb are: $\gamma_{e-{\rm ph}} \approx 20$ meV and $\gamma_{e-e} \approx 0$–300 meV for energies up to a few eV above the Fermi level. This energy dependence implies that, in order to obtain semiquantitative WPP results, in principle, it is necessary to perform an independent calculation for each energy or small energy region with the corresponding value of γ_{e-e}.

4.4. Information extraction

In principle, the solution $\psi(\mathbf{r}, t)$ of Eq. (4.1) contains all the information about the system characterized by the potential $V(\mathbf{r})$. The possibility to access the properties of the system is only a matter of adequate choice of the initial conditions. In this section we present the formulation allowing to perform the resonance analysis and to extract the scattering matrix from the propagated solution $\psi(\mathbf{r}, t)$ of the TDSE. In particular, we discuss the calculation of the projected density of electronic states and the one-electron transmission and reflection probabilities in case of the 1D potential barrier. The former is discussed in Subsection 4.4.1. For the latter quantities we provide two different methods, namely, the amplitude method and the flux method. Subsection 4.4.4 is devoted to the discussion of the conditions to be fulfilled by the initial wave packet in scattering calculations, which is a fundamental issue in the present WPP approach.

4.4.1. Projected density of states

The link between the initial wave packet and the density of states is given by the time-to-energy Laplace transform $\mathcal{L}(\omega)$ applied to the propagated wave,

$$\mathcal{L}(\omega)\psi(\mathbf{r},t) \equiv \int_0^\infty e^{i(\omega+i\eta)t}\psi(\mathbf{r},t)dt = \int_0^\infty e^{i(\omega+i\eta)t}e^{-i\hat{H}t}\psi_0 dt, \tag{4.38}$$

where $\eta \to +0$. Further development gives,

$$\lim_{\eta\to+0}\int_0^\infty e^{i(\omega-\hat{H}+i\eta)t}\psi_0 dt = \lim_{\eta\to+0}\left[\frac{e^{i(\omega-\hat{H})t}}{i(\omega-\hat{H}+i\eta)}\right]_0^\infty \psi_0$$
$$= i\underbrace{\lim_{\eta\to+0}\left(\frac{1}{\omega-\hat{H}+i\eta}\right)}_{G_\omega^+}\psi_0. \tag{4.39}$$

The term inside the brackets is the retarded Green function G_ω^+. Expansion of G_ω^+ in the basis of the eigenfunctions $|\phi_j>$ of $\hat{H}$ gives

$$\lim_{\eta\to+0}\frac{1}{\omega-\hat{H}+i\eta} = \lim_{\eta\to+0}\sum_j \frac{|\phi_j><\phi_j|}{\omega-E_j+i\eta}, \tag{4.40}$$

where E_j is the corresponding eigenvalue. Then, projecting $|\psi_0>$ on Eq. (4.39) we obtain

$$<\psi_0|G_\omega^+|\psi_0> = \lim_{\eta\to+0}\sum_j \frac{|c_j|^2}{\omega-E_j+i\eta}, \tag{4.41}$$

where $c_j =< \phi_j|\psi_0 >$ and recalling the Sokhatsky-Weierstrass theorem [95], the energy integral gives (here $i \equiv \sqrt{-1}$):

$$i\int_{-\infty}^\infty d\omega <\psi_0|G_\omega^+|\psi_0> =$$
$$i\mathcal{P}\int_{-\infty}^\infty d\omega\ \left(\frac{1}{\omega-E_j}\right) + \pi\sum_j |c_j|^2\int_{-\infty}^\infty d\omega\ \delta(\omega-E_j), \tag{4.42}$$

where $\mathcal{P}$ denotes the Cauchy principal value. The first term in the right hand side (RHS) of Eq. (4.42) is an imaginary number, whereas the second term is real. Note that by setting $|c_j|^2 = 1$ the latter term turns out to be π times the number of states. Then, it is natural to define the projected density of states (PDOS) onto ψ_0 as

$$n(\omega) = \frac{1}{\pi}\mathrm{Re} <\psi_0|G_\omega^+|\psi_0> = \sum_j |c_j|^2\delta(\omega-E_j), \tag{4.43}$$

or alternatively

$$n(\omega) = \frac{1}{\pi}\mathrm{Re}[\lim_{\eta\to+0}\lim_{T\to\infty}\int_0^T dt\, e^{i(\omega+i\eta)t}\underbrace{\int dz\psi_0^*(z)\psi(z,t)}_{A(t)}], \tag{4.44}$$

where $A(t)$ is the autocorrelation function. Observe that in Eq. (4.43) the c_j are the coefficients of the initial wave packet decomposition into the eigenbasis. Thus, only those states of the system which are already in overlap with the initial state can be accessed by the WPP. This feature allows us to either show up or suppress the states of a given symmetry.

In the PDOS one can find two kind of contributions, those of bound states and those of the continuum. Furthermore, in the continuum energy region some special states can emerge: quasi-stationary states or resonances. These states are solutions of the TISE with the Siegert or outgoing wave boundary conditions [96], i.e., $(\partial_z \mp ik_z)\psi(z)|_{z\to\pm\infty} = 0$. These solutions form a discrete set of states with complex eigenvalues $\mathcal{E} = E_R - \frac{i}{2}\gamma$, where E_R is the resonant energy and γ is the width. Quasi-stationary states will show up in several quantities, such as the scattering cross-sections and (as we will see later on) in the PDOS usually through Breit-Wigner profiles [97], from which one can extract the resonant parameters, namely, E_R and γ by Lorentzian fits. Although there are several methods for the extraction of these resonance parameters, such as the stabilization method [98] and the complex scaling method [99], the WPP approach appears to be efficient and versatile for this task.

Due to their smoothness and compactness, static GWPs localized in the spatial region of interest are used as initial states for the calculation of PDOS in this work. They can be also weighted by a special function (or by a previously calculated state) of a given symmetry. For an overall sampling of the eigenstates of the Hamiltonian within certain energy window, we might use a set of several GWPs. This allows us to avoid unexpected suppressions of eigenstates, due to the eventual coincidence of the initial state ψ_0 with nodes of their wave function, or because of symmetry reasons. Using several GWPs also improves the convergence of the PDOS as compared to the use of a unique GWP.

For the particular case of the study of QWRs in metallic overlayers in Chapter 6, the use of Gaussians localized *inside* the overlayer did give PDOS results strongly dependent on the initial wave packet position and width. The resonance analysis turned out to be difficult in this case. The origin of the above difficulty is found in the high number of oscillations in the wave functions of the underlying continuum. The homogeneous sampling of the states with GWPs centered inside the quantum well is

then complicated. We found that the results for PDOS can be largely improved when the initial state is given by a narrow set of GWPs centered at the overlayer-vacuum *interface*. The expected physical resonance peaks in the PDOS are then obtained. This is because on the vacuum side, far enough from the surface, the wave functions decay exponentially and they are free from oscillations.

Apart from the above considerations, it is important to take into account that the infinite time limit in the integral of Eq. (4.44) is approximated by a finite propagation time. Convergence of results has to be checked with respect to this calculation parameter.

As an illustrative example of the effect of truncating the calculation by a finite time, we consider the contribution of a bound state of energy E_0 to the density of states with a final time T, which can be easily obtained from Eq. (4.44) by performing the required integrals as

$$n_0(\omega) = \frac{1}{\pi}\frac{\sin[(\omega - E_0)T]}{(\omega - E_0)}. \tag{4.45}$$

Thus, $n_0(\omega)$ appears as a peak oscillating with ω and centered at E_0 (a sinc function). Taking the limit $T \to \infty$ in Eq. (4.45) the PDOS converges to a Dirac delta function, as expected from Eq. (4.43). We can smooth the oscillations in the PDOS by multiplying the solution by $\exp(-t^2/\tau^2)$ (with $\tau < T$) in Eq. (4.44). Then, the non physical broadening caused by the applied Gaussian filter corresponds to the width ΔE of a peak in PDOS

$$\Delta E \sim 2/\tau, \tag{4.46}$$

consistent with the time-energy uncertainty principle. This relation (with $\tau = T$) is also obtained by comparing the expansions of $n_0(\omega)$ and that of a Gaussian peak in the limit when $\omega \to E_0$.

The contribution of a resonant state to the PDOS is straightforward to obtain by performing the required integrals in Eq. (4.44). In this case, the solution is substituted by the time-evolution of the quasi-stationary state of the form $e^{-\gamma t/2}\phi_R(z)e^{-iE_R t}$, from which we obtain:

$$n_R(\omega) = \frac{1}{\pi}\lim_{T\to\infty}\frac{\gamma/2}{(\omega - E_R)^2 + (\gamma/2)^2}\times \left[1 + e^{-\gamma T/2}\left(\frac{\omega - E_R}{\gamma/2}\sin[(\omega - E_R)T] - \cos[(\omega - E_R)T]\right)\right]. \tag{4.47}$$

When the limit $T \to \infty$ is evaluated, the second factor of the RHS of Eq. (4.47) is one, and a Breit-Wigner profile [97] is obtained. In the limit $\gamma \to +0$ of this expression a Dirac delta function is retrieved, being consistent with a bound state.

The above discussion shows that, for the extraction of the lifetimes $\tau_{\text{res}} = 2/\gamma$ of the quasi-stationary states from the width of the resonant structures in PDOS, physically sound results are obtained only for the states with $\tau_{\text{res}} \ll T$.

All the resonant parameter extractions presented in this thesis are obtained by direct fit to the resonant peaks in the converged PDOS (or in the energy resolved transmission at narrow resonant structures in scattering problems), usually with Lorentzian functions, i.e., a Breit-Wigner profile. The fits are done with the general purpose fitting program `fityk` [100].

In case of narrow resonances, however, a too long propagation time is needed to get a converged result. Several techniques have been developed to circumvent this problem [14]. One can quote here the filter diagonalization approach [101, 102] or the direct fit of the autocorrelation function, with several exponentially decaying terms [15]. Both methods allow one to retrieve the narrow resonances with relatively short propagation times.

Once the energy E_R of a resonance or stationary bound state is determined from the PDOS, the corresponding wave functions can be obtained from

$$\psi_R(z) = \lim_{T\to\infty} \int_0^T e^{i(E_R+i\eta)t} \psi(z,t) dt. \tag{4.48}$$

Summarizing the discussion presented in this subsection, the procedure for extracting energies and lifetimes of the quasi-stationary states (resonances) used here consists of several steps:

(i) Obtain a preliminary $n(\omega)$ by putting a trial initial state composed of several GWPs in the region of interest, where the sought states are supposed to be localized.

(ii) Extract the resonance energies and decay rates from the PDOS.

(iii) Check the PDOS results with respect to *reasonable* variations of the initial wave packet, the absorbing potential parameters and final time step.

(iv) Extract the resonant wave functions.

(v) Finally, use these resonant states to optimize the initial state which allows accurate extraction of resonant energy and width. This last step might be obviated. With respect to the choice and variations of the calculation parameters above, it must be noticed that this is something dictated by the experience and the very problem at hand.

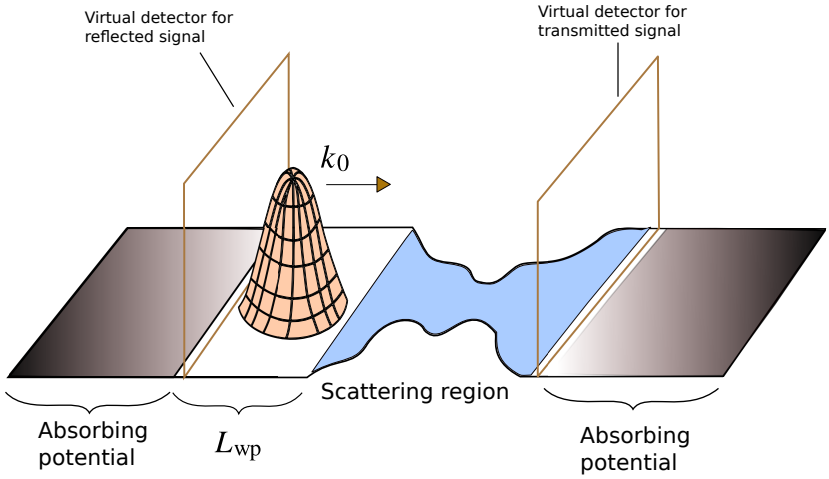

Figure 4.2.: Schematic representation of the calculation box configuration for scattering matrix extraction in the WPP approach. The different regions of the potential and the initial wave packet, together with the virtual detectors, are represented (see main text for further details). L_{wp} stands for the space required in the asymptotic region to allocate the incident initial wave packet.

4.4.2. Amplitude method

In this subsection we deal with the scattering matrix extraction from the WPP. Our approach is essentially the virtual detector method as reported in Ref. [103]. We consider the case of a 3D electron scattering by a potential barrier, and we show how to obtain the transmission and reflection coefficients from the propagated wave packet. We assume also that the asymptotic propagation is along the z-coordinate. Basically, with virtual detectors placed in the asymptotic region one records the transmitted and/or reflected wave function at $z = z_d$. In what follows, we only consider plane wave asymptotic solutions and only ingoing initial wave packets. Even though the solution is formally known on the positive time semi-axis $t \geq 0$, by causality, there cannot be any signal in the transmission region prior to the scattering event, i.e. for $t < 0$. That means, that time integrals to be used in the following analysis of the signals can be extended from the numerical $\int_0^T$ to that required in Fourier transforms: $\int_{-\infty}^{T}$. In Fig. 4.2 the initial incident wave packet is represented in the calculation grid.

By assumption, the transmitted signal in the asymptotic region has decoupled the z-motion with respect to the rest of the degrees of freedom. Then, the signal at the virtual detector can be represented by

$$\psi(z_d, \mathbf{r}_\parallel, t) = \sum_\mu \chi_\mu(\mathbf{r}_\parallel) \int \frac{e^{ikz_d}}{\sqrt{2\pi}} b^{\mathrm{tr}}_{k,\mu} e^{-i(k^2/2+E_\mu)t} dk, \tag{4.49}$$

where χ_μ refers to the quantized state in the perpendicular direction with ν, in principle, representing a set of quantum numbers. This signal can be further decomposed according to the different perpendicular states so that we obtain the ν-resolved signal by projecting the signal on the perpendicular states:

$$\psi_\nu(z_d,t)=\int \chi_\nu(\mathbf{r}_\parallel)\psi(z_d,\mathbf{r}_\parallel,t)d\mathbf{r}_\parallel=\int \frac{e^{ikz_d}}{\sqrt{2\pi}}b^{\rm tr}_{k,\nu}e^{-(k^2/2+E_\nu)t}dk. \tag{4.50}$$

Consistent with the causality principle, this representation contains only outgoing waves: $b^{\rm tr}_{k,\nu}=0$ if $k<0$. The time-to-energy Fourier transform of the signal in Eq. (4.50) is

$$S^{\rm tr}_\nu(\omega)=\int_{-\infty}^{\infty}e^{i\omega t}\psi^{\rm tr}_\nu(z_d,t)dt=\frac{1}{\sqrt{2\pi}}\int_0^\infty dk\, e^{ikz_d}b^{\rm tr}_{k,\nu}\underbrace{\int_{-\infty}^{\infty}e^{i(\omega-k^2/2-E_\nu)t}dt}_{2\pi\delta(\omega-k^2/2-E_\nu)}, \tag{4.51}$$

and denoting $k^{\rm tr}_\nu=\sqrt{2(\omega-E_\nu)}$, we arrive to

$$S^{\rm tr}_\nu(\omega)=\sqrt{2\pi}\frac{1}{k^{\rm tr}_\nu}e^{ik^{\rm tr}_\nu z_d}b^{\rm tr}_{k,\nu}. \tag{4.52}$$

Taking the square norm of the above expression, we obtain the useful relation

$$|b^{\rm tr}_{k,\nu}|^2=(k^{\rm tr}_\nu)^2|S^{\rm tr}_\nu(\omega)|^2/2\pi. \tag{4.53}$$

Similarly for the incident asymptotic region, the solution in the parallel direction is quantized, in general, with another set of states, ϕ_μ with the corresponding energies E_μ so that $k^{\rm in}_\mu=\sqrt{2(\omega-E_\mu)}$, then

$$|b^{\rm in}_{k,\mu}|^2=(k^{\rm in}_\mu)^2|S^{\rm in}(\omega)|^2/2\pi. \tag{4.54}$$

The probability to find a transmitted electron in the scattering ν *channel* is obtained by integrating the square norm of the probability amplitude in k-space (or also in their energy representation) for the corresponding ν-resolved signal:

$$P^{\rm tr}_\nu=\int_0^\infty |b^{\rm tr}_{k,\nu}|^2dk=\int_0^\infty \underbrace{|b^{\rm tr}_{k,\nu}|^2\frac{1}{k^{\rm tr}_\nu}}_{|b^{\rm tr}_{\omega,\nu}|^2}d\omega \tag{4.55}$$

and for the incident one (with no scattering):

$$P_\mu^{\text{in}} = \int_0^\infty |b_{k,\mu}^{\text{in}}|^2 dk = \int_0^\infty \underbrace{|b_{k,\mu}^{\text{in}}|^2 \frac{1}{k_\mu^{\text{in}}}}_{|b_{\omega,\mu}^{\text{in}}|^2} d\omega, \tag{4.56}$$

from which the k-resolved and energy-resolved asymptotic coefficients $b_{k,\mu}$ for each transmission/incident channel can be identified. Then, to calculate energy- and incident state (μ)-resolved transmission probabilities we proceed as follows. We start with an initial wave packet of the form

$$\psi_0 = \varphi(z)\phi_\mu(\mathbf{r}_\parallel), \tag{4.57}$$

where $\varphi(z)$ is (typically) a GWP. The $|b_{\omega,\nu\leftarrow\nu}^{\text{tr}}|^2$ are calculated as $k_\nu^{\text{tr}}|S_{\nu\leftarrow\mu}^{\text{tr}}(\omega)|^2$. Then the energy and final state resolved transmission probability is given by the ratio of outgoing and incident fluxes,

$$T_{\mu\to\nu}(\omega) = \frac{|b_{\omega,\nu\to\mu}^{\text{tr}}|^2}{|b_{\omega,\mu}^{\text{in}}|^2}, \tag{4.58}$$

where $\mu \leftarrow \nu$ denotes the quantities associated with the ν-resolved transmitted signal corresponding to the incident μ channel. The total transmission is given by the sum of $T_{\mu\leftarrow\nu}(\omega)$ over all possible open final channels, with $E_\nu < \omega$,

$$\mathbb{T}_\mu(\omega) = \sum_\nu^{\text{open}} \underbrace{\frac{|b_{\omega,\nu\leftarrow\mu}^{\text{tr}}|^2}{|b_{\omega,\mu}^{\text{in}}|^2}}_{\mathbb{T}_{\mu\nu}} = \sum_\nu^{\text{open}} \frac{k_{\nu\leftarrow\mu}^{\text{tr}}|S_{\nu\leftarrow\mu}^{\text{tr}}(\omega)|^2}{k_\mu^{\text{in}}|S_\mu^{\text{in}}(\omega)|^2}. \tag{4.59}$$

Similarly, for the reflection probability

$$\mathbb{R}_\mu(\omega) = \sum_\nu^{\text{open}} \underbrace{\frac{|b_{\omega,\nu\leftarrow\mu}^{\text{ref}}|^2}{|b_{\omega,\mu}^{\text{in}}|^2}}_{\mathbb{R}_{\mu\nu}} = \sum_\nu^{\text{open}} \frac{k_{\nu\leftarrow\mu}^{\text{ref}}|S_{\nu\leftarrow\mu}^{\text{ref}}(\omega)|^2}{k_\mu^{\text{in}}|S_\mu^{\text{in}}(\omega)|^2}. \tag{4.60}$$

These results can be obtained in a more rigorous treatment based on the Laplace transform of the signal on detectors, and not relying on the causality principle [103]. One essentially ends up with expressions common for the Green's function analysis, where the causality naturally stems from the formal equations.

In a unitary propagation the norm is preserved in the "physical" region delimited by the onset of the complex absorbing potentials. Then, from the flux conservation,

$$\mathbb{T}_\mu + \mathbb{R}_\mu = 1. \tag{4.61}$$

The above relation can be used to check the accuracy of numerical results.

In practice, both the transmission and the reflection for different incident channels μ are calculated with the second identity in Eqs. (4.59) and (4.60), by performing the Fourier transform to the transmitted and reflected signal in the respective virtual detector, as in Eq. (4.51). The signal of the incident wave packet can be calculated numerically, by propagating the incident wave packet in the asymptotic region, or can be obtained from the Gaussian analytic formula in Eq. (4.14), when GWPs are used as initial solution.

The amplitude method is much more complicated when the scattering states are not plane waves. This is the case in asymptotically periodic potentials describing a crystal lattice. We can use, however, an alternative flux method described in next subsection. It should be stressed that both amplitude and flux methods are equivalent and the choice of one or another is a question of convenience.

4.4.3. Flux method

The general solution to the 1D TISE of a particle under the effect of a periodic potential (which might represent an effective crystal lattice) of periodicity $V(z+L) = V(z)$, is a Bloch state given by the general form

$$\psi_k(z) = \frac{1}{\sqrt{2\pi}} e^{ikz} \varphi_k(z), \tag{4.62}$$

with $\varphi_k(z+L) = \varphi_k(z)$, where k is the crystal momentum, which is the equivalent to the plane wave momentum in free space. Although a periodic potential is not constant, it can be shown that at any point in space these states carry a constant flux given by

$$J(z) = \mathrm{Im}\left[\psi^*(z)\partial_z\psi(z)\right]. \tag{4.63}$$

This above statement is expressed mathematically as $\partial_z J(z) = 0$. To prove this, we take the partial derivative of Eq. (4.63),

$$\partial_z J = \frac{1}{2i}\left[\cancel{(\partial_z\psi^*)(\partial_z\psi)} + \psi^*(\partial_{zz}\psi) - (\partial_{zz}\psi^*)\psi - \cancel{(\partial_z\psi^*)(\partial_z\psi)}\right]. \tag{4.64}$$

Noting that $\partial_{zz}\psi = -2(V-E)\psi$, which also holds for the complex conjugate ψ^* (assuming real V), the rest of the terms are also cancelled, thus $\partial_z J = 0 \rightarrow J =$ *constant*. This invariance provides an alternative method, here called the flux method, for extracting transmission and reflection probabilities of the system.

The underlying idea is to consider the asymptotic solutions in the *energy representation*,

$$\begin{aligned} \hat{H}|_{z\to-\infty}\psi^{+}_{\rm in}(E) &= E\psi^{+}_{\rm in}(E) \\ \hat{H}|_{z\to+\infty}\psi^{+}_{\rm out}(E) &= E\psi^{+}_{\rm out}(E), \end{aligned} \tag{4.65}$$

where the + sign means that only ingoing/outgoing solutions in the z-positive direction are considered. The parallel and perpendicular motion are assumed to be decoupled as in Eq. (4.49) of previous subsection. We assume also that the incident wave packet is of the form given by Eq. (4.57). By applying the Fourier transform to the signal at the virtual detector (at $z = z_d$), we have

$$S^{\rm tr}_{\nu\leftarrow\mu}(z_d,\omega) = \int_{-\infty}^{\infty} dt\, e^{i\omega t} \int dE\, \psi^{+}_{\rm tr}(E,z_d) b^{\rm tr}_{\nu\leftarrow\mu}(E) e^{-iEt} = 2\pi\psi^{+}_{\rm tr}(\omega,z_d) b^{\rm tr}_{\nu\leftarrow\mu}(\omega), \tag{4.66}$$

where for convenience, it is explicitly denoted the dependence on z_d. The transmission (reflection) coefficients can be calculated from the ratio between the transmitted (reflected) and incident electron fluxes. These fluxes are calculated with the flux defined by Eq. (4.63) in the energy representation, i.e., $J = {\rm Im}(\psi^{*}_{\omega}\partial_z\psi_{\omega})$, from which the flux at z_d is obtained:

$$J^{\rm tr}_{\nu\leftarrow\mu}(\omega) = {\rm Im}\left[\left(\frac{1}{2\pi}S^{\rm tr}_{\nu\leftarrow\mu}(z_d,\omega)\right)^{*} \partial_z \left(\frac{1}{2\pi}S^{\rm tr}_{\nu\leftarrow\mu}(z,\omega)\right)\Big|_{z=z_d}\right]. \tag{4.67}$$

Having similar expressions for the incident flux $J^{\rm in}$ and the reflected flux $J^{\rm ref}$, we arrive to the following formula

$$\mathbb{T}_{\mu}(\omega) = \frac{J^{\rm tr}_{\nu\leftarrow\mu}(\omega)}{J^{\rm in}_{\mu}(\omega)} = \frac{{\rm Im}\left[\left(S^{\rm tr}_{\nu\leftarrow\mu}(z_d,\omega)\right)^{*} \partial_z \left(S^{\rm tr}_{\nu\leftarrow\mu}(z,\omega)\right)\big|_{z=z_d}\right]}{{\rm Im}\left[\left(S^{\rm in}_{\mu}(z_d,\omega)\right)^{*} \partial_z \left(S^{\rm in}_{\nu\leftarrow\mu}(z,\omega)\right)\big|_{z=z_d}\right]}, \tag{4.68}$$

and similarly, in the respective virtual detectors,

$$\mathbb{R}_{\mu}(\omega) = \frac{J^{\rm ref}_{\nu\leftarrow\mu}(\omega)}{J^{\rm in}_{\mu}(\omega)} = \frac{{\rm Im}\left[\left(S^{\rm ref}_{\nu\leftarrow\mu}(z_d,\omega)\right)^{*} \partial_z \left(S^{\rm tr}_{\nu\leftarrow\mu}(z,\omega)\right)\big|_{z=z_d}\right]}{{\rm Im}\left[\left(S^{\rm in}_{\mu}(z_d,\omega)\right)^{*} \partial_z \left(S^{\rm in}_{\mu}(z,\omega)\right)\big|_{z=z_d}\right]}. \tag{4.69}$$

We have obtained the flux at $z = z_d$ numerically by an average and a finite difference approach on the signals at two different detectors separated by a small distance $2\delta z$ (in practice at two consecutive grid points):

$$S^{\rm tr}(z_d) \approx \frac{1}{2}\left[S^{\rm tr}(z_d+\delta z) + S^{\rm tr}(z_d-\delta z)\right], \tag{4.70}$$

$$\partial_z S^{\rm tr}(z)\big|_{z=z_d} \approx \frac{S^{\rm tr}(z_d+\delta z) - S^{\rm tr}(z_d-\delta z)}{\delta z}. \tag{4.71}$$

Results derived from the expressions above appear to be accurate enough. Nevertheless, the derivative above might be calculated "exactly" by performing a Fourier transform of the wave function and by multiplying by ik. This procedure, however, requires at each time step two additional computationally costing (direct and inverse) FFTs, with respect to the approximated approach.

4.4.4. Choice of the initial state

Up to now, for scattering problems, we assumed that the general initial wave packet should contain only incident waves, which is a convenient numerical demand. Here we develop the meaning of this statement for GWPs.

Let us consider an initial GWP of width Δz and average momentum k_0 given by Eq. (4.9). The choice of this kind of wave packets is dictated by practical reasons, in particular their smoothness and compactness both in real and k-space [83]. Also an initial convenient k-distribution can be easily set in such a way that it predominantly contains the ingoing components (here positive k), and the weight of the negative k-components can be made as small as desired due to the exponentially decaying amplitude far from the maximum. We have observed empirically that, by propagating these wave packets, we can extract well-converged information within the momentum window

$$|k - k_0| \lesssim (2\text{–}2.5)\Delta k. \tag{4.72}$$

Outside the above limits, because of the small amplitude of the corresponding spectral components, the errors coming from the non-perfect absorption at the boundaries, finite propagation time, and the numerical noise, render the results poorely converged. The magnitude of the error can be easily estimated from the flux conservation condition given by Eq. (4.61). Then, the loss of precision is manifested in the departure of the numerical results from unity.

Usually we are only interested in results within a given energy window defined by $E_{\min}$ and $E_{\max}$ (or in $k-$space $(k_{\min}, k_{\max})$ with $k = \sqrt{2E}$), where some special states or resonances exist, or basically because the system is physically well described only in that region. Thus, the spectral width of the incident GWP must be tuned to this window. Once the width Δk is set, the spatial extension of the wave packet Δz is also set via Eq. (4.12). The latter sets the space required for allocating the initial GWP in the asymptotic region. This space is determined by the requirement of no overlap between the initial wave function and the absorbing potential at the grid-boundary on one hand, and no overlap between the initial wave function and the scattering

potential on the other hand (see Fig. 4.2). We have chosen to use the criterion given by the computer precision, by noting that numerically the precision of the zero value is determined by the machine epsilon $\epsilon = 2^{-p}$, where p refers to the number of significant binary digits in a finite floating-point represention of numbers. The machine precision characterized by ϵ is defined as the upper bound on the relative error due to roundoff in floating point arithmetic operation [104]. Since we work within a scheme where the norm is conserved, a natural criterion to set the space $L_{\rm wp}$ needed to hold the initial GWP centered at z_0 is to demand that for $|z - z_0| > L_{\rm wp}/2$

$$|\Psi|^2 \leq \epsilon, \tag{4.73}$$

where, from the normalized GWP as given in Eq. (4.9), we obtain the following relation:

$$L_{\rm wp} > \sqrt{2}\Delta z \sqrt{p\ln(2) - \ln(\Delta z) - \frac{1}{2}\ln\left(\frac{\pi}{2}\right)}. \tag{4.74}$$

In a double precision number representation with $p = 53$, the space to be allocated for the initial wave packet in the asymptotic region for values of $\Delta z \sim 0.1$–100 a.u. is

$$L_{\rm wp} \gtrsim (8.8\text{–}8.0)\Delta z. \tag{4.75}$$

Similarly, for the wave packet in the reciprocal space, we demand that numerically the probability of finding an electron with negative momentum k is zero (assuming an incident wave packet with positive k_0): $|\tilde{\Psi}|^2 < \epsilon$ at $k = 0$. Then, the following criterion is obtained:

$$\frac{k_0}{\Delta k} \gtrsim 4.1\text{–}4.5. \tag{4.76}$$

The conditions in Eqs. (4.72) and (4.76) are not always compatible. Substituting $k = k_{\rm min}$ (where $k_{\rm min}$ is the minimum k of the energy window one is interested in) in Eq. (4.72), and using again Eq. (4.76), we have

$$(4.1\text{–}4.5) \lesssim \frac{k_0}{\Delta k} \lesssim (2\text{–}2.5) + \frac{k_{\rm min}}{\Delta k}, \tag{4.77}$$

and taking into account the zero condition in Eq. (4.76) we obtain the strong and weak conditions:

$$\left(\frac{k_{\rm min}}{\Delta k}\right) \gtrsim 1.5\text{–}2.5. \tag{4.78}$$

There might be the cases when the above inequality cannot be fulfilled because the information has to be extracted within a large spectral range. The solution then consists in performing independent calculations by sampling smaller energy ranges and

joining the corresponding results. Another alternative would be to construct an initial wave packet as a superposition of incident GWPs with smaller Δk (and thus larger but still reasonable Δz) and different k_0. Here each GWP is tuned to cover a partial region in k-space. In particular, an efficient configuration is obtained by setting a common width for all the Gaussians with the same center z_0 point and by only changing the incidence momentum k_0:

$$\psi_0(z) = e^{-(z-z_0)^2/\Delta z^2} \sum_{j=1}^{J} e^{ik_0^{(j)}(z-z_0)}, \tag{4.79}$$

where $k_0^{(j)}$ is the average momentum of the jth wave packet and J is the total number of wave packets, which is determined by the energy window to be covered. To have a uniform sampling for $k \in (k_{\min}, k_{\max})$ equally spaced $k_0^{(j)}$ values can be set. Note that, in the limit of a large number of wave packets with $\Delta k \to 0$ (thus $\Delta z \to \infty$),

$$\lim_{J\to\infty} \sum_{j=1}^{J} e^{ik_0^{(j)}(z-z_0)} \Delta k \sim e^{iK_0(z-z_0)} \mathrm{sinc}[\alpha(z-z_0)], \tag{4.80}$$

we obtain sinc (defined as $\sin(z)/z$) wave packets [105] where $\alpha{=}(k_{\max} - k_{\min})/2$ and $K_0 = (k_{\max} + k_{\min})/2$. The emerged sinc wave packets have a long range $\sim 1/z$ asymptotic behavior, which leads to allocation of a too large initial space in the asymptotic region. In our calculations we have used Eq. (4.79) with $J = 1$ and $J = 2$.

At this point it is worth mentioning that, when the scattering matrix has to be extracted for very small energies, $k_{\min} \ll 1$, it follows from Eq. (4.78) that we would need a $\Delta k \ll 1$, which implies $\Delta z \gg 1$. In this case there is need of a huge extra space for supporting the initial GWP.

The systems studied in the present thesis are free from the above difficulty. Indeed, (i) in general the scattering energies of interest require a $k_{\min} \sim 0.2 - 1$, and (ii) the relative low dimensionality of the calculation grid provides certain flexibility on the allocatable space for the initial wave packet.

As an example, in the study of the Na nanocontacts considered in Chapter 8, one of the scattering channels is associated with a small energy with $E_{\min} = 0.6$ eV. Then an incident Gaussian is used with $k_{\min} = 0.2$ a.u. and $\Delta k = 0.05$ a.u., which, according to the analysis above, implies that nearly 300 a.u. of an asymptotic space is needed *only* for allocating the initial wave packet. Due to the reduced dimensionality, i.e., the 2D character of the system, it has been still possible to perform the calculations reasonably fast.

In the systems where large extension of the spatial grid is impossible because of the memory and computing time constraints, the solution consists in using the Lippmann-Schwinger formalism reformulated in the time-domain. In this case the initial wave packet is not localized in the asymptotic region, but it has a finite support coinciding with the range of the scattering potential [106].

4.5. 1D propagation

In the particular case of only z-dependent effective potential $V(z)$, the motion along the z-coordinate and the motion in the (x, y)-plane can be decoupled. The solution $\psi(\mathbf{r}, t)$ of the TDSE takes the form:

$$\psi(\mathbf{r}, t) = \sum_{\mathbf{k}_\parallel} a_{\mathbf{k}_\parallel} \phi_{\mathbf{k}_\parallel}(z, t) e^{i(\mathbf{k}_\parallel \cdot \mathbf{r}_\parallel - \frac{1}{2}\mathbf{k}_\parallel^2 t)}, \tag{4.81}$$

where $\mathbf{r}_\parallel$ and $\mathbf{k}_\parallel$ are, respectively, the position vector and the momentum in the (x, y)-plane. We use the $\parallel$ notation for these quantities to link with the studies of quantum well states on metal surfaces as in Chapter 6 of this thesis, where the (x, y)-plane is the plane parallel to the surface and z-coordinate is perpendicular to the surface. The evolution of the wave function $\phi_{\mathbf{k}_\parallel}(z, t)$ is governed by the 1D-TDSE

$$i\partial_t \phi_{\mathbf{k}_\parallel}(z, t) = \hat{H}_z \phi_{\mathbf{k}_\parallel}(z, t), \tag{4.82}$$

with Hamiltonian

$$\hat{H}_z = \underbrace{-\frac{1}{2}\frac{\partial^2}{\partial z^2}}_{\hat{T}_z} + \underbrace{V_{\text{eff}}(z) + V_{\text{abs}}(z)}_{V}, \tag{4.83}$$

and initial condition $\phi_{\mathbf{k}\parallel}(z, t = 0) = \phi_{0\mathbf{k}_\parallel}$. The $\hat{T}_z$ operator is local in momentum (one-dimensional) k_z-space. Then, the propagation is performed by the dynamic Fourier method associated to the split-operator technique. Each short-time propagation is calculated as

$$\phi_{\mathbf{k}_\parallel}(z, t + \Delta t) = e^{-iV\Delta t/2} \mathcal{F}^{-1}\, e^{-ik_z^2 \Delta t/2} \mathcal{F}\, e^{-iV\Delta t/2} \phi_{\mathbf{k}_\parallel}(z, t), \tag{4.84}$$

where the numerical implementation of the FFT denoted by $\mathcal{F}$ is done by the efficient `FFTW` subroutines [107] applied to the wave function discretized on the uniform mesh. *A priori*, the step of the mesh Δz depends on the energy range to be covered. It is deduced from the Nyquist-Shannon sampling theorem [108] relating the maximum

wave vector accounted for in this pseudo-spectral approach so that $k_{\max} = \pi/\Delta z$. This is true for a free wave packet propagation. However, proper description of the potential in the real space grid reduces this upper bound. In present 1D applications we have used typically $\Delta z = 0.2$ a.u..

4.6. 2D propagation

4.6.1. Systems with cylindrical symmetry

To efficiently solve the TDSE of a given problem one has to adapt the coordinates to the symmetry of the effective potential characterizing the system. In our model for the breakage of Na nanowires considered in Chapter 8, the system has a cylindrical symmetry with respect to the nanowire axis. Then, cylindrical coordinates $\mathbf{r} = (\rho, \varphi, z)$ form the natural spatial coordinate system to use, where the z-direction is set along the symmetry axis. The Hamiltonian in Eq. (4.2) is rewritten in cylindrical coordinates as

$$H = \underbrace{-\frac{1}{2}\frac{\partial^2}{\partial z^2}}_{\hat{T}_z} \underbrace{-\frac{1}{2\rho}\frac{\partial}{\partial\rho}\rho\frac{\partial}{\partial\rho} - \frac{1}{2\rho^2}\frac{\partial^2}{\partial\varphi^2}}_{\hat{T}_{\rho\varphi}} + V(\rho, \varphi, z), \tag{4.85}$$

and the corresponding wave functions can be expanded in the angular basis as

$$\psi(\rho, \varphi, z, t) = \sum_m \frac{1}{\sqrt{2\pi}} e^{im\varphi}\psi_m(\rho, z, t), \tag{4.86}$$

where m is the azimuthal quantum number.

For the potential V independent of φ-coordinate, $V = V(\rho, z)$, the different m-symmetry subspaces can be treated independently. Using the wave function representation given by Eq. (4.86) in the TDSE with Hamiltonian given by Eq. (4.85), and integrating both sides with $\int_0^{2\pi} d\varphi e^{-iM\varphi}/\sqrt{2\pi}$, the M-symmetry Schrödinger equation is

$$i\partial_t\psi_M = H_M\psi_M, \tag{4.87}$$

with Hamiltonian

$$H_M = -\frac{1}{2}\frac{\partial^2}{\partial z^2} \underbrace{-\frac{1}{2\rho}\frac{\partial}{\partial\rho}\rho\frac{\partial}{\partial\rho} + \frac{M^2}{2\rho^2}}_{\hat{T}_\rho^{(M)}} + V(\rho, z). \tag{4.88}$$

Similarly to the 1D case we use the short-time propagation and the split-operator technique. The resulting short-time evolution operator is:

$$e^{-i\hat{H}\Delta t} = e^{-i(\Delta t/2)V} e^{-i\Delta t\hat{T}_\rho^{(M)}} e^{-i\Delta t\hat{T}_z} e^{-i(\Delta t/2)V} + O(\Delta t^3), \tag{4.89}$$

where the order of terms has been optimized to reduce the number of FFT transformations used in the calculation of $e^{-i\Delta t\hat{T}_z}$. Note that the kinetic energy operators $\hat{T}_\rho^{(M)}$ and $\hat{T}_z$ commute: $[\hat{T}_\rho^{(M)}, \hat{T}_z] = 0$. Thus the exponentials $e^{-i\Delta t\hat{T}_\rho^{(M)}}$ and $e^{-i\Delta t\hat{T}_z}$ can be applied in any order. The wave function ψ_M is discretized on a mesh of points in ρ and z coordinates. A uniform mesh is used in z and in ρ we use the non-uniform mesh detailed below. Fourier grid pseudo-spectral technique for calculating the action of the operators $e^{-i\Delta T_z}$ and $e^{-i\Delta V}$ has been detailed in the previous section. The method still holds with corresponding operations performed independently for each ρ-point of the grid.

The calculation of the action of the $e^{-i\Delta t\hat{T}_\rho^{(M)}}$ operator is more involved. One can use the fast Hankel transform (FHT), which is the analog transformation of the FFT, but in cylindrical coordinates instead of Cartesian coordinates [109]. An alternative approach has been adopted in this thesis. We use a Crank-Nicholson scheme combined with three point finite differences for the evaluation of spatial derivatives. The implemented technique has the following desirable properties: (i) It is stable, (ii) the propagation error scales as $O(\Delta t^3)$, and (iii) it is fast, because the numerical effort of the method consists in the solution of a tridiagonal system of linear equations. Additionally, the method allows large flexibility in wave function mapping with non-uniform mesh, which in general improves the convergence of the solution with the number of points, as compared to a uniform one.

It is convenient to propagate the modified wave function $\tilde{\psi}_M$ defined as

$$\psi_M = \frac{\tilde{\psi}_M}{\sqrt{\rho}}. \tag{4.90}$$

The time evolution of $\tilde{\psi}_M$ is governed by the TDSE with Hamiltonian given by Eq. (4.88), where $\hat{T}_\rho^{(M)}$ is transformed to a symmetric form as

$$\hat{T}_\rho^{(M)} \to \hat{T}^M = -\frac{1}{2\sqrt{\rho}}\frac{\partial}{\partial\rho}\rho\frac{\partial}{\partial\rho}\frac{1}{\sqrt{\rho}} + \frac{M^2}{2\rho^2}. \tag{4.91}$$

Note above that $\hat{T}_\rho^{(M)}$ and $\hat{T}^M$ are two different operators. The preference for the symmetric form of the operator is dictated by the easiness in obtaining Hermitian grid-Hamiltonian. Let us consider the action of this operator onto a wave function F.

The idea is to consider a three point finite differences for representing the first and second derivatives in Eq. (4.91). Here, F is discretized on a uniform ρ mesh with step $\Delta\rho$. For notation simplicity $F_j \equiv F(\rho_j)$, and $F_{j\pm1/2} \equiv F(\rho_j \pm \Delta\rho/2)$. Then

$$\left(\hat{T}^M F\right)_k = -\frac{1}{2}\frac{1}{\sqrt{\rho_k}}\frac{\rho\frac{d}{d\rho}\left.\frac{F}{\sqrt{\rho}}\right|_{k+1/2} - \rho\frac{d}{d\rho}\left.\frac{F}{\sqrt{\rho}}\right|_{k-1/2}}{\Delta\rho} + \frac{M^2}{2\rho_k^2}F_k, \tag{4.92}$$

and, applying again the finite difference to the derivatives, we have

$$\left(\frac{-1}{2\Delta\rho^2}\right)\frac{1}{\sqrt{\rho_k}}\left\{\rho_{k+1/2}\left(\frac{F_{k+1}}{\sqrt{\rho_{k+1}}} - \frac{F_k}{\sqrt{\rho_k}}\right) - \rho_{k-1/2}\left(\frac{F_k}{\sqrt{\rho_k}} - \frac{F_{k-1}}{\sqrt{\rho_{k-1}}}\right)\right\} + \frac{M^2}{2\rho_k^2}F_k. \tag{4.93}$$

By rearranging and collecting the different terms, the action of $\hat{T}^M$ can be represented in matrix form as

$$(\mathbb{T}^M F)_k = \sum_{k'} T^M_{kk'} F_{k'}, \tag{4.94}$$

where the tridiagonal matrix $\mathbb{T}^M$ is:

$$\begin{pmatrix} T^M_{11} & T^M_{12} & 0 & 0 & 0 & 0 \\ T^M_{21} & T^M_{22} & T^M_{23} & 0 & 0 & 0 \\ 0 & T^M_{32} & T^M_{33} & \ddots & 0 & 0 \\ 0 & 0 & \ddots & \ddots & \ddots & 0 \\ 0 & 0 & 0 & \ddots & T^M_{N-1,N-1} & T^M_{N-1,N} \\ 0 & 0 & 0 & 0 & T^M_{N,N-1} & T^M_{NN} \end{pmatrix}, \tag{4.95}$$

with

$$T^M_{k,k+1} = -\frac{1}{2}\frac{1}{\Delta\rho^2}\rho_{k+1/2}\frac{1}{\sqrt{\rho_k\rho_{k+1}}}, \tag{4.96}$$

$$T^M_{k,k} = \frac{1}{2}\frac{1}{\Delta\rho^2}\left(\frac{\rho_{k+1/2}}{\rho_k} + \frac{\rho_{k-1/2}}{\rho_k}\right) + \frac{M^2}{2\rho_k^2}, \tag{4.97}$$

$$T^M_{k,k-1} = -\frac{1}{2}\frac{1}{\Delta\rho^2}\rho_{k-1/2}\frac{1}{\sqrt{\rho_k\rho_{k-1}}}. \tag{4.98}$$

Concerning the boundary conditions, we impose $F_{N+1} = 0$, i.e., the Dirichlet boundary condition at the external boundary. For the interior grid-boundary, the divergence at ρ_0 in Eq. (4.98) is solved by adding the $\Delta\rho/2$ onset to the discretized grid:

$$\rho_j = \frac{\Delta\rho}{2} + \Delta\rho(j-1). \tag{4.99}$$

Thus, when $k = 1$ in Eq. (4.98), $T^M_{10} = 0$. The matrix above is real and symmetric, as can be directly checked by substituting $k \to k + 1$ in $T^M_{k,k-1}$.

With the present discretized form of the $\hat{T}^M$ operator the action of the $e^{-i\Delta t\mathbb{T}^M}$ on the vector corresponding to the wave function values at the grid points is calculated via the Cayley transform [see Eq. (4.28)]. The exact

$$\mathfrak{F} = e^{-i\Delta t\mathbb{T}^M} F \tag{4.100}$$

($\mathfrak{F}$ and F are vectors) is replaced by the approximate expression

$$\mathfrak{F} = (1 + i\frac{\Delta t}{2}\mathbb{T}^M)^{-1}(1 - i\frac{\Delta t}{2}\mathbb{T}^M)F, \tag{4.101}$$

with an error $O(\Delta t^3)$. Since $\mathbb{T}^M$ is Hermitian, the norm is preserved, $\|\mathfrak{F}\| = \|F\|$, i.e., the operation is unitary. In practice we do not perform the matrix inversion as in Eq. (4.101), but a linear system of equations is solved:

$$(1 + i\frac{\Delta t}{2}\mathbb{T}^M)\mathfrak{F} = (1 - i\frac{\Delta t}{2}\mathbb{T}^M)F, \tag{4.102}$$

with unknown vector $\mathfrak{F}$ and known RHS. Because of the tridiagonal structure of the $\mathbb{T}^M$ matrix the solution of Eq. (4.102) can be efficiently performed with a numerical effort linearly proportional to the number of the ρ-mesh points.

Note that the above Cayley transform is not by itself a short-time propagation, but an intermediate step in the real short-time propagation of Eq. (4.89).

4.6.2. Coordinate mapping

From the experience acquired while running the WPP routines we could conclude that, when finite difference techniques are used, an accurate representation of the wave function at small ρ requires a tight mesh. For a uniform mesh this leads to the oversampling of the wave functions at large ρ, with the consequent loss of efficiency in the calculation. This drawback can be circumvented in the above method by performing a variable change and mapping properly the regions where dense sampling is needed. A particular choice, which has been used for the study of the sodium nanocontacts in Chapter 8, is the following:

$$\rho \to \rho = f(\xi) = \xi - \frac{b}{\sqrt{a}} \tan^{-1}\left(\frac{\xi}{\sqrt{a}}\right), \tag{4.103}$$

where a and b parametrize the family of transformations. For convenience we introduce the parameter c by $b = (1-c)a$. The derivative is then obtained:

$$d\rho/d\xi = f' = 1 - \frac{(1-c)a}{\xi^2 + a}, \tag{4.104}$$

and the desirable limits are easily evaluated (with $c \ll 1$):

$$\lim_{\xi\to 0} \rho' \sim c \Rightarrow \Delta\rho = c\Delta\xi, \tag{4.105}$$

$$\lim_{\xi\to\infty} f' \sim 1 \Rightarrow \Delta\rho = \Delta\xi, \tag{4.106}$$

where $\Delta\xi$ is the constant step in ξ-mesh. From the equation above, it follows that $\sqrt{a}$ defines the extension in ξ-space where the physical grid is tight (observe the almost linear dispersion above $\xi \sim \sqrt{a} \approx 26$ in Fig. 4.3). The c parameter defines the smallest sampling step on the physical ρ-grid [see Eq. (4.105)]. The normalization condition of the wave function is

$$\int f(\xi) f'(\xi) |\psi_M(\xi, z, t)|^2 d\xi = 1. \tag{4.107}$$

The non-weighted Euclidean norm of the grid-projected wave function can be obtained by applying the propagation to the wave function $\tilde{\psi}_M(\xi, z, t)$ defined as:

$$\psi_M(\rho, z, t) = \frac{\tilde{\psi}_M(\xi, z, t)}{\sqrt{f f'}}. \tag{4.108}$$

The $\tilde{\psi}_M$ fulfills the TDSE equation with Hamiltonian

$$H_\xi^M = -\frac{1}{2}\frac{\partial^2}{\partial z^2} \underbrace{-\frac{1}{2}\frac{1}{\sqrt{ff'}}\frac{d}{d\xi}\frac{f}{f'}\frac{d}{d\xi}\frac{1}{\sqrt{ff'}} + \frac{M^2}{2f^2}}_{\hat{T}_\xi^M} + V(\xi, z). \tag{4.109}$$

We can calculate, as in the previous subsection, the matrix elements of the operator $\hat{T}_\xi^M$. By defining the funtion $g(\xi) = \sqrt{f(\xi)f'(\xi)}$, the matrix elements read:

$$T_{k,k+1}^M = -\frac{1}{2}\frac{1}{\Delta\xi^2}\frac{1}{g_k g_{k+1}}\frac{f_{k+1/2}}{f'_{k+1/2}} \tag{4.110}$$

$$T_{k,k}^M = \frac{1}{2}\frac{1}{\Delta\xi^2}\frac{1}{g_k^2}\left\{\frac{f_{k+1/2}}{f'_{k+1/2}} + \frac{f_{k-1/2}}{f'_{k-1/2}}\right\} \tag{4.111}$$

$$T_{k,k-1}^M = -\frac{1}{2}\frac{1}{\Delta\xi^2}\frac{1}{g_k g_{k-1}}\frac{f_{k-1/2}}{f'_{k-1/2}}, \tag{4.112}$$

with grids

$$\xi_j = \frac{\Delta\xi}{2} + \Delta\xi(j-1). \tag{4.113}$$

The resulting $\mathbb{T}_\xi^M$ matrix is Hermitian (specifically tridiagonal, real and symmetric). The action of the $e^{-i\Delta t\mathbb{T}_\xi^M}$ operator is then calculated via a Cayley transform, as in the uniform mesh case. The rest of the propagation is identical for mapped and uniform grids.

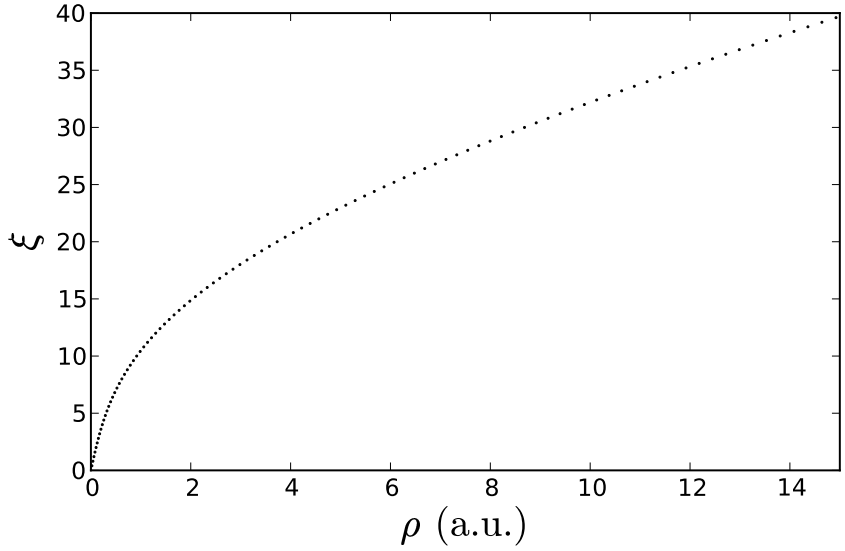

Figure 4.3.: Calculation grid points, under the variable change given by Eq. (4.103), with respect to the physical space. The parameters are $\Delta\xi = 0.4$, $a = 700$ and $c = 0.05$.

4.7. Elastic electronic transport in mesoscopic systems

In the particular cases studied in this thesis the WPP is by itself a simulation of electron propagation, and thus, it could be considered as a charge transfer process in certain cases. It is worth stressing that in our work the WPP method has been used as a tool for extracting the dynamical and scattering properties of some particular systems. A related issue is the electronic transport properties of a mesoscopic or molecular/atomic junction. In this case further assumptions have to be made, since we deal with a

steady-state of the system, and its description should be based on a self-consistent treatment and the electronic current itself. Thus, the description becomes much more complicated.

Fortunately, there appear to be simple relations between the scattering properties and transport properties of the systems, at least in the ballistic regime (here understood as an elastic process in which the electron transport is only limited by scattering with the boundaries of the sample). Early during the foundations of quantum mechanics, the connection between the one-electron tunneling and the current was understood in certain experiments, such as in studying insulating films between two metal electrodes [110]. However, the corresponding tunneling/scattering probability was not related to point contact currents until Landauer's formula [111].

The state-of-the-art calculations of transport properties in nanosized devices are based on the non-equilibrium Green's function formalism (NEGF) [112], where the inelastic current is also taken into account. In this thesis we have restricted ourselves to the elastic transport (within the Landauer formalism), which might be considered as the zero-order approximation (no interaction in the scatterer) to the NGFE equations [113]. The inelastic effects, however, can be taken in a limited phenomenological way within the WPP by absorbing potentials (see Subsection 4.3).

In this section we provide the necessary equations for evaluating the electronic currents in the systems considered in this thesis with the scattering quantities calculated with the WPP. First we present the expression providing the current between two metallic plates separated by an insulating layer. The insulating layer is basically characterized by a potential barrier. In our calculations it consists of a vacuum space. Second, we derive the Landauer formula in a similar fashion, and finally, we provide the multichannel generalization.

To derive the electronic transport equations we will follow closely the formulation given in Ref. [114].

4.7.1. Tunneling current between a flat tip and a metallic surface

For the theoretical study of the constant-current characteristics in scanning tunneling spectroscopy experiments studied in Chapter 7 the flat-tip approximation has been used, which is well justified for the high-bias case [115, 116]. Indeed, under high bias, the electrons tunnel into the surface, not only from the group of the last atoms at the tip apex, but from the mesoscopic surface of the tip as well. The flat-tip approximation results in the 1D model potential description of the STM junction. With the present model description the system is invariant with respect to translations parallel to the surface.

In the following we assume a one-electron picture of electron tunneling, as that depicted in Fig. 4.4, with only a z-varying potential. The motion in the plane parallel to the surface is free-electron like. We also assume an energy conserving tunneling process. Then, in the tunneling process the parallel momentum $\mathbf{k}_{\|}$ is conserved and, in the perpendicular direction, the incident electron from the left side with momentum $k_{z,l}$ is transmitted with $k_{z,r}$ momentum to the right side. By energy conservation we have:

$$U_0 + V + k_{z,l}^2/2 = k_{z,r}^2/2 = E_z, \tag{4.114}$$

where $U_0 + V$ is the inner potential in the left side, raised by the bias V, and in the RHS it is taken as zero. E_z is the energy in the perpendicular direction.

By considering infinitesimal electron current densities in both sides at a given perpendicular energy, and integrating over all $\mathbf{k}_{\|}$, an expression is obtained for the net current density, commonly referred to as the Tsu-Esaki formula [117]:

$$J(V,Z) = \frac{k_B\theta}{2\pi^2}\int_{U_0+V}^{\infty} dE_z T(E_z,V)\ln\left(\frac{1+e^{(E_F+V-E_z)/k_B\theta}}{1+e^{(E_F-E_z)/k_B\theta}}\right), \tag{4.115}$$

where θ is the temperature, k_B is the Boltzmann constant and $T(E,V,Z)$ is the transmission probability which depends on energy, on the applied bias and also in the tip-surface distance Z. The logarithmic factor in the integrand is called the supply function. At the low temperature regime Eq. (4.115) reduces to

$$J(V,Z) = \frac{1}{2\pi^2}\left[V\int_{U_0+V}^{E_F} dE_z T(E_z,V,Z) + \int_{E_F}^{E_F+V} dE_z T(E_z,V,Z)(E_F+V-E_z)\right]. \tag{4.116}$$

There exist different expressions for current calculations: Eq. (4.115) might be generalized for the case when the tip and the sample are described by different effective masses in parallel motion [118]. On the other hand, by treating self-consistently the tunneling

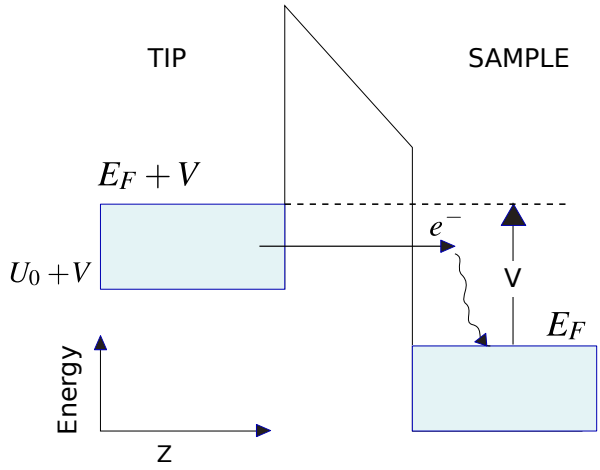

Figure 4.4.: Schematic representation of electron tunneling from the STM tip into the sample and (possible) eventual termalization by many-body scattering.

current, the bias voltage and electron densities in the sample and in the tip, an alternative equation can be derived. Then Eq. (4.116) would appear as an approximated expression to the self-consistent one [119].

Provided free-electron motion parallel to the surface in the model Pb/Cu(111) system, the constant-current scanning tunneling spectroscopy (STS) characteristics in the Pb/Cu(111) system considered in Chapter 7 have been obtained with Eq. (4.116). Several authors have worked with this equation in related studies [115, 120]. The transmission entering the equation has been calculated with the WPP, as explained in Subsection 4.4.3.

4.7.2. Landauer-Büttiker formalism for the conductance

In the following we consider a finite system connected adiabatically to two leads, coupled to two electron reservoirs (see Fig. 4.5). We assume that electrons are emitted from the left, and collected at the right. By considering only one conducting channel, the original Landauer formula at 0 K temperature [111] is obtained:

$$G = G_0 T(E = E_F) = G_0 T, \tag{4.117}$$

where $G_0 = \frac{2e^2}{h} \approx 7.75 \times 10^{-5} \Omega^{-1}$ is the so-called conductance quantum and T is the electron transmission probability evaluated at the Fermi level. The generalization to the two-terminal multichannel case usually called the Landauer-Büttiker formula [121],

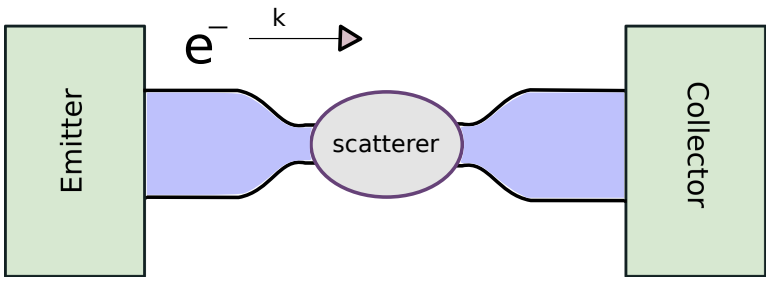

Figure 4.5.: Schematic illustation of a nanosized scatterer adiabatically connected to two leads. Electrons are emitted and collected in the boundaries by electron reservoirs.

reads:

$$G = G_0 \sum_{\mu\nu}^{\text{open}} T_{\mu\nu}(E = E_F), \tag{4.118}$$

where the set of μ, ν indexes denote the scattering open channels, with asymptotic μ-labeled initial incident state (from the emitter side) and ν-labeled final scattered state (at the collector side), as considered in Section 4.4 devoted to the scattering.

The conductance formula above, which corresponds to the small bias limit, only contains information around the Fermi level E_F. Experimentally, scattering properties (and resonances in particular) of the system above or below E_F can be probed by applying a voltage difference V between the leads. In a symmetric system, the Fermi level of the scatterer (it might be considered as a molecular entity) is set at $V/2$. In this case, under a voltage difference V, the induced current between the leads is given by

$$I(V) = G_0 \sum_{\mu\nu}^{\text{open}} \int_{E_F - \frac{V}{2}}^{E_F + \frac{V}{2}} dE\, T_{\mu\nu}(E, V) \approx G_0 \sum_{\mu\nu}^{\text{open}} \int_{E_F - \frac{V}{2}}^{E_F + \frac{V}{2}} dE\, T_{\mu\nu}(E), \tag{4.119}$$

where the bias dependence of the transmission T has been neglected. Then, by applying the Leibniz integral rule to the derivative of the current in Eq. (4.119), the differential conductance is obtained:

$$\frac{dI}{dV} = \frac{G_0}{2} \sum_{\mu\nu}^{\text{open}} \left[T_{\mu\nu}\left(E_F - \frac{V}{2}\right) + T_{\mu\nu}\left(E_F + \frac{V}{2}\right) \right]. \tag{4.120}$$

It should be noted that, due to the superposition between transmission contributions from above and below the Fermi level, not all the resonances found in the transmission might show up in a resolvable way in the differential conductance.

For larger bias, inelastic transport effects are expected to have a considerable influence in the actual current. Concerning Eq. (4.120), the major failure in the description comes from the assumption that the density of states and thus the transmission, does not change upon applied bias. The results obtained with this simplified treatment have to be taken with caution since, in principle, in this out-of-equilibrium situation the current and the transmission should be found self-consistently.

Finally, it is worth noting the equivalence between the ballistic formalism presented for a finite system in this subsection, and that presented for the tunneling current between a flat tip and a metallic surface, in the previous one. For a system with translational symmetry, the labels μ, ν in Eq. (4.119) correspond to the parallel momentum $\mathbf{k}_\parallel$, which is assumed to be conserved through the scattering. In this case, a current through an effective area A is assumed. Then, by performing the integration over $\mathbf{k}_\parallel$ (by the usual prescription $\frac{1}{A}\sum_{\mathbf{k}_\parallel} \rightarrow \frac{1}{(2\pi)^2}\int d\mathbf{k}_\parallel$) and realizing that $T_{\mathbf{k}_\parallel}(E) = T(E - \mathbf{k}_\parallel^2/2) = T(E_z)$, the current density $J = I/A$ of Eq. (4.116) can be obtained. Note also that in atomic units (a.u.) $G_0 = 1/\pi$.

Chapter 5

Confined electronic states in metallic overlayers: simple models

5.1. Introduction

In a very simple picture, conduction electrons in a free-standing metallic thin film populate all the available energy levels following the Pauli exclusion principle and forming a "Fermi sea". The highest occupied level is the Fermi level. In practice, these thin films can be materialized as metallic overlayers grown on a substrate. If the (metallic) substrate contains a (projected) energy band gap, together with the vacuum barrier, a quantum well potential is formed in the corresponding energy region leading to the localization of the available states. Under an external perturbation (for example by a laser pulse) an electron can be excited to a higher energy state. However, this situation is unstable and the electron will only remain in this state a finite time τ before it decays to the Fermi sea. This *lifetime*, combined with the velocity of the electron v at the excited state, defines the mean free path of the electron: $\lambda_{\mathrm{fp}} = \tau v$. If the thickness of the overlayer is of the order or smaller than the electron mean free path in the perpendicular direction of motion, quantization of the energies in this direction appear (standing waves can be formed). Assuming an ideal free-electron motion in the parallel direction, the quantization leads to a band structure formed by parabolic bands as sketched in Fig. 5.1. Then, the band structure is said to be composed of quantum well state bands and the states at $\overline{\Gamma}$ are simply referred to as the quantum well states.

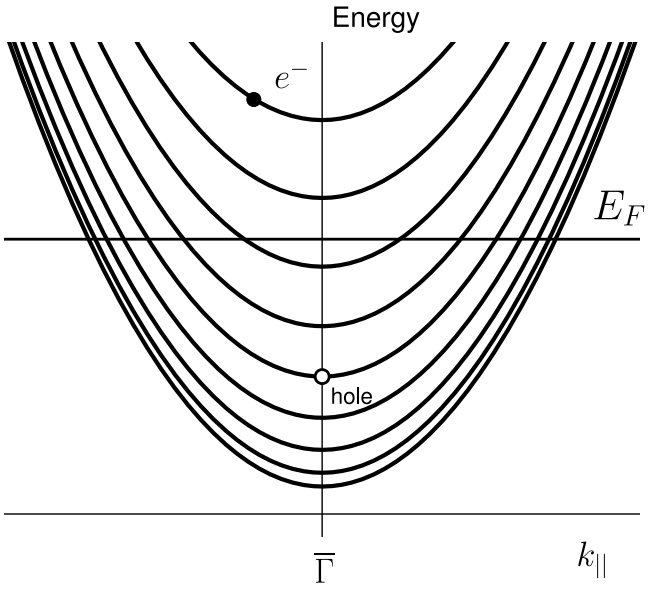

Figure 5.1.: Diagram representing the electronic parabolic band structure of an ideal quantum well potential. Electrons (holes) can be excited above (below) the Fermi level (E_F).

On metallic surfaces, in addition, image states can appear close to the vacuum level. These states are almost entirely localized in the vacuum side, due to the long range image potential barrier at these energies. Therefore, they are very sensitive to external perturbations, as for example, an external electric field. Then, image states are Stark shifted and evolve into field emission resonances, i.e., (quasi-) confined states between the metallic surface and the electric field barrier.

The aim of this chapter is to provide a basic background and to discuss some fundamental physics concerning the quantum well states (QWSs), quantum well resonances (QWRs), image states (ISs) and field emission resonances (FERs). For this purpose analytic solutions of simple one-dimensional models are derived in this section. The states mentioned above, together with crystal-induced surface states [122], form the basic variety of the different electronic states in metallic overlayers and metal surfaces, resulting from the confinement in one dimension.

First, and for the sake of completeness, some simple quantum mechanical results concerning the electron confinement in square potential wells are surveyed. After that, the phase accumulation model (PAM) is introduced, which is a very useful tool for discussing the electronic energy quantization in metal overlayers and surfaces through phase shifts associated to the confinement barriers at the interfaces. With this back-

ground, in the subsequent sections the properties of QWSs, QWRs, ISs and FERs are described together with their phase shift models. Furthermore, the use of the phase accumulation model is discussed with very simple potentials. This serves as an illustration of the concepts that underlie the discussions of the results in the study of the Pb/Cu(111) system to be presented in Chapters 6 and 7.

The main original results provided in this chapter are: (i) the derivation of the analytic expressions for the resonance energies and widths found in the asymmetric square potential, which is an extension of the results reported by E. Ogando *et al.* in Ref. [19] and (ii) the discussion of the suitability of the linear ramp barrier phase shift formula for describing the FERs energy series.

5.2. Square well confining potentials

5.2.1. Infinite square well

The simplest model for describing the basic features of QWSs in a metallic overlayer is the well known 1D infinite square well potential. The z-coordinate dependence of the potential in this case is given by

$$V(z) = \begin{cases} 0 & |z| < d/2 \\ \infty & \text{elsewhere,} \end{cases} \tag{5.1}$$

where d is the thickness of the potential well and the potential insided the well is set to zero without loss of generality. The motion in parallel direction $\mathbf{r}_{\|} = (x, y)$ is assumed to be that of the free-electron particle. We also assume a parallel effective mass m^*, which accounts for the effects of the underlying crystal structure on the electron motion in this direction. The eigenfunctions of the Schrödinger equation are of the form:

$$\Psi_{n\mathbf{k}_{\|}}(z, \mathbf{r}_{\|}) = \psi_n(z) \frac{1}{2\pi} e^{i\mathbf{k}_{\|}\cdot\mathbf{r}_{\|}}, \tag{5.2}$$

with energy

$$E_{n\mathbf{k}_{\|}} = E_n + \frac{\mathbf{k}_{\|}^2}{2m_n^*}, \tag{5.3}$$

where ψ_n and E_n are the eigenfunctions and energy eigenvalues for the 1D-Schrödinger equation fulfilled by $\psi(z)$, with boundary conditions $\psi(-d/2) = \psi(d/2) = 0$ imposed by the infinite barrier. Note that, in principle, the parallel effective mass also depends on n.

The plane waves $e^{\pm ikz}$ with wave vector $k = \sqrt{2m_{\perp}^{*}E}$ (where $m_{\perp}^{*}$ is the effective mass in the perpendicular direction of motion, entering the kinetic energy in the 1D-Schrödinger equation) are solutions for a discrete set of k fulfilling the condition

$$kd = \pi n, \tag{5.4}$$

where $n = 1, 2, \ldots$ for nontrivial solutions. Then, the eigenfunctions can be expressed with a well defined parity as:

$$\psi_n(z) = \begin{cases} \sqrt{2/d}\cos\left(\frac{\pi n z}{d}\right), & n \text{ odd} \\ \sqrt{2/d}\sin\left(\frac{\pi n z}{d}\right), & n \text{ even}, \end{cases} \tag{5.5}$$

and the energies of the one-electron motion in the direction perpendicular to the overlayer are

$$E_n = \frac{\pi^2 n^2}{2m_{\perp}^{*}d^2}. \tag{5.6}$$

Then the energy difference between two consecutive states is

$$\Delta E_n = E_{n+1} - E_n = \frac{\pi^2}{2m_{\perp}^{*}d^2}(2n+1), \tag{5.7}$$

thus, $\Delta E_n \propto n$ for high n. It follows from Eq. (5.5) that ψ_n has $n-1$ nodes for $|z| < d/2$. On the other hand, it follows from Eq. (5.6) that the energy of a state with fixed n decreases as $\propto 1/d^2$ when the width d of the well is increased.

Despite the crude approximation of setting the confinement barriers to infinite, this model has been successfully used to reproduce the series of QWS state energies in STM studies of Pb/Cu(111) [10,11]. However, it is not adequate for discussing the properties related to the penetration of the wave functions into the substrate and vacuum, and naturally, QWRs cannot exist within this picture. These features are included in the following model.

5.2.2. Finite square well: resonances

The next step improving the simple model above for describing an overlayer-substrate system is to consider the (asymmetric) finite potential well, as sketched in Fig. 5.2. This might be considered as an approximation to the self-consistent DFT-LDA calculations with a jellium model description (see Ch. 2) of both the metal substrate and metal overlayer. The U_1 and U_2 potential heights appearing in Fig. 5.2 correspond to

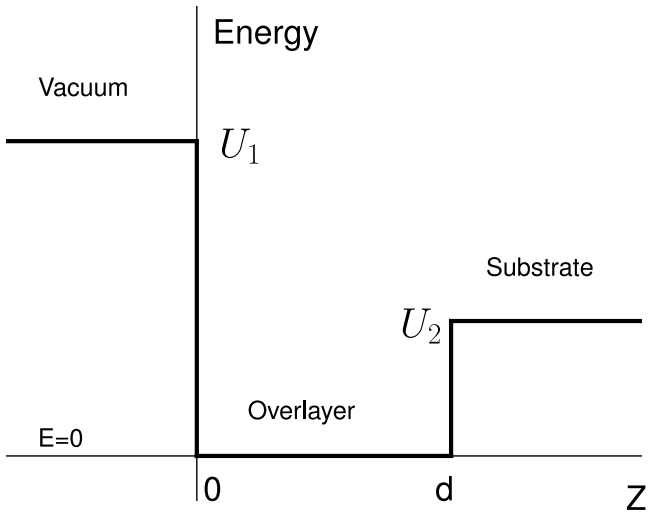

Figure 5.2.: Schematic diagram of an asymmetric square potential well of thickness d and barrier heights U_1 and U_2.

the averaged one-electron effective potential of the underlaying crystal lattice in the perpendicular direction. In the following it is assumed that the average potential of the substrate is above that corresponding to the overlayer, i.e., $U_2 > 0$, as it happens in the jellium description of the Pb/Cu(111) system. However, in systems like Na/Al(111) the jellium description has a corresponding $U_2 < 0$ [19]. The latter situation is not considered here. U_1 corresponds to the overlayer-vacuum barrier.

The potential represented in Fig. 5.2 has three well defined energy regions: (i) $E < U_2$, (ii) $U_2 < E < U_1$ and (iii) $E > U_1$. In the first one, bound states are found similar to those found in the infinite potential well, which is used to introduce the concept of the effective thickness. In the second case, the quasi-stationary states (resonances) are extracted following the procedure of Ref. [19] and the elastic decay rate into the substrate is also obtained. In the third case, the electron energy is above the vacuum level, thus, it can propagate from vacuum into the solid. This last case is not considered here.

Case: $E < U_2$

In this case the particle is confined by the two finite potential barriers. The boundary conditions at the interfaces, in addition to $\lim_{z\to\pm\infty} \psi(z) = 0$, lead to the quantization

condition, given by the transcendental equation [123]:

$$kd = \pi n - \arcsin[k/\sqrt{2m_\perp^* U_1}] - \arcsin[k/\sqrt{2m_\perp^* U_2}], \tag{5.8}$$

where $n = 1, 2, 3, \ldots$ In order to obtain analytic solutions, it is convenient to continue by assuming a symmetric potential. The main conclusions, however, are applicable to the asymmetric case. Then $U_1 = U_2 = U_0$ and, introducing $\xi = kd/2$, eigenenergies can be expressed as

$$E_n = \frac{2\xi_n^2}{m_\perp^* d^2}, \tag{5.9}$$

where $\xi = \xi_n$ are the roots of the following equations

$$\cos\xi = \pm\gamma\xi, \quad n \text{ odd} \tag{5.10a}$$

$$\sin\xi = \pm\gamma\xi, \quad n \text{ even}, \tag{5.10b}$$

with $\gamma = \frac{1}{d}\sqrt{2/(m_\perp^* U_0)}$. After some algebra, energies in Eq. (5.9) can be represented in the form of Eq. (5.6) as

$$E_n = \frac{\pi^2 n^2}{2m_\perp^* d_{\text{eff}}^2}, \tag{5.11}$$

with an *effective thickness*:

$$d_{\text{eff}} = d + \left| \frac{2}{k(E_n)} \arcsin\left(k(E_n)/\sqrt{2m_\perp^* U_0}\right) \right|. \tag{5.12}$$

Thus, the energies of a finite symmetric quantum well can be always represented as those of the infinite well, but with an effective width given by the original width plus an energy-dependent positive correction, $d_{\text{eff}} = d + \delta_0(E)$. For the values $U_0 = 13.0$ eV and $k_F = 0.85\, a_0^{-1}$, corresponding approximately to our effective potentials describing the Pb/Cu(111) system, a thickness correction of $\delta_0 \approx 2.5 a_0$ is obtained. This correction is physically interpreted as follows: Due to the finite height of the potential walls, the electron wave functions can penetrate through the barriers. This penetration increases with the kinetic energy because the barrier height seen by the electron is smaller. Then, the energy dependent effective width accounts for the spilling of wave functions out of the potential well.

Case: $U_1 > E > U_2$

This case is more complicated to analyze, since the states lying at this energy range are not confined anymore. However, resonant states can exist, i.e., the quasi-stationary

states. The general solutions of the Schrödinger equation in the different spatial regions are given by:

$$\psi_\kappa(z) = A_\kappa e^{\kappa z} \qquad z < 0, \quad \text{vacuum}, \tag{5.13a}$$

$$\psi_k(z) = B_k \sin(kz + \varphi) \qquad 0 < z < d, \quad \text{overlayer}, \tag{5.13b}$$

$$\psi_\chi(z) = C_\chi \sin(\chi z + \phi) \qquad z > d, \quad \text{substrate}, \tag{5.13c}$$

where the corresponding wave vectors (assuming here, for simplicity, $m^*_\perp = 1$) as a function of energy are given by:

$$\kappa = \sqrt{2(U_1 - E)}, \tag{5.14a}$$

$$k = \sqrt{2E}, \tag{5.14b}$$

$$\chi = \sqrt{2(E - U_2)}. \tag{5.14c}$$

The phases φ and ϕ are energy dependent. Using matching conditions of the wave function at the interfaces, one can derive the following equations:

$$k/\kappa = \tan(\varphi), \tag{5.15a}$$

$$A_\kappa = B_k \sin(\varphi), \tag{5.15b}$$

$$\chi \tan(kd + \varphi) = k \tan(\chi d + \phi), \tag{5.15c}$$

$$B_k \sin(kd + \varphi) = C_\chi \sin(\chi d + \phi). \tag{5.15d}$$

Since these are continuum states, one could look at the density of states in the overlayer in order to extract the energies of the quasi-stationary states (alternatively, one could follow the conventional scattering theory approach and to look at the scattering phase shift [123]). As already discussed in Subsection 4.4.1 of Chapter 4, devoted to the wave packet propagation method, the resonances appear as Lorentzian peaks in the (projected) density of states. In the present context, the density of states in the overlayer is accessed by integrating the space-resolved (or local) density of states from the vacuum into the overlayer by several monolayer thicknesses of distance l. This distance l ($\sim$ 5–15 Å) can be associated to the metal region, from which photoemitted electrons in photoemission experiments emerge without serious degradation at metals surfaces [124, 125]. Then, the local density of states (LDOS) at $\overline{\Gamma}$ is given by:

$$\text{LDOS}(z, E) \sim |\psi_E(z)|^2. \tag{5.16}$$

By integrating $|\psi_E(z)|^2$ from the vacuum to a distance l inside the overlayer, and using Eqs. (5.15d) and (5.13c), the following analytical expression of the integrated local density of states (ILDOS) is obtained:

$$\text{ILDOS}(E) = \int_{-\infty}^{l} |\psi|^2 dz = \frac{|C_\chi|^2}{\frac{k^2}{\kappa^2}\cos^2(kd + \varphi) + \sin^2(kd + \varphi)} f(k, \kappa), \tag{5.17}$$

where $f(k,\kappa)$ is a factor which varies smoothly (with realistic parameters)

$$f(k,\kappa) = \frac{k^2}{\kappa^3 + k^2\kappa} + l + \frac{\sin(2\varphi)}{2k} - \frac{\sin[2(kl+\varphi)]}{2k}, \tag{5.18}$$

and since $|C_\chi|$ does not depend on energy for large enough (infinite) substrate, the factor

$$\frac{1}{\frac{k^2}{\kappa^2}\cos^2(kd+\varphi) + \sin^2(kd+\varphi)} \tag{5.19}$$

in Eq. (5.17) determines the structure of the ILDOS. For $U_2 > 0$ the resonance energies are determined approximately when $\cos(kd+\varphi) = 0$, which yields the resonance condition:

$$kd + \varphi = \frac{\pi}{2}(2n+1), \tag{5.20}$$

from which resonance energies E_R in the ILDOS are calculated. The corresponding widths of the resonances can be obtained by expanding in Taylor series around E_R the denominator in Eq. (5.17), and by comparing the result to a Lorentzian profile. Finally, using Eqs. (5.14), the Lorentzian width is determined:

$$\Gamma/2 = \sqrt{\frac{2(E_R - U_2)E_R}{U_2(d + \varphi'\sqrt{2E_R})^2}} \approx \sqrt{\frac{2(E_R - U_2)E_R}{U_2}}\left(\frac{1}{d}\right), \tag{5.21}$$

where φ' is the derivative of the phase φ with respect to the energy evaluated at the resonant energy. Note that the approximation in Eq. (5.20) corresponds to the limit when $U_1 \to \infty$ (thus, φ and $\varphi' \to 0$). In this limit, the resonant energies were obtained in Ref. [19] by the same procedure as followed in this subsection.

From the similarity between Eqs. (5.8) and (5.20) it follows that in the jellium-like description QWRs are expected to appear as a series of states, similar to conventional QWSs present for a perfectly reflecting substrate barrier. The elastic decay rate of these resonant states depends almost linearly on energy (for small U_2) and it is decreasing as $\sim 1/d$ with overlayer thickness. In the following subsection we retrieve the same behavior in terms of more general arguments.

This model has been tested against the WPP code for the ensuing study of the quasi-stationary states in metallic overlayers of Chapters 6 and 7. The numerical WPP results and the analytic solutions given above have been found to be well consistent.

5.2.3. Resonant decay rate of quantum well resonances

In the quasi-classical picture, an electron confined in a quantum well is moving back and forth in the quantum well, hitting the barriers so that the QWSs are formed. If a finite

tunneling probability through one of the barriers exists, the resonant QWS is called a quantum well resonance (QWR). The population of QWRs decay via one-electron energy conserving tunneling into the bulk metal. One of the differences between the QWS and the QWR is that in the latter, in principle, all the terms of Eq. (3.1) contribute to the lifetime, and in particular the elastic one, which is not present in the QWSs. In a metallic overlayer the "weak" barrier might be the overlayer-substrate interface. Then, the elastic decay rate due to the electron tunneling through the film/substrate interface can be estimated from the simple expression

$$\Gamma_{\rm res} = (1-\mathcal{R})\Delta E = (1-\mathcal{R})\pi\sqrt{E}/d, \tag{5.22}$$

where $\omega = \Delta E$ is the attempt (revival) frequency at which an electron is hitting the interface. ΔE is the energy difference between the levels in the electron energy range of interest and $\mathcal{R}$ is the reflection probability of the interface. Thus, when $\mathcal{R} \to 1$ the decay rate $\Gamma_{\rm res}$ tends to zero (a QWS is formed). An important conclusion can be derived from this simple model: for fixed energy interval the resonant decay rate decreases as $1/d$ with increasing thickness d. Essentially the same conclusions follow from the more refined analytical treatment of the properties of QWRs, as developed in previous Subsection 5.2.2.

5.3. Phase accumulation model (PAM)

The phase accumulation model is based on a multiple reflection approach. Originally, it was used to analyze the surface states in metallic crystals [126], but it has been often used for discussing general (quasi-)bound states in one dimension. In the following we consider the scattering approach to derive the phase accumulation equation.

Let us consider, for example, a metallic overlayer, where the electron is trapped by the substrate-overlayer interface barrier at $z = 0$ and the vacuum barrier at $z = d$. Then let us consider the asymptotic solutions a^+ and a^- at these barriers, as shown in Fig. 5.3. An incident plane wave propagating from the substrate toward the interface, $a_{in}\exp(ikz)$, leads to a transmitted wave with amplitude $a_{in}t$ at $z = 0$. Additionaly, the solution a^+ contains a contribution from the reflected wave $\mathcal{R}_L a^- e^{ikd}$, where $\mathcal{R}_L$ is the (complex) reflection amplitude of the barrier at the left side. On the other hand, the amplitude at the right side is related to the amplitude of the left side as $a^- = \mathcal{R}_R a^+ e^{ikd}$, where $\mathcal{R}_R$ is the corresponding reflection amplitude of the right barrier. The total amplitude due to the transmitted and reflected waves is then written as:

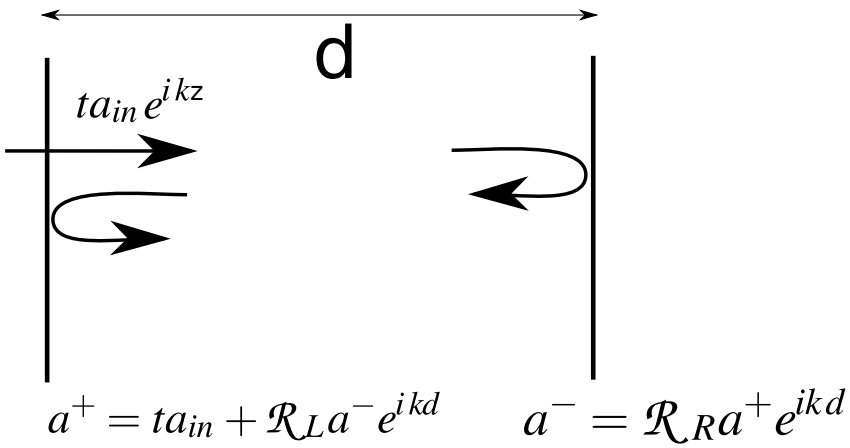

Figure 5.3.: Asymptotic solutions for an electron in a quantum well of width d, delimited by the left (L) and right (R) barriers with reflection amplitudes $\mathcal{R}_L$ and $\mathcal{R}_R$, respectively. See main text for details.

$$a^+ = ta_{in} + a^+ e^{ikd}\mathcal{R}_R e^{ikd}\mathcal{R}_L, \tag{5.23}$$

thus,

$$a^+ = \frac{ta_{in}}{1 - \mathcal{R}_R\mathcal{R}_L e^{2ikd}}. \tag{5.24}$$

It is convenient to use the polar representation of the complex numbers $\mathcal{R}_L = r_C e^{i\phi_C}$ and $\mathcal{R}_R = r_B e^{i\phi_B}$, where the original labels of Ref. [126] have been used (B for surface *barrier* and C for bulk *crystal*). In the above expression a bound state is represented by a pole, thus, the condition $r_B = r_C = 1$ is required together with the well known phase condition:

$$\phi_B + \phi_C + 2kd = 2\pi n, \tag{5.25}$$

with $n = 0, 1, 2, ...$ The phases [127] are given by

$$\phi_B = 2\tan^{-1}\left(\frac{\psi^{+\prime}(z_B)}{k\psi^+(z_B)}\right), \tag{5.26}$$

and similarly for the left barrier with the ingoing waves ψ^-,

$$\phi_C = 2\tan^{-1}\left(\frac{-\psi^{-\prime}(z_C)}{k\psi^-(z_C)}\right), \tag{5.27}$$

where the prime denotes the spatial derivative of the wave function. From these expressions above, for the finite step barrier ($U_1 = 0$ and $k_2 = \sqrt{E - U_2}$) we have ($i = \sqrt{-1}$):

$$\phi_{\text{step}} = 2 \arctan\left(\frac{ik_2}{k}\right). \tag{5.28}$$

The limit $U_2 \to \infty$ corresponds to the infinite potential barrier which implies $ik_2 \to -\infty$, thus, there is no penetration of the wave function, but from Eq. (5.28) it follows that the phase does change:

$$\phi_{\text{inf}} = -\pi. \tag{5.29}$$

In general, the usefulness of Eq. (5.25) lies on the phase shift models for different interfaces. Such an example is that of a substrate induced projected gap, for which the phase shift [128] is given by:

$$\phi_{\text{subs}} = 2 \arcsin \sqrt{\frac{E - E_L}{E_U - E_L}} - \pi, \tag{5.30}$$

where E_U and E_L are the upper and lower edges of the band gap, respectively.

As a final remark, in principle, we could also obtain the bound state energies of the potential considered in previous subsection with the phase accumulation model, by calculating the corresponding reflection coefficients $\mathcal{R}_L$ and $\mathcal{R}_R$. In the case of resonances, $r_C < 1$, and the quasi-classical description of the system, in this case, is equivalent to a Fabry-Perot approach [9, 129, 130].

5.4. Image potential barrier in quantum wells

It is well known that an electron in front of a metallic surface induces a screening charge inside the metal [126] [see Fig. 5.4(a)]. In the classical electrostatic approximation, the interaction between an electron and its screening charge is given by the image potential

$$V(z) = \frac{-1}{4(z - z_{\text{im}})}, \tag{5.31}$$

where z represents the distance from the surface and z_{im} is the image plane position. In front of a metal possessing a projected band gap, the electron penetration inside the metal is impossible, therefore, the image state electron is confined in front of the surface. The energy levels of the corresponding quantized states form a *Rydberg* series (after the analogous series found in hydrogenic atoms):

$$E_n^{\text{IS}} = \frac{-0.85\,\text{eV}}{(n + a)^2}, \tag{5.32}$$

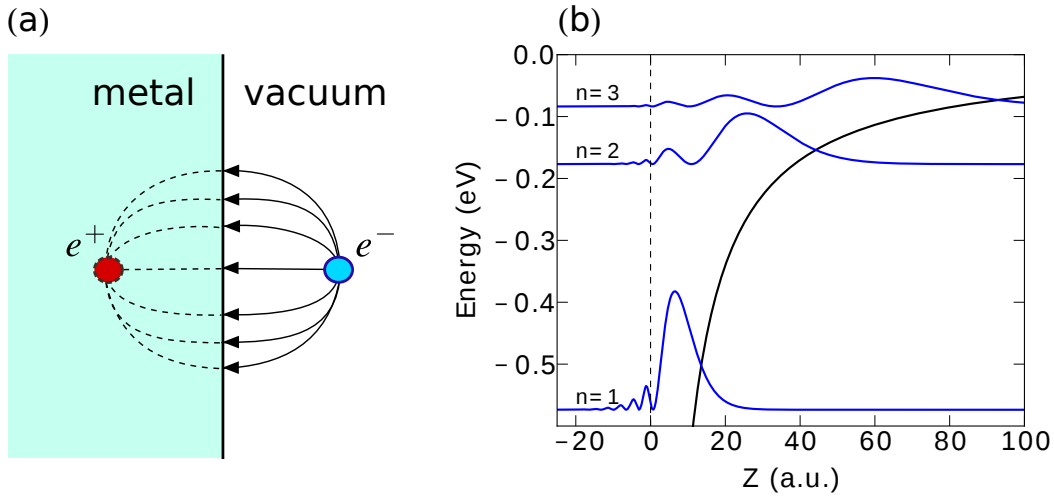

Figure 5.4.: (a) Schematic representation of the induced image charge (note that it is not the actual positive charge distribution [133] inside the metal) in front of a metallic surface (b) Image potential (black) and charge density of the first image states (blue) in front of a Cu(100) surface [131]. The vertical dashed line denotes the image plane position $z = 0$.

for $n = 1, 2, 3, \ldots$ and a is a quantum defect. Then, the level spacing for the image states is $\Delta E_n \sim 1/n^3$.

As an illustrative example, the first image states of the Cu(100) surface as obtained in a 1D model [131] are plotted in Fig. 5.4(b).

In the absence of a projected band gap around the vacuum level, quasi-stationary states can exist in front of a metallic surface. These states decay resonantly into the bulk and are called image state resonances (ISRs) [66].

For the image potential barrier, a phase shift (suitable for a phase accumulation analysis of image state energies) can be derived within the Wentzel-Kramers-Brillouin (WKB) approximation [128, 132] as:

$$\phi_{\text{vac}}(E) = \pi/\sqrt{8(E_V - E)} - \pi, \tag{5.33}$$

where E_V is the vacuum level.

In this subsection the application of the phase accumulation model is illustrated in a simple 1D potential with an image potential barrier (see continuous line in Fig. 5.5). The potential considered is basically a quantum well with a constant inner potential $U_0 = -13.55$ eV measured with respect to the vacuum level ($E_V = 0$), and thickness $d = 32.46a_0$. In the left side of the well an infinite barrier is set at $z = -d$ and in the

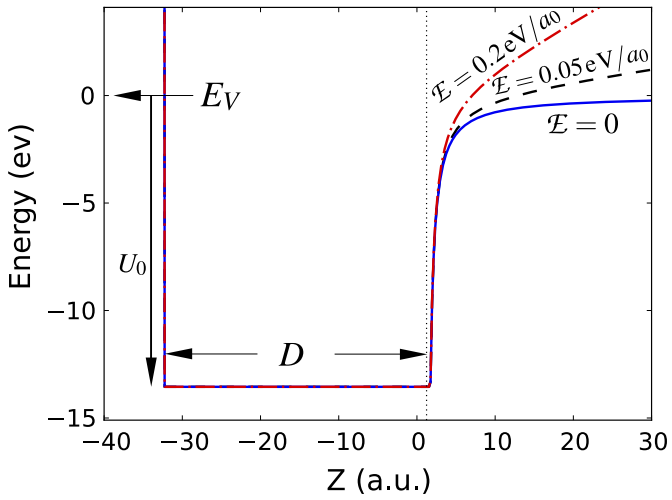

Figure 5.5.: Simple potential wells representing a metallic overlayer with different barriers in the vacuum-metal interface at $z = 0$. The continuous line corresponds to the potential having only the image potential barrier; the dashed line includes an additional electric field of 0.05 eV/a_0, whereas for the dash-dotted line the electric field is 0.2 eV/a_0. The vertical dotted line denotes the position at which the image potential and the well are matched ($z = 1.73a_0$).

right, above the image plane position at $z_{\mathrm{im}} = 1.23a_0$, the image potential barrier is included.

In order to avoid the divergence when $z \to z_{\mathrm{im}}$ in Eq. (5.31), the image potential is cut at U_0 energy, which corresponds to $z = 1.73a_0$. Then, the image potential and the constant potential in the well are matched by a simple extension ($+0.5a_0$) of the well up to the cut position. The above parameters are taken from the more elaborated effective potentials to be used in the following chapters for describing the Pb/Cu(111) system. In fact, the thickness d corresponds to a Pb coverage of 6 MLs. In the following discussion, however, it is convenient to use the width of the total constant well $D = d + 1.73a_0$.

Within the phase accumulation model, the bound state energies are obtained from $E_n = \frac{1}{2}k_n^2 - U_0$, where

$$2\pi(n-1) - 2k_n D = \phi_{\mathrm{inf}} + \phi_{\mathrm{vac}}, \tag{5.34}$$

with $n = 1, 2, ...$ and ϕ_{vac} and ϕ_{inf} are given by Eq. (5.33) and Eq. (5.29), respectively. Then the equation to be solved reads:

$$2\pi n - 2k_n D = \frac{\pi}{\sqrt{8(E_V - E_n)}}. \tag{5.35}$$

The above equation, however, does not reproduce exactly the energies. This is due to the approximations used to derive the image potential barrier phase shift. A procedure to solve this problem is to fit different parameters entering the PAM equation in order to reproduce some of the exact (or experimental) energies. Then, all the rest of the state energies are expected to be reproduced by the model. When experimental data of electronic confined states in metal overlayers are intended to be reproduced, several parameters are unknown, thus, the fitting is a necessary practice.

In principle, this can be done by variation of the quantum number n, the band dispersion $E(k)$ (including implicitly the perpendicular effective mass inside the metal), the model phase shift parameters, or adding an offset to the thickness. However, one should be cautious when interpreting the results derived from such a fitting, as follows from the discussion of the spectroscopy of QWSs by STM in Chapter 7.

In the present case, we include a correction to the overlayer thickness (an effective thickness), which can be interpreted in terms of wave function spilling through the barriers. This has been discussed in Subsection 5.2 presenting the analytical results for the finite quantum well potential. To assess the suitability of this approach, the exact energies are calculated numerically and then the effective thickness is evaluated via

$$\delta_0 = \frac{\pi}{k}\left(1 - \frac{1}{2\sqrt{8(E_V - E_n)}}\right) - D, \tag{5.36}$$

where the above equation is derived from Eq. (5.35) with $D \to D + \delta_0$. The energies have been recalculated by Eq. (5.35) with the averaged thickness correction $D \to D + \langle\delta_0\rangle$. Observing the values quoted in Table 5.I the suitability of the PAM in this particular case is confirmed.

The discussion of the QWS-IS mixed character of the wave functions is left for Chapters 6 and 7.

5.5. Field emission resonances

5.5.1. Linear ramp barrier phase shift

When a metallic surface is exposed to an external electric field the electronic surface states are perturbed. An example of such a situation is the case of the scanning tunneling microscopy (STM) experiment with a biased tip in front of the surface [see Fig.5.6(a)]. As has been widely discussed in the literature, the image potential states

Table 5.I.: Comparison between exact energies and energy values derived from the phase accumulation model (PAM) for the potential described in Fig. 5.5 by the continuous line. See the main text for further details.

n	E_{exact} (eV)	PAM ($\langle\delta_0\rangle = -0.23a_0$) (eV)	δ_0 (a.u.)
11	-1.447	-1.392	-0.17
12	-0.466	-0.441	-0.13
13	-0.164	-0.164	-0.28
14	-0.080	-0.081	-0.32

of the pristine metal surface evolve then into field emission resonances (FERs) of the STM junction [115, 116, 120, 134–137].

The simplest description of the situation sketched above is based on a one-dimensional model with an infinite potential barrier at the left, which might represent the projected band gap of a metallic sample, and a linear ramp barrier in the right, due to a uniform electric field $\mathcal{E}$:

$$V(z) = \begin{cases} \mathcal{E}z, & z > 0 \\ \infty, & z < 0. \end{cases} \tag{5.37}$$

The 1D-Schrödinger equation is solved by the change of variable $z = \rho\zeta$, with $\rho = (2\mathcal{E})^{-1/3}$. The solutions are given by the Airy functions:

$$\psi_n(z) = C_n \text{Ai}(z/\rho - \zeta_n), \tag{5.38}$$

with normalization constant [138–140]:

$$C_n = \frac{1}{\sqrt{\rho}|\text{Ai}'(-\zeta_n)|}, \tag{5.39}$$

where the ζ_n are the zeros of the Airy function. For large n [82] the asymptotic expansion for ξ_n can be used:

$$\zeta_n = f\left[\frac{3\pi}{2}(n - \frac{1}{4})\right], \tag{5.40}$$

where the function f is given by

$$f(x) \sim x^{2/3}\left(1 + \frac{5}{48}x^{-2} + \ldots\right). \tag{5.41}$$

Then, keeping the first order term, the FER energies are obtained:

$$E_n \approx \frac{1}{2}\left[3\pi\mathcal{E}(n-\frac{1}{4})\right]^{2/3}. \tag{5.42}$$

On the other hand, the asymptotic standard solution can be estimated in the semi-classical approach [141] with momentum $k=\sqrt{2E(x)}$ as:

$$2\pi n = 2\int_0^l k(x)dx = 2\int_0^l \sqrt{2\mathcal{E}(l-x)}dx = \frac{2}{3\mathcal{E}}(2\mathcal{E}l)^{3/2}, \tag{5.43}$$

and noting that $E=\mathcal{E}l$, the eigenenergies are finally given by:

$$E_n = \frac{1}{2}\left(3\mathcal{E}\pi n\right)^{2/3}. \tag{5.44}$$

This solution provides the recipe to obtain the phase shift due to a linear potential by recalling Eq. (5.42), and by subtracting $-\pi$ in the phase due to the infinite barrier reflection [Eq.(5.29)], which finally leads to:

$$\phi_{\rm vac}(E) = -\frac{\pi}{2} + \frac{2}{3\mathcal{E}}[2(E-E_0)]^{3/2}, \tag{5.45}$$

where we explicitly introduce the energy reference E_0 from which states are measured. It should be noted that the phase shift above might be derived directly from the analysis of the classical turning points in the semi-classical method, together with the asymptotic properties of the Airy functions [141].

In Fig. 5.6(b) the charge densities of the first wave function solutions are plotted for a potential given by Eq. (5.37).

5.5.2. Overriding the image potential by an electric field

In principle, it is not obvious that the phase shift given in Eq. (5.45) must be valid for the states formed when an uniform electric field is applied to a metallic crystal surface. In the linear response regime, the crystal responds independently to applied perturbations, i.e., the total potential in the vacuum region is given by the image potential plus the potential due to the applied electric field. Then, the electronic states having a large weight in the vacuum region, such as the ISs, are affected by the field and evolve into the FERs. As previously mentioned, the phenomenon that an applied electric field destroys the Rydberg series of ISs at a metallic surface is a well

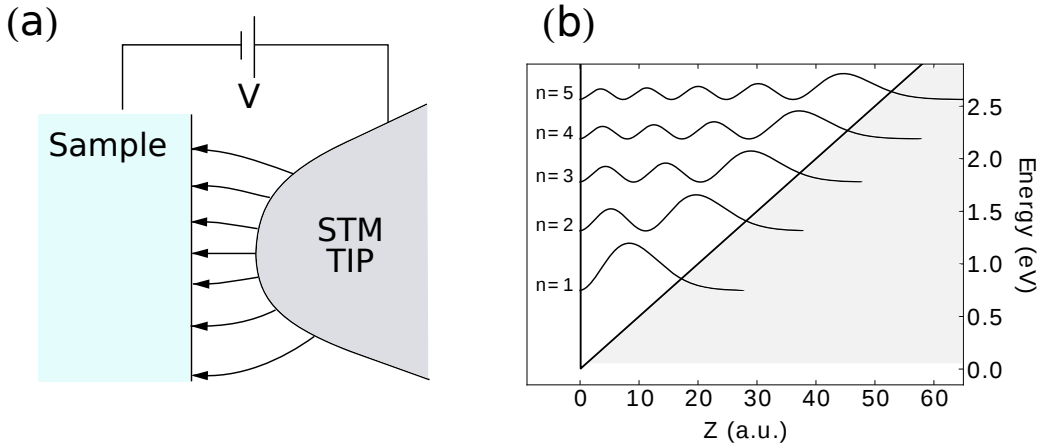

Figure 5.6.: (a) Schematic representation of a STM tip in front of a metallic surface with applied bias V (the arrow denotes the field line direction in atomic units). (b) Charge density (in arbitrary units) of the first bound states (shifted according to their energy) formed between an infinite barrier at $z = 0$ and a linear barrier (triangular potential) representing an electric field of strength $\mathcal{E} = 0.05$ eV/a_0.

documented fact. The question then is to what extent does the phase shift for the linear ramp barrier reproduce the FERs.

To answer this question the same system as in the previous section is considered, but including two different constant electric fields, as shown in Fig. 5.5. In this particular case, in principle the FERs are hybridized with QWSs, however, for the sake of simplicity we will refer to these states in this section simply as FERs. Detailed discussion is left for Chapter 7.

We first calculate the effective thickness ($D \rightarrow D + \delta_0$) of the states by using Eq. (5.34) with the vacuum phase shift ϕ_{vac} of the linear ramp barrier of Eq. (5.45):

$$\delta_0 = \frac{1}{2k}\left(2\pi n - \frac{\pi}{2} - \frac{2}{3\mathcal{E}}[2(E - E_V)]^{3/2}\right) - D, \tag{5.46}$$

where we have taken the energy reference as $E_0 = E_V$ in Eq. (5.45). Note, however, that the energy reference is not well defined close to the image plane. Whereas this energy reference might be only valid for very extended states in the vacuum (at high energies), in the following discussion it is shown that the present choice is reasonable in that it reproduces the FERs series close to E_V. With this choice, only states above the vacuum level can be addressed. The use of energy references of several eV below E_V do not provide correct results. Nevertheless, we have checked, that if one is interested in Stark shifted ISs below the vacuum level, an energy reference slightly below the vacuum level can be used.

Table 5.II.: Comparison between exact and approximate results for a linear ramp barrier phase shift model for the vacuum-metal interface in a quantum well potential. Energies are given in eV with respect to the vacuum level of the non perturbed potential. The field $\mathcal{E}$ is given in units of eV/a_0 and δ_0 in atomic units. The phase accumulation model (PAM) results are obtained with the averaged $\langle\delta_0\rangle$ value. Note that for $\mathcal{E} = 0.05$ eV/a_0 case, the $n = 12$ state lies below the vacuum level.

	$\mathcal{E}$ =0.05 (eV/a_0)			$\mathcal{E}$ = 0.2 (eV/a_0)		
n	E_{exact} (eV)	PAM ($\langle\delta_0\rangle = 3.27a_0$) (eV)	δ_0 (a.u.)	E_{exact} (eV)	PAM ($\langle\delta_0\rangle = 1.97a_0$) (eV)	δ_0 (a.u.)
12				0.421	0.432	1.99
13	0.625	0.631	3.30	1.509	1.623	2.29
14	1.113	1.122	3.33	2.638	2.603	1.86
15	1.537	1.537	3.27	3.562	3.484	1.71
16	1.935	1.911	3.07	4.359	4.301	1.77

The calculated δ_0 of the first FERs are quoted in Table 5.II for two different values of $\mathcal{E}$, representing the minimum and maximum values found in our constant current scanning tunneling spectroscopy (STS) simulations, to be presented in Chapter 7 (see also Fig. 7.2).

For the low electric field, the variation of δ_0 with the state quantum number is small. Using the mean value $\langle\delta_0\rangle = 3.27a_0$ within the PAM equation allows to reproduce very well the energy series, with a relative error of $\approx 1\%$. The higher value of $\langle\delta_0\rangle$ with respect to that found for the image potential case can be understood by the influence of the underlaying image potential, which affects the actual barrier.

For the case with higher field strength, $\mathcal{E} = 0.2$ eV/a_0, in general a larger error of $\approx 2\%$ between the PAM and the exact value is found with the corresponding $\langle\delta_0\rangle = 1.97a_0$. For the $n = 13$ state the error reaches 7%. On the other hand, the effective thickness average is notably smaller in comparison to the $\mathcal{E} = 0.05$ eV/a_0 case. Thus, the effective thickness depends upon the electric field. Taking into account that in a typical constant-current experiment the electric field changes upon bias, FERs cannot be reproduced solely by the phase accumulation model together with the phase shift of the linear ramp barrier: there is need for the bias dependence of $\langle\delta_0\rangle$ parameter. We conclude that the phase shift of Eq. (5.45) is useful for the qualitative description

of the FER energy series, however, the quantitative description requires a constant electric field, which is not fulfilled in the STS experiments.

An alternative to avoid the problem above would be to consider the spectroscopy in which the tip-surface distance is changed linearly with the bias. For a flat tip, the electric field is maintained constant. Such an example is given in the theoretical part of a recent work [142] studying by STM the FERs induced in alkali metal clusters deposited on a Cu(100) surface. In that study, for numerical efficiency, the linear ramp approximation was used for the $Z - V$ characteristics. It should be noted, however, that since the real tip is not flat, at different regions of the surface there is a different local electric field. Furthermore, the effective area from which electrons are injected through the tip depends on the tip distance and bias [115]. Thus, even in a $Z - V$ characteristic given by a linear ramp, the average electric field might not be constant.

Summarizing, the following conclusions are obtained: (i) the image potential is overridden by the applied electric field even for a field strength as low as 0.05 eV/a_0. (ii) For a given electric field, the phase shift of the linear ramp barrier correctly describes the dispersion of the FERs within the PAM. (iii) However, the effective thickness parameter δ_0 used to match the phase accumulation model depends on the electric field strength. This dependence can hinder the quantitative description of experimental FERs data by means of the linear ramp barrier phase shift.

As it is shown in Chapter 7, the overriding of the image potential is a fundamental issue to be addressed in the correct interpretation of STS experiments in Pb/Cu(111).

5.6. Summary

In this chapter we have presented the basic quantum solutions for simple potentials used to describe the 1D electron confinement at metallic surfaces and in metallic overlayers. In Fig. 5.7 we summarize the presented results and we advance some additional concepts. We briefly comment on these new features.

In the top panel the three basic (approximate) solutions for the simplest potentials are provided, where the crystal (surface or substrate) barrier is described by an infinite potential barrier. The finite step can also correspond to an exponentially decaying potential barrier, as that found in the DFT-LDA effective potentials, which is indicated by a dashed curve. For the sake of generalization, in the uppest potential of the panel, we have included the bottom constant potential region as a part of the step barrier. So, the $2kd$ term is added in the phase shift describing the barrier. Then, the classification

of a given confined state as a QWS, IS or FER basically follows from the character of the phase shift of the potential barrier.

In the panel of the center some mixtures of the different barriers are considered. The energy regions indicated by the braces correspond to the different character of the confined states or the way they are referred to in the literature. The overlap between the braces represents the transition regions between the different confined states.

Finally, in the bottom panel we collect some different potential configurations that can lead to resonant states. The third situation, starting from the left, corresponds to that of the Pb/Cu(111) system to be studied in the next chapter.

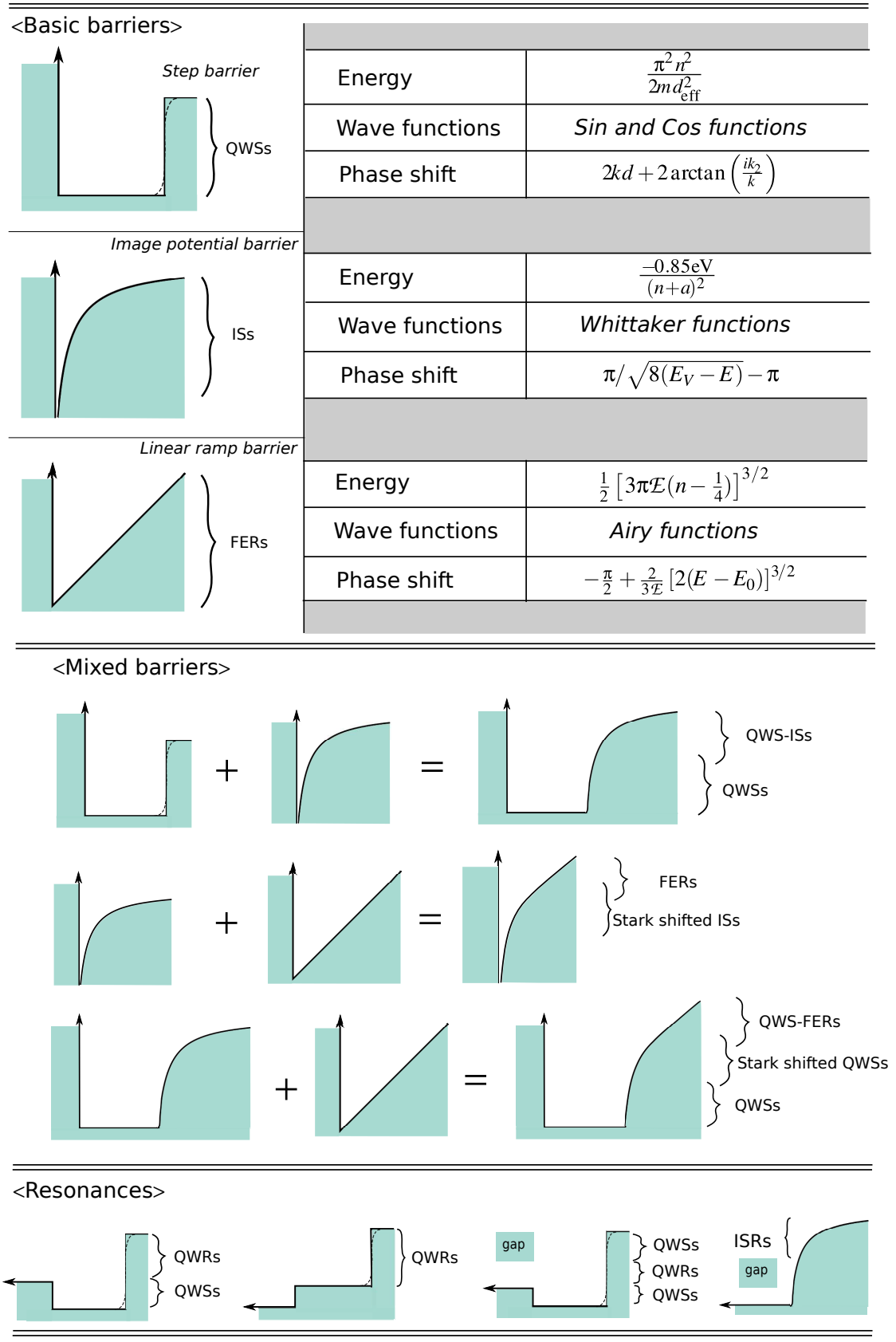

Figure 5.7.: Summary of the one-dimensional confining barriers at the surface. See main text for the details.

Chapter 6

Lifetime of QWSs and QWRs in Pb/Cu(111)

6.1. Introduction

Confinement of valence electrons in metallic films, as thin as a few electron Fermi wavelengths, results in discrete quantum well states (QWSs), which are at the origin of quantum size effects in the properties of the system [8, 9]. In metallic overlayers adsorbed on metals or semiconductors the confinement is due to the vacuum barrier and the reflecting barrier at the interface, caused by the energy gap in the substrate band structure projected onto the plane parallel to the interface. In the absence of a confining energy gap, another type of states of resonant character extending over the whole system, called quantum well resonances (QWRs), can exist. Furthermore, when the energies of the states are close to the vacuum level, QWSs are affected by the image potential and hybridize with image states (IS) forming the QWS-ISs [30]. The existence of these states can be understood by simple one-dimensional (1D) model potentials, as has been shown in previous Chapter 5.

Among various systems, the growth of Pb on Si(111) and Cu(111) has attracted much interest. Since the pioneer studies by Toennies and co-workers with He atom scattering [143, 144] different experimental techniques, such as scanning tunneling microscopy [11, 145] or surface X-ray diffraction, have been used to probe the most stable heights of Pb islands on Cu(111) and Si(111) substrates (Ref. [146]). In favorable conditions, the islands cover wide areas forming overlayers of "magic" heights.

The overlayer thickness can be crucial for the properties of the system, as for example the superconducting transition temperature [147–153]. The existence of magic heights with bilayer periodicity and the corresponding oscillations in the energetics of the overlayers as a function of the coverage have been studied theoretically using different approaches. Calculations for freestanding Pb films have been reported within density functional theory (DFT), first-principles [27] and jellium model [154]. In this context, a one-dimensional (1D) pseudopotential for the entire overlayer-substrate systems has been used to calculate the electronic structure of Pb/Cu(111) with different thicknesses of the Pb overlayer. This model has described well the electron confinement in the overlayers [17,18] and has given fairly good account of the experimental measurements of magic height distributions [11].

Angle-resolved photoemission has been used to probe Pb thin films grown on different substrates [16,21,155]. The photoemission spectrum directly maps the QWS electronic structure of overlayers, however, there are also peaks which are considered as QWSs but appearing out of the projected gap of Cu(111), i.e., strictly speaking they are QWRs. This confinement in the absence of a band gap has also been pointed out in other quantum well systems such as Al/Si(111), Pb/Si(111), and Na/Al(111) [22,156,157].

Most theoretical studies in the past have focused on the electronic structure of these systems [26, 28, 158] and less attention has been paid to the study of the electronic excitations. Electronic excitations in metal surfaces play an important role in many chemical and physical phenomena [31, 32]. They are characterized by their lifetime, which sets the duration of the excitation and, when combined with the group velocity, determines the mean free path, i.e., spatial range of the excitation. It was shown that on clean metal surfaces the decay of excited electrons and holes is closely related to the dimensionality of the system, i.e., intraband transitions within the surface state band itself are mostly responsible for the final lifetime of the excited quasiparticle [159,160]. Similarly, for a QWS in a 1 monolayer (ML) Na/Cu(111) the intraband transitions are crucial for the description of the hole decay in this state [33].

In recent years, however, a new interest has emerged in Pb overlayers, and particularly, in their QWS lifetimes. Kirchmann and Bovensiepen [23] used time-resolved two-photon photoemission technique, which allows the direct monitoring of the decay of excited electrons in the time domain [161,162], to investigate the dynamics of QWSs in the Pb/Si(111) system as a function of the Pb thickness. They concluded that the intersubband decay in low-dimensional metallic systems is very important in order to interpret correctly experimental results. They also suggested the Pb/Cu(111) system as a possible candidate to compare the decay of QWSs in Pb overlayers on different substrates. Hence, theoretical studies of the dynamics of the Pb/Cu(111) system would

be very helpful for the understanding of future experiments on Pb overlayers. In the following years several works, both experimental and theoretical, have been published studying the lifetime of QWSs in Pb overlayers, including the major part of the results presented in this thesis [24, 25, 29, 47, 61, 163–166].

In the following sections we present the calculations of decay rates of excited electrons and holes in Pb overlayers on Cu(111) for different coverages [163]. The electronic structure of the entire Pb/Cu(111) system is computed by using the 1D pseudopotential for the substrate-overlayer system, described in Chapter 2. The contributions to the lifetime broadening are calculated using two approaches. The inelastic electron-electron ($e-e$) or many-body contribution to the lifetime broadening of both occupied and unoccupied QWSs is evaluated using the *GW* approximation, as explained in Chapter 3, whereas the elastic (one-electron energy-conserving transfer through the Pb/Cu interface) contribution is calculated within the wave packet propagation (WPP) method (see Chapter 4). The latter method, with the inclusion of effective absorbing potentials, can also be used to estimate the total many-body decay rate of QWSs.

The rest of the chapter is structured as follows: In Section 6.2 the electronic structure of the Pb/Cu(111) system is discussed and some analytical expressions are derived for reproducing the set of QWSs close to the Fermi level. Section 6.3 presents the *GW* results and their comparison with available experimental photoemission lifetimes. Section 6.4 presents the WPP results for the elastic decay rates, and the competition with the additional electron-electron inelastic decay rate of QWRs is discussed. In Section 6.5, the results of previous sections are used to study the lifetime of QWSs with partial image state (IS) character, close to the vacuum level. Finally a summary of the chapter is provided in Section 6.6.

6.2. QWSs and QWRs: electronic structure

Before starting the discussion of the lifetimes, we dedicate this section to a detailed survey of the main characteristics of the electronic structure in Pb/Cu(111), as considered in this chapter. In particular, we discuss the QWSs and QWRs formed in the Pb overlayer. Part of the following results have been previously discussed in detail in several papers by E. Ogando *et al.* [17–19]. In this chapter, however, resonant energies are obtained from the WPP study, which is an exact quantum mechanical calculation for the given potential. This is in contrast to earlier works where approximate treatments have been used. In addition, a direct comparison with available experimental data of Ref. [16] for the states below the Fermi level is provided. We also derive some

analytical equations to be used in the analysis of decay rate results as a function of the overlayer thickness, developed in Section 6.4.

We start assuming a Pb overlayer of effective width d on Cu(111). The effective width d is not simply given by the number of Pb MLs, but effectively accounts for the scattering properties of the Pb/vacuum and Pb/Cu(111) interfaces. This concept has been already introduced in Chapter 5, where an illustrative derivation of the effective width [Eq. (5.12)] in a finite symmetric potential well has been derived. An example of the one-electron potential for such a system is shown in Fig. 6.1(a) for the case of the 6-ML-thick Pb overlayer.

For a freestanding Pb overlayer of thickness d one expects a series of quantized states at $\overline{\Gamma}$ with energies $E_n \simeq 0.5(n\pi/d)^2$, given with respect to the bottom of the potential well. For the supported overlayer, one of the Pb/vacuum interfaces of the freestanding film is replaced by the Pb/Cu(111) interface so that different types of states are formed in Pb depending on their energy E_n with respect to the projected band structure of Cu(111) (see also Fig. 2.2):

(i) E_n is in energy resonance with propagating electronic states inside the Cu(111) [white energy region inside Pb in Fig. 6.1(a)]. In this case, the electron initially localized in the overlayer quantum well can be transferred into the Cu(111) substrate. The corresponding overlayer state becomes quasi-stationary with the width given by the rate of the energy-conserving (resonant) electron transfer into the substrate $\Gamma_{\rm res}$. We refer to these states as QWRs.

(ii) E_n is in the projected band gap of Cu(111) [top colored (blue) energy region in Fig. 6.1(a)]. The resonant electron transfer from the jellium Pb overlayer into the Cu substrate is then impossible. The overlayer localized states are stationary in a one-electron sense, and the only possible decay channel is due to the many-body interactions. These are the gap QWSs or g-QWSs.

(iii) E_n is below the bottom of the Cu(111) *sp* band. Then the resonant electron transfer into the Cu substrate is impossible, similar to the situation described in (ii). The corresponding energy range is the bottom colored region (green) in Fig. 6.1(a), with the difference of ($\approx$ 2 eV) between the average Cu(111) and Pb potentials. In this chapter we use the notation deep QWSs (d-QWSs) for the states existing in this energy region to distinguish them from the g-QWSs.

In Fig. 6.1(b), the energies of the QWSs and QWRs are plotted for $\mathbf{k}_{\|} = 0$ as a function of their quantum number n for the 6 ML Pb/Cu(111). The energies of the QWSs correspond to the eigenvalues of the effective 1D Hamiltonian, as calculated within

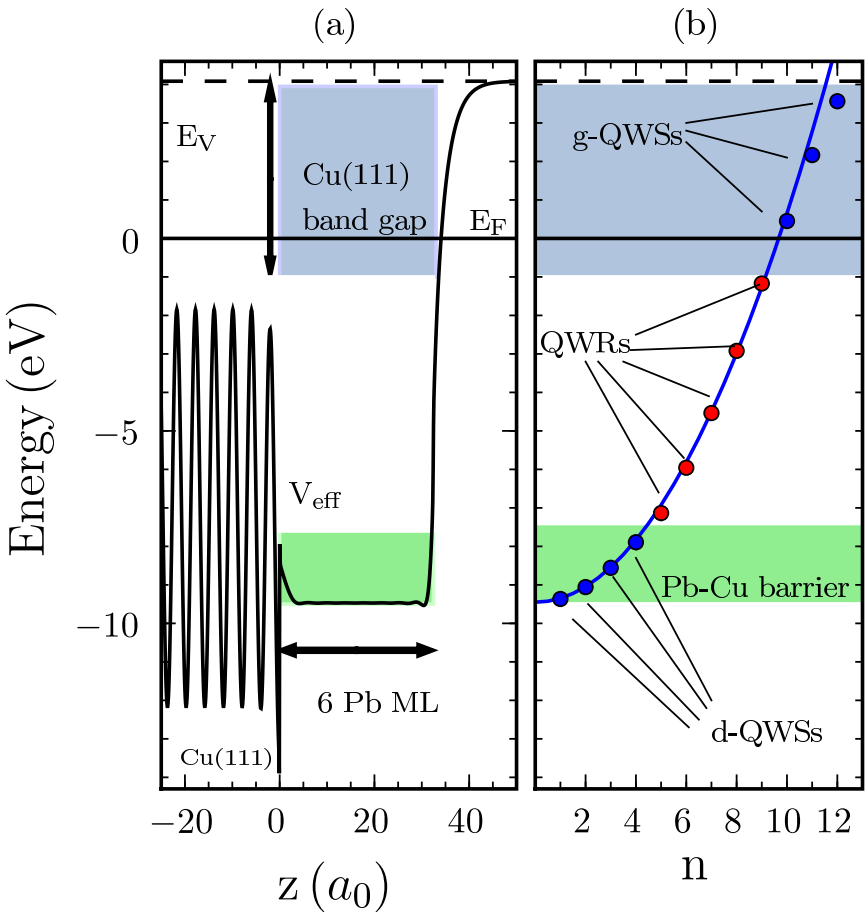

Figure 6.1.: (a) Effective potential V_{eff} (solid line) for 6 ML of Pb on a Cu(111) surface. The origin $z = 0$ is set at one half of the Cu(111) interlayer spacing from the Cu surface layer (it coincides with the Pb jellium edge). The energies are given with respect to the Fermi level, E_F. The horizontal dashed line represents the vacuum level. The energy regions where QWSs localized in Pb overlayer can exist are shaded with colors. The top colored region (blue) corresponds to the projected Cu(111) band gap and the bottom colored region (green) corresponds to the differences in average potentials in Pb and Cu(111). In between these two energy regions the overlayer localized states are in resonance with bulk propagating states of the substrate so that QWRs are formed. (b) Energy eigenvalues as a function of their quantum number n. Dots (blue) in colored regions are localized QWSs and (red) dots in white region represent QWRs. The parabola (continuous blue line) is plotted as a reference.

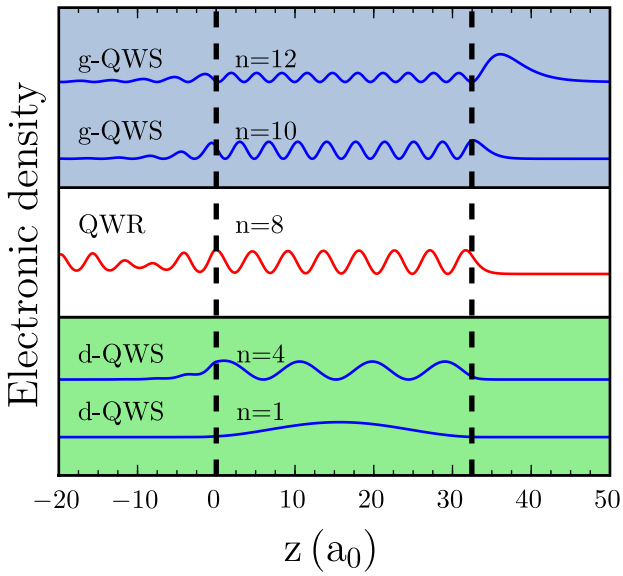

Figure 6.2.: Charge density of some QWSs (blue lines in colored regions) and QWRs (red line in white region) for the 6ML-Pb/Cu(111) system. Results are shown as a function of the z coordinate perpendicular to the surface. For the definition of the z axis and shaded regions see caption of Fig. 6.1. The states are labeled according to their n quantum number, reflecting the nodal structure inside the Pb potential well. Vertical dashed lines delimit the Pb overlayer region.

DFT approach. The energies of the QWRs have been obtained from the positions of the peaks in PDOS as calculated with WPP. The quantum number of the state n has been assigned from the nodal structure of the corresponding wave function inside the Pb overlayer.

In Fig. 6.2 the electronic densities of the QWSs and QWRs are shown for the 6 ML Pb/Cu(111) system. Despite different behaviors inside the metal, i.e., exponentially decaying bound state for QWSs and propagating state for QWRs, the number of nodes inside the Pb overlayer forms a continuous sequence with increasing energy of the states. This reflects the common origin of the QWSs and QWRs as the states confined in the Pb overlayer due to the reflectivity of the Pb/Cu(111) interface. Thus, the energies of the states irrespective of their stationary or quasi-stationary character can be well described with a single parabolic fit,

$$E_n = 0.5(n\pi/d)^2 \sim (n/J)^2, \tag{6.1}$$

where d stands for the effective thickness of the overlayer and J is the number of MLs. However, it should be noted that, despite common energy dispersion, there is an

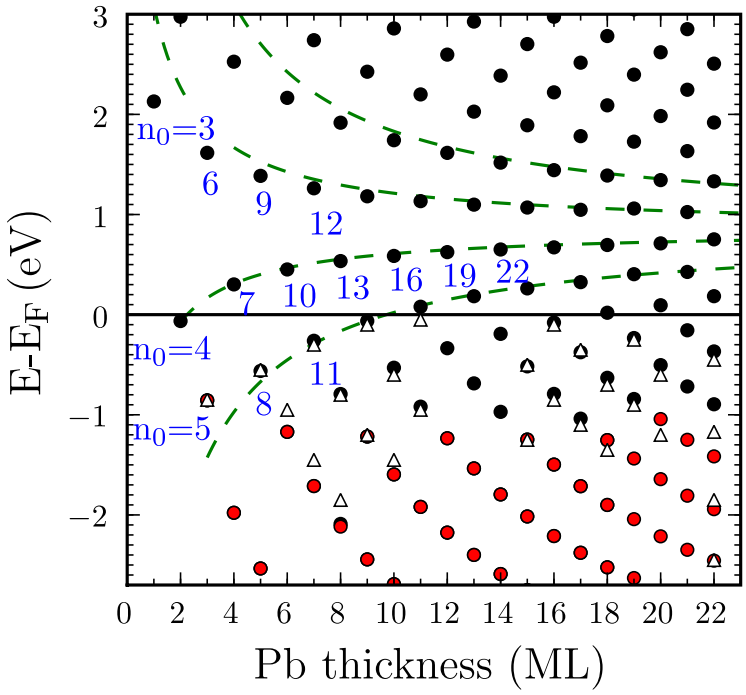

Figure 6.3.: Calculated energies of the gap QWSs (black dots) and QWRs (red dots, in the bottom region below ~ -1 eV) for Pb overlayers on Cu(111). Results are shown as a function of the overlayer thickness. Triangles: Angle-resolved photoemission experimental data (Ref. [16]) are plotted for comparison. Dashed lines connecting the states are the closest-energy lines calculated with Eq. (6.2). Some states are marked with the corresponding n quantum numbers. n_0 are the initial quantum numbers which label the lines. The energies are given with respect to the Fermi level (horizontal line).

essential difference between QWSs and QWRs: for the former the reflectivity of the Pb/Cu barrier is $\mathcal{R} = 1$ and for the latter $\mathcal{R} \neq 1$, allowing one-electron decay into the bulk via tunneling.

In Fig. 6.3 the calculated energies of the gap QWSs (black dots) and QWRs (red dots, in bottom region below ~ -1 eV) are shown as a function of the overlayer thickness for Pb/Cu(111). Present results are compared with angle-resolved photoemission experimental data [16] shown with triangles. The agreement between the calculated and measured energies of the QWSs and QWRs is noteworthy. This gives a confidence in the modeling of the overlayer-substrate system. Indeed, the calculations match the experimental data even for Pb coverages as low as 3 ML, where the jellium description of the Pb overlayer could be questioned. For the state with a given quantum number, the calculated energies show the $1/J^2$ dependence with Pb overlayer thickness, in full

agreement with Eq. (6.1). Experimentally, assignation of a given quantum number to an observed feature and following the change in the energy of this state are not trivial tasks [18]. Therefore, for the connection between theoretical results and an experiment, the way the experimental data are analyzed is of central importance. In a number of experimental studies, appearance of the states within certain energy intervals has been addressed, as has been done in scanning tunneling spectroscopy studies of Pb overlayers on Cu(111) [11, 20]. One characteristic feature of those experimental results was the observation of QWSs at 0.65 eV above E_F for an even number of MLs. In our DFT calculations, shown in Fig. 6.3, we also find that for an even number of MLs, above the 6 MLs coverage, there is systematically a state with an energy close to 0.65 eV. However, it is important to realize that the quantum number n of this state changes with changing coverage.

In Fig. 6.3 we show "closest-energy lines" which connect the closest in energy QWSs near the Fermi level for variable Pb overlayer thickness. In this sense, the electronic structure of Fig. 6.3 can be viewed as a branch structure. In what follows, we present a simple analytical description of these branches. It appears useful in the discussion of experimental results, because it allows an assignment of the quantum numbers for the states appearing close in energy for increasing coverage. We start from the observation that for the calculated states close to the Fermi level, which are at about 9.5 eV above the bottom of the overlayer confining potential, the quantum number n increases by approximately three units every 2 ML of Pb (the thickness of a Pb ML is taken $a = 5.41a_0$). Then, the closest-energy lines can be derived from this observation and Eq. (6.1) as follows:

$$E_{n_0,d_0,\Delta J} = \frac{\pi^2}{2}\left[\frac{n_0 + \frac{3}{2}(J - J_0)}{d_0 + a(J - J_0)}\right]^2, \tag{6.2}$$

where n_0 and d_0 are some initial quantum number and corresponding effective thickness that label the given line, and J_0 corresponds to the initial number of MLs from which the closest-energy line is traced. $\Delta J = J - J_0$ is the change in the coverage as measured in number of MLs, $n_{n_0,\Delta J} = n_0 + \frac{3}{2}(J - J_0)$ is an "effective" continuous quantum number of the states along the line, and $d = d_0 + a(J - J_0)$ is an effective thickness. This effective thickness is also expressed as $d = Ja + \delta$, where δ is the width associated to the electron charge spilling, which can be either considered as a free parameter or it can be obtained from DFT calculations and using the phase accumulation model [126] to evaluate the phase shifts for the confinement barriers, as it was done by Ogando *et al.* [18]. Notice that δ varies with the energy of the state. However, a constant value of $\delta = 4.2a_0$ fits the energy of calculated states around the Fermi level.

Using the relation $J - J_0 = (d - d_0)/a$, the energy can also be defined as a function of the total width d,

$$E_{n_0,d_0} = \frac{\pi^2}{2d^2}\left[n_0 + \frac{3}{2a}(d - d_0)\right]^2. \tag{6.3}$$

With $n_0 = 3, 4, 5$ and the corresponding d_0, this equation provides a fairly good description of the branches shown in Fig. 6.3. For the thick overlayers, such that $d \gg d_0$, Eq. (6.3) leads to the following asymptotic expansion:

$$E - E_F = \alpha/d + \beta, \tag{6.4a}$$

$$\alpha = \frac{3\pi^2}{2a}\left(n_0 - \frac{3}{2}\frac{d_0}{a}\right), \tag{6.4b}$$

$$\beta = \frac{9\pi^2}{8a^2} - E_F. \tag{6.4c}$$

Thus, e.g., observing the photoemission peaks for thick layers one would have an impression that QWSs basically do not change their energy with increasing thickness and periodicity of 2 ML. However, this has to be taken with caution, since the underlying quantum number of the QWSs does change.

6.3. Decay of quantum well states: GW results

6.3.1. Energy dependence

We have performed GW calculations (the corresponding description of the method is given in Chapter 3) of the lifetime broadening at the $\overline{\Gamma}$ point for the occupied and unoccupied QWSs in Pb overlayers of thicknesses ranging from 1 to 18 ML. Some results are shown in Tables 6.I and 6.II. The calculated electron-electron inelastic decay rates of d-QWSs are in the range of 1–2 eV, which places their lifetime values in the order of 100 attoseconds. This is an evident consequence of the deep energy position of these states so that the large phase space is available for the many-body energy relaxation process. On the other hand, depending on the overlayer thickness, the g-QWSs can *a priori* appear at energies close to the Fermi level.

In Fig. 6.4 we present the calculated many-body decay rates Γ_{e-e} of the g-QWSs as a function of their energy measured with respect to the Fermi level. Results are shown up to the QWS energy of 3 eV. For states with higher energies, the image potential tail of the electron-surface interaction becomes important [126, 128, 167], and it is not well

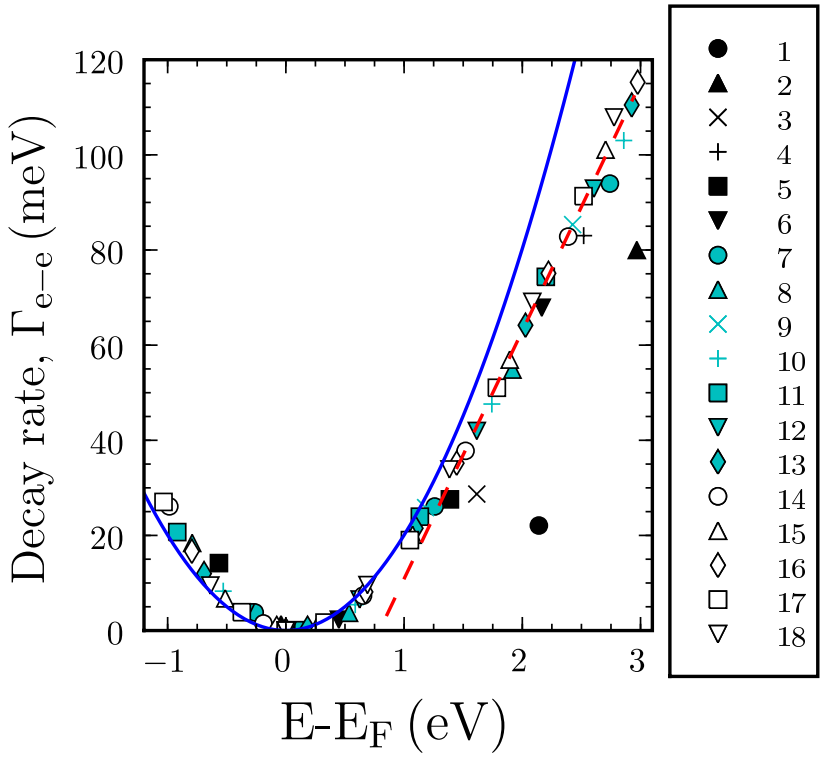

Figure 6.4.: Calculated inelastic $e-e$ decay rates (denoted by different symbols and colors) of QWSs laying in the gap energy region of the Pb/Cu(111) system. Results for the Pb overlayers from 1 to 18 ML thick are shown as a function of the energy, measured with respect to the Fermi level of the corresponding system. The Quinn-Ferrell curve, given by Eq. (3.3) (continuous line) for the density of bulk Pb ($r_s = 2.3a_0$) and a linear fit (dashed line), are plotted for reference.

described within the DFT treatment. The necessary correction to the present DFT potential and the effect on the confined states in Pb is addressed in Section 6.5.

The computed decay rates are compared with those for excited electrons and holes in a homogeneous electron gas, obtained from the Quinn-Ferrell (QF) formula [67] (see Eq. (3.3) in Chapter 5). The absence of data points in the energy region between 0.7 and 1 eV is consistent with the overlayer thickness dependence of the energies plotted in Fig. 6.3. Note that this energy region corresponds to the change from the "nearest-energy line" with the positive slope ($n_0 = 4$) to that with the negative one ($n_0 = 3$).

As seen in Fig. 6.4, the calculated many-body decay rate of states near the Fermi level closely follows quadratic dependence given by Eq. (3.3). For the states with higher energies, from 1 up to 3 eV, a quasilinear dependence of the calculated Γ_{e-e} on energy is observed, signaling the deviation of the Random Phase Approximation (RPA) linewidth from simple quadratic dependence [168]. This is further illustrated by the straight line with a slope of 52 meV eV^{-1}, which intercepts the vertical axis at -41 meV and fits the evaluated decay rate for the states between 1.3 and 3 eV and thicknesses above 6 ML. This quasilinear dependence is attributed to the inclusion of the Cu substrate and the overlayer-vacuum interface in our description. This conclusion follows from the comparison of our results to *ab initio* and free-electron gas calculations (see Appendix D, Fig. D.3) where a parabolic dispersion of the decay rates with energy has been found [24, 29, 61].

Recently, the same linear trend has been reported in an experimental STS study in Pb/Ag(111) with a slope of 53 meV·eV^{-1} [25]. The experimental results, however, appear much more scattered around the linear fit than our theoretical results and the intercept also is different. This differences might be explained in part by the non ideal conditions that are found in any real experimental system. In Table D.I of Appendix D we compare linear-fit parameters of experimental and *ab initio* decay rate data with our results. With respect to the results of Ref. [25], when attempting to make a meaningful comparison with STS experiments, in principle, one should take into account the effect induced by the STM tip on the lifetimes of the (Stark shifted) QWSs. This issue is addressed in Chapter 7 (see also Fig. 7.5).

For the Pb overlayers with small thickness (1–3 ML), the QWSs with energies above 1 eV have many-body decay rates well below the general trend obtained for thick overlayers. This can be understood from the relative weight of the wave function of the corresponding states in the vacuum and inside the film. For small binding energies the wave function of the state spills more into the vacuum so that, for the thin overlayers, the probability to find an electron inside the overlayer reduces, thus leading to the reduction in Γ_{e-e}. This effect plays a central role in the discussion of the states affected by the image potential in Section 6.5.

6.3.2. Decay rate channels and thickness dependence

Detailed analysis of the contribution of the different decay channels to the many-body decay rate of the g-QWSs is presented in Fig. 6.5 as a function of the Pb overlayer thickness. The states are along the $n_0 = 5$ branch, as appears in Fig. 6.3. As was discussed in the previous section, this way of the data analysis is consistent with that

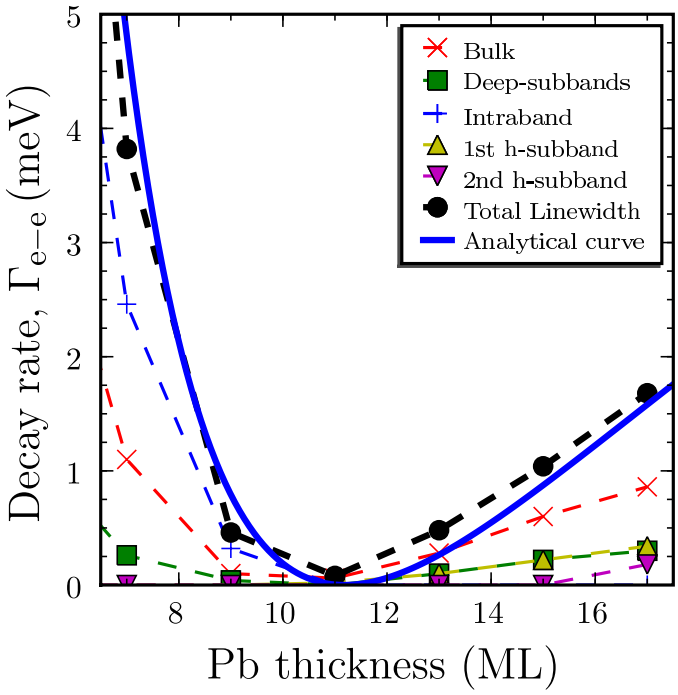

Figure 6.5.: Linewidths and contributions of different decay channels to the many-body decay of the QWSs located throughout the n_0=5 branch in Fig. 6.3. Different decay processes are related to first and second highest subbands (h-subbands), deep QWS subbands, and, for occupied states, the intraband process. The solid line corresponds to the analytic formula in Eq. (6.5) with $r_s = 2.3a_0$ and width correction $\delta = 4.2a_0$

often used experimentally, i.e., one traces the overlayer thickness dependence of the given property of the QWSs that appear closest in energy. Moreover, the choice of this sequence of QWSs allows us to follow the energy evolution from below to above the Fermi level.

From Fig. 6.5 one can conclude that, even though the g-QWSs and the d-QWSs are well localized in the overlayer so that their overlap is large, the inelastic electron or hole transfer into the d-QWSs is small. This is because the d-QWSs have large binding energy at the $\overline{\Gamma}$ point so that the decay of an excited electron or hole from the g-QWS to the d-QWSs is accompanied by a large momentum transfer. This renders the process inefficient. The hole relaxation is associated with mostly intraband transitions and the bulk contribution is nearly one half smaller than the intraband one. This is similar to the results reported for the surface states [159]. As far as the excited electron is concerned, the intraband transitions are impossible from the $\overline{\Gamma}$ point. Transitions into

the bulk bands (substrate + overlayer) contribute then one half of the total decay rate. Another half of the decay rate comes from the interband scattering between QWSs.

Now we discuss briefly the total $e-e$ decay rate of the QWSs as a function of the Pb coverage. Substituting the energies of the QWSs in Pb/Cu(111) system, as given by Eq. (6.4), into the QF formula given by Eq. (3.3), leads to:

$$\Gamma_{e-e} \approx 68.08 r_s^{5/2} \frac{(\alpha + \beta d)^2}{d^2}. \tag{6.5}$$

This result for the inelastic $e-e$ decay rate of the QWSs close to the Fermi level is shown by the solid line (labeled as "analytical curve") in Fig. 6.5. The good agreement between the numerical data and the analytical prediction is not surprising in view of the parabolic dependence of the calculated decay rate with energy close to E_F (see Fig. 6.4).

6.3.3. Comparison with photoemission experiments

Before giving a direct comparison of the calculated results with available experimental data on lifetimes, we discuss the sensitivity of the calculated lifetimes to the choice of the effective mass. As stated in the section devoted to the theoretical methods, $m_n^* = 1$ has been used in the previously presented results. In the angle-resolved photoemission study of Ref. [16], effective masses ranging from 1.1 to 1.6 were reported for occupied QWSs. In order to estimate a possible effect of $m^* > 1$, we have repeated calculations ascribing an effective mass of 1.6 to the occupied QWSs of 18 ML system and observed a slight increase in linewidths of the order of 10%. It means that the presented results are rather robust to effective mass variations. In any case, corrections coming from a more elaborated modeling of the overlayer are expected to be more important. Indeed, it has been argued that the band folding and the underlaying symmetry-character of the bands in the realistic Pb-overlayer band structure (in contrast to the ideal parabolic bands of our model) can influence the decay rates [24]. These effects should be less dramatic for electron states at $\overline{\Gamma}$ than for states with nonzero $\mathbf{k}_{\|}$ (see also Fig. D.2 of Appendix D).

In the following our theoretical results are compared with the lifetimes reported in a recent time-resolved two-photon photoemission study of Pb/Cu(111) by Mathias *et al.* [165]. In this experimental study the lifetimes of two limiting coverages were discussed, i.e., the 1ML-Pb/Cu(111) (the wetting layer) and the large overlayer thickness case (bulk Pb). Here we restrict ourselves to the QWS energy of the lowest unoccupied state of the 1ML-Pb/Cu(111) system at $\overline{\Gamma}$. In our theoretical study this state lies at $E - E_F = 2.14$ eV, whereas in experiments it is found at $E - E_F = 2.76$ eV.

Without the electron-phonon contribution to the electron lifetime, the latter can be estimated as the inverse of the electron-electron inelastic scattering rate Γ_{e-e}:

$$\tau_{e-e} = \Gamma_{e-e}^{-1}, \tag{6.6}$$

For nonzero temperatures, the electron-phonon scattering might be an important decay channel. Calculated electron-phonon broadenings for unoccupied QWSs in Pb free-standing slabs have been presented in Ref. [61]. Values of $\Gamma_{e-\mathrm{ph}}$ of approximately 20 meV and 50 meV are reported for temperatures of 5 K and 50 K, respectively. For the experimental sample temperature of 150 K used in Ref. [165] we estimate for $\Gamma_{e-\mathrm{ph}}$, by linear extrapolation, an electron-phonon broadening of ≈ 100 meV.

The inclusion of an additional electron-phonon decay channel leads to a many-body lifetime:

$$\tau_{\mathrm{mb}} = \left(\Gamma_{e-e} + \Gamma_{e-\mathrm{ph}}\right)^{-1}. \tag{6.7}$$

Since scattering events leading to the decay of the QWSs take place inside the metal, for states with a non negligible weight of the wave function in the vacuum side, the electron-electron many-body decay rate is expected to be reduced, as compared to that inside the metal. With the weight of a QWS (or penetration probability) inside the metal:

$$\beta = \int_{\mathrm{metal}} |\psi(z)|^2 dz, \tag{6.8}$$

we can heuristically estimate the electron-electron decay rate of the QWS as

$$\Gamma_{\mathrm{e-e}} \approx \beta\, \Gamma_{\mathrm{e-e}}^{\mathrm{bulk}}, \tag{6.9}$$

where $\Gamma_{\mathrm{e-e}}^{\mathrm{bulk}}$ is the corresponding electron-electron decay rate in bulk at the corresponding energy. Here $\Gamma_{e-e}^{\mathrm{bulk}}$ is assumed to be given by the quasilinear trend found in the calculations shown in Fig. 6.4 for the energies to be considered here. The renormalization procedure of the bulk decay rates described above is shown to be a reasonable estimation of the *GW* electron-electron decay rates in the context of the QWSs with IS character to be discussed in Section 6.5. Indeed, the ratio between the theoretical electron-electron decay rate in bulk and that of the QWS in 1ML-Pb/Cu(111) at $E - E_F = 2.14$ eV is

$$\frac{\tau_{e-e}^{\mathrm{bulk}}}{\tau_{e-e}^{\mathrm{1ML}}} = \frac{9.36\ \mathrm{fs}}{29.8\ \mathrm{fs}} \approx 0.31, \tag{6.10}$$

which is not far from the actual weight $\beta \approx 0.5$ of the calculated QWS in 1ML-Pb/Cu(111). One expects that the same procedure applies to the electron-phonon

decay rate [169]. Thus, for the theoretical lifetime estimation of the 1ML-thickness QWS we have used

$$\tau_{\rm mb} = \left(\Gamma_{e-e}^{\rm 1ML} + \beta\Gamma_{e-{\rm ph}}\right)^{-1}, \tag{6.11}$$

with $\beta = 0.5$ and the calculated *GW* result $\Gamma_{e-e}^{\rm 1ML} = 22.08$ meV. For the theoretical estimation of the lifetime at $E - E_F = 2.76$ eV the same Eq. (6.11) is used but, since we do not have at this energy the corresponding theoretical QWS electron-electron decay rate, the weighted theoretical bulk decay rate value is estimated as $\Gamma_{e-e}^{\rm 1ML} = 102.52\,\beta$ meV. For this energy β is taken from the ratio between the corresponding bulk and QWS experimental lifetimes [165]:

$$\beta = \frac{\tau_{\rm exp}^{\rm bulk}}{\tau_{\rm exp}^{\rm 1ML}} = \frac{3.4\ {\rm fs}}{8.4\ {\rm fs}} \approx 0.405. \tag{6.12}$$

For the $\tau_{\rm e-e}$ and $\tau_{\rm mb}$ lifetime estimations in bulk Eqs. (6.6) and (6.7) are used, respectively.

Table 6.I.: Theoretical estimations and experimental lifetimes [165] for bulk Pb and the first unoccupied QWS in 1ML-Pb/Cu(111) system. The experimental error is indicated inside parentheses next to the $\tau_{\rm exp}$ values.

	$E - E_F = 2.14$ eV		$E - E_F = 2.76$ eV	
	τ_{e-e} (fs)	$\tau_{\rm mb}$ (fs)	$\tau_{\rm mb}$ (fs)	$\tau_{\rm exp}$ (fs)
Bulk	6.4	3.86	3.25	3.4 (1.5)
1 ML	29.8	9.13	8.02	8.4 (1.5)

In Table 6.I our theoretical estimations (τ_{e-e} and $\tau_{\rm mb}$) are compared with experimental data ($\tau_{\rm exp}$). The theoretical τ_{e-e} qualitatively reproduces the larger lifetime of the QWS in 1ML-Pb/Cu(111), as compared to that for the bulk Pb at the same energy. The origin of this difference in the present theoretical study is attributed mainly to the high weight of the QWS wave function in the vacuum side. However, accounting only for Γ_{e-e} leads to an overestimation of the lifetime values. When the $\Gamma_{e-{\rm ph}}$ broadening is included in the lifetime estimation ($\tau_{\rm mb}$), theoretical results are in agreement with experimental data at $\overline{\Gamma}$ within the reported experimental error.

To conclude this section, we briefly review the lifetimes of the QWSs in Pb/Si(111) probed with TR-2PPE by Kirchmann *et al.* [23, 24]. In contrast to the analysis above, devoted to the Pb/Cu(111) system, the reported lifetime values for Pb/Si(111) are fairly well reproduced by only taking into account the electron-electron contribution calculated in bulk, the latter being approximately reproduced by the Quinn-Ferrell formula (see Appendix D). Note that the measurements in Refs. [23, 24] were made at a sample temperature of 100 K, in order to avoid island formation and surface difussion, for which an electron-phonon broadening of 67 meV can be estimated following the same arguments as above. The inclusion of this broadening leads to a strong underestimation of the lifetime, thus our lifetime results in Pb/Cu(111) do not appear directly comparable to those of Pb/Si(111).

On the other hand, the QWS for the 1 ML coverage, in Pb/Si(111), appears at $E - E_F \approx 1.65$ eV, which is ~ 1 eV below that probed in Pb/Cu(111). Since at lower energies the confinement of the states in Pb is stronger, the lifetime of the 1-ML-thick QWS (5 fs) is expected to be also close to the general trend. However, the value is significantly smaller than the Quinn-Ferrell estimate (10.4 fs). This difference is attributed by the authors of Ref. [24] to the additional resonant decay contribution opened above the Si gap at $E - E_F \approx 0.7$ eV.

Finally, in Ref. [23] Kirchmann *et al.* have found for the 15 ML coverage that the lifetime of the QWS with energy $E - E_F = 1.2$ eV is 30 fs (a linewidth of 21 meV) whereas the decay rate of (part of) the band associated to this QWS to the low-lying QWS band ($E - E_F = 0.5$ eV) is found to be 12.2 meV (54 fs). The latter value is approximately one half ($\sim 50\%$) of the total decay rate which is significantly higher than the 20–25% found in our calculations (see Fig. 6.5).

6.4. Decay of quantum well resonances: WPP results

6.4.1. Elastic decay rate

The calculated one-electron resonant decay rates $\Gamma_{\rm res}$ of QWRs are shown in Fig. 6.6. Results are presented as a function of the energy of the quasi-stationary states measured with respect to the Fermi level. For the given overlayer thickness, $\Gamma_{\rm res}$ is smallest for the lowest energy states energetically close to the bottom of the substrate valence band and for the highest energy states close to the onset of the Cu(111) L gap. As we have already stated in Chapter 5, in connection with Eq. (5.22), this result can be explained by the high reflectivity of the substrate in the corresponding energy regions [34]. As found

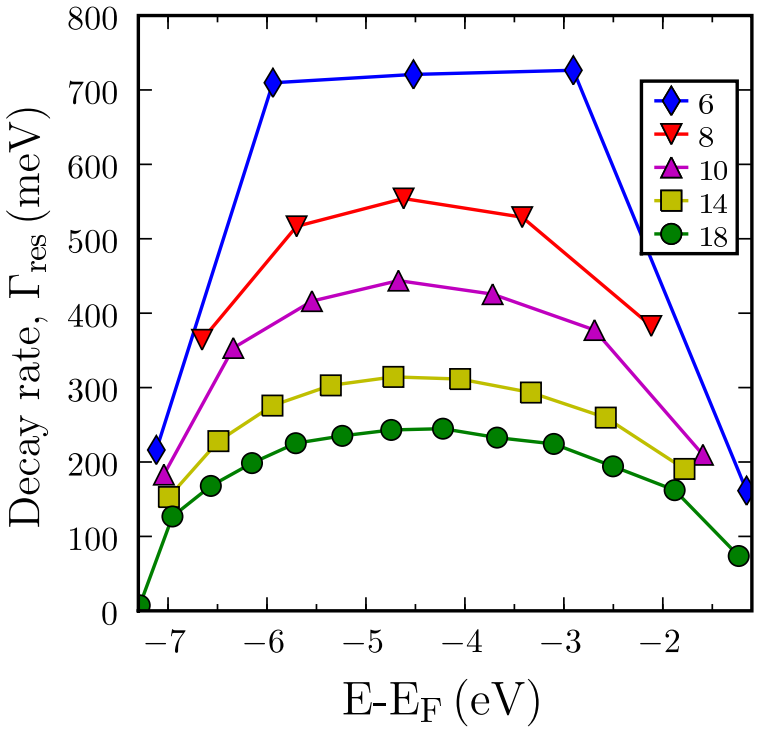

Figure 6.6.: Calculated one-electron decay rates of QWRs for jellium Pb overlayers on Cu(111). Results are shown as a function of the energy, measured with respect to the Fermi level. Different symbols stand for the different overlayer thicknesses measured in number of Pb MLs, as indicated in the inset of the figure.

in the simple models analyzed in Chapter 5, the decay rate is expected to decrease as $1/d$ with increasing thickness d of the Pb overlayer. This is fully supported by present numerical results shown in Fig. 6.6. Intuitively, the resonances become narrower, but their density increases so that in the limit of large d the continuum of Pb states is retrieved. Note that the energy separation between the QWSs is $\propto 1/d^2$, as follows from Eq. (5.7).

It is noteworthy that, in some cases, the resonant peaks in the PDOS appear very close to the Cu(111) band gap so that the usual Lorentzian resonant shape (see Eq. (4.47) in Chapter 4) is distorted. In those cases, the decay rate was estimated from the low energy part of the peak. However, this result has to be taken with caution, since non-Lorentzian shape of the PDOS reveals nonexponential decay. In Table 6.II these QWRs are marked explicitly.

Table 6.II.: Calculated energy, E, linewidth, Γ, inverse decay rate, Γ^{-1}, and corresponding quantum number, n, of some QWSs (many-body decay) and QWRs (resonant decay), for selected Pb overlayer thicknesses. The "Small" ("High") widths (lifetimes) denote the low reliability of the calculated small linewidth values due to the high relative error. In this table the electron-phonon broadening is not taken into account for the lifetime estimation.

No. of MLs	$E - E_F$ (eV)	Γ (meV)	Γ^{-1} (fs)	n
6[a]	−1.17	161	4	9
6	0.45	2	289	10
6	2.16	68	10	11
8	−2.12	380	2	11
8	−0.79	18	36	12
8	0.53	4	177	13
8	1.92	55	12	14
9	−2.44	411	2	12
9[a]	−1.22	117	6	13
9	−0.06	Small	High	14
9	1.18	26	26	15
9	2.43	85	8	16
10	−2.69	377	2	13
10	−1.60	210	3	14
10	−0.53	8	83	15
10	0.59	5	121	16
10	1.74	48	14	17
10	2.86	103	6	18
18	−2.53	194	3	23
18	−1.91	162	4	24
18	−1.26	74	9	25
18	−0.64	10	70	26
18	0.01	Small	High	27
18	0.69	10	69	28
18	1.38	34	19	29
18	2.08	69	10	30
18	2.78	108	6	31

[a]Result has to be taken with caution because the calculated peak overlaps with the energy gap region.

6.4.2. Competition between elastic and inelastic decay processes

Along with resonant one-electron transfer through the Pb/Cu interface, the QWRs can decay by many-body processes, so that their total lifetime broadening depends on both decay channels. The exact calculation of the many-body decay of the QWRs is a nontrivial task. However, by simulating the inelastic electron-electron decay rate inside the metal by an absorbing potential (see Chapter 3 for technical details), we have checked within the WPP method that for the QWRs the total decay rate is $\approx \Gamma_{\rm res} + \Gamma_{e-e}$. Thus, the QF curve with $r_s = 2.3a_0$ (see Fig. 6.4) should give a reasonable upper bound for the possible many-body contribution to the lifetime broadening of the QWRs.

Figure 6.7 is aimed at the qualitative discussion of the general trends determining the lifetimes of the QWRs. It shows the calculated many-body and one-electron decay rates of the QWSs and QWRs. The QF curve with $r_s = 2.3a_0$ allows extrapolation of the parabolic energy dependence of the inelastic decay rate of the QWSs into the energy region of the QWRs. As follows from the comparison between the calculated resonant decay rates and the QF estimation of the many-body decay, the latter will be the dominating decay channel for the low energy QWRs below -6 eV. For the QWRs at higher energies and near the projected band gap, the dominating decay mechanism will strongly depend on the overlayer thickness d. For thin layers, the resonant one-electron decay should dominate. However, since the resonant decay rate decreases as $1/d$, we estimate that for the overlayers of thickness above 30 ML the inelastic many-body scattering will be the dominating decay channel of the QWRs. This appears physically sound since, for the thick Pb films, the QWRs merge and form the Pb bulk continuum of electronic states, where only many-body decay is operative.

In the angle-resolved photoemission study of thin Pb films on Cu(111) carried out by Dil *et al.* [16] the states below the projected band gap of Cu(111) were observed along with conventional QWSs with energies inside the projected band gap of copper. In Ref. [16] these states were not associated with QWRs because their linewidths appeared comparable to those of the QWSs, i.e., without noticeable effect of the resonant charge transfer broadening. Based on the results of the present study we argue that, for the thick Pb overlayers on Cu(111), the QWRs appearing close to the projected band gap indeed show the linewidth comparable to that of the QWSs. It is noteworthy that the energies of the QWRs calculated with the present model, and experimental observations in Ref. [16] compared in Fig. 6.3, are in good agreement for thick layers. The general absence of experimental states for energies below $E - E_F \sim -2$ eV (except for the 22 ML coverage case, where incidentally the agreement with experimental data appears

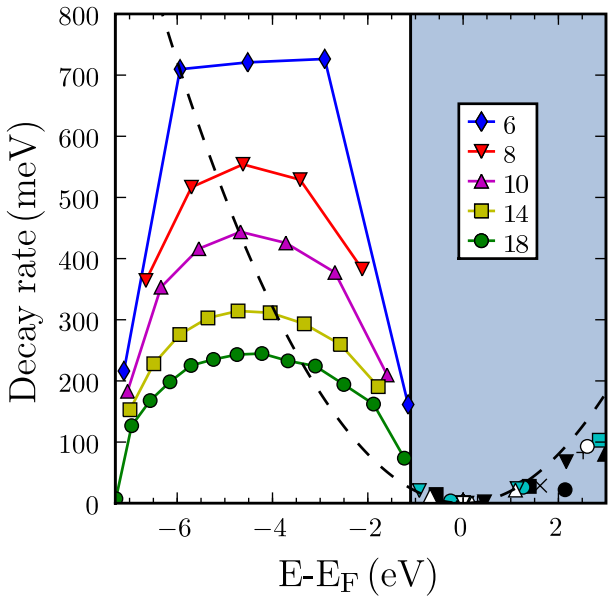

Figure 6.7: Calculated many-body (inelastic) decay rates of the QWSs and resonant (elastic) decay rates of the QWRs as a function of the energy, measured with respect to the Fermi level. The shaded energy region corresponds to the projected band gap of the Cu(111) surface where the QWSs exist. The states appearing below the projected band gap are the QWRs. For the QWRs different symbols correspond to the overlayer thickness (see the inset). For the QWSs the symbols are the same as in Fig. 6.4. Parabolic QF curve with Pb charge density parameter $r_s = 2.3a_0$ is shown by the dashed line.

not so good), might be linked with the non (nearly-) free-electron band structure of Cu along Γ-L, just below this energy (see Fig. 2.2), because of the *d* electron bands.

6.5. Inclusion of the image potential: quantum size effects

In the previous section we have presented a theoretical study of the electron-electron inelastic decay rates of QWSs in Pb/Cu(111) for energies up to 3 eV, described by the self-consistent effective potential calculated within DFT. It has been found that the calculated electron-electron decay rate follows a parabolic dispersion, as a function of energy close to the Fermi level, and a quasilinear dispersion above 1 eV. Only some deviations from the general trends have been found at small (1–3 ML) overlayer thicknesses (see black-filled symbols in Fig. 6.4). In this section we take a step further and include the classical image potential correction to the DFT potential (as explained in Chapter 2), which allows the discussion of the QWSs at energies close to the vacuum level.

6.5.1. Electronic structure

The discussion is started by revisiting the electronic structure of the Pb/Cu(111) system (see Fig. 6.3), but focusing on the previously uncovered energy region close to the vacuum level, where the image potential tail becomes important. Figure 6.8, where QWS energies up to -0.05 eV are shown for thicknesses in the range of 1 to 30 MLs, will allow us to perform a transparent analysis of the following numerical results. The states with energies $E - E_V \leq -1.5$ eV are almost unaffected by the image potential, i.e., they correspond to those obtained by the DFT-LDA effective potential. Due to the inclusion of the image potential, for each thickness, an infinite set of bound states converging toward the vacuum level is retrieved. This is in sheer contrast with the original DFT-LDA potentials vanishing exponentially in the vacuum side, and only allowing for a finite number of states to be accommodated (as shown in Fig. 6.1). Another feature resulting from the corrected potential is that there is a state with an energy close to -0.79 eV systematically appearing every 3 MLs (at coverages of 3, 6, ... MLs). These states are characterized by a wavelength $\lambda \approx 6a/5$, where a is the interlayer distance ($a = 5.41a_0$). This regularity is similar to the series of unoccupied QWSs observed in Pb overlayers close to the Fermi level, at $E - E_F \approx 0.65$ eV, for an even number of MLs (see, e.g., the series of states labeled as $n_0 = 4$ in Fig. 6.3). In the latter case, however, the states are characterized by $\lambda \approx 4a/3$.

The inclusion of the image potential has an important consequence on the QWS wave functions. As the energies of the QWSs approach the vacuum level, they start to develop an IS character, i.e., the weight of the wave function outside the metal rapidly increases and the characteristic nodal structure is developed in the vacuum side [30]. This is illustrated in Fig. 6.9(a), where the calculated charge densities of the first hybrid QWS-ISs for the Pb coverage of 9 ML are displayed. Despite the strong IS character of the states, the penetration into the overlayer still determines their precise binding energy.

The set of states lying at -0.79 eV allows us to discuss unambiguously the dependence of the properties of QWS-ISs on the overlayer thickness for a fixed energy. In Fig. 6.9(b) the wave functions of these states are compared. In the displayed overlayer region the wave functions show a similar shape. Indeed, the maximum of the wave functions in the vacuum side and the nodes inside the overlayer are found essentially at the same z position for different overlayer thicknesses. However, when computing the weight in the vacuum side ($\int_{\text{vacuum}} |\psi|^2 dz$) a quantum size effect is found: the wave function weight in the vacuum decreases from 0.65 to 0.41 in the 6–18 ML coverage range. This effect cannot be explained by the small energy differences between the

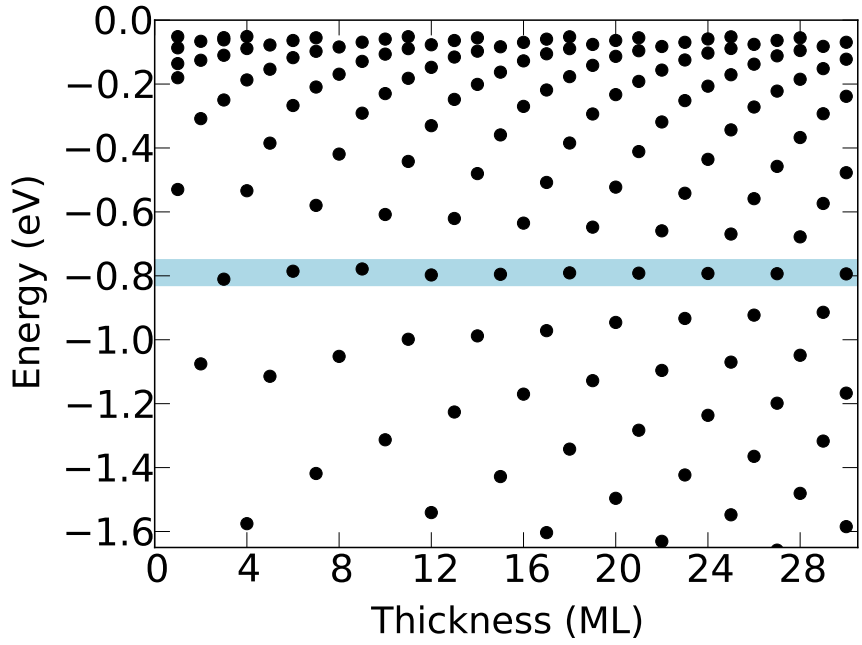

Figure 6.8.: Calculated energies of the QWS-ISs close to the vacuum level as a function of the overlayer thickness for the Pb/Cu(111) system. Energies are given with respect to the vacuum level. The shaded area denotes the set of states lying at energy ≈ -0.79 eV.

states, instead, it should be connected with the wave function penetration into the metal at different overlayer thicknesses.

In order to get insight into the thickness dependence of the wave function weight outside the overlayer, we analyze the simple model of a metallic overlayer, similar to that discussed in the introductory Chapter 5. In this case the metallic overlayer of thickness d is modeled as a quantum well with an infinite potential barrier, representing the substrate barrier at $z = -d$, and a constant potential U_0 from $-d$ to 0. Then, the solution is of the form $A\sin(kz + \varphi)$ inside the metal, with normalization constant A, wave vector $k = \sqrt{2(E - U_0)}$ and phase $\varphi = kd$. In the vacuum region ($z > 0$) a general solution of the form $\sqrt{w}f(z)$ is considered, with $\int_0^\infty |f(z)|^2 dz = 1$, so that w is the weight in the vacuum side. The wave function normalization condition for a given state ψ_n reads:

$$1 = \int_{-d}^{\infty} |\psi_n(z)|^2 dz = A^2 \frac{d}{2}\left(1 - \frac{\sin(2kd)}{2kd}\right) + w. \tag{6.13}$$

By matching the wave function and its spatial derivative at $z = 0$, the necessary conditions are obtained for solving A as a function of w. Finally, the weight can be

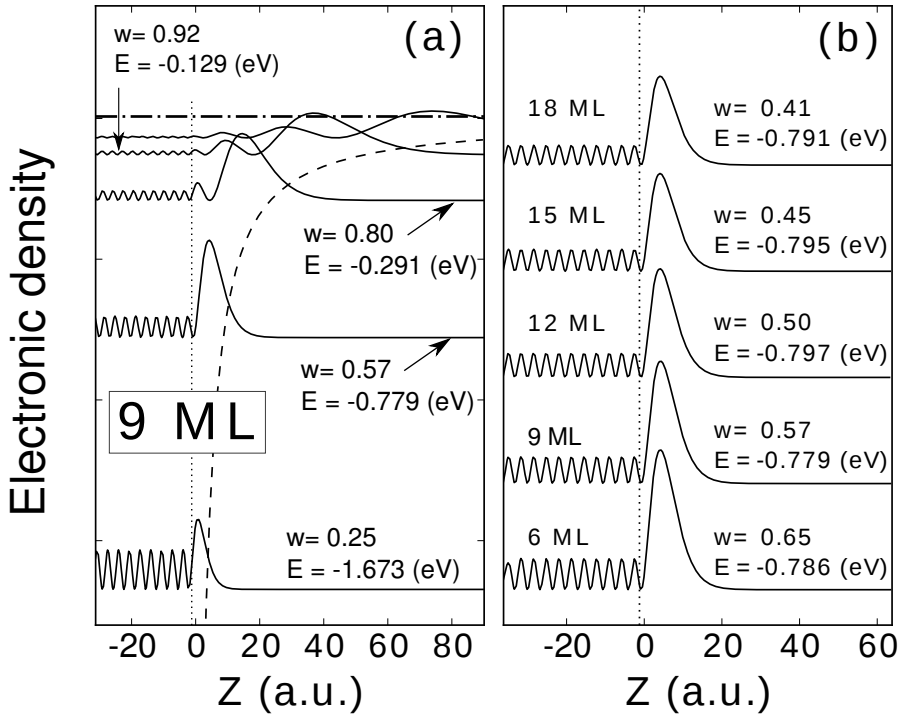

Figure 6.9.: (a) Electronic charge density of the QWS-ISs close to the vacuum level $E_V = 0$ (horizontal dashed-dotted line) shown up to -50 meV for the 9ML-Pb/Cu(111) system (dashed line corresponds to the image potential barrier). States are shifted according to their energy. (b) Charge density of the states with energy close to -0.79 eV (see shaded area of Fig. 6.8) for several Pb overlayer thicknesses. For each state the energy E and weight w in the vacuum region are indicated. The origin $z = 0$ is placed at the image plane position and the vertical dotted line corresponds to the jellium edge at $z = -1.23a_0$ in both panels.

expressed as:

$$w = (1 + \mu d)^{-1}, \tag{6.14}$$

with

$$\mu = \frac{f_0^2 \left(1 - \frac{\sin(2kd)}{2kd}\right)}{2\sin^2(kd)} \approx \frac{f_0^2}{1 + \cos(\phi_{\text{vac}})}, \tag{6.15}$$

where $f_0 = f(z = 0)$, and the phase accumulation model [Eq. (5.25)] has been used with ϕ_{vac} as the vacuum barrier phase shift. The approximation in Eq. (6.15) is valid for $kd \gg 1$, which is the case for the present range of magnitudes even for 1 ML thickness. As far as f_0 does not change, as is the case for the states lying at -0.79 eV [as follows from Fig. 6.9(b)], μ can be considered as a constant. The dependence of w on d is consistent with the trends observed in Fig. 6.9(b) and is physically sound: (i)

For infinitely large overlayer thicknesses, the weight of the wave function approaches zero in the vacuum. In the limit $d \to \infty$, however, the density of states evolves from a discrete to a continuous density of states, corresponding to that of the bulk metal surface. (ii) For $d = 0$, the situation would correspond to an image state in front of an infinite crystal band gap. Then, the wave function would be localized entirely on the vacuum side.

6.5.2. Decay rates of QWS-ISs

According to the previous subsection, the overlap of the QWS-ISs with the metal overlayer is expected to be strongly reduced for energies close to the vacuum level. Furthermore, this overlap is also dependent on the overlayer thickness. Since the inelastic relaxation takes place mainly inside the metal, similar effects are expected on the electron-electron decay rates of the QWS-ISs.

For ISs at noble metal surfaces localized in vacuum (see, e.g., Fig. 5.4(b) of Chapter 5), it is well known that their penetration into the bulk plays an important role in determining their lifetimes. The bulk contribution to the decay rate of a given IS with energy E_0 can be approximated by the value of the decay rate in bulk at the same energy E_0, weighted by the overlap between the bulk and the IS wave function. Although in Ref. [170] it is illustrated that the heuristic approach does underestimate the actual lifetime of the ISs, this approach, together with the previous model results concerning the weight of the QWS-ISs, appears very useful for analyzing the following many-body decay rate results.

The heuristic approach above neglects the non-local effects in the self-energy, i.e., $\Sigma(z, z') \to \Sigma(z)\delta(z-z')$ and the decay is only considered inside the metal (see Chapter 3 for further details on the self-energy calculation). In this respect, the WPP method appears as an equivalent approach for estimating the decay rates of the QWS-ISs by effective many-body absorbing potentials, as it is explained in Chapter 4. In this approach different absorbing potentials can be ascribed for different metallic regions. In the following analysis, the quasilinear dependence found in the previous section is used for describing the decay rate inside the Pb overlayer and a Quinn-Ferrell dependence of the decay rate is used inside Cu. Note that the quasilinear dependence derived from the *GW* calculations already does take into account the decay rate inside Cu. The reason why we use a different absorbing potential inside Cu is basically to adjust accurately the many-body decay rate of the Pb localized states to the *GW* data. Nevertheless, the effect of using a different decay rate inside Cu is small, because of the small penetration of the wave function into the band gap.

Fig. 6.10(a) shows the many-body GW calculations (open squares) of the decay rates for the states lying at −0.79 eV from 3 to 18 MLs. In the same figure, the WPP results and the heuristic estimations based on weight arguments are also plotted. All of them give similar results. Note the following two observations: (i) The calculated decay rates are strongly reduced with respect to the value expected for a state inside the Pb overlayer (130.1 meV) at the same energy. In the 3 ML coverage case, for the state with energy −0.811 eV and $w = 0.75$, a decay rate value as low as 32 meV is obtained, which is of the order of the decay rates of image states [170] at noble metal surfaces. (ii) A remarkable quantum size effect is found for the Γ_{e-e} decay rate of QWS-ISs in Pb/Cu(111): For fixed energy the decay rate strongly depends on the overlayer thickness. Between the 6 ML and 18 ML coverages there is a difference in the decay rate of 34 meV at energy ≈ -0.79, which doubles the decay rate value found in the QWS-IS for the 3 ML coverage.

It follows from the above comparison between *GW* and simple model results that the decay rate of a QWS-IS can be approximated as $\gamma \approx (1 - w)\gamma_0$, where γ_0 is the decay rate of a state completely confined inside the metal and w is the wave function weight inside the metal. Then, from Eq. (6.14) it is straightforward to obtain

$$\gamma = \gamma_0 \frac{d}{d + \alpha}, \tag{6.16}$$

where $\alpha = 1/\mu$ [Eq.(6.15)]. Taking α and γ_0 as parameters, we fit Eq. (6.16) to the *GW* data. A remarkable agreement with $\gamma_0 = 129.6$ meV and $\alpha = 8.67$ is obtained using this expression, as can be observed in Fig. 6.10(a). In Eq. (6.16) d is simply given by $d = Ja$, where J is the number of monolayers and a the interlayer distance. The fitted value of γ_0 is in good agreement with that expected (130.1 meV) from the quasilinear dispersion found in our previous calculations (Fig. 6.4).

Figure 6.10(b) shows the QWS-IS decay rates, for thicknesses up to 30 ML and energies up to −50 meV, obtained from the heuristic approach. First, in contrast to what is expected for the quasilinear trend, a saturation of the decay rate increase with energy is found around $E - E_V \sim -1$ eV. For energies closer to the vacuum level E_V, the states are pushed away from the metal into the vacuum and the decay rate drops. The accumulation of decay rate values close to the vacuum level reflects the high number of states in this energy region (see Fig. 6.8). Second, for smaller coverages the overall decay rates are smaller (see the trend of the green line in Fig. 6.10). This is directly linked to the previously discussed quantum size effect. Indeed, this quantum size effect, together with the particular electronic structure shown in Fig. 6.8, leads to the branch structure appearing in Fig. 6.10(b), and particularly, the states at −0.79 appear in a vertical branch, which is denoted by a shaded area.

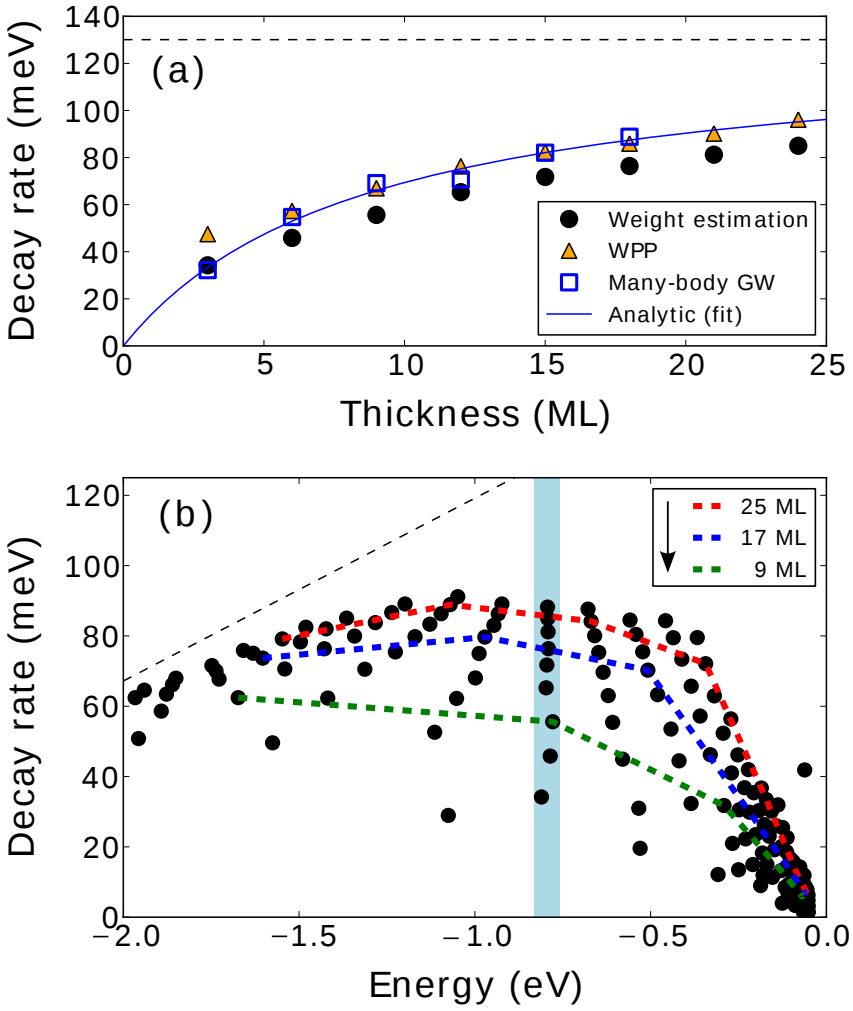

Figure 6.10.: (a) Calculated electron-electron decay rates of the states lying at −0.79 eV as a function of overlayer thickness. Open squares: many-body *GW* results. Triangles: WPP results. Dots: Bulk decay rates weighted by the penetration. Solid line: fit to the *GW* data with Eq. (6.16) (see main text for details). The horizontal dashed line at 130.1 meV denotes the theoretical bulk decay rate for the energy −0.79 eV. (b) Estimated decay rates of the QWS-ISs for overlayer thicknesses ranging from 1–28 ML, as a function of energy (with respect to the vacuum level). Thick dashed lines connect the decay rates for a few selected overlayer thicknesses (see the legend). The thin dashed line represents the bulk-like many-body quasilinear dispersion of the decay rates derived from *GW* calculations (see Fig. 6.4). The vertical shadowed strip represents the narrow energy window of the shadowed area of Figure 6.8 at ≈ −0.79 eV.

6.5.3. Thick overlayer limit

As previously mentioned, as the overlayer thickness increases, eventually the QWS-ISs would retrieve the bulk decay rate $\Gamma_{e-e}^{\text{bulk}}$. However, the number of states increases as well, which might render the states unresolvable. Here, we estimate that for the thickness $d \sim 60$ MLs, $\Gamma/2 > \Delta E$ at E $= -0.79$ eV, with ΔE being the energy difference between adjacent states.

To illustrate the above point, the calculated projected density of states with WPP for different overlayer thicknesses is shown in Fig. 6.11. The absorbing potential entering the WPP calculation to simulate the inelastic decay rate has been set in order to reproduce the theoretical electron-electron decay rate value (130 meV) at energy $E = -0.79$ eV. The figure clearly shows a smooth transition from a QWS-IS peak structure to the bulk Pb surface limit. From the point of view of electron dynamics, the thick overlayer case corresponds to this bulk limit: Due to the many-body scattering processes, the electron localized at the surface of a thick overlayer does not return once it escapes into the metal.

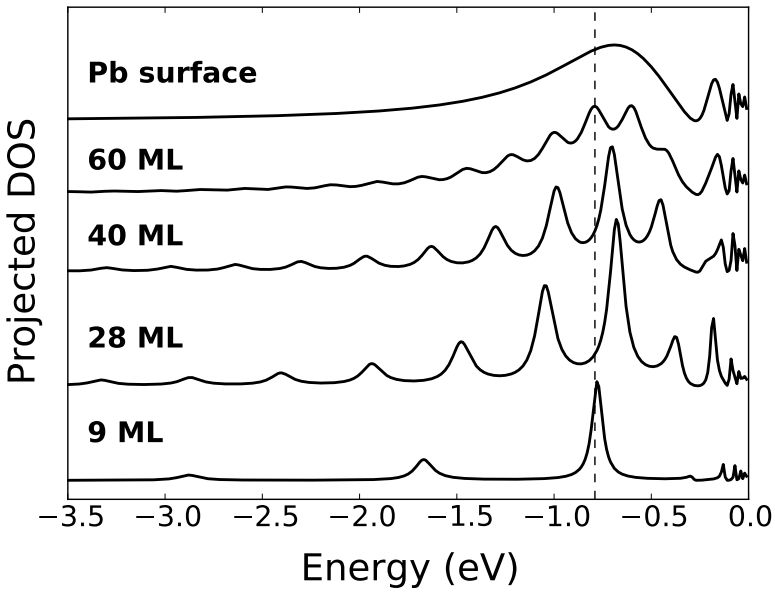

Figure 6.11.: Projected density of states onto the surface calculated for different Pb overlayer thicknesses in Pb/Cu(111) system, including the limit for the infinite thickness (bulk Pb surface). The vertical dashed line denotes the energy level at -0.79 eV.

6.5.4. Experimental evidence of quantum size effects in lifetimes

With respect to the possibility of probing experimentally the present findings, we notice that in a recent 2PPE study of the Pb/Si(111) system, for all overlayer thicknesses, an IS has been reported lying at -0.79 eV with respect to the vacuum level [24]. This energy coincides with the approximate energy of the set of states indicated by a shaded area in Fig. 6.8, which in our calculations appear at coverages of 3, 6, 9, ... MLs.

As already discussed in Subsection 6.3.3, the interpretation of the lifetimes of QWSs for the Pb/Si(111) system is not straighforward. Thus the experimental search for the quantum size effects on lifetimes described in this chapter should be focused on less complex systems, such as Pb/Cu(111) and Pb/Ag(111), where a projected band gap exists close to the vacuum level. Indeed, in Subsection 6.3.3, we have discussed the time-resolved 2PPE experiments by Mathias *et al.* [165]. The lifetime reported for the QWS in Pb/Cu(111) for the 1 ML coverage is significantly larger than the corresponding bulk value. This result has been explained by the wave function penetration arguments. With respect to larger thicknesses, the TR-2PPE measurements in Ref. [165] were reported up to the energies where a systematic quantum size effect in the lifetime might be distinguished, according to our results. Another possibility would be to perform an inverse photoemission experiment.

The possibility of observing these quantum size effects in QWS-ISs by STS experiments is discarded, as far as the the image potential is overridden by the STM-induced electric field (see Chapter 5 and also next chapter). It should be noted, however, that similar lifetime variations, under the effect of different electric fields on Stark shifted ISs in Cu(100), were discussed in terms of the wave function overlap with the Cu metal in Ref. [171]. Thus, the possibility to see a similar overlayer thickness effect is open, as for the QWS-ISs, in the linewidths of QWS hybridized with field emission resonances (FERs), as follows from the strong spilling of the QWS-FERs into the vacuum (see, e.g., Fig. 7.3 which is introduced in next Chapter 7). Nevertheless, care should be taken with respect to a possible electric field effect. The overlayer thickness effect in QWS-FER linewidths is likely to be probed with substrates possessing a projected band gap up to the vacuum level, or above, in order to avoid the resonant decay contribution to the linewidth. The QWS-FERs in the Pb/Cu(111) system do not appear suitable for showing clear QSEs in their lifetimes, due to the nontrivial band structure of the actual Pb overlayer, as it is discussed in detail in next chapter.

6.6. Summary

We have calculated decay rates of QWSs and QWRs in Pb overlayers (up to ~ 30 MLs) supported on a Cu(111) substrate. In addition, we have discussed the hybridization between the QWSs and ISs, and their lifetime, using simple model arguments based on the penetration of the wave function into the metal. The system has been modeled with self-consistent 1D pseudopotential obtained from the DFT calculations, with proper account for the projected band gap structure of the Cu(111) substrate and free-electron (jellium) representation of the Pb overlayer. The classical image potential has also been included.

For QWSs, the inelastic electron-electron contribution to the broadening has been calculated within many-body theory, using the *GW* approximation. Our results show that d-QWSs located below -8 eV with respect to the Fermi level, i.e., below the bottom of the Cu(111) *sp* band, have many-body decay rates larger than 1 eV. Taking into account the small energy separation, the corresponding peaks in, e.g., photoemission spectra should completely overlap, rendering impossible resolution of individual states. The QWSs laying in the projected energy gap of Cu(111) have much longer lifetimes. At small energies with respect to the Fermi level we find that the many-body decay rate approximately follows the QF parabolic dependence with energy. For the QWSs located at higher excitation energies a quasilinear dependence of the many-body decay rate with energy is found. These results are in agreement with recent STS results in Pb/Ag(111) [25]. As a general trend, we have found that the contribution of the Cu(111) bulk into the many-body decay of the overlayer localized states is comparable to that of the interband and intraband transitions involving directly QWSs. QWRs appear energetically below the projected band gap of the substrate inside the Cu(111) *sp* band. Thus, an electron initially localized in the quantum well can escape into the substrate via energy-conserving tunneling through the Pb/Cu(111) interface. The one-electron elastic decay rates of the QWRs have been calculated with the WPP method for variable thickness of the overlayer, revealing several general trends:

(i) The one-electron decay rate of the QWRs is small whenever the reflectivity of the Pb/Cu(111) interface is high, in particular close to the onset of the Cu(111) projected band gap. In this energy region the QWRs have widths comparable to those of the QWSs.

(ii) When the width d of the Pb overlayer increases, the decay rate of the QWRs decreases in overall as $1/d$. This can be understood on the basis of the simple quasi-classical arguments developed in previous chapter (Sec. 3.1).

(iii) Comparing the elastic decay rate of the QWRs with their many-body decay rate estimated from the QF formula, we conclude that for the overlayers thicker than 30 ML the inelastic decay dominates. Basically this sets the transition to the limit of the thick Pb film, where only inelastic decay will be possible.

For the connection between theoretical results and experiment the issue of the way the experimental data are analyzed appears of central importance. Since experimentally the assignment of the given quantum number is not a trivial task, one can follow the energy evolution of the states with increasing overlayer thickness, focusing at the given energy intervals. For the QWSs near the Fermi level, which are explored in (two-photon) photoemission and scanning tunneling spectroscopy experiments, we have derived an analytical expression for the lifetime and energy evolution with the overlayer thickness.

We have compared our theoretical results with available excitation lifetimes derived from TR-2PPE experiments in Pb/Cu(111) [165] and Pb/Si(111) [23,24]. Our theoretical lifetime estimates in Pb/Cu(111) are in agreement with experiments on the same system when the electron-phonon broadening is taken into account. Direct comparison with experimental data in Pb/Si(111) appears difficult, because of the large differences in electronic structure of the Cu(111) and Si(111) substrates.

The hybridization between the QWSs and ISs in Pb/Cu(111) has also been addressed by amending the DFT potential in such a way that the image potential tail is accounted for. We have found that, as the energies of the QWSs approach the vacuum level, the states develop partial IS character. Then, the electron is pushed into the vacuum, which reduces the coupling with many-body excitations in the metal. For a given energy, the weight of a QWS-IS in the vacuum side depends on the overlayer thickness. This in turn, induces a QSE in the corresponding electron-electron inelastic lifetime. We have also derived an analytic expression reproducing this QSE based on the wave function penetration into the metal.

The transition of the PDOS from small Pb overlayer thicknesses to a thick one has been discussed. For thick overlayers the QWS-IS peaks are merged and the PDOS of the bulk Pb surface is retrieved.

Finally, we have discussed the possibility of probing systematically the QSEs in the lifetimes of QWS-ISs by photoemission experiments or QWS-FERs in STS experiments.

Chapter 7

Constant current scanning tunneling spectroscopy in Pb overlayers

7.1. Introduction

Previous Chapter 6 has been focused on the energies and lifetimes of the quantum well states (QWSs), quantum well resonances (QWRs) and QWSs with partial image state (IS) character in Pb/Cu(111) overlayers. The theoretical results have been mainly compared with photoemission experiments. The photoemission spectrum is assumed to map directly the density of states of the probed surface. This is not the case with the spectra obtained by the scanning tunneling microscopy (STM), when large biases are used, as will be explained in this chapter. Thus, for a faithful comparison between calculated results and experiments, recent STM and scanning tunneling spectroscopy (STS) experiments on confined states in large Pb(111) islands deposited on Cu(111) and Ag(111) surfaces [20, 25] are addressed. Our calculations explicitly include the STM tip and the potential due to the applied bias [47, 172]. These experimental STS studies were performed at constant current regime so that high-energy QWSs could be sampled, as compared to previous works [10, 11].

When the lateral extension of the Pb island is large enough, the quantization in the plane parallel to the surface resulting from the reflection by the island boundaries can be neglected because of the lifetime broadening. It is the quantization of the electron motion perpendicular to the surface that determines the discrete energy spectrum so that the electronic structure of the system is represented by the QWSs of the complete

overlayer. The STM/STS studies have the advantage of dealing with well-characterized systems, where the information is not averaged over possible structural variations. This is why it has become a valuable complementary tool to photoemission and inverse photoemission techniques allowing to gain information on the band structure [173], quasiparticle lifetimes [33, 159, 174, 175], phase-shifts for impurity or defect scattering [176], etc. On the other hand, and in particular for high bias, the electric field in the STM junction can *a priori* modify the energies of the electronic states at surfaces, so that the technique is not noninvasive. A classical example of this effect is the evolution of the image potential states (ISs) of the pristine metal surface [126, 177, 178] into the field emission resonances (FERs) of the STM junction [115, 116, 120, 134–137, 179]. The point raised above is one of the central issues of the present chapter: to what extent the QWSs are modified by the applied bias in the STM junction? Once this question is answered, we could address the role of the realistic Pb band structure in the experimentally observed trends.

We use the flat-tip approximation with given 1D model potential description of the STM junction (adlayer+substrate+tip) designed on the basis of the density-functional theory (DFT) calculations performed for Pb/Cu(111). The corresponding description is provided in the following Section 7.2. The constant current dZ/dV spectra are calculated with the wave packet propagation (WPP) treatment of the electron transmission from the tip into the sample. The WPP method and its implementation in the 1D case, as required in this chapter, is explained in detail in Chapter 4. The numerical procedure for obtaining the dZ/dV spectra is detailed in Appendix E.

We have found that, for a broad range of overlayer thicknesses, the present model calculations reproduce the experimental data for the QWSs within the energy range where the free-electron description of Pb holds. Based on the comparison between experimental data and theoretical calculations performed with and without biased STM tip, it is shown that at high bias, the energies of the QWSs are strongly affected by the tip-induced electric field. With the above findings, the measured departure of the QWSs energies from the particle-in-a-box [Eq. (5.6)] prediction in the bias range of $4 < V < 4.5$ eV is explained as due to the realistic Pb band structure in Γ-L direction.

7.2. Model potential for a STM tip in front of a surface

In this section we describe the different potentials used in the wave packet propagation (WPP) calculations of the present chapter. The scanning tunneling microscope (STM)

tip is included in the study of the constant current spectroscopy of Pb/Cu(111), which is characterized by the 1D DFT-LDA effective potential with the image potential correction described earlier, which in the following is referred as V_s. For convenience, we give the Schrödinger equation to be solved in the wave packet propagation. The time evolution of $\psi(z,t)$ is given by the time-dependent Schrödinger equation $\hat{H}\psi = i\partial_t\psi$ with Hamiltonian:

$$\hat{H} = -\frac{1}{2}\frac{\partial^2}{\partial z^2} + \frac{k_\parallel^2}{2m^*} + \mathbb{U}(z) + V_{\rm abs}(z) + V_{\rm mb}(z), \tag{7.1}$$

where $V_{\rm abs}$ and $V_{\rm mb}$ are the absorbing potentials. The STM tip is represented with a 1D (flat-tip approximation) jellium model. The electron-tip interaction $V_{\rm tip}(z)$ is given by the Jones-Jennings-Jepsen potential [180]:

$$V_{\rm tip}(z) = \begin{cases} \frac{1-\exp[\lambda(z-z_{\rm tip})]}{4(z-z_{\rm tip})}, & z < z_{\rm tip} \\ \\ \frac{U_0}{A\exp[-B(z-z_{\rm tip})]+1}, & z \geq z_{\rm tip}, \end{cases} \tag{7.2}$$

where parameters A and B are fixed from continuity conditions at $z_{\rm tip}$, the image plane position of the tip [180]. The potential inside the tip has been set to $U_0 = -15.9$ eV (Al), and $\lambda = 0.9\ a_0^{-1}$ has been used. We have checked that results of the following sections do not change with $U_0 = -13.55$ eV (as calculated with present DFT for Pb). Indeed, in the tunneling regime the transmission resonances are determined by the energies and lifetimes of the QWSs of the Pb overlayer on Cu(111). As far as the tip does not present resonant features in the electronic density of states (DOS), the tip properties have little impact on the resonance tunneling profile.

For an electron between two infinite conductor plates ($z_{\rm im} < z < z_{\rm tip}$), the potential due to the multiple electrostatic images, and due to the applied bias reads [115]:

$$V_{\rm mi}(z) = \frac{1}{4}\sum_{n=1}^{\infty}\frac{-1}{(z-z_{\rm im})+nZ} + \frac{-1}{(z-z_{\rm tip})+nZ} + \frac{2}{nZ}\Bigg\} + (z-z_{\rm im})V/Z, \tag{7.3}$$

where the tip-Pb/Cu(111) surface distance is defined as $Z = z_{\rm tip} - z_{\rm im}$.

Finally, the total effective potential acting on the tunneling electron is given by:

$$V_\Sigma(z) = \begin{cases} V_s(z), & z \leq z_{\rm im} \\ V_s(z) + V_{\rm tip}(z) + V_{\rm mi}(z), & z_{\rm im} < z < z_{\rm tip} \\ V_{\rm tip}(z) + V, & z \geq z_{\rm tip}. \end{cases} \tag{7.4}$$

Depending on the problem at hand, the WPP calculations of present chapter have been performed with potential $\mathbb{U}(z)$ [see Eq. (7.1)] given by all or some terms entering

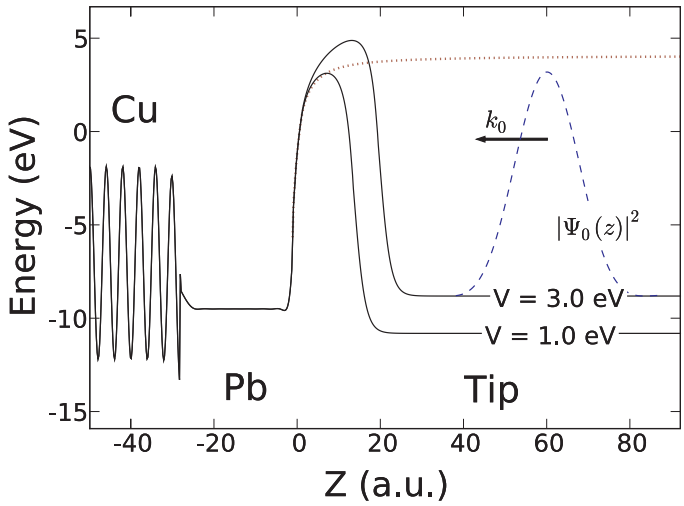

Figure 7.1.: Black curves: Model potential of the tip+5ML-Pb/Cu(111) system at two different bias V and the same current density. Energies are given with respect to the Fermi level. Red dotted curve: the potential of the bare 5ML-Pb/Cu(111) system. $z = 0$ corresponds to the image plane position of the Pb overlayer surface. The probability density of the Gaussian wave packet with average momentum k_0, used in the WPP calculations (Chapter 4), is sketched with dashed curve.

Eq. (7.4). Thus, for the search of the reference QWSs of the unperturbed Pb/Cu(111) system, $\mathbb{U}(z) = V_s(z)$ has been used. The evolution of the QWSs under the applied electric field in the junction, $\mathcal{E} = V/Z$, has been studied with:

$$\mathbb{U}(z) = V_s(z) + (z - z_{\rm im})\ \mathcal{E}\ \theta(z - z_{\rm im}), \tag{7.5}$$

where $\theta(z)$ is the Heaviside step function. Finally, the transmission of the junction has been calculated with the full potential: $\mathbb{U}(z) = V_\Sigma(z)$.

Fig. 7.1 shows the total potential V_Σ for a system comprising 5 ML of Pb on Cu(111) and the STM tip placed at distance $Z = 11.5\,(17.6)a_0$ from the image plane position at bias $V = 1.0$ (3.0) eV.

The many-body contribution is accounted for as explained in Chapter 4 (Section 4.3). It is designed from the many-body results on electron-electron decay rates of Chapter 6:

$$\gamma_{e-e} = \begin{cases} 2.5019 r_s^{5/2}(E - E_F)^2 & E - E_F \leq 1 \text{ eV} \\ \alpha(E - E_F) + \beta & E - E_F > 1 \text{ eV}, \end{cases} \tag{7.6}$$

where the screening radius $r_s = 2.3a_0$ (Pb), $\alpha = 52$ meV$\cdot$eV^{-1}, and $\beta = -41$ meV. We have checked that changing absorption in Cu substrate does not affect final results.

The main broadening of the QWSs thus comes from the inelastic scattering in Pb overlayer.

The energy dependence of the γ_{e-e} implies that, in principle, for each energy, the transmission $T(E, V, Z)$ at $\overline{\Gamma}$ should be calculated with the corresponding γ_{e-e}. This approach is extremely time consuming and would be out of reach. However, we have checked that using γ_{e-e} at the energy given by the applied bias $E = V + E_F$ does change the energy dependence of the transmission, but does not affect the calculated distance-voltage dZ/dV characteristic. This is because the dZ/dV spectroscopy is mainly sensitive to the narrow energy interval close to the tip Fermi level, where the electrons injected into Pb/Cu(111) have energy $E \simeq V + E_F$.

Observe that, for an electron injected from the STM tip into the surface along $\Gamma - \mathrm{L}$, the one-electron reflectivity of the Pb/Cu(111) interface is one within Cu(111) projected band gap. With the flat tip approximation the tunneling flux through the junction, in this case, is only possible due to the inelastic energy relaxation processes described by V_{mb}.

Further details on the calculation of dZ/dV characteristics are given in Appendix E.

7.3. Effect of the tip: Stark shift

We start our discussion with the effect of the electric field in the STM junction on the QWSs. In Fig. 7.2, we show the calculated energies $E_n(\mathcal{E})$ of the QWSs as a function of the applied field in the STM junction $\mathcal{E} = V/Z$. Here, the WPP method with a potential given by Eq. (7.5) has been used, where the tip is not considered, but just the linear bias potential. Results are shown within the energy range of $1 < E < 5$ eV with respect to the Fermi level, i.e., the one encompassed in the constant current STS experiments [20, 25]. The principal quantum number n of the states, as indicated in the figure, corresponds to the nodal structure of the wave function, as discussed in Chapter 6.

At zero field, the QWSs hybridize with image potential states (ISs) forming Rydberg-like series converging toward the vacuum level. The mixed character of these QWS-ISs has been discussed in the previous chapter (Section 6.5). Briefly, the mixed QWS-IS character of the states close to the vacuum level is reflected in their electronic densities. Appreciable part of the electron density is moved from inside the Pb film into the vacuum, as seen in Fig. 7.3, where we show the calculated wave functions ψ_n of the states. From the nodal structure in vacuum, one can infer the principal quantum

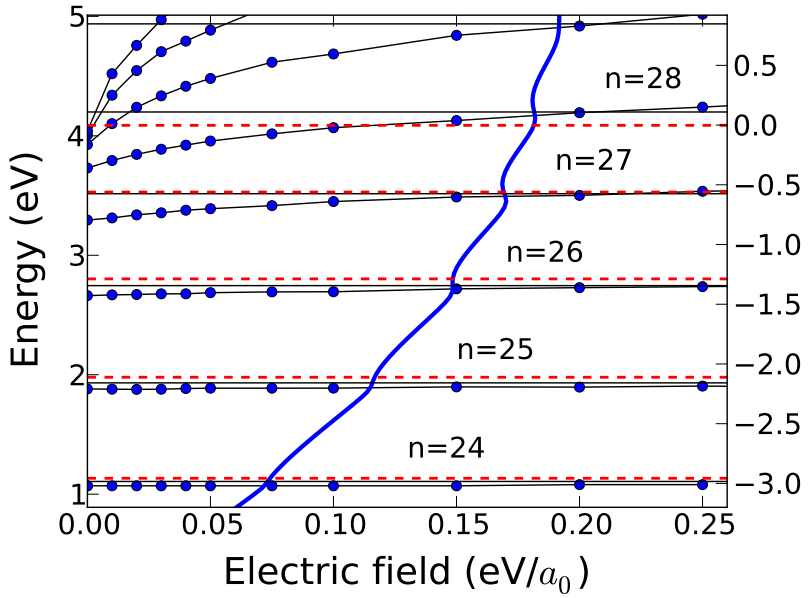

Figure 7.2.: Applied field dependence of the energies of the QWSs. Solid lines with dots: calculated energies of the QWSs as a function of the applied uniform electric field $\mathcal{E}$ for the system comprising the STM tip + 15ML-Pb/Cu(111) system. Energies are given with respect to the Fermi (vacuum) level, as indicated in the left (right) axis. Horizontal dashed lines: energies of the QWS peaks in STS experiments [20]. Horizontal solid lines: energies of the QWS peaks in the calculated dZ/dV spectra. The blue curve represents the electric field, as calculated at each bias (energy with respect to the Fermi level) for the constant current spectroscopy.

number of the IS (denoted by n') providing the leading contribution to ψ_n (indicated in parenthesis in the figure).

When the bias (electric field) is applied to the junction, the low-energy QWSs localized mainly inside the Pb layer experience only minor energy shift, in agreement with experimental results [181, 182]. At variance, the states with partial IS character, close to the vacuum level, are very sensitive to the applied electric field because of the high probability of the electron presence above the surface of the film. These states experience appreciable energy shift (Stark shift) so that the Rydberg-like series converging toward the vacuum level is destroyed already for fields as low as 0.05 eV/a_0. Note that the field $\mathcal{E}$ =0.05 eV/a_0 corresponds to a tip-surface distance as large as 4 nm for a bias of 4 eV. The actual electric fields obtained with the WPP for the conditions of constant current STS experiments (see below) of Yang *et al.* in Ref. [20] are also shown in Fig. 7.2. The field dependence of the Stark shift of the states with mixed

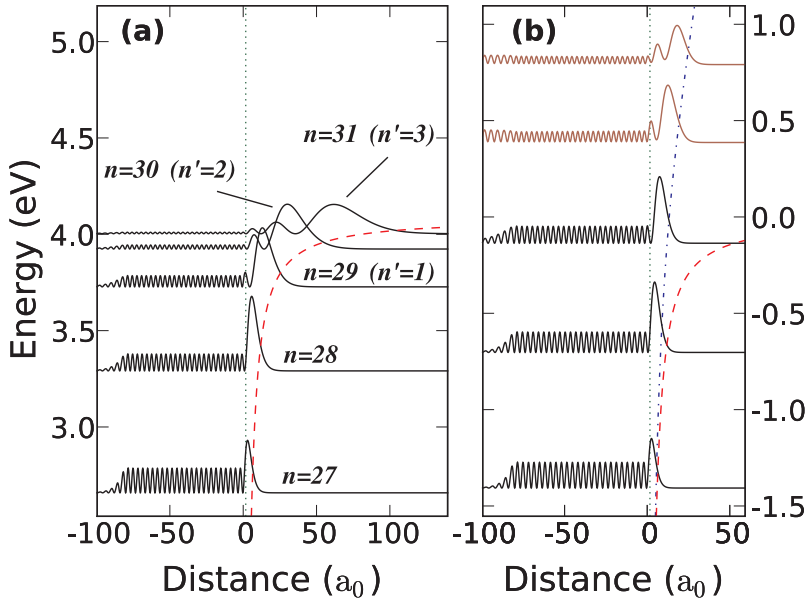

Figure 7.3.: Change of the wave functions of the QWSs in the 15ML-Pb/Cu(111) system under applied electric field. Solid lines represent electronic densities of the QWSs. The principal quantum number n is indicated above each state. The image plane position is denoted by a vertical dotted line. Energies are given with respect to the Fermi (vacuum) level labeled at the left (right) axis. (a) Zero field case. The number in parenthesis indicates the n' - quantum number of the IS with leading contribution to the hybrid QWS-IS state. The image potential at the vacuum side of the Pb film is shown by dashed line. (b) The case of the uniform electric field of strength $\mathcal{E}$= 0.05 eV/a_0. The densities of the quasi-stationary states with energies above Cu(111) projected band gap, and so decaying via one-electron transfer into the substrate, are represented with red color. Dashed line: image potential at the vacuum side of the Pb film. Dashed dotted line: total (image + linear ramp) potential.

QWS-IS character calculated here is very close to the *ab initio* results [116], as well as the experimental data supported by model calculations for the ISs [134].

Thus, the electric field in the junction overrides the image potential. For the pristine metal surfaces, the ISs evolve into the field emission resonances (FERs) with energy quantization given by Eq. (5.44). Similarly, for the Pb overlayer, the states with mixed QWS-IS character evolve into the states with mixed QWS-FER character, as reflected in their wave functions. The WPP results for the wave functions of the QWS in biased STM junction are shown in Fig. 7.3 for the electric field $\mathcal{E}$ =0.05 eV/a_0. Compared to the bare Pb/Cu(111) case, the electronic densities of the high-energy states are pushed by the constant electric field toward the surface. However, partial electron spread from the Pb film into vacuum is preserved. The same features have been reported for the Stark-shifted ISs [171].

The Stark shift of the ISs (which is as strong as 0.3 eV for $n' = 1$ IS at clean Cu(111) surface [137]) shows that for the STM junction under the bias, the phase accumulation model with the vacuum scattering phase described with Eq. (5.33) cannot provide an adequate description of the system. The scattering phase shift $\varphi_{\rm vac}$ at the Pb vacuum interface is rather that of the linear potential barrier given in Eq. (5.45). The discussion of the validity of the latter phase shift for reproducing the FERs has been given in Chapter 5 (Subsection 5.5.2). We would like to emphasize here that the present WPP calculations are performed with the complete potential given by Eq. (7.4) and, therefore, are free from any approximative description of $\varphi_{\rm vac}$.

To summarize, the STS experiment does *not* appear to be noninvasive, as far as the QWSs close to the vacuum level are concerned. Because of the electric field in the STM junction, the energy of these states is raised by the Stark shift. As a result, the QWSs with mixed IS character transform into QWSs with mixed FER character. Both, the energy upshift and change in the wave function would increase the rate of the inelastic decay of the states [171] and, therefore, the linewidth of the structures in dZ/dV and dI/dV spectra. Note that above 4.1 eV with respect to the Fermi level (above the L gap of Cu), the QWSs are in resonance with propagating electronic states of the Cu(111) substrate, in contrast to the idealized model with an infinite barrier considered in Chapter 5. The resonant electron transfer into the substrate constitutes then an additional channel of the QWSs population decay. The effect of this resonant channel on the underlaying quasi-stationary QWSs is discussed in Section 7.5.

7.4. STS spectra I: QWS energies

The constant current dZ/dV curves were calculated for overlayer thicknesses ranging from 4 to 18 ML. The current density was kept constant for all calculations, and it was set to $I = 5 \times 10^{-2}$ nA/Å^2, such that the experimentally measured energy (3.52 eV) of the n =27 peak is well reproduced for the 15-ML Pb film case. This implies a tip-surface distance of $Z = 22a_0$ at the bias $V = 3.52$ eV. It is desirable to fit the results to such a high-bias peak, since the flat tip approximation is expected to perform better at the high-bias than at the low-bias regime. If the effective radius of the tip $R_{\rm eff} = 20$ Å is assumed, the corresponding current through the STM junction is $\mathcal{I} = \pi R_{\rm eff}^2 \approx 63$ nA. The above choice of parameters appears quite reasonable when comparing with existing approaches [115, 120].

The dZ/dV curves obtained for the Pb coverages of 10 ML and 17 ML are displayed in Fig. 7.4 together with experimental STS spectra of Ref. [20]. The QWS energies

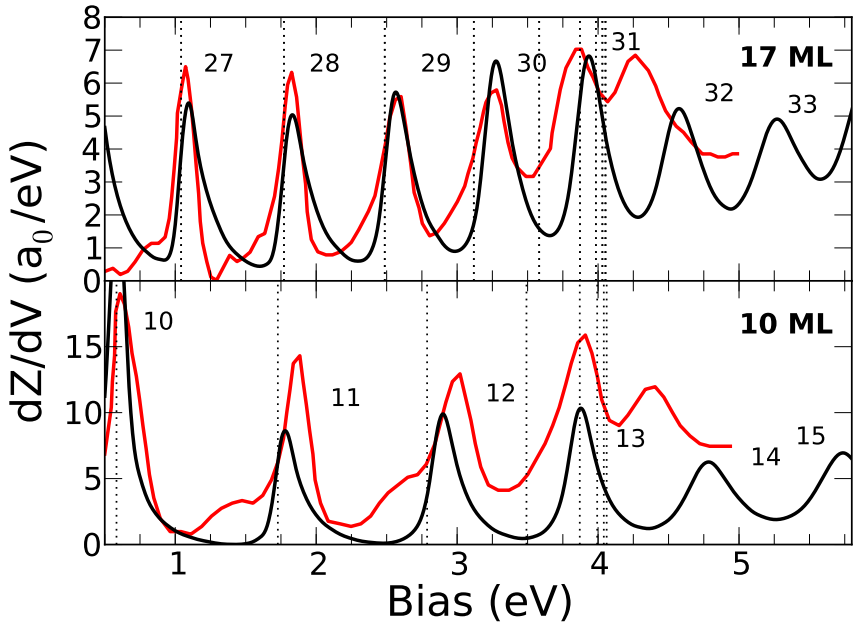

Figure 7.4.: Comparison between calculated dZ/dV curves (black) and experimental spectra (red) by Yang *et al.* [20]. Experimental spectra are re-scaled for the sake of comparison. For further details see the main text. The calculated QWS energies of the bare Pb/Cu(111) system are denoted by vertical dotted lines.

calculated for the bare Pb/Cu(111) without tip are also shown in the figure with vertical dashed lines. We use the labeling n of the spectral peaks according to the principal quantum number of the underlying QWSs obtained from the calculated nodal structure of their wave functions. Note that in Ref. [20] the labels n_{exp} differ from the present definition of n as $n_{\mathrm{exp}} = n - 1$. However, n_{exp} were not directly obtained but were deduced from the modeling of the data with the phase accumulation model. Furthermore, we refer to the thickness of the Pb film with respect to the Cu(111) surface, while in Ref. [20] the thickness is referred with respect to the Pb wetting layer. Thus, e.g., the present 17-ML case has to be compared to the 16-ML result as reported in the experimental work.

With the above remarks, the calculated STS spectra are in good agreement with experimental data for the energies below 4 eV, with respect to the Fermi level of the surface. The flat-tip approximation used here allows us to reproduce experimental energy positions of the resonant features as well as to their widths, including the overall peak broadening with increasing energy. At high energy (bias) above 4.12 eV, i.e., above the L gap of Cu(111), the calculated peaks broaden and loose their intensity. This is linked with opening of the QWSs decay channel via resonant one-

electron tunneling into the Cu(111) substrate. At the same time, the regular energy progression of the calculated peaks is maintained, in contrast to experimental data. The difference between the theoretical and experimental data in the 4–5 eV energy range is directly linked to the Pb band structure, as is discussed in detail in Section 7.7.

The good agreement between theory and experiment for $V < 4$ eV allows us to discuss some issues linked with the tunneling spectroscopy studies of the QWSs.

First, the difference between the energies of the resonant structures in the calculated dZ/dV spectra, E_n^{STS}, and the energies of the QWSs of the bare Pb/Cu(111) system, E_n, sets the energy shift Δ_n^{STS} inherent to the experimental procedure as:

$$\Delta_n^{\mathrm{STS}} = E_n^{\mathrm{STS}} - E_n. \tag{7.7}$$

We show Δ_n^{STS} in Fig. 7.5(a) for the case of the 17-ML Pb film. In full agreement with the discussion presented in the previous section (see Fig. 7.2), the measured peak positions reflect the energies of the QWSs of bare Pb/Cu(111) only for the bias below $\approx$ 2 eV, where Δ_n^{STS} is small. At higher bias the Stark shift modifies the energies of the QWSs. This effect becomes particularly important for the QWSs with mixed IS character close to the vacuum level of the Pb overlayer. Thus, the spectroscopic feature at the vacuum level (4 eV) is associated with the Stark shift of the underlying QWS by 0.4 eV, which is of the same order of magnitude as reported for the first IS at Cu(111) [137].

Second, the peaks in the STS spectra show an additional broadening of 0.2 eV, as compared to the decay rates of the underlying QWSs resonances. A similar result has been reported in the studies of the FERs [120]. The broadening of the spectroscopic features is illustrated in Fig. 7.6. The calculated energy-dependent transmission $T[E, V, Z(V)]$, dynamic transmission $T[V, V, Z(V)]$, and dZ/dV spectrum are presented for the 17-ML Pb coverage case. We recall that $Z(V)$ is defined by the constant current condition. The figure spans the energy range of the $n = 29$ QWS peak (as appears in Fig. 7.4). The $T[E, V, Z(V)]$ has a well-defined Lorentzian profile centered at the resonance energy and a width γ_n corresponding to the inverse lifetime of the $n = 29$ QWS resonance. There is only a minor energy shift and nearly no width change for the bias variations within the resonance. The bias is varied by steps of 0.05 eV, and the precise V value corresponding to each curve is set by the open dot located at $E = V$. Similar to the transmission, the dynamic transmission given by the thick line connecting the $E = V$ points also shows quite a symmetric profile with no additional broadening. At variance, the calculated peak in dZ/dV is asymmetric with a width $\gamma_n' \approx \gamma_n + 0.2$ eV, and a maximum position shifted by $\sim$30 meV. This small energy shift appears nearly

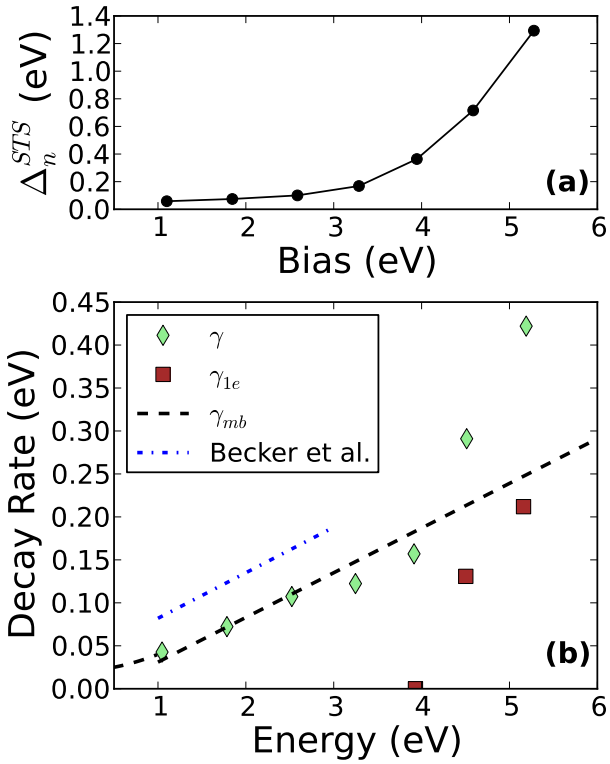

Figure 7.5: (a) Energy shift Δ_n^{STS} of the QWS peaks in the calculated dZ/dV spectra. Δ_n^{STS} is defined with respect to the energies of the QWSs in the bare 17ML-Pb/Cu(111) system. (b) Calculated decay rates γ_n of the QWSs for the same system, as a function of their energy E_n with respect to the Fermi level. γ_n is obtained for the fixed bias V and position of the tip $Z(V)$, where $E_n = V$. We also plot the many-body decay rate $\gamma_{e-\mathrm{ph}} + \gamma_{e-e}$ for the excited states inside the overlayer. The dashed-dotted line represents the linear fit to the QWS linewidths, as deduced from experimental data in Ref. [25].

independent on the QWS under study. It is at the origin of the nonzero onset of Δ_n^{STS} for low bias, as seen in Fig. 7.5.

7.5. STS spectra II: Decay rate of the QWSs

Because of the asymmetric structure of the measured and calculated STS peaks, as well as because of the peak broadening inherent to the STS at high bias, the extraction of the corresponding decay rates is not a trivial task. We have not attempted any transformation of the experimental data of Yang *et al.* in Ref. [20]. The WPP allows a direct extraction of the decay rates γ_n from the calculations performed for the fixed bias $V = E_n$ and fixed position of the tip $Z(V)$. Thus, the Hamiltonian is fixed so that the quasi-stationary states of the system can be rigorously defined. Here E_n is the energy of the quasi-stationary QWS under study. We note that, *a priori*, γ_n comprises several contributions: $\gamma_n = \gamma_{\mathrm{mb}} + \gamma_{1e} + \gamma_{\mathrm{tip}}$. The term γ_{mb} stands for the inelastic many-body decay, γ_{1e} is the rate of the elastic one-electron tunneling into the Cu(111) substrate for the energies above the L gap of Cu(111) at $\overline{\Gamma}$ (i.e., above 4.12 eV), and finally, γ_{tip} is the rate of the elastic one-electron tunneling into the STM tip. Since in

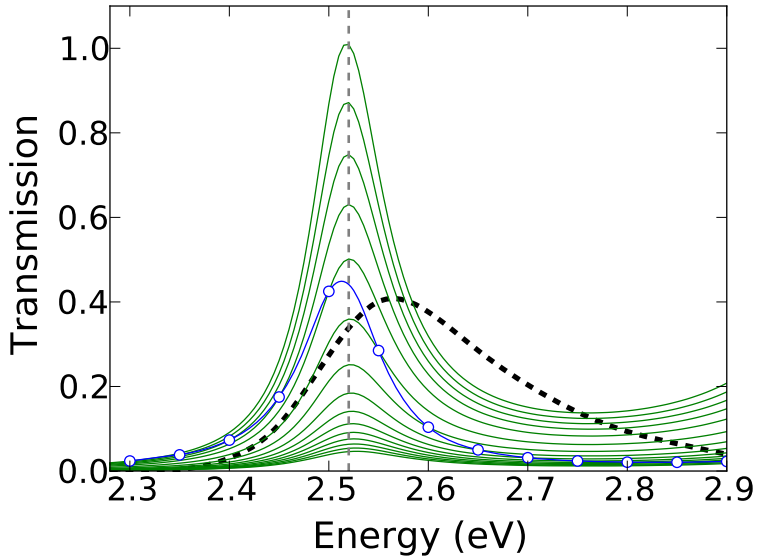

Figure 7.6.: The transmission $T[E, V, Z(V)]$ (normalized to $5 \cdot 10^{-3}$), dynamic transmission $T[V, V, Z(V)]$, and dZ/dV spectrum for the $n = 29$ QWS peak of the 17ML-Pb/Cu(111) system. The calculated transmission (thin lines) is shown as a function of the electron energy for different bias values. The V-value corresponding the each curve is set by the open dot located at $E = V$. The dynamic transmission is given by the thick line connecting the $E = V$ points. The gray vertical dashed line denotes the approximate peak energies in the transmission at $E = 2.52$ eV. The dZ/dV curve (dashed line) has been renormalized for the sake of comparison.

the present conditions the tip-surface distances are such that the transmission is in the 10^{-4}–10^{-3} range, the contribution of the latter decay channel can be safely neglected.

In Fig. 7.5 we show the WPP results for the case of the 17-ML Pb film, together with the decay rates extracted in Ref. [25] from the experimental study of Pb/Ag(111). The difference in the substrate affects the γ_{1e}. However, for the QWSs inside the projected band gap $\gamma_{1e} = 0$, and $\gamma_{\rm mb}$ is determined mainly by the inelastic hot-electron decay in the Pb overlayer, as we have checked with WPP calculations by varying the absorbing potential inside the Cu(111) substrate. Thus, the comparison with experimental data of Ref. [25] is meaningful. The present theoretical results can be well understood on the basis of the wave function penetration arguments often involved in the discussion of the lifetimes of the ISs at surfaces, in the same way as it is done for the QWS-ISs in Chapter 6. At low energies, the wave functions of the QWSs are confined within the Pb overlayer (see Fig. 7.3). The $\gamma_{\rm mb}$ decay rate is then given by the sum of the electron-electron and electron-phonon contributions $\gamma_{\rm mb} = \gamma_{e-{\rm ph}} + \gamma_{e-e}$ to the excited state population decay inside the Pb film. It is directly included in the many-body

absorbing potential (see Chapter 4), and represented by the dashed line in Fig. 7.6. For the energy range between 3 and 4 eV, the QWSs hybridize with FERs. Part of the electron density is moved into the vacuum, reducing the probability of interaction with possible excitations. As a result, the many-body decay rate of the corresponding states becomes smaller than that inside the Pb film. For the energies above 4.12 eV, the one-electron decay channel into the Cu(111) bulk opens. The γ_{1e} decay rate rapidly increases when the energy rises above the band-gap threshold. The QWSs acquire an additional broadening, and the total width of the resonances is brought into the 0.3–0.4 eV range.

7.6. STS results for different Pb coverages

Figure 7.7 summarizes our results on the STS of the Pb/Cu(111) system. The energies of the calculated QWS peaks in the dZ/dV spectra are presented as a function of overlayer thickness for Pb coverages ranging from 4 to 18 ML. Theoretical data are compared with STS experiments [20]. As a reference, we also show the calculated energies of the QWSs in the bare Pb/Cu(111) system (no tip-induced perturbation), as well as the QWSs energies obtained from the two-photon photoemission (2PPE) experiments [165]. Our calculations are in agreement with available experimental data for the energies below ~ 4 eV. The correspondence between the calculated and measured STS peak positions is particularly remarkable for coverages above 11 ML. When comparing the STS data with the QWS energies of the bare Pb/Cu(111) system, the importance of the Stark shift due to the applied bias, as discussed in the previous section, is evident for the high energy states. We stress here that this effect has not received enough attention in the previous analysis of the experimental STS data on Pb overlayers [20, 25].

At low coverages the calculated spectroscopic peak positions are systematically below the experimental data. This cannot be the deficiency of the present modeling of the STM junction since all the QWSs, including those close to the Fermi level, are concerned. Indeed, the low-energy QWSs are well-localized inside the overlayer and thus are not sensitive to the potential above the Pb surface. We tentatively attribute the difference between calculated and measured data to the present DFT-LDA modeling of the bare Pb/Cu(111) system. It results in the underestimation of the energies of the QWSs at low coverages, as has been discussed by Ogando *et al.* [18]. The effects such as the specificity of the wetting layer as compared to the next layers and oscillations, both in work function and Pb interlayer spacings with overlayer thickness, determines the precise value of the QWS energies. In fact, the good agreement between theoretical

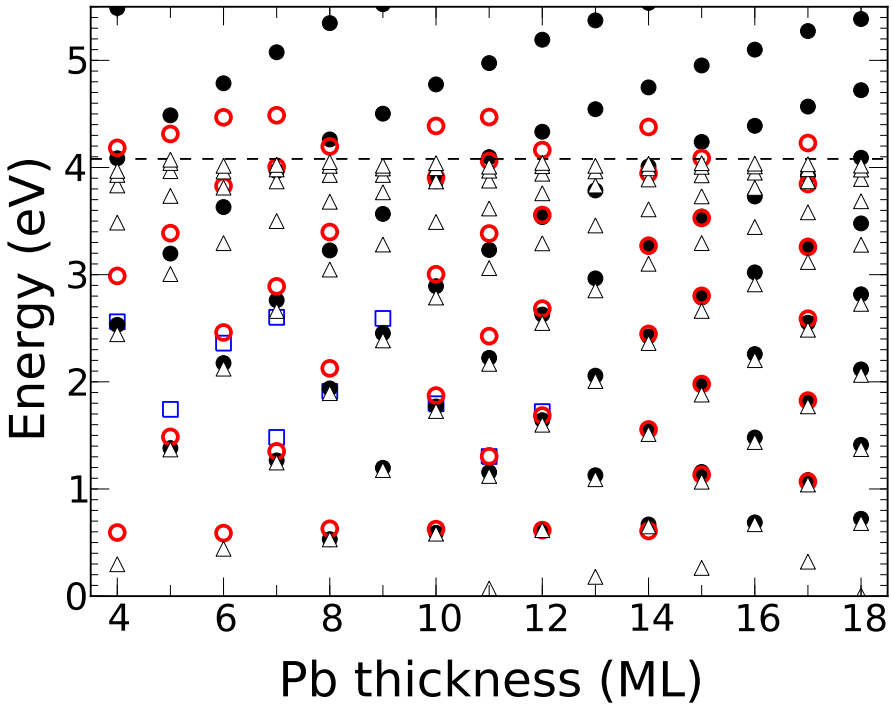

Figure 7.7.: QWS energies at $\overline{\Gamma}$. Results are shown as a function of overlayer thickness. Full dots: calculated energies of the QWS peaks in the dZ/dV spectra. Open dots: experimental QWS peak positions obtained from the dZ/dV spectra of Ref. [20]. Open squares: the two-photon photoemission data [165]. Theoretical results for the bare Pb/Cu(111) system (without tip) are shown with open triangles. The horizontal dashed line denotes the vacuum level (work function $\Phi = 4.08$ eV).

and experimental data above 11 ML coincides with coverages having converged work function, i.e., that of Pb(111) within 0.05 eV (see also Refs. [183] and [22]).

7.7. Effect of the realistic band dispersion of Pb(111) along Γ-L

As follows from the results reported in Fig. 7.7 (see also Fig. 7.4), above 4 eV the theoretically calculated peaks in the STS spectra, and thus, the underlying QWSs continue a regular progression towards higher energies E_n with increasing principal quantum number. In contrast, the experimental data show the energy separation $E_{n+1} - E_n$ decreasing with n in this energy range. Finally, measured QWSs peaks level off at 4.6 eV energy. In some way, the energy dispersion of the experimental STS

peaks resembles that of the ISs that level off at vacuum level. This interpretation was used by the authors of Ref. [20]. Similarly, authors of Ref. [25] analyzed their data within the phase accumulation model with the scattering phase at the Pb/vacuum interface given by Eq. (5.33) in Chapter 5. Thus, it has been assumed that an electron moving in the vacuum region of the STM junction is subject to the image potential only. However, according to our results this explanation does not hold.

First, it places the vacuum level at 4.6 eV, which is inconsistent with experimental data and *ab initio* calculations that report a Pb work function of 4.25 eV at most [22, 63, 183–186]. The work function oscillations with film thickness cannot explain this difference. These are of the order of ±0.1 eV for thin films, and become much smaller with increasing coverage [22, 183].

Second, and most important, it follows from the present results that the electric field in the STM junction destroys the ISs-like series causing the Stark energy shift of the QWSs. This effect is well documented in the literature on the example of the ISs transformation into FERs [115, 116, 120, 134–137, 179]. The vacuum potential barrier (for energies close to the vacuum level and above) becomes essentially a linear ramp potential as known for FERs, with the corresponding scattering phase shift given by Eq. (5.45) (see also Subsection 5.5.2 for the derivation of this phase shift and the discussion of its suitability for describing the FERs).

The question naturally arises: why the theoretical model does a good job in describing the experimental data up to ≈ 4 eV with respect to the Fermi level and fails for the higher energies? This cannot be the deficiency of the modeling of the STM junction. Indeed, reproducing the peaks in the STS spectra up to ≈ 4 eV implies reproducing the Stark shift, and so the potential in the junction.

At this point it is useful to recall Eq. (5.25) that defines the energies of the quantized states in the framework of the phase accumulation model. It is reproduced here for convenience (with slightly different notation):

$$2\pi n = 2k(E_n)D + \varphi_{\mathrm{Cu}}(E_n) + \varphi_{\mathrm{vac}}(E_n). \tag{7.8}$$

Provided the nearly free-electron Cu(111) band structure in this energy range, the 4.6 eV "anomaly" is not linked with $\varphi_{\mathrm{Cu}}(E_n)$. It can be then reproduced by the energy dependence of the vacuum phase shift φ_{vac}, as done in Ref. [20]. Alternatively, it can be associated with the Pb(111) band structure $k(E_n)$ along the direction perpendicular to the film surface. Since the former explanation was ruled out, it is reasonable to expect that the disagreement between calculated and experimental data is directly related to the present free-electron description of the overlayer. In the limit of the bulk Pb, the

DFT-derived potential for the Pb film results in the

$$E = k^2/2 - U_0 \tag{7.9}$$

energy dispersion of the states with k along Γ-L direction and Pb band bottom $U_0 \approx 13.55$ eV. When compared to the *ab initio* band structure of Pb(111) [29, 61, 63] (see Fig. 2.2), this free-electron model breaks exactly within the 4.5 eV energy range where different Pb bands experience avoided crossing. The *ab initio* result shows $dE/dk \to 0$ for $k \to \Gamma$, which would explain the observed experimental trend and the difference with the calculated data.

The direct evidence of the Pb(111) band structure effect is obtained with the following data analysis based on the phase accumulation model [25]. Assume that for the two overlayers with thickness D_1 and D_2 one can find the respective spectroscopic peaks E_{n_1} and E_{n_2} such that $E_{n_1} = E_{n_2} = E$. Then, subtracting Eq. (7.8) for the (D_1, n_1)-case from that for the (D_2, n_2)-case allows, within the first approximation, to remove the contribution of the scattering phase shifts due to the interfaces. The parent bulk band dispersion along Γ-L can be then obtained as:

$$k(E) = \pi(n_2 - n_1)/(D_2 - D_1). \tag{7.10}$$

However, when performing constant current spectroscopy for the overlayers with different thickness $D_2 > D_1$, the tip-surface distance Z is not the same when probing the states at the same energy. This is because the number of the electronic states to tunnel to is higher for the thicker overlayer, which has to be compensated with increasing Z. For the same bias, the electric field in a junction is then smaller for D_2, and the cancelation of the vacuum phase shifts is an approximation. To assess the validity of this approximation, we have first transformed the calculated data according to Eq. (7.10). The STS peaks were assumed to have the same energy if they fall within a 40-meV energy window: $|E_{n_1} - E_{n_2}| < 40$ meV. The extracted band dispersion is shown in Fig. 7.8(a). It appears very close to the free-electron parabola given by Eq. (7.9), so that the $k(E)$ extraction procedure holds.

Having checked the validity of the method outlined above, we have applied it to the experimental data of Ref. [20]. The subsequent obtained Pb(111) band dispersion along Γ-L is presented in Fig. 7.8(b), together with the *ab initio* DFT-LDA relativistic calculations of the Pb band structure which has been shifted +0.4 eV in order to fit the photoemission data of Ref. [63] below the Fermi level. We also plot the $k(E)$ derived by the same method for Pb/Ag(111) as published in Ref. [25]. In sheer contrast with the free-electron parabola, the *ab initio* band dispersion saturates at Γ point for $E - E_F = 5.4$ eV and for $k = 1.161 a_0^{-1}$ (reciprocal lattice vector). The dispersion relation

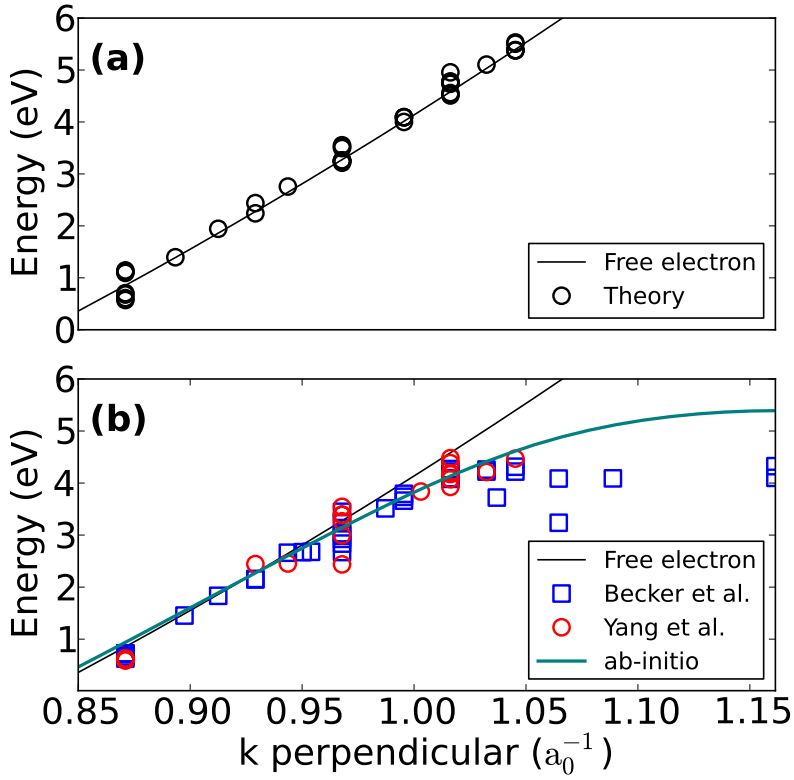

Figure 7.8.: Electronic bulk Pb band structure along symmetry direction $\Gamma - \mathrm{L}$ in the extended representation. The thin solid curve in both panels corresponds to the free-electron parabolic dispersion given by Eq. (7.9). (a) Open dots: dispersion derived with Eq. (7.10) from calculated energies of the STS peaks (see Fig. 7.7). (b) Open dots: dispersion extracted from experimental data reported for Pb/Cu(111) in Ref. [20]. Rectangles: dispersion extracted from experimental data reported for Pb/Ag(111) in Ref. [25]. The relativistic ab-initio DFT-LDA dispersion of the p_z band of bulk Pb [29,61] is represented with thick blue curve.

extracted from STS experiments agrees with *ab initio* results and photoemission data. This fully validates our interpretation of the experimentally observed trends in the QWS series at high bias, as a direct consequence of the realistic band structure of Pb(111). Obviously, it cannot be reproduced with the present approach based on the free-electron modeling of Pb overlayer, which explains disagreement between calculated and measured STS peak positions at bias above 4 eV.

Recently, a larger set of the STS spectra for Pb/Cu(111) has been shown with bias range extending up to 9.0 eV [187,188]. The FERs with energies independent of the Pb film thickness were reported for the bias above 5 eV. According to the model results

of the present thesis, the free-electron-like description of Pb would not explain the experimental data, since we obtain thickness-dependent peak energies at high bias.

The detailed discussion of the experimental results for the bias above 5 eV is beyond the scope of this thesis, thus it is left as an open question: The nontrivial Pb band structure above 4.5 eV, as shown in Fig. 2.2, should be at the origin of the observed effects. Several possible explanations, all based on the Pb band structure effect, can be advanced: (i) increased surface reflectivity in the corresponding energy range, (ii) flat dispersion of the underlying Pb bands, (iii) high electron transmission through the Pb/Cu(111) interface above the projected band gap of Cu(111) so that the electron does not return to the Pb/vacuum interface and all confinement is at the vacuum side (a resonant state).

7.8. Summary

We have performed a theoretical study of the constant current scanning-tunneling spectroscopy of thin Pb films on a Cu(111) substrate. The dZ/dV spectra have been calculated for the 4–18 ML film thickness range. The tip-sample system is represented within the flat-tip approximation, so that well-developed approaches for modeling the STM junction [115] could be applied.

Within the studied range of overlayer thicknesses, the energies of the calculated peaks in the STS spectra reproduce the experimental data for bias below 4 eV. Particularly remarkable agreement with respect to the energies, widths, and relative intensities of the STS peaks, is obtained for thicknesses above 11 ML, i.e., in the range where the quantum size effects on the Pb film work function and the effect of the wetting layer can be considered as negligible.

Simultaneous calculations of the (i) dZ/dV spectra, (ii) quasi-stationary QWSs in the tip-sample system at fixed tip-sample distance and bias, and (iii) QWSs of bare Pb/Cu(111) without the tip have been performed. This allows detailed discussion of the physics underlying experimental observations. It appears that only low-energy QWSs are unperturbed by the tip. At high bias, the tip-induced Stark shift determines the energies of the QWSs and so the peaks in the STS spectra. Here, the effect of the electric field in the junction is similar to that often evoked in discussion of the transformation of ISs into FERs [116, 136]. Indeed, the electronic density of the high-energy QWSs in the bare Pb/Cu(111) system is shifted from the inside Pb film into the vacuum, indicating partial IS character (see also Chapter 6).

Good agreement between the calculated and measured data in the energy range corresponding to the free-electron-like dispersion of the Pb band along Γ-L direction validates the present theoretical approach. The departure of the experimentally measured energies of the STS peaks from the theoretical results above 4 eV bias is then sound. It reflects the departure of the bulk Pb band structure along Γ-L from free-electron parabola. Comparison between the *ab initio* band structure of Pb, the two-photon photoemission data, and $k(E)$ dispersion curves extracted from experimental data of Refs. [20] and [25] fully confirms the above interpretation. Thus, the STS performed at different coverages can be used as a complementary tool to inverse photoemission to probe the dispersion of the bulk bands of the overlayer material at energies well above the Fermi level.

Chapter 8

Conductance and clustering of Na nanocontacts

8.1. Introduction

Owing to fundamental and practical interest, metallic nanowires are a subject of considerable experimental and theoretical effort [4]. Not only is the nanowire a natural component of molecular electronics devices, but it can also serve as an efficient chemical and biological sensor [5]. From the fundamental point of view, when drawn to the atomic dimension, nanowires exhibit quantum conductance behavior [13, 189, 190], thus offering an excellent playground for theoretical developments. Nowadays, systematic studies of electronic and mechanical properties of nanocontacts are possible thanks to the mechanically controllable break junction (MCBJ) and scanning tunneling microscopy experiments [4, 191]. In particular, MCBJ experiments (see Fig. 8.1) are very well suited for conductance measurements, providing histograms for large sets of individual contact-breaking events as the basic input for further analysis. For simple metals, the conductance curves upon stretching show clear plateaus at values close to $nG_0 = n2e^2/h$ (n is an integer) followed by more or less abrupt jumps to lower conductance plateaus [12, 192]. The appearance of plateaus is considered as a fingerprint of a stable nanowire structure in the contact neck, whereas abrupt conductance jumps are associated with instabilities and consequent sudden rearrangements of the neck. Thus, the electronic (atomic) shell structures of nanowires could be demonstrated with this technique [13, 183, 189], where the stable nanowire configurations are characterized by

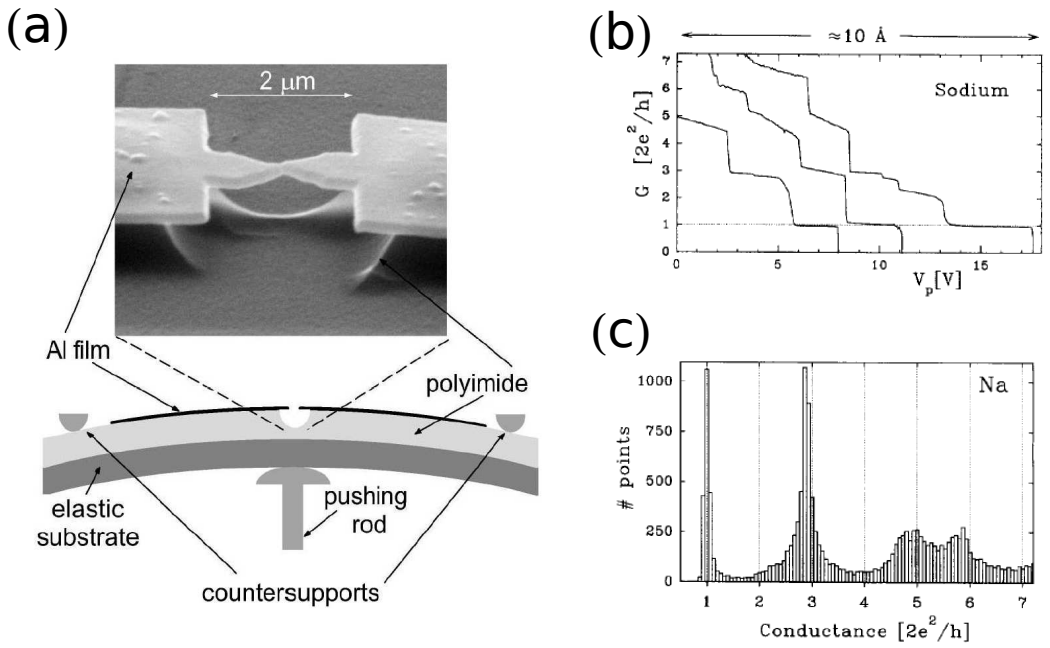

Figure 8.1.: (a) Micrograph and sketch of a MCBJ experimental setup [194] (b) Typical conductance curves of sodium contacts as a function of the voltage pulling the contact leads apart [192]. (c) Histogram of conductance values obtained for a large set of sodium conductance curves [192].

"magic radii" in analogy to the well-known "magic numbers" of abundance in metal clusters of different sizes [193].

Although great progress has been made in observing new structures in high-resolution transmission electron microscopy [190,195], the structural details of nanowires and their dynamical properties are far from being well understood. From the theoretical side, different approaches have been used to elucidate the atomistic rearrangements taking place during the breakage of a nanowire. Classical and semiclassical methodologies have been used along with *ab initio* calculations based on density functional theory (DFT) [35, 38–40, 42–45, 196–205]. The latter, in particular when combined with electronic transport calculations [35, 42, 204, 205], provides the most advanced description of the system, allowing direct connection with experimental data. However, DFT-based calculations are computationally extremely demanding, which severely limits the number of atoms (the size of the break junction) that can be addressed. Molecular dynamics (MD) remains then as a useful alternative if one wants to explore large sets of possible configurations [38].

Another way of tackling the complex problem of the evolution of the geometry and conductance of stretched nanowires is to reduce the level of complexity in the de-

scription of the atomic structure of the system and to use DFT methodology, but based on jellium models for the nanowire material. Despite its apparent simplicity, such an approach can often capture the main physics of the process at hand, as has been proven with many studies of metal nanostructures and metal surfaces [206], including the representation of electrodes in conductance studies [207]. Among metallic nanowires sodium is the prototype system for the jellium description, allowing one to efficiently explore various structures [4, 208, 208]. The nearly free character of sodium valence electrons fully validates the applicability of the jellium approach, as shown in a number of works [41, 208, 208–210] based on comparisons with *ab initio* studies and experimental data (see also Fig. 8.3). Thus, in full agreement with first-principles molecular dynamics simulations [38–40], Ogando *et al.* reported the formation of clusterlike arrangements of atoms, preceding the breakage of a stretched nanowire [41]. In that work the ultimate jellium (UJ) was applied. It is worth mentioning that, as far as closed-shell sodium clusters are concerned, the jellium model gives adequate description of many physical properties [211]. As for the nanowire breakage, the UJ approach can be interpreted as giving directly some kind of average configuration, so that large MD statistics is not needed.

In this chapter we investigate how the conductance of an elongated Na nanowire is affected by the formation of a stable clusterlike arrangement of atoms in the break junction nanocontact [172]. We use a combined approach where the nanowire breakage is simulated with self-consistent electronic structure calculations within the density functional theory. The self-consistent calculations provide an input for the follow-up wave packet propagation (WPP) study of the ballistic electron transport through the break junction.

We find that clustering leads to delayed and rounded conduction jumps upon the stretching of the nanowire. The results are analyzed in terms of the evolution of the transmission resonances originating from the cluster-localized electronic states. The situation at hand then closely corresponds to the electron transport through molecular junctions studied in great detail in the context of molecular electronics [4, 212–217], where the cluster is playing the role of the molecular object. According to our results to be discussed, the resonant character of the transmission reveals itself particularly clearly in the bias voltage dependence of the differential conductance, suggesting experimental ways to evidence the presence of clusters in the break junction. It should be pointed out that the main conclusions and results reported in this chapter are not determined by the specific choice of the nanowire material (Na), but rather by the very fact of the clustering at the break junction. The latter phenomenon is of quite general

nature, as it not only happens for the stretched Na nanowires [38–41] but has also been reported for gold nanowires [42–45].

8.2. Breakage of Na nanowires

The DFT calculations are based on the UJ description of nanowires (see Chapter 2 for details on the DFT method and its implementation, together with the UJ model). Within the UJ model the background positive charge is fully relaxed in shape and density, so that it equals at every point the electron density, and the shape of the system is obtained self-consistently. In this way, it is possible to mimic the rearrangements of atoms during the elongation and breakage of a nanowire with MCBJ techniques, for example. The system considered in the simulations is sketched in Fig. 8.2. It consists of two cylindrical UJ leads (we restrict the shapes of the nanowires to those having axial symmetry), whose potential is frozen after self-consistent calculations for an infinite wire of stable magic radius R. Rearrangements are only allowed in the central part (break junction) between the leads, which is deformable upon stretching of the nanowire. The shape in this region is updated in a self-consistent process.

Setting the size L of the deformable part allows one to define the number of electrons N_e in the deformable constriction. This is a key quantity as it determines whether clusterlike structures are or are not formed in break junctions [41]. We note that the procedure of constraining the number of electrons in the deformable part is equivalent to the usual methodology followed in *ab initio* approaches, where only some atoms are allowed to relax between the frozen leads.

The results reported in this chapter are obtained for the breakage of a nanowire of radius $R = 10.7a_0$. This is a typical example of a stable Na nanowire structure, allowing one to study the change of the conductance both in the presence and in the absence of cluster-derived structures in the deformable constriction during the stretching process.

We find that for the nanowire of radius $R = 10.7a_0$, a minimum of seven initial electrons in the deformable constriction is needed to enable the appearance of the eight-electron cluster structures in the break junction. The "extra" electron density is supplied in this case by the leads. In Fig. 8.2, we represent the two different evolutions of the charge density of the systems with $N_e = 5$ and $N_e = 10$ electrons in the corresponding initial deformable constrictions, which will be used as representative examples throughout this chapter (we refer from now to these systems as $5e$ and $10e$, respectively). Two fundamentally different breakage patterns are observed with the

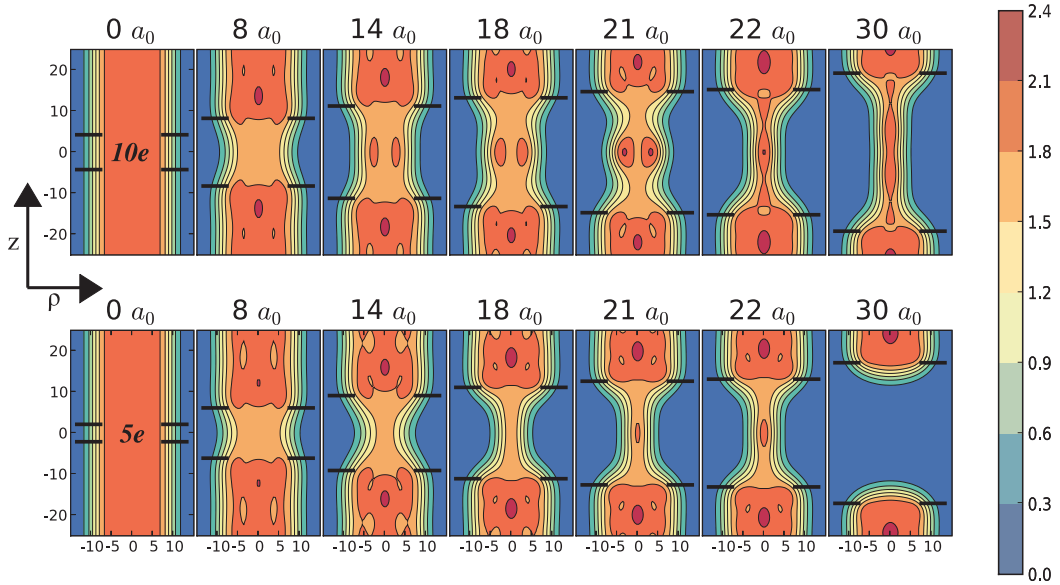

Figure 8.2.: Snapshots of the electron charge density for elongations $\Delta L = 0$, $8a_0$, $14a_0$, $18a_0$, $21a_0$, $22a_0$, and $30a_0$ during the stretching of a nanowire of magic radius $10.7a_0$. The charge density values in the color bar are multiplied by a factor of 1000. The figures at the top (bottom) correspond to the simulations with ten (five) electrons initially in the deformable constriction. The deformable constriction is delimited by the horizontal marks. The $10e$ system is broken at $\Delta L = 31a_0$

appearance of cluster-derived structures in the $10e$ system at elongations from $14a_0$ to $21a_0$, just before the "monatomic chain" configuration stage. In what follows we shall focus on the consequences of these two breakage patterns on the conductance curves.

8.3. Conductance calculations: WPP method

As already shown by Ogando *et al.* in Ref. [41], the finite size of the nanowires of Fig. 8.2 determines their conductance. This is directly linked with the number of electronic subbands allowed by the effective radius of the wire in the center of the constriction. While clustering in the break junction was reported in Ref. [41], no effect of the cluster derived structures on the conductance was observed. For the $R = 10.7\,a_0$ system, three sharp conductance jumps were reported as a function of the nanowire stretching ΔL. These results were obtained within the quasiclassical Wentzel-Kramers-Brillouin (WKB) approach used in Ref. [41] for the calculation of the electron transmission through the junction. In the following sections, these results are revisited within the

WPP approach, which in principle provides the exact one-electron elastic transmission probabilities entering the Landauer-Büttiker formula (4.118). Thus, the effective one-electron potential obtained in the DFT study is used in the WPP calculation of the evolution of the conductance curves upon elongation. The details of the WPP technique are found in Ch. 4, however, some specific equations are quoted here for convenience.

In the asymptotic regions far from the deformable constriction the nanowire potential is a function of only the ρ coordinate: $V = V(\rho)$. The electron confinement in the ρ direction perpendicular to the nanowire axis leads then to a series of quantized states $\phi_n^m(\rho)$ with energies E_n^m:

$$\left[-\frac{1}{2\rho}\frac{\partial}{\partial\rho}\rho\frac{\partial}{\partial\rho} + \frac{m^2}{2\rho^2}\right]\phi_n^m(\rho) = E_n^m\phi_n^m(\rho). \tag{8.1}$$

Tables 8.I and 8.II contain the energies E_n^m of the transverse states obtained in the present calculations for the two nanowire radii of $10.7a_0$ and $7.7a_0$. The second case appears useful for the discussion on the evolution of the conductance under the stretching process (see the next section). The energy is given with respect to the Fermi level of the undistorted Na nanowire. Notice that the $\pm m$ states are degenerate.

In order to obtain the conductance of the system, one is interested in the energy-dependent transmission $T_{nn'}^m(E)$ and reflection $R_{nn'}^m(E)$ coefficients describing the ballistic electron transport through the deformable constriction. The labels n and n' refer here to the asymptotic initial (incident) and final (reflected or transmitted) channels, respectively. Note that this label pair corresponds to the μ for the incident channel and ν for the transmitted (or reflected) one, used in the Subsections 4.4.2 and 4.4.3, devoted to the electron wave packet scattering of Chapter 4. In the discussion below, for the simplicity of the presentation, we also use the (m, n) labeling of the channels. An asymptotic channel is described by the wave function

$$\Phi_n^m(\rho, z) = \frac{1}{\sqrt{2\pi}}e^{ikz}\phi_n^m(\rho). \tag{8.2}$$

It corresponds to an electron of a given energy $E = E_n^m + k^2/2$ propagating along the nanowire in the z direction and confined in the ρ direction. The (m, n) channel is open when $E > E_n^m$.

The $T_{nn'}^m(E)$ and $R_{nn'}^m(E)$ coefficients are calculated within each m subspace from the time-dependent solution $\psi_m(\rho, z, t)$ to Eq. (4.87) (with the DFT-derived one-electron effective potential $V = V_{\text{eff}}$), propagated as described in Section 4.6 and using the amplitude method with virtual detectors, as explained in Subsection 4.4.2. Finally, the

Table 8.I.: Transverse eigenenergies E_n^m for the $R = 10.7a_0$ Na nanowire (up to 1.5 eV). The results are given in eV with respect to the Fermi level.

	$n=1$	$n=2$	$n=3$
$m=0$	−2.58	−0.62	1.28
$\|m\|=1$	−1.75	0.42	
$\|m\|=2$	−0.79	1.30	
$\|m\|=3$	0.25		
$\|m\|=4$	1.30		

Table 8.II.: Transverse eigenenergies E_n^m for the $R = 7.7a_0$ Na nanowire (up to 1.5 eV). The results are given in eV with respect to the Fermi level.

	$n=1$	$n=2$
$m=0$	−2.30	0.39
$\|m\|=1$	−1.01	1.36
$\|m\|=2$	0.34	

zero-bias conductance (see Section 4.7) is obtained with the Landauer-Büttiker formula

$$G = G_0 \sum_{m,n,n'} T_{nn'}^m (E = E_F), \tag{8.3}$$

where E_F stands for the Fermi level energy, and the summation runs over the open channels. From Table 8.I it follows that, for the nonstretched perfect $10e$ nanowire, $G = 6G_0$, and it is determined by the $(m = 0, n = 1)$, $(m = 0, n = 2)$, and doubly degenerate $(m = \pm 1, n = 1)$ and $(m = \pm 2, n = 1)$ channels. Indeed, for the uniform (undeformed) wire $T_{nn'}^m = \delta_{nn'}$, with $\delta_{nn'}$ being the Kronecker delta symbol.

8.4. Conductance during nanowire breaking

The calculated change in conductance during the nanowire stretching is shown in Fig. 8.3 for the $5e$ and $10e$ prototype breakages (see Fig. 8.2). It follows from the present results that, at the initial stages of the elongation, the conductance change from $6G_0$ to $3G_0$ happens in a similar way in both systems. As well, inspection of

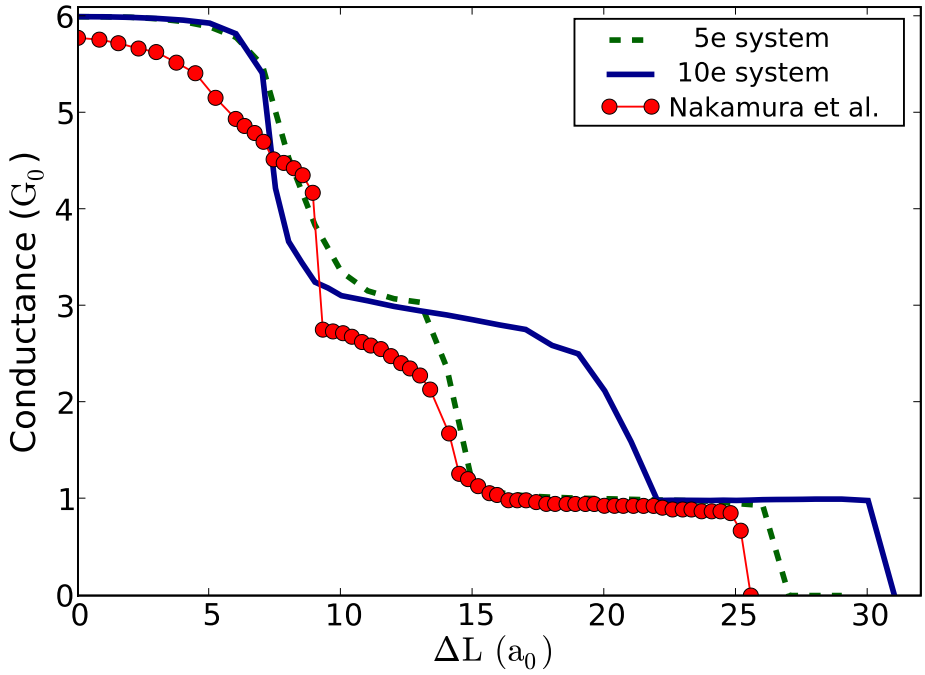

Figure 8.3.: Calculated conductances as a function of the nanowire elongation ΔL. The results for $10e$ and $5e$ systems are shown, together with *ab initio* data by Nakamura *et al.* (Ref. [35]).

Figs. 8.3 and 8.2 shows that the final $G = G_0$ plateau is related in both systems to the existence of the monatomic chain supported between the metal leads. However, two different behaviors are distinguished in the change from the $G = 3G_0$ to the $G = G_0$ plateau. Specifically, in the breakage of the $10e$ system the conductance $G \simeq 3G_0$ is maintained over a much broader range of nanowire elongations, as compared to the $5e$ case. As follows from Fig. 8.2, this is exactly the region of the elongations where clustering happens for the $10e$ system. We thus tentatively attribute the difference in the conductance change from $3G_0$ to G_0 for the $5e$ and $10e$ systems to the formation of a cluster structure in the break junction in the $10e$ case.

The (red) dots in Fig. 8.3 show the results of *ab initio* calculations performed by Nakamura *et al.* [35] within the supercell geometry. The fact that no clustering was reported in Ref. [35] might be explained by the limited size of the supercell. The *ab initio* and present $5e$ results are in agreement with respect to the nanowire elongations, corresponding to the conductance steps and the conductance values at the plateaus which reflect the quasidegeneracy of the transverse eigenstates. This shows that the jellium model allows adequate description of the system. We return to the comparison between the present and *ab initio* calculations in Section 8.7.

8.5. Conductance channels

To get further insight into the calculated change in conductance with elongation, we have presented in Fig. 8.4 the decomposition of the conductance curve into different (m, n) incident channels, defined as:

$$G_n^{|m|} = \alpha_{|m|} G_0 \sum_{n'} T_{nn'}^{|m|}(E = E_F). \tag{8.4}$$

The transmission probabilities are summed over all possible final states so that $G_n^{|m|}$ represents the contribution of the nth incident channel within $\pm m$ symmetry to the total conductance. The $\alpha_{|m|}$ coefficient (1 for $m = 0$, and 2 otherwise) accounts for the degeneracy of the $\pm m$ states.

As follows from Fig. 8.4, the initial decrease of the conductance from $6G_0$ to $3G_0$ for the nanowire elongation $\Delta L = 8a_0$ is linked with the drop of the transmission for the $(m = 0, n = 2)$ and doubly degenerate $(m = \pm 2, n = 1)$ incident channels in both $10e$ and $5e$ cases. For this elongation range the break junction forms a neck, which can be approximately described as a portion of the nanowire of magic radius $R = 7.7a_0$ smoothly attached to the $R = 10.7a_0$ leads. Assuming the adiabatic approximation [4] to be valid in the present case (i.e., that the transverse quantum number n is preserved upon propagation through the junction), from Tables 8.I and 8.II one concludes that transmission at the Fermi energy is only possible for the $(m = 0, n = 1)$ and $(m = \pm 1, n = 1)$ incident channels. The E_2^0 and $E_1^{\pm 2}$ energies rise well above the Fermi level for the $R = 7.7a_0$ nanowire, forming an efficient tunneling barrier for electrons arriving from the $R = 10.7a_0$ leads. The corresponding channels are then closed.

The validity of the adiabatic approximation in the present case stems from the nearly diagonal structure of the calculated transmission matrix $T_{nn'}^{|m|}(E)$. In this respect the (m, n) channels closely correspond to the conductance eigenchannels [4,218,219]. However, the adiabatic approximation breaks down for values of the electron energy or the nanowire elongation for which the overall transmission for the given incident channel becomes small. Thus, e.g., the $(m = 0, n = 2)$ channel is never extinguished completely. G_2^0 reaches the $\sim 0.03G_0$ minimum at $\Delta L \approx 15a_0$ and, during the following stretching, it slightly increases to $\sim 0.05G_0$ until complete breakage occurs. It follows from our results that for $\Delta L > 14a_0$, G_2^0 is entirely given by the nondiagonal $T_{21}^0(E = E_F)$ matrix element. Thus, the transmission is due to the interchannel coupling between the $(m = 0, n = 2)$ and $(m = 0, n = 1)$ channels. In accordance with the principle of detailed balance [141] and, because of the mirror symmetry of the system, we also find that $T_{21}^0 = T_{12}^0$, i.e., an electron incident at the break junction within the $(m = 0, n = 1)$

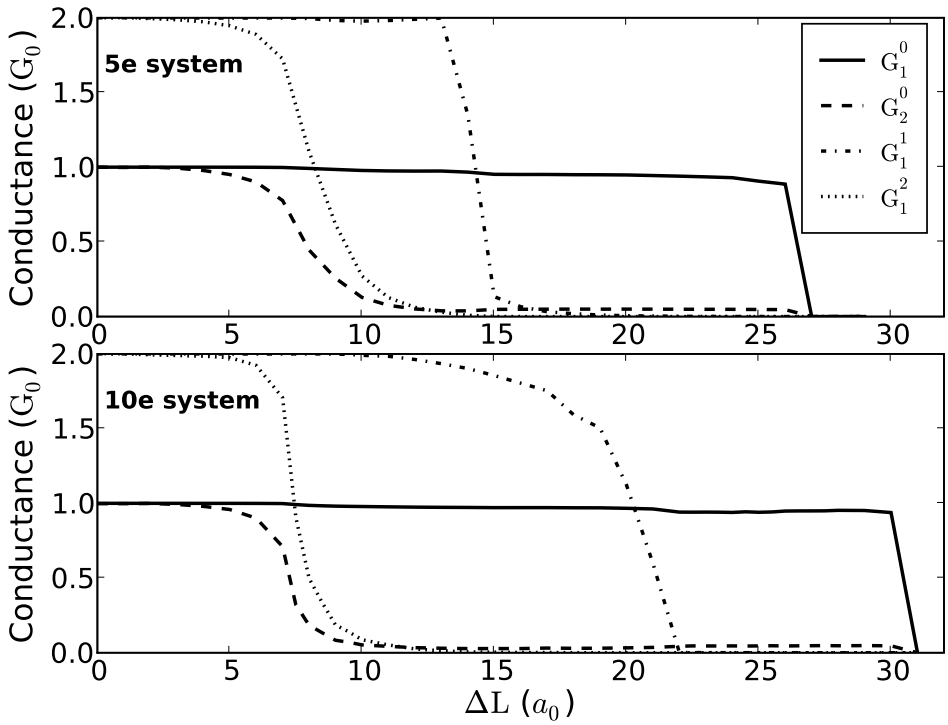

Figure 8.4.: Contributions of different incident channels to the total conductance $G_n^{|m|}$ [see Eq. (8.4)] as a function of the nanowire elongation ΔL. The upper (lower) panel corresponds to the simulations with five (ten) electrons initially in the deformable constriction.

channel has a nonzero probability to be transmitted into the $(m = 0, n = 2)$ subband. This has been also used to check the accuracy of the calculations.

The final $G = G_0$ conductance plateau is mainly due to the transmission within the incident $(m = 0, n = 1)$ channel [there is also a small contribution of the $(m = 0, n = 2)$ channel, as discussed above]. During this final stretching stage, a monatomic UJ wire of average radius $R = 4.5a_0$ is formed, as shown in Fig. 8.2. This monatomic wire is broken at the elongation $\Delta L = 27a_0$ for the $5e$ system and at $\Delta L = 31a_0$ for the $10e$ system. During the monatomic configuration of the neck, the conductance is in the range of $0.98G_0$–$1.0G_0$, which is in good agreement with published *ab initio* conductance data of suspended monatomic chains [35–37].

8.6. The eight-electron cluster

Let us now turn to the detailed discussion of the conductance curves in the $14a_0 \leqslant L \leqslant 21a_0$ elongation range, where the clustering happens for the $10e$ system (see Fig. 8.2). We argue that it is the formation of the cluster in the break junction for the $10e$ system that is responsible for the shape of the conductance change from $G = 3G_0$ to $G = G_0$, as calculated in the present system. The cluster in the break junction appears particularly clear in the $\Delta L = 21a_0$ panel of Fig. 8.2. The analysis of the cluster charge from the calculated electronic density shows that it is close to 8, i.e., the break junction represents the nearly spherical $8e$ magic cluster smoothly attached to the $R = 10.7a_0$ leads.

The situation at hand then closely corresponds to the case of a molecule attached to two metal electrodes, the problem currently studied in the field of molecular electronics [4, 213–217]. Intuitively, the electron transmission through the junction should show resonant structures corresponding to the transient trapping of ballistic electrons inside the cluster. On the other hand, resonances can be seen as discrete cluster states which are broadened because of the coupling to the continua of the propagating electronic states inside the leads [213, 214]. Table 8.III lists the lowest energy levels of the free-standing spherical $8e$ cluster, as obtained with the present UJ jellium DFT calculations. The results are reported with respect to the Fermi level of the pristine $R = 10.7a_0$ nanowire. The occupied $s\,(\ell = 0)$ and $p\,(\ell = 1)$ shells and the unoccupied $d\,(\ell = 2)$ shell fall into the energy range relevant for electron transport through the break junction. Here, ℓ stands for the angular momentum. Figure 8.5 shows calculated free-standing UJ clusters for different number of electrons. Note the spherical symmetry of the two- and eight-electron (stable) clusters.

In order to reveal the role of the resonances in the electron transport through the break junction, we show in Fig. 8.6 the energy-resolved transmission probability defined for the given incident channel as follows:

$$\mathbb{T}_n^{|m|}(E) = \sum_{n'} T_{nn'}^{|m|}(E), \tag{8.5}$$

where the summation runs over all open final channels. Obviously $\alpha_{|m|} G_0 \mathbb{T}_n^{|m|}(E_F) = G_n^{|m|}$, as given by Eq. (8.4). For the $10e$ constriction at the elongation $\Delta L = 21a_0$ one clearly observes a well-resolved low-energy resonant structure in the transmission within each m-symmetry subspace. The transmission reaches unity at the resonance, as is well documented for molecular junctions [214, 215, 218], and can be demonstrated on the basis of the Lippmann-Schwinger equation in the case of the resonance-dominated

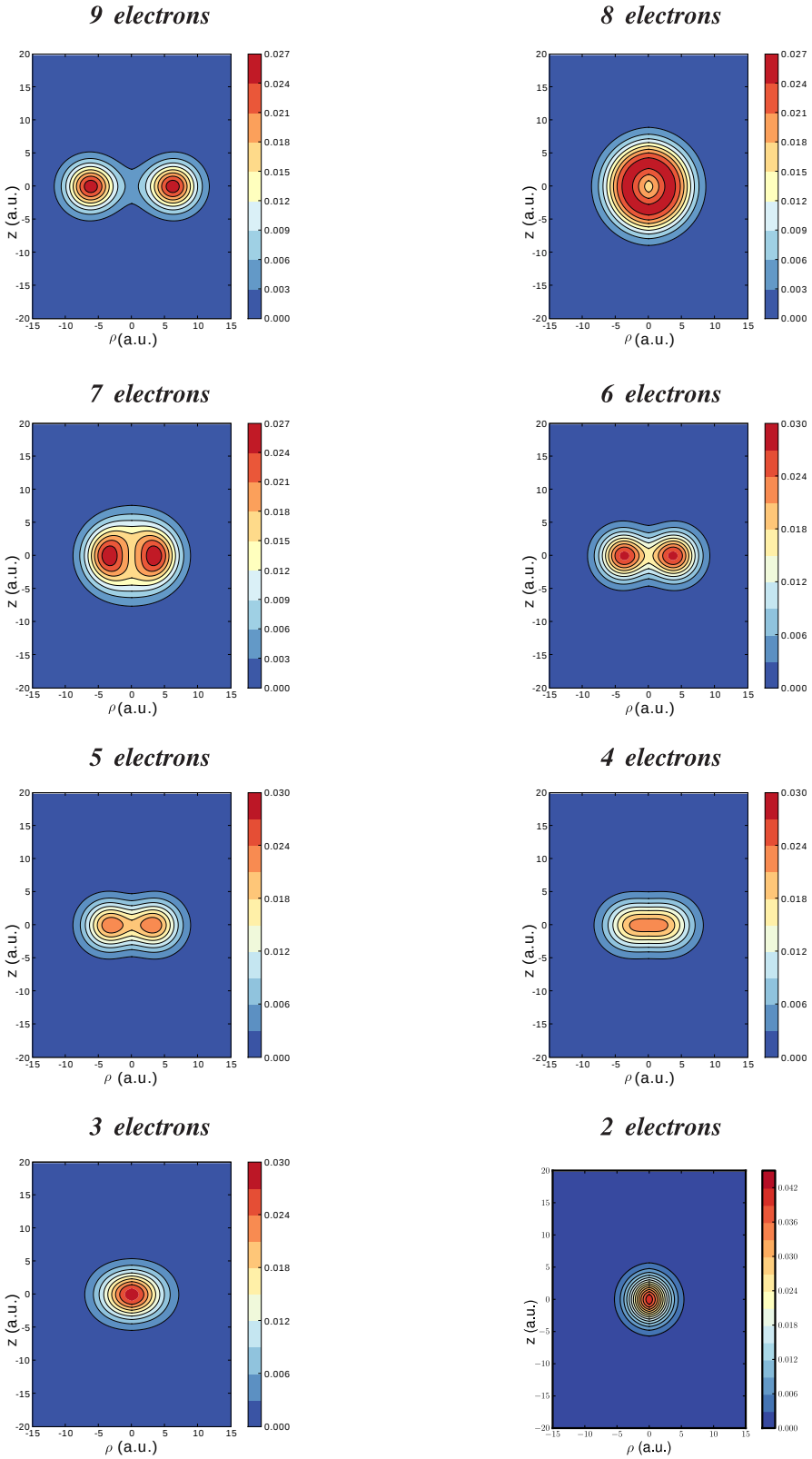

Figure 8.5.: Charge density of UJ free-standing clusters for different number of electrons.

Table 8.III.: Energies of the lowest-lying shells of the spherical free-standing $8e$ UJ cluster. The results are given in eV with respect to the Fermi level of the $R = 10.7a_0$ nanowire.

Shell	Energy
$s\,(m = 0)$	-1.93
$p\,(m = 0, \pm 1)$	-0.57
$d\,(m = 0, \pm 1, \pm 2)$	0.81

transmission [220, 221]. Comparison with the data reported in Table 8.III shows that the resonant energies correspond to the s, p, and d shells of the free-standing $8e$ cluster for the $m = 0$, 1, and 2 symmetries, respectively. For the $m = 0$ symmetry data, with the $(m = 0, n = 2)$ incident channel, we also observe a d-shell resonance in $\mathbb{T}_2^0$. This is energetically degenerate, with a resonant structure in $\mathbb{T}_1^2$ for the $m = 2$ symmetry. Thus, the junction can indeed be seen as a spherical cluster attached to the leads. The resonant character of the electron transmission reflects, then, transient electron trapping inside the cluster. Another valuable piece of information comes from the evolution of the transmission curve and, in particular, that of the resonances as a function of the elongation ΔL. While the energy position is preserved through the sequence $14a_0$-$18a_0$-$21a_0$, the width of the resonance decreases, i.e., the resonant structure sharpens [the minimum full width at half maximum (FWHM) is approximately 0.1 eV for a Lorentzian fit]. This points at the change in the coupling between the cluster-localized states and leads. Comparison of the $\Delta L = 14a_0$ and $\Delta L = 21a_0$ panels of Fig. 8.2 shows that for $\Delta L = 21a_0$ the necks on each side of the cluster are much better defined. The cluster appears less strongly coupled to the leads, consistent with the smallest widths of the resonances in each m subspace. Finally, the resonances vanish for $\Delta L = 22a_0$, when the $8e$ cluster structure disappears from the break junction.

While the well-defined lowest-lying transmission resonance within each m-symmetry subspace can be unambiguously identified as the corresponding state of the free-standing cluster broadened by the electron coupling with the leads, the number of resonances observed in Fig. 8.6 is less than the number of states in the cluster. For example, the resonance at -0.5 eV observed within the $m = 1$ symmetry emerges from the p shell of the cluster and thus has to have its counterpart within the $m = 0$ symmetry. However, it is not revealed by the calculation. Similarly, the resonance at $+0.8$ eV, observed within the $m = 2$ symmetry, emerges from the d shell of the spherical cluster. It thus has to appear within the $m = 0$ and $m = 1$ symmetry subspaces. This d-shell-derived resonance is indeed present for the $m = 0$ symmetry, as follows from

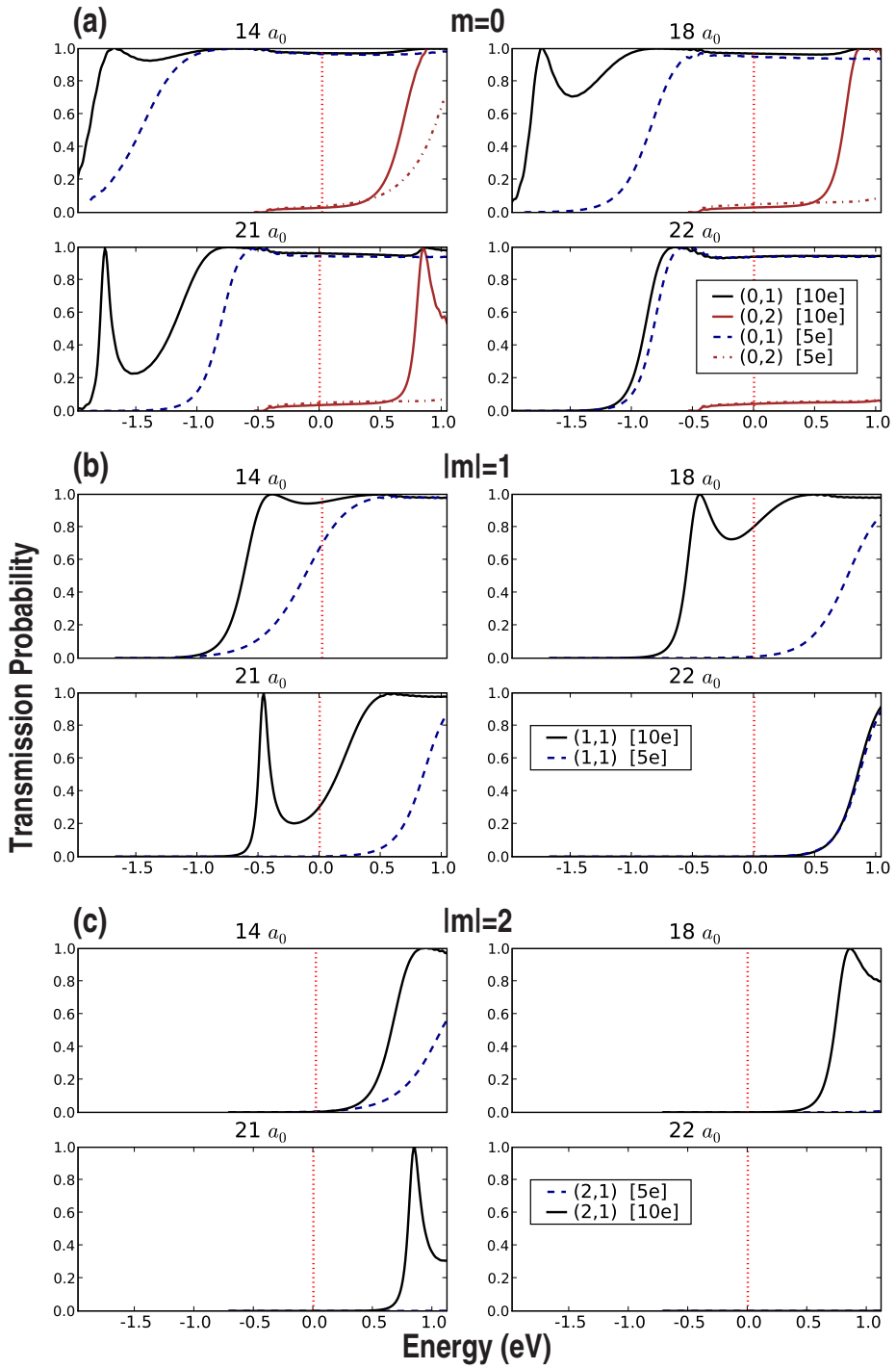

Figure 8.6.: Transmission probability $\mathbb{T}_n^{|m|}$ for different (m, n) incident channels. Results are shown as a function of the energy of the incident electron for different elongations of the nanowire (defined above each panel). The energy is measured with respect to the Fermi level, denoted by the vertical dotted line. The solid (dashed) lines correspond to the system with ten (five) electrons in the initial UJ deformable constriction. For further details, see the legends.

the $(m = 0, n = 2)$ transmission curve, $\mathbb{T}_2^0$. At the same time, the $m = 1$ symmetry results do not show a clear resonant structure within the corresponding energy range.

The "missing states" can be explained by a strong coupling between electronic states trapped in the cluster and those propagating in the leads. Potential barriers between the cluster and the leads are formed by the necks on each side of the cluster. Well-defined resonances in transmission appear when the energy of the underlying cluster state is below the potential barriers, so that only resonant transmission is possible. For the energies above the potential barriers the resonant structures are broad. Moreover, the contrast for the resonance observation is much reduced, since the nonresonant over-the-barrier transmission is high [213]. To support this idea we have performed additional calculations where the reflectivity of the potential barrier between the cluster structure and the leads has been artificially increased. The self-consistent attractive potential in both necks between the cluster structure and the leads has been set to zero (i.e., to the vacuum level) in the regions with a width of $2a_0$ in the z coordinate around each neck.

Results of this calculation are reported in Fig. 8.7. All the resonances expected from the shell structure of the freestanding cluster emerge (see Table 8.III). An important result follows from this calculation: both for the over-the-barrier and under-the-barrier character of the transmission, $\mathbb{T}_n^{|m|}(E)$ reaches unity for the electron energy close to the cluster-derived resonance. As far as the energy of the transmission resonance is determined by the underlying Na cluster state, it is not surprising that the results reported in Fig. 8.7 closely resemble those obtained within density functional formalism for a sodium cluster attached to monatomic sodium chains [222]. Indeed, the coupling of the cluster states to the leads represented by monatomic chains is small, allowing well-defined resonances to be observed.

8.7. Cluster formation and conductance

We are now in a position to explain the difference in the calculated conductance jump from $3G_0$ to G_0 observed within the $14a_0 \leqslant \Delta L \leqslant 21a_0$ elongation range for the cases with five and ten electrons initially in the deformable constriction. The change in the conductance appears over a much broader elongation range in the latter case. As follows from Fig. 8.4, the conductance variation in this elongation range is determined by the change in transmission probability at the Fermi level for the doubly degenerate $(m = \pm 1, n = 1)$ incident channel. The energy-resolved data presented in Fig. 8.6 allow us to elucidate the underlying physics.

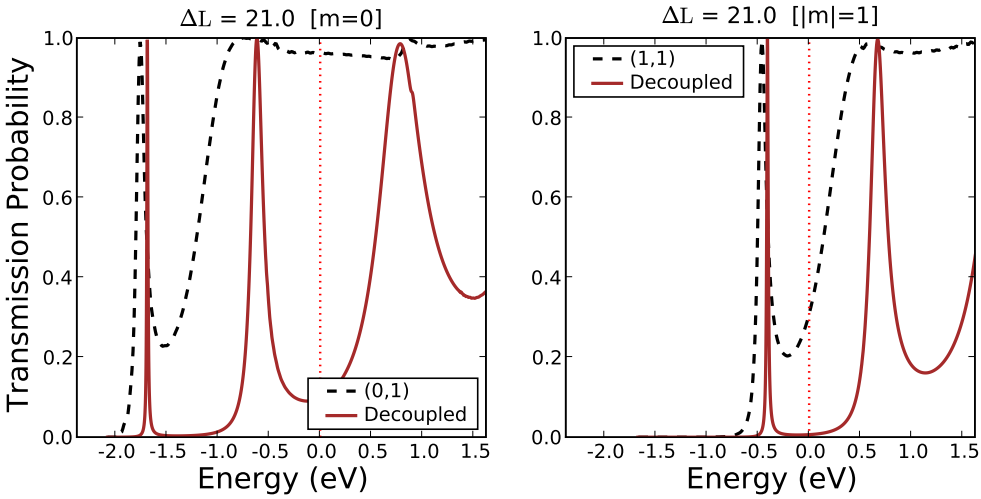

Figure 8.7.: Transmission probability $T_n^{|m|}(E)$ for the $(m = 0, n = 1)$ and $(m = \pm 1, n = 1)$ incident channels for the $10e$ case. The results are shown as a function of the energy of the incident electron, measured with respect to the Fermi level, denoted by the vertical dotted lines. The calculations are performed for the nanowire elongation $\Delta L = 21a_0$. The dashed and solid lines correspond to the results obtained with the self-consistent potential and the potential with artificially increased reflectivity at the necks separating the cluster from the leads, respectively.

For the $5e$ system the transmission probability grows from zero to unity within a narrow energy range above a certain threshold energy E_{th}. Recalling that no clustering happens in the break junction, this is a typical behavior for the change from the under-barrier to over-barrier transmission. The height of the potential barrier separating the two $R = 10.7a_0$ leads is determined by the width of the neck formed in the middle of the deformable constriction. For $14a_0 \leqslant \Delta L \leqslant 21a_0$ the neck between the leads shrinks (see Fig. 8.2). The potential barrier and, correspondingly, E_{th} is raised well above the Fermi level. The transmission at the Fermi level and so the contribution of the $(m = \pm 1, n = 1)$ incident channel to the total conductance for the $5e$ system then sharply drops to zero.

The situation is strikingly different for the $10e$ system, where the $8e$ cluster is formed in the deformable constriction between the leads. The Fermi level is sandwiched between the cluster-localized p and d shells. Transient electron trapping in the cluster-localized states manifests itself through the resonances in the energy-resolved electron transmission through the break junction. According to the discussion above, the transmission is then fixed to unity at the resonance energies below and above the Fermi level. Upon stretching, the cluster-localized states do not change their energy position, since the underlying cluster structure is preserved. At the same time, since the necks sepa-

rating the cluster from the $R = 10.7a_0$ leads shrink (see Fig. 8.2), the coupling between the cluster states and leads decreases, causing the resonances to narrow. A dip in the transmission probability gradually develops at E_F. However, $\mathbb{T}_1^1(E_F)$ never reaches zero, as long as the cluster structure is present in the deformable constriction. Thus, the decrease of the contribution of the $(m = \pm 1, n = 1)$ incident channel to the total conductance upon stretching is much softer, as compared to the $5e$ system, where it reflects the energy shift of the transmission threshold.

The $8e$ cluster structure in the break junction disappears for $\Delta L = 22a_0$. The $\mathbb{T}_1^1(E)$ curves then merge for the $5e$ and $10e$ systems, reflecting similar geometries of the deformable constrictions where the monatomic wire with magic radius $R = 4.5a_0$ is basically formed. As follows from Fig. 8.6(a), the $\mathbb{T}_1^0(E)$ is also very similar for the $5e$ and $10e$ cases.

For the $m = 0$ symmetry, the resonances derived from the p shell and d shell of the $8e$ cluster in the deformable constriction are energetically well above the potential barrier formed by the necks separating the cluster from the leads. While a dip in the transmission develops between the s- and p-shell resonances, as in the $m = \pm 1$ case, the transmission at the Fermi level is nearly unity within the relevant range of elongations. The $(m = 0, n = 1)$ incident channel then contributes nearly G_0 to the total conductance.

Coming back to Fig. 8.3, we observe that the results of Nakamura *et al.* [35] also show a rounded shape in the jump from $3G_0$ to $1G_0$, which resembles our $10e$ curve. This is while no clustering was observed. Nakamura *et al.* connect the shape of this jump with the gradual conductance drop of two almost degenerate eigenchannels during smooth atomic displacements. However, in contrast to our $10e$ system, the local density of states integrated over the neck, calculated in Ref. [35], showed wide peaks due to the strong coupling to the leads, i.e., no sharp resonances were found. With respect to the overall length of the conductance curve and, in particular, in the jump from $3G_0$ to $1G_0$, their results are equivalent to our $5e$ conductance curve.

The above discussion shows that, while the presence of the cluster-derived structures in the break junction is a robust phenomenon, as follows from a number of works [41, 44, 205], the particular shape of the conductance change is a much more subtle effect depending on the exact properties of the system at hand [194, 219]. Thus, from the experimental point of view, the evidence for clustering should come from the observation of the resonant structures in transmission. These are directly linked to the very existence of the cluster structures in the break junction. This might be possible by measuring the differential conductance, i.e., applying a bias voltage U to

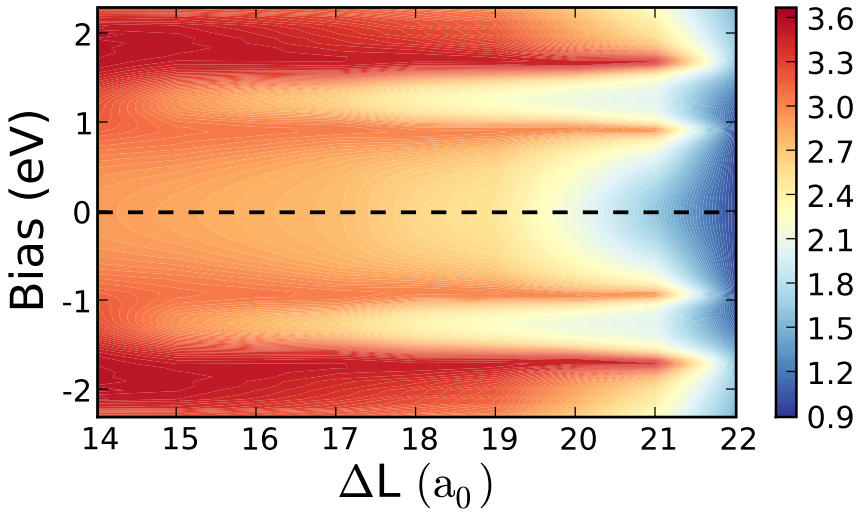

Figure 8.8.: Differential conductance dI/dU map for the breakage of the $R = 10.7a_0$ Na nanowire with ten electrons in the deformable construction. The results are shown as a function of the applied bias voltage and nanowire elongation ΔL. The contributions coming from the incident channels $(\pm 1, 2)$ and from channels with $|m| > 2$ are negligible in the given bias energy range. The horizontal dashed line denotes the zero-bias conductance. For further details see the main text.

the break junction and performing dI/dU spectroscopy [see Eq. (4.120)] upon elongation [4, 214–216].

The calculated elastic differential conductance is shown in Fig. 8.8 for the breakage of the $R = 10.7a_0$ Na nanowire with ten electrons in the deformable constriction. The cluster-derived transmission resonances appear as peak structures in dI/dU, as follows from the comparison of Figs. 8.8 and 8.6.

Thus, the well-defined peak in dI/dU at ± 1 eV energy corresponds to the -0.5 eV resonance within $|m| = 1$ symmetry (see Fig. 8.6). The structure at ± 1.7 eV arises from the superposition of the resonances at $+0.8$ eV within $m = 0$ and $|m| = 2$ symmetry, and partially, from the broad resonance at -0.8 eV within $m = 0$ symmetry. Observe that the resonant structures remain at fixed energies and sharpen upon elongation. As explained above, the resonance energy is determined by the cluster structure in the break junction, which is particularly stable for the magic clusters. The resonance width depends on the coupling to the leads and thus on the elongation.

This finding suggests experimental ways to evidence the presence of clusters in the break junction by dI/dU spectroscopy, although care should be taken with the underlaying approximations assumed in our study. In particular, the change in structural

geometry and energy resolved transmission upon applied bias is neglected, which might lead to resonant peak suppression. Furthermore, inelastic transport effects have not been accounted for.

8.8. Summary

We have presented a detailed study of the conductance during the elongation and breakage of Na nanowires described with the ultimate jellium model. Self-consistent density functional theory calculations have been performed for the nanowire structure. The resulting one-electron potential has been used then in the follow-up wave packet propagation treatment of the ballistic electron transport through the break junction.

A nanowire of magic radius $R = 10.7a_0$ has been studied here. This is a typical example of a stable Na nanowire structure allowing us to address the change of the conductance both in the presence and in the absence of cluster-derived structures in the deformable constriction during the stretching process. Indeed, depending on the size of the deformable constriction, with ten (or five) electrons the breakage of the nanowire is preceded (or not) by the formation of magic clusters of eight electrons in the break junction [41].

We observe that the clustering changes the conductance G of the break junction, in particular the shape of the $G = 3G_0$ to $G = G_0$ step upon elongation. Calculations of the energy- and symmetry-resolved transmission through the break junction reveal the underlying physics. Basically, when a cluster is formed, the electron transport is strongly affected by the transient trapping of ballistic electrons inside the cluster structure. These cluster-localized states sandwich the Fermi level of the Na leads, and appear as resonances in the transmission of the break junction. It is important that (i) the transmission reaches unity at resonances, and (ii) the energy of the resonances does not change upon elongation, as long as a stable "magic" cluster structure is present in the break junction. As a result, the decrease of the conductance upon elongation merely reflects the decrease of the resonance width within the $m = 1$ symmetry subspace, i.e., the reduction of the coupling between the cluster and the leads. The conductance $G \simeq 3G_0$ is then maintained over a much broader range of nanowire elongations, with a rounded transition to $G = G_0$, as compared to the case when no clustering occurs.

For the case when no clustering occurs, the transmission through the break junction shows a threshold behavior. It rapidly grows from zero to unity when the electron energy approaches the height of the potential barrier formed by the neck between the leads. Since the neck shrinks upon elongation, the threshold energy for electrons

arriving from the $R = 10.7a_0$ leads within the $m = 1$ subspace quickly shifts above the Fermi level. This results in an abrupt steplike drop of the conductance from $G = 3G_0$ to $G = G_0$.

The study of the differential conductance shows the cluster-derived resonances and their evolution upon elongation. For the particularly stable "magic" cluster, the resonant structures in the differential conductance maintain their energy within a certain elongation range. This is an indication that the cluster geometry is preserved. The resonance width decreases as a result of the decreasing coupling between cluster structure and leads. This finding suggests experimental ways to evidence the presence of clusters in the break junction.

Chapter 9

Summary and general conclusions

In this chapter we summarize the most important results obtained in this thesis work.

(I) Our studies are based on the following theoretical **methods**:

1. We have used jellium models and model potentials together with density functional theory (DFT) formalism to obtain the one-electron description of confined electron systems in metallic nanosized systems.
2. Many-body perturbation theory results have been used within the GW approximation for the calculation of the electron-electron decay rates of electron (hole) excitations.
3. The wave packet propagation method has allowed us to calculate:
   (i) Projected density of states of electronic systems.
   (ii) The one-electron resonance energies, elastic widths and wave functions of quasi-stationary states.
   (iii) One-electron energy-resolved transmission probabilities through small (tunneling) junctions.

(II) We have studied several aspects of the electronic structure, dynamics and spectroscopy of the following **systems**:

1. Pb thin overlayers on Cu(111) surfaces, where we have performed:

(i) Self-consistent calculations of one-electron effective potentials describing the Pb/Cu(111) system.

(ii) Electron-electron inelastic decay rate calculations of quantum well states (QWSs) and QWSs hybridized with image states (IS) in Pb overlayers.

(iii) Extraction of one-electron resonant decay rates of quantum well resonances (QWRs).

(iv) Calculations of the dZ/dV characteristics of the Pb/Cu(111) system, directly comparable with scanning tunneling spectroscopy (STS) experiments.

2. Nanocontacts formed during the breaking of a Na nanowire. In this systems we have performed:

(i) Simulations of the stretching process of a Na nanowire (until breaking) for different number of electrons in the deformable nanoconstriction.

(ii) Calculations of the zero-bias and differential ballistic conductance through the above formed Na nanocontacts.

(III) Based on the studies of the above systems with the corresponding methods, we have obtained the following original **results**.

1. The QWSs located at energies well below the Fermi level (~ -8 eV) would not be resolvable by photoemission experiments. This is because of the large many-body decay rate compared to the energy separation between the QWSs ($\Delta E_n \lesssim 0.5$ eV), with $\Gamma_{e-e} > 1$ eV ($\tau_{e-e} \lesssim 0.5$ fs).

2. The QWSs in front of the projected gap of Cu(111) have much longer lifetimes ($\gtrsim 5$ fs):

(i) At small energies with respect to the Fermi level, the many-body decay rate of the QWSs (both electron excitation and holes) approximately follows the Quinn-Ferrell parabolic dependence with energy.

(ii) For the unoccupied QWSs located at higher excitation energies, a quasilinear dependence of the electron-electron decay rate with energy has been found. The same quasilinear trend has been reported (Ref. [25]) in a recent constant current scanning tunneling spectroscopy (STS) study of the Pb/Ag(111) system.

(iii) Only some deviations from the above trends are found for small overlayer thicknesses (1–3 MLs), where smaller decay rate values are found. This is understood, in part, in terms of the QWS wave function enhanced spilling into the vacuum side for low coverages.

(iv) The contribution of the bulk states into the many-body decay of the QWSs is comparable to that of the interband and intraband transitions involving directly QWSs.

3. QWRs appear energetically below the projected band gap of the substrate inside the Cu(111) *sp* band. The one-electron elastic decay rates of the QWRs have been calculated for variable thickness of the overlayer, revealing several general trends:

   (i) The one-electron decay rate of the QWRs is small whenever the reflectivity of the Pb/Cu(111) interface is high, in particular close to the onset of the Cu(111) projected band gap. In this energy region the QWRs have decay rates comparable to those of the QWSs.

   (ii) When the width d of the Pb overlayer increases, the decay rate of the QWRs decreases in overall as $1/d$. This is understood on the basis of simple quasiclassical arguments.

   (iii) Comparing the elastic decay rate of the QWRs with their many-body decay rate estimated from the Quinn-Ferrell formula, we conclude that, for the overlayers thicker than 30 ML, the inelastic decay dominates. Basically this sets the transition to the limit of the thick Pb film, where only inelastic decay is possible.

4. We have compared our theoretical results with available QWS and QWR energies in Pb/Cu(111) observed by angle-resolved photoemission and with electron excitation lifetimes in Pb/Cu(111) and Pb/Si(111), derived from time-resolved two-photon photoemission (TR-2PPE) experiments:

   (i) Calculated theoretical energies of occupied QWSs and QWRs, and experimental observations in Pb/Cu(111) in Ref. [16], are in good agreement for thick layers.

   (ii) Our theoretical lifetime estimates in Pb/Cu(111) are in agreement with experiments, when the electron-phonon broadening is taken into account.

(iii) The interpretation of the experimental lifetime data of Refs. [23] and [24] obtained by TR-2PPE for Pb/Si(111), does not appear straightforward in terms of our theoretical results in Pb/Cu(111). This is due to the large differences found between the electronic structures of Cu(111) and Si(111) substrates.

5. The hybridization between the QWSs and ISs in Pb/Cu(111) has been studied by modifying the one-electron effective potential as extracted from DFT studies. It has been amended to properly account for the image potential tail. We have found the following:

   (i) As the energies of the QWSs approach the vacuum level E_V, the electronic density of the states piles up in the vacuum side and acquires an IS character.

   (ii) In contrast to what it is expected from the quasilinear increase of the electron-electron decay rate for "pure" QWSs, the decay rates of the hybridized QWS-ISs saturate at around $E - E_V \sim -1$ eV, and then drop. This is because an electron in a QWS-IS is moved away from the surface into the vacuum so that the inelastic coupling to the metal excitations is reduced.

   (iii) For a given energy, the weight of a QWS-IS in the vacuum side depends on the overlayer thickness. This in turn, induces a quantum size effect (QSE) in the corresponding electron-electron inelastic lifetime. We have derived an analytic expression reproducing this QSE based on the wave function penetration into the metal for fixed energy.

   (iv) For thick overlayers the QWS-IS peaks merge, leading to the continuum states of the bulk Pb surface.

6. We have performed a theoretical study of the constant current STS of Pb overlayers supported on Cu(111). The dZ/dV spectra have been calculated for the 4–18 ML film thickness range. The tip-sample system is represented with the flat-tip approximation. Relevant results are obtained for the correct interpretation of recent constant current STS experiments in Pb/Cu(111) of Ref. [20] and in Pb/Ag(111) of Ref. [25]:

   (i) Within the studied range of overlayer thicknesses, the energies of the calculated peaks in the STS spectra reproduce the experimental data for bias below 4 eV. Particularly remarkable agreement with respect to

the energies, widths, and relative intensities of the STS peaks is obtained for thicknesses above 11 ML.

(ii) Only low-energy QWSs are unperturbed by the tip. At high bias, the tip-induced Stark shift determines the energies of the QWSs and so the peaks in the STS spectra.

(iii) The departure of the experimentally measured energies of the STS peaks from the theoretical results above 4 eV bias reflects the departure of the bulk Pb band structure along Γ-L from free-electron parabola.

(iv) The STS performed at different coverages can be used as a complementary tool to inverse photoemission in order to probe the dispersion of the bulk bands of the overlayer material at energies well above the Fermi level.

7. We have calculated the conductance during the elongation and breakage of Na nanowires described with the ultimate jellium model. Self-consistent DFT calculations have been performed for the nanowire structure. The resulting one-electron potential has been used then in the follow-up wave packet propagation treatment of the ballistic electron transport through the break junction:

(i) We have observed that the formation of a cluster-like structure in the nanocontact, during the elongation process, changes the conductance G of the break junction, in particular, the shape of the $G = 3G_0$ to $G = G_0$ step upon elongation. The conductance $G = 3G_0$ is maintained over a much broader range of nanowire elongations with a rounded transition to $G = G_0$, as compared to the case when no clustering occurs.

(ii) The above trends are explained by the existence of cluster-localized states that sandwich the Fermi level of the Na leads, and appear as resonances in the transmission of the break junction. The decrease of the conductance upon elongation merely reflects the decrease of the underlaying resonance widths, i.e., the reduction of the coupling between the cluster and the leads.

(iii) The study of the differential conductance shows the cluster-derived resonances and their evolution upon elongation. For the particularly stable "magic" cluster, the resonant structures in the differential conductance maintain their energy within a certain elongation range. This is an indication that the cluster geometry is preserved. The width of the

resonance in the differential conductance decreases as a result of the decreasing coupling between cluster structure and leads. This finding suggests experimental ways to evidence the presence of clusters in the break junction by differential conductance spectroscopy.

Appendices

Appendix A

Acronyms

a_0	Bohr radius (0.529 Å)
a.u.	Atomic units
DFT	Density functional theory
DOS	Density of states
FER	Field emission resonance
FFT	Fast Fourier transform
FGH	Fourier grid Hamiltonian
GW	G: Green's function and W: Screened Coulomb interaction (from the German word *Wechselwirkung*)
GWP	Gaussian wave packet
ILDOS	Integrated local density of states
IS	Image state
ISR	Image state resonance
KS	Kohn Sham
LDA	Local density approximation
MD	Molecular dynamics

ML	Monolayer
PAM	Phase accumulation model
PDOS	Projected density of states
QF	Quinn-Ferrell
QSE	Quantum size effect
QWR	Quantum well resonance
QWS	Quantum well state
g-QWS	Gap quantum well state
d-QWS	Deep quantum well state
QWS-FER	Mixed quantum well and field emission resonance state
QWS-IS	Mixed quantum well and image potential state
RPA	Random phase approximation
SOC	Spin orbit coupling
STM	Scanning tunneling microscope
STS	Scanning tunneling spectroscopy
TDSE	Time dependent Schrödinger equation
TISE	Time independent Schrödinger equation
TR-2PPE	Time-resolved two-photon photoemission
UJ	Ultimate jellium
WKB	Wentzel Kramers Brillouin
WPP	Wave packet propagation

Appendix B

Electronic structure calculations: further details

B.1. Electrostatic potential in slabs

Here we derive the expression for the electrostatic potential appearing in Eq. (2.19). Thus we have to evaluate the following term:

$$V_H(z) = \int_{-\infty}^{\infty} \frac{\varrho_-(z') - \varrho_+(z')}{|\mathbf{r} - \mathbf{r}'|} d\mathbf{r}', \tag{B.1}$$

which due to the symmetry in parallel direction, should be only a function of z-coordinate. This integral must be evaluated by the Coulomb interaction regularization technique [68] to avoid divergences [although, quite heuristically, the correct solution might be guessed by dropping the infinite terms obtained by the direct integration of Eq. (B.1)]. The usual way to apply this technique is by replacing the Coulombic interaction by the Yukawa's one, so we obtain $\tilde{V}_H$ with the desired property:

$$\lim_{\kappa \to 0^+} \tilde{V}_H = \lim_{\kappa \to 0^+} \int_{-\infty}^{\infty} \left[\varrho_-(z') - \varrho_+(z')\right] \frac{e^{-\kappa|\mathbf{r}-\mathbf{r}'|}}{|\mathbf{r} - \mathbf{r}'|} d\mathbf{r}' = V_H. \tag{B.2}$$

After transforming the (x, y)-coordinates in parallel direction into the more convenient polar coordinates (ρ, θ), the integration in θ gives a factor 2π and by an additional variable change $(x - x')^2 + (y - y')^2 = \rho^2 = \xi$ with $d\xi = 2\rho d\rho$, we obtain for the

following integral:

$$\frac{1}{2}\int d\xi \frac{e^{-\kappa\sqrt{(z-z')^2+\xi}}}{\sqrt{(z-z')^2+\xi}} = -\frac{1}{\kappa}\, e^{-\kappa\sqrt{(z-z')^2+\xi}}\Big|_0^\infty = \frac{1}{\kappa}e^{-\kappa|z-z'|}. \tag{B.3}$$

Thus we arrive to the expression

$$\tilde{V}_H = \frac{2\pi}{\kappa}\int_{-\infty}^{\infty} dz'\ [\varrho_-(z') - \varrho_+(z')]e^{-\kappa|z-z'|}. \tag{B.4}$$

Note that at this point, the evaluation of the limit $\kappa \to 0$ still gives a divergent answer. This problem is solved by representing the exponential term in a Taylor series,

$$\tilde{V}_H = \frac{2\pi}{\kappa}\int_{-\infty}^{\infty} dz'\ [\varrho_-(z') - \varrho_+(z')]\left(1 - \kappa|z-z'| + O(\kappa^2)\right). \tag{B.5}$$

Due to the assumed total charge neutrality condition, the term going as $\sim 1/\kappa$ is canceled out and the rest of the terms containing κ-dependence go to zero when the limit $\kappa \to 0$ is evaluated. Thus the only term left is the z-dependent potential

$$V_H(z) = -2\pi\int_{-\infty}^{\infty} [\varrho_-(z') - \varrho_+(z')]|z-z'|\, dz'. \tag{B.6}$$

It is worth mentioning that the same solution can be obtained without any regularization by solving the Poisson equation with help of Green's functions as used in the solution of differential equations.

B.2. Rayleigh Quotient Multigrid method for solving Kohn-Sham equations

The self-consistent results shown in this thesis are obtained with real-space grid methods. The subroutines solving the Kohn-Sham equations are implemented in the computational package MIKA (Multigrid Instead of K-spAce), nowadays out of further development. Instead, the GPAW (Grid-based Projector-Augmented Wave method) package has taken over the development efforts [223].

All self-consistent effective potentials used in this thesis have been calculated with the MIKA code. On the other hand, further diagonalizations of built or modified one-electron effective potentials has been obtained with the Fourier Grid Hamiltonian

approach. All methods have been checked to give consistent results (including the results derived from the wave packet propagation method).

In the Rayleigh quotient multigrid method (RQMG), the eigenvalues are obtained by solving the (discretized) eigenvalue problem

$$Hu = \lambda Bu, \tag{B.7}$$

by minimizing the Rayleigh quotient:

$$\frac{< u|H|u >}{< u|B|u >}, \tag{B.8}$$

where H and B are matrix operators originated from the discretization of the Schrödinger equation on a real space grid. The u estimation is replaced by $\tilde{u} = u + \alpha d$, where d is a unit vector (one at a given grid point and zero elsewhere) and then, the minimization of Eq. (B.8) reduces the problem to a quadratic equation on α. To avoid the convergence slowing down due to the local character of the correction, a multigrid approach is taken, where coordinate relaxation are done in coarser grids. In the MIKA package, additionally, a generalization of the RQMG method leads to the possibility of the simultaneous solution of several mutually orthogonal eigenpairs. Further details can be found in Ref. [224].

In the particular case of 1D-systems, we have a finite set of N grid-points $\{z_i\}$, where $z_i = z_0 + h \cdot i$ for $i = 0, 1...N$. In the MIKA code it is used a fourth order central-difference discretization in the calculation grid,

$$f'(z_i) = \frac{-f(z_i + 2h) + 8f(z_i + h) - 8f(z_i - h) + f(z_i - 2h)}{12h}, \tag{B.9}$$

$$f''(z_i) = \frac{f(z_i + 2h) + 16f(z_i + h) - 30f(z_i) + 16f(z_i - h) - f(z_i - 2h)}{12h^2}, \tag{B.10}$$

where the calculation grid is set by adding 2 ghost points in order to define the derivatives at the boundaries of the system volume. For the particular case of a finite system, the boundary conditions are set such that the wave functions should vanish at the ghost points.

B.3. Fourier Grid Hamiltonian method

The Fourier grid Hamiltonian (FGH) method is used to construct a matrix representation of the system Hamiltonian which is straightforward to implement. Then the

eigenvalues and eigenfunctions in the grid can be obtained by diagonalization of the matrix. The FGH is a powerful method in the sense that the potential is evaluated locally and the description of the kinetic energy operator is only limited by inherent grid description. Thus, in principle the unique numerical parameters to be set are the grid size N (number of grid points) and the uniform step in mesh Δz. The drawbacks are that the diagonalization effort of a sparse matrix scales as $O(N^3)$, and that the amount of memory required for the matrix diagonalization might limit the system size being able to be addressed.

The matrix elements of the discretized Hamiltonian are calculated by projecting the Hamiltonian in the discretized grid-points:

$$(0,\ldots,\underset{\substack{\uparrow\\ i}}{1},\ldots,0)H\begin{pmatrix}0\\ \vdots\\ 1\\ \vdots\\ 0\end{pmatrix}\leftarrow j, \tag{B.11}$$

so the Hamiltonian matrix elements are given by $H_{ij} = T_{ij} + V_{ij}$, with $V_{ij} = V(z_i)\delta_{ij}$, and T_{ij} can be evaluated analytically (for N even [14]):

$$T_{ij} = \begin{cases} \frac{K^3}{6}(1+\frac{2}{N^2}) & (i=j) \\ \frac{K^2}{N^2}\frac{(-1)^{j-i}}{\sin^2(\pi\frac{j-i}{N})} & (i\neq j), \end{cases} \tag{B.12}$$

where $K = \pi/\Delta z$ is the maximum k (energy cutoff) in the description of the system which is allowed by the grid.

Appendix C

Matrix elements of the noninteracting density response

The Fourier components of the noninteracting density response function, entering Eq. (3.48), are calculated explicitly (see Ref. [79]):

$$\chi^{0,+}_{n,n'}(\mathbf{q},\omega) = \frac{\mu_n \mu_{n'}}{d^2} \left\{ \sum_{l_{\text{even}}}^{\text{occ}} \sum_{l'_{\text{even}}}^{\infty} F_{l,l'}(q,\omega) G^{++}_{n;l,l'} G^{++}_{n';l,l'} + \sum_{l_{\text{odd}}}^{\text{occ}} \sum_{l'_{\text{odd}}}^{\infty} F_{l,l'}(q,\omega) G^{--}_{n;l,l'} G^{--}_{n';l,l'} \right\} \tag{C.1}$$

and

$$\chi^{0,-}_{n,n'}(\mathbf{q},\omega) = \frac{4}{d^2} \left\{ \sum_{l_{\text{even}}}^{\text{occ}} \sum_{l'_{odd}}^{\infty} F_{l,l'}(q,\omega) G^{+-}_{n;l,l'} G^{+-}_{n';l,l'} + \sum_{l_{\text{odd}}}^{\text{occ}} \sum_{l'_{\text{even}}}^{\infty} F_{l,l'}(q,\omega) G^{-+}_{n;l,l'} G^{-+}_{n';l,l'} \right\}, \tag{C.2}$$

where

$$\mu_n = \begin{cases} 1 & \text{for } n = 0 \\ 2 & \text{for } n \geq 1, \end{cases} \tag{C.3}$$

and

$$F_{l,l'}(q,\omega) = \int dk k [F^{+}_{l,l'}(q,k,\omega) - F^{-}_{l,l'}(q,k,\omega)], \tag{C.4}$$

with

$$F^{\pm}_{l,l'}(q,k,\omega) = \theta\left(\epsilon_F - \epsilon_l - \frac{k^2}{2m_l}\right) \times \left[\frac{q^2k^2}{m_{l'}^2} - \left(\frac{q^2}{2m_{l'}} + \epsilon_{l'} - \epsilon_l + \frac{k^2}{2m_{l'}} - \frac{k^2}{2m_l} \pm \omega \pm i\eta\right)^2\right]^{-1/2}, \tag{C.5}$$

$$G^{++}_{n;l,l'} = c^+_{l,0}c^+_{l',0}\delta_{n,0} + \frac{1}{\sqrt{2}}\sum_{n'\neq 0}(c^+_{l,n'}c^+_{l',0} + c^+_{l,0}c^+_{l',n'})\delta_{n,n'} + \frac{1}{2}\sum_{n'\neq 0}\sum_{n''\neq 0} c^+_{l,n'}c^+_{l',n''}(\delta_{n+n'',n'} + \delta_{n+n',n''} + \delta_{n'+n'',n}), \tag{C.6}$$

$$G^{--}_{n;l,l'} = \frac{1}{2}\sum_{n'\neq 0}\sum_{n''\neq 0} c^-_{l,n'}c^-_{l',n''}(\delta_{n+n'',n'} + \delta_{n+n',n''} - \delta_{n'+n'',n}), \tag{C.7}$$

$$G^{+-}_{n;l,l'} = \frac{1}{\sqrt{2}}c^+_{l,0}c^-_{l',n} + \frac{1}{2}\sum_{n'\neq 0}\sum_{n''\neq 0} c^+_{l,n'}c^-_{l',n''}(-\delta_{n+n'',n'} + \delta_{n+n',n''} + \delta_{n'+n'',n}), \tag{C.8}$$

$$G^{-+}_{n;l,l'} = \frac{1}{\sqrt{2}}c^-_{l,n}c^+_{l',0} + \frac{1}{2}\sum_{n'\neq 0}\sum_{n''\neq 0} c^-_{l,n'}c^+_{l',n''}(\delta_{n+n'',n'} - \delta_{n+n',n''} + \delta_{n'+n'',n}). \tag{C.9}$$

Here δ is the kronecker delta:

$$\delta_{nn'} = \begin{cases} 1 & \text{if } n = n' \\ 0 & \text{if } n \neq n'. \end{cases} \tag{C.10}$$

For the particular case in which the effective masses of two bands are equal, i.e., $m_l = m_{l'} = m_0$, Eq. (C.4) can be directly integrated [78], so it is obtained

$$F_{l,l'}(q,\omega) = -\frac{m_0^2}{\pi q_\parallel^2}\left[2a_{l,l'}(q) + i\left[\frac{1}{m_0^2}q^2k_l^2 - \left[a_{l,l'}(q) - \omega - i\eta\right]^2\right]^{1/2} - i\left[\frac{1}{m_0^2}q^2k_l^2 - \left[a_{l,l'}(q) + \omega + i\eta\right]^2\right]^{1/2}\right], \tag{C.11}$$

with

$$a_{l,l'}(q) = \frac{1}{2m_0}q^2 - (E_l - E_{l'}), \tag{C.12}$$

and

$$k_l = \left[2m_0\left(E_F - E_l\right)\right]^{1/2}. \tag{C.13}$$

For most of the calculations Eq. (C.11) has been evaluated with $\eta = 0.01$ and $m_0 = 1$. For different effective masses ($m_l \neq m_{l'}$) we have integrated numerically Eq. (C.4). We also have checked that the numerically integrated solution is consistent with that obtained from the analytical solution when $m_l, m_{l'} \to m_0$. Eq. (C.11) diverges at $q = 0$. This is circumvented by substituting the $q = 0$ value by a small q number, $q \to 10^{-6}$.

Appendix D

Bulk Pb and Pb slabs: Supplementary material

In this appendix a few issues concerning the electronic band structure and lifetime of bulk Pb and (free standing) Pb slabs are briefly discussed.

We start with a simple discussion of the density of states in Pb slabs. The density of states (DOS) of a homogeneous 3D electron gas [59] is given by

$$g_{3\mathrm{D}}(E) = \frac{1}{\pi^2}\sqrt{2E}, \tag{D.1}$$

where E is the energy. For a 2D gas, the constant DOS per surface area unit is $g_{2D} = 1/\pi$. For an infinite potential well of finite thickness d, the DOS per unit volume is

$$g_{\mathrm{well}}(E) = \frac{1}{\pi}\sum_n \theta(E - E_n)/d, \tag{D.2}$$

where E_n are the eigenenergies given by Eq. (5.6) and θ is the Heaviside function. Figure D.1 shows the DOS calculated with Eq. (D.2) for a 4-ML thickness ($d = 21.64a_0$) free-standing Pb slab modeled by jellium. This is compared with the 3D DOS for the same material. The energies are measured with respect to the inner potential of the Pb slab (≈ -13.55 eV). Both DOS plots almost coincide when a new QWS band starts to contribute to the DOS. Furthermore, in overall, both densities show similar trends, from which it can be inferred the 3D character of the QWS electron-electron decay rates. The overall increase of the DOS of the Pb slab appears stronger than that of the 3D gas because the effective width of the Pb well increases with energy (the concept

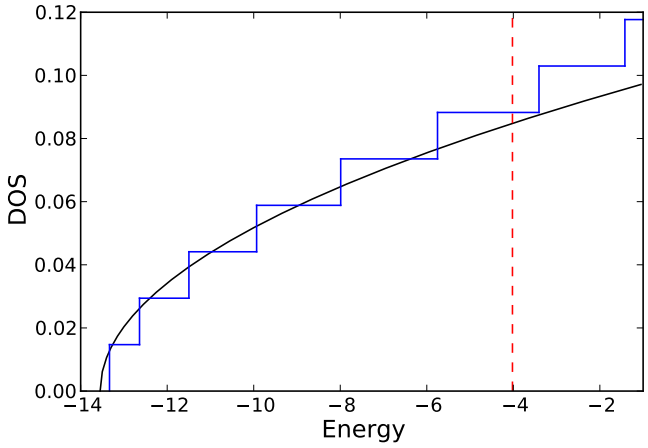

Figure D.1.: Comparison of density of states (DOS) for the 3D Pb electron gas (black line) and for a Pb free-standing jellium slab of 4 ML thickness (stepped blue line). The vertical dashed line denotes the Fermi level.

of the effective width is introduced along the discussion of the solutions of the finite square well potential in Chapter 5).

It is instructive to compare the electronic structure followed from a jellium model (including the image potential) for Pb slabs with the realistic *ab initio* calculations, as done in Fig. D.2. One observes that the low-lying gap from -8 eV to -4 eV is not reproduced by the jellium approach. However, the bands close to the Fermi level (E_F) are well described around $\overline{\Gamma}$. Furthermore, the number of bands below E_F and crossing $\overline{\Gamma}$ are the same. Thus, the main physical properties depending on the density of states at E_F are expected to be reproduced at a qualitative level in the jellium approach. From the same figure, one can also observe the variation of the effective mass of the bands with energy as well as the band folding, in order to avoid the crossing with dropped high-lying bands. The latter effects are out of the scope of the jellium description.

In Fig. D.3 different theoretical decay rates for bulk Pb and Pb overlayers on Cu(111) (the results of this thesis) are compared. At energies close to the Fermi level they are essentially lying at the Quinn-Ferrell parabola of Eq. (3.3) with $r_s = 2.3$ (Pb). The good agreement, even at energies up to 2 eV with respect to E_F, between the *ab initio* (dots and squares) and the Quinn-Ferrell formula is surprising, as far as the latter is derived for high electron densities and close to the Fermi energy. However, at higher energies, we have found a quasilinear trend for Pb/Cu(111) within the jellium model for Pb. The differences between theoretical Pb free-electron gas results and our results indicates an effect derived from the inclusion of the Cu-Pb and Pb-vacuum interfaces.

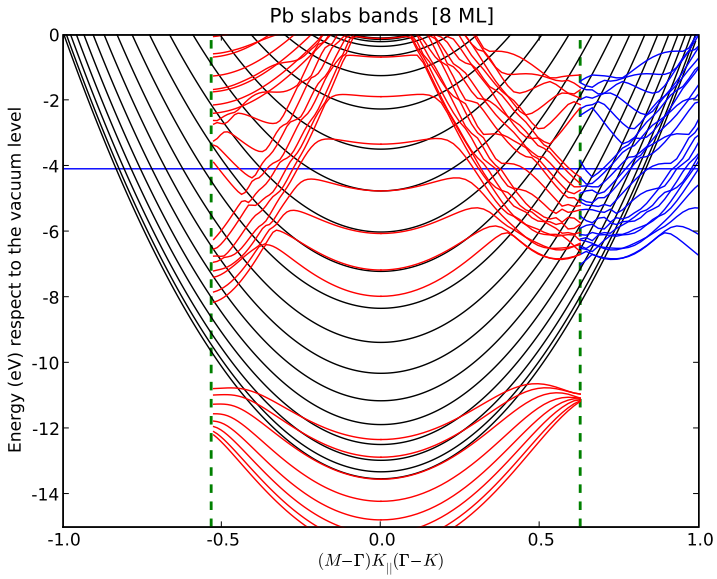

Figure D.2.: Electronic band structure for the 8-ML-thick free-standing Pb slab along $\overline{\mathrm{M}}-\overline{\Gamma}$ and $\overline{\Gamma}-\overline{\mathrm{K}}$ high-symmetry lines. Black: Parabolic band structure derived from the 1D jellium description. Red: *ab initio* band structure in the reduced zone. Blue: Part of the *ab initio* electronic structure is mirrored in the extended zone for direct comparison with the simple model parabolic bands. Vertical dashed lines denote the $\overline{\mathrm{M}}$ (left) and $\overline{\mathrm{K}}$ (right) high-symmetry points in the reciprocal space. The horizontal line denotes the Fermi level (*Ab initio* data are provided by courtesy of Xabier Zubizarreta).

Finally, we quote in Table D.I the linear fits for the electron-electron decay rate theoretical data discussed above and, in addition, we include the reported fit derived from experimental data of QWSs in the Pb/Ag(111) system [25]. The agreement between the experimental data and our theoretical results is remarkable. In fact, the difference in b_0 is of the order of the electron-phonon decay rate at the experimental temperature of 5 K ($\Gamma_{e-\mathrm{ph}} \approx 20$ meV, see Ref. [61]).

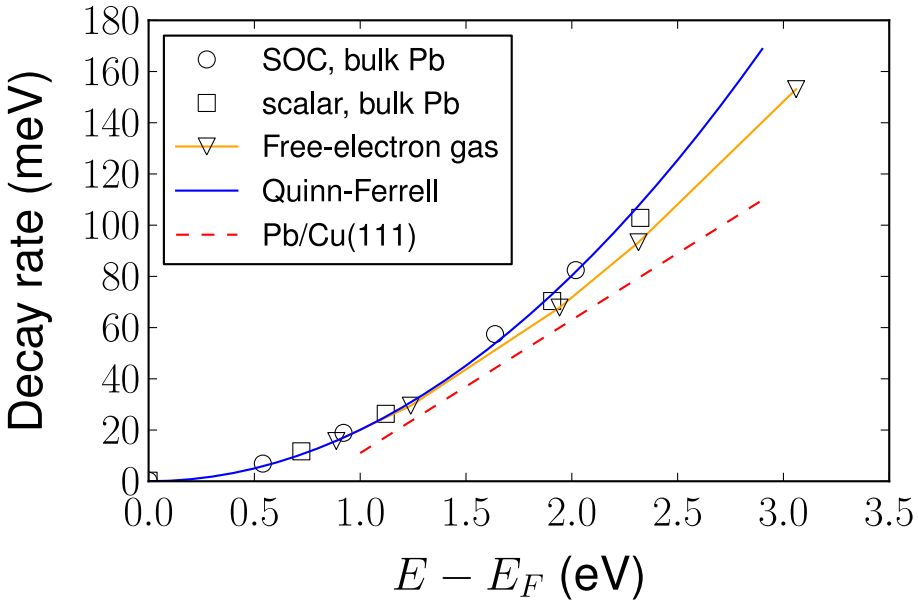

Figure D.3.: Comparison of the inelastic electron-electron decay rates in bulk Pb (symbols) along Γ-L for free-electron gas and *ab initio* calculations [for the latter both scalar and including spin-orbit coupling (SOC) are shown] from Refs. [61] and [29], together with Pb/Cu(111) results obtained in this thesis (dashed line, for energies above 1 eV). The solid blue line corresponds to the Quinn-Ferrell formula of Eq. (3.3) with $r_s = 2.3$ (Pb).

Table D.I.: Comparison of different linear fits $[b_0 + b_1(E - E_F)]$ to available experimental decay rate data of Ref. [25] for QWSs with energy above ≈ 1 eV in Pb/Ag(111) and *ab initio* data for bulk Pb [scalar and including spin-orbit coupling (SOC)] reported in Ref. [61].

	SOC [61]	Scalar [61]	This thesis	Becker *et al.* [25]
b_1 (meV/eV)	65.5	61.1	52	53
b_0 (meV)	−49.8	−42.7	−41	−23

Appendix E

Calculation of dZ/dV characteristic

Here we discuss the numerical procedure used to calculate the constant current dZ/dV characteristic. At large enough tip-sample distances, we assume for the tip position a well behaved function of the bias voltage V and electric current I, i.e., $Z \equiv Z(V, I)$, thus

$$dZ = \left(\frac{\partial Z}{\partial V}\right)_I dV + \left(\frac{\partial Z}{\partial I}\right)_V dI. \tag{E.1}$$

Assuming small δV and δI variations, and recasting Eq. (E.1) together with initial conditions, if necessary, determined by a simple root finding bisection method [225] applied to the equation $I(V, Z) = I_0$,

$$Z_0^0 \equiv Z(V_0, I_0), \tag{E.2a}$$
$$Z_1^0 \equiv Z(V_0 + \delta V_1, I_0 + \delta I_0), \tag{E.2b}$$
$$Z_1^1 \equiv Z(V_0 + \delta V_1, I_0), \tag{E.2c}$$

we calculate iteratively the corresponding $Z(V_j, I_0) \approx Z_j^{i_c} = Z_{j-1}^{i_c} + \sum_{i=0}^{i_c} \delta Z_j^i$ for fixed I_0, and each $V_j = V_{j-1} + \delta V_j$ $(j = 2, 3, ...)$. The index value i_c corresponds to the ith iteration for which convergence is reached, defined by the convergence condition $|I^{i_c} - I_0|/I_0 < \Delta_c$. We obtain $Z_j^0 = Z_{j-1}^{i_c} + \delta Z_j^0$, with

$$\delta Z_j^0 = \left\{ \frac{Z_{j-1}^{i_c} - Z_{j-2}^{i_c}}{V_{j-1} - V_{j-2}} \right\} \delta V_j, \tag{E.3}$$

and $Z_j^i = Z_j^{i-1} + \delta Z_j^i$ (for $i_c > 0$), with

$$\delta Z_j^i = \left\{ \frac{Z_k^{i_c} - Z_k^{i_c - 1}}{I_k^{i_c} - I_k^{i_c - 1}} \right\} \left\{ I_0 - I_j^{i-1} \right\}, \tag{E.4}$$

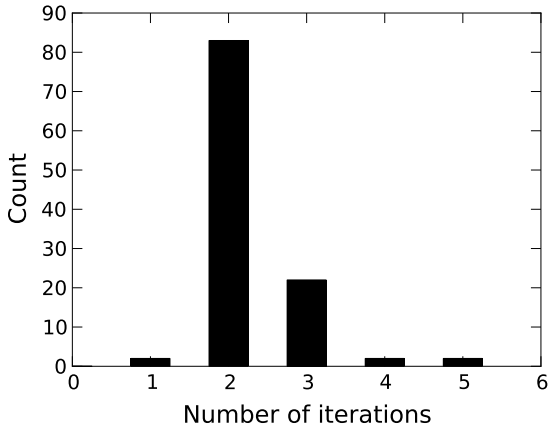

Figure E.1.: Histogram of number of iterations required to obtain convergence at each V_j during the calculation of a $Z-V$ characteristic. Above data correspond to 111 calculated points of the $Z-V$ characteristic in the 15ML-Pb/Cu(111) system. The parameters used are Δ_c =0.001 and constant $\delta V = 50$ meV, with initial and final bias 0.45 eV and 5.95 eV.

where the k index refers to the highest $k < j$ for which $i_c > 0$. If $i_c > 1$, the following might be used for i running from 2 to i_c:

$$\delta Z_j^i = \left\{ \frac{Z_j^{i-1} - Z_j^{i-2}}{I_j^{i-1} - I_j^{i-2}} \right\} \left\{ I_0 - I_j^{i-1} \right\} . \tag{E.5}$$

We have performed most of the calculations with Δ_c =0.001 and constant $\delta V_j = 50$ meV. The latter value should be taken with care, because resonant peak energies converge faster than linewidths. A histogram of the number of iterations needed to reach self-consistency for the above parameters at each V_j is shown in Fig. E.1. It is observed that only two iterations ($i_c = 1$) are needed for most j.

The above procedure is essentially the application of the Newton-Raphson method [Eq. (E.5)] to the equation $I(V_j, Z) - I_0 = 0$, with an efficient prescription [Eqs. (E.3) and (E.4)] for the initial guess of the root Z_j.

Finally, the constant current dZ/dV spectra are obtained by numerical differentiation of the calculated $Z-V$ characteristics [see Fig. E.2(a)] as

$$\left. \frac{dZ}{dV} \right|_{V=V_j} = \frac{1}{2\delta V} \left(Z_{j+1}^{i_c} - Z_{j-1}^{i_c} \right) . \tag{E.6}$$

More efficient schemes, than the above one, for the calculation of the $Z-V$ characteristics are under study, where the information inside the calculated energy-resolved

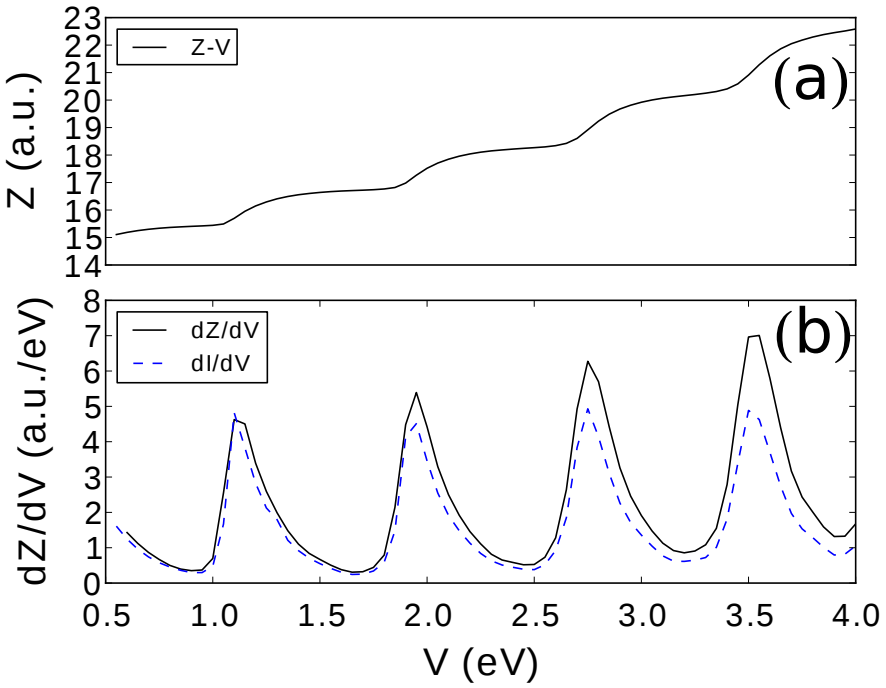

Figure E.2.: (a) An example of calculated $Z-V$ characteristics for the 15ML-Pb/Cu(111) system. (b) The corresponding dZ/dV (solid line) and dI/dV (dashed line) spectra, the latter being scaled for the sake of comparison.

transmission corresponding to a previous Z_{j-1} could offer a better extrapolation for the next Z_j point, thus reducing the number of total iterations needed to reach the convergence. This is an important issue when the computational effort required for each calculated point is large, as for example, in the 3D calculations of a recent study of the field emission resonances induced by alkali ad-islands on a Cu(100) surface [142]. In that work, the constant current $Z-V$ characteristic was approximated by a linear ramp. Then, resonances were obtained from the dI/dV spectra (through the $Z-V$ linear ramp) which were shown to be comparable to their *constant current* dI/dV counterpart.

We have also calculated the constant current dI/dV spectra. This is done by perfoming two additional calculations at the converged Z_j tip position: $I_\pm = I(Z_j, V_j \pm \delta\tilde{V})$ with $\delta\tilde{V} = 10$ meV. Then,

$$\left.\frac{dI}{dV}\right|_{V=V_j} = \frac{1}{2\delta\tilde{V}}(I_+ - I_-). \tag{E.7}$$

As observed in Fig. E.2(b), the QWSs of the system appear as peak structures equally well resolved in both dZ/dV spectra and differential conductance dI/dV. Indeed,

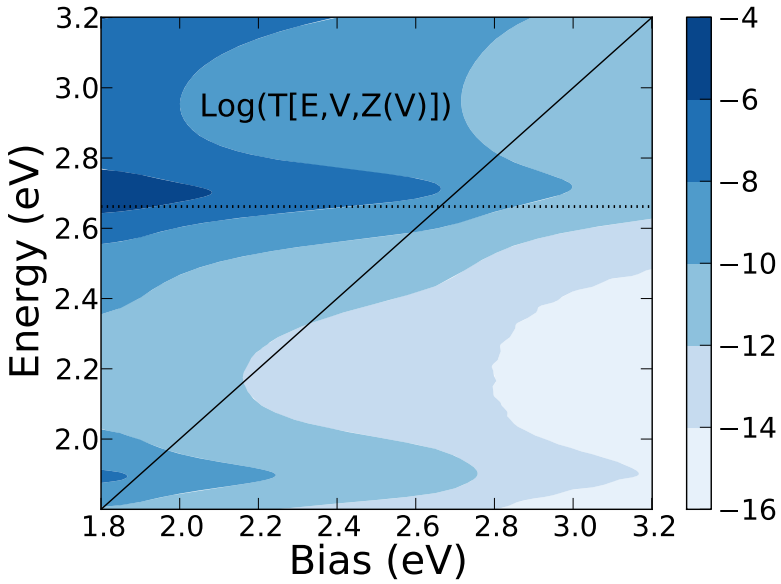

Figure E.3.: Calculated logarithmic transmission as a function of electron energy E and applied bias for 15ML-Pb/Cu(111). The dotted line shows the energy of the $n = 26$ QWS calculated for the bare system (no tip), where n is a principal quantum number. The solid line $E = V$ defines a cut of the $T[E, V, Z(V)]$ 2D plots corresponding to the spectroscopic constant current mode (see Fig. 7.6).

$I = I(V, Z)$ and $Z = Z(V, I)$, so that the partial derivatives are related by [with $(\partial I/\partial Z)_V \neq 0$]:

$$(\partial Z/\partial V)_I = -(\partial I \partial Z)_V^{-1}(\partial I/\partial V)_Z. \tag{E.8}$$

The similarity between the two spectroscopies is a consequence of the fact that $(\partial I/\partial Z)_V$ is a smooth function of V, merely reflecting the evolution of the tunneling barrier between the tip and the surface.

The illustrative example of the calculated transmission probability $T[E, V, Z(V)]$ is shown in Fig. E.3 for the 15-ML-thick Pb overlayer on Cu(111). The results are presented as a function of the applied bias V, and electron energy E measured with respect to the Fermi level. Note that the tip-surface distance Z is bias-dependent because of the constant current mode, where the constant current density has been set as: $I = 5 \times 10^{-2}$ nA/Å^2. The transmission resonances observed in Fig. E.3 correspond to the QWSs of the system. We would like to stress that the rigorous definition of these states assumes that the Hamiltonian is fixed, i.e., that the resonance analysis is performed for the constant bias V cut of the 2D figure. For the fixed bias the transmission probability rises in overall with electron energy, reflecting decrease of the tunneling barrier. When the bias is increased, the tip moves away from the surface to

reestablish the constant current via overall reduction of the transmission probability. This is nicely seen in the figure when comparing data at the same energy, but for increasing bias. The solid line $E = V$ in the figure defines a cut of the $T[E, V, Z(V)]$ 2D plots corresponding to the spectroscopic constant current mode. Basically, the spectroscopically observed peaks are those of the $T[E = V, V, Z(V)]$ function.

List of Figures

List of Tables

Bibliography

[1] T. Heinzel, *Mesoscopic electronics in solid state nanostructures* (Wiley-VCH, Weinheim, 2007).

[2] M. Nielsen and I. Chuang, *Quantum computation and quantum information* (Cambridge University Press, 2000).

[3] M. Stoneham, Physics **2**, 34 (2009).

[4] N. Agraït, A. L. Yeyati, and J. M. van Ruitenbeek, Physics Reports **377**, 81 (2003).

[5] U. Yogeswaran and S.-M. Chen, Sensors **8**, 290 (2008).

[6] Z. I. Alferov, Rev. Mod. Phys. **73**, 767 (2001).

[7] F. J. Garcia de Abajo, J. Cordon, M. Corso, F. Schiller, and J. E. Ortega, Nanoscale **2**, 717 (2010).

[8] M. Milun, P. Pervan, and D. P. Woodruff, Reports on Progress in Physics **65**, 99 (2002).

[9] T.-C. Chiang, Surf. Sci. Rep. **39**, 181 (2000).

[10] R. Otero, A. L. V. de Parga, and R. Miranda, Surf. Sci. **447**, 143 (2000).

[11] R. Otero, A. L. Vázquez de Parga, and R. Miranda, Phys. Rev. B **66**, 115401 (2002).

[12] J. M. Krans, van, V. Fisun, I. Yanson, and de, Nature **375**, 767 (1995).

[13] A. I. Yanson, I. K. Yanson, and J. M. van Ruitenbeek, Nature **400**, 144 (1999).

[14] D. Tannor, *Introduction to quantum mechanics: a time-dependent perspective* (University Science Books, 2007).

[15] E. V. Chulkov *et al.*, Chem. Rev. **106**, 4160 (2006).

[16] J. H. Dil, J. W. Kim, S. Gokhale, M. Tallarida, and K. Horn, Phys. Rev. B **70**, 045405 (2004).

[17] E. Ogando, N. Zabala, E. V. Chulkov, and M. J. Puska, Phys. Rev. B **69**, 153410 (2004).

[18] E. Ogando, N. Zabala, E. V. Chulkov, and M. J. Puska, Phys. Rev. B **71**, 205401 (2005).

[19] E. Ogando, N. Zabala, E. V. Chulkov, and M. J. Puska, Journal of Physics: Condensed Matter **20**, 315002 (2008).

[20] M. C. Yang *et al.*, Phys. Rev. Lett. **102**, 196102 (2009).

[21] J. H. Dil, J. W. Kim, T. Kampen, K. Horn, and A. R. H. F. Ettema, Phys. Rev. B **73**, 161308 (2006).

[22] P. S. Kirchmann, M. Wolf, J. H. Dil, K. Horn, and U. Bovensiepen, Phys. Rev. B **76**, 075406 (2007).

[23] P. S. Kirchmann and U. Bovensiepen, Phys. Rev. B **78**, 035437 (2008).

[24] P. S. Kirchmann *et al.*, Nat. Phys. **6**, 782 (2010).

[25] M. Becker and R. Berndt, Phys. Rev. B **81**, 205438 (2010).

[26] G. Materzanini, P. Saalfrank, and P. J. D. Lindan, Phys. Rev. B **63**, 235405 (2001).

[27] C. M. Wei and M. Y. Chou, Phys. Rev. B **66**, 233408 (2002).

[28] A. Ayuela, E. Ogando, and N. Zabala, Phys. Rev. B **75**, 153403 (2007).

[29] X. Zubizarreta, V. M. Silkin, and E. V. Chulkov, Phys. Rev. B **84**, 115144 (2011).

[30] R. Fischer and T. Fauster, Phys. Rev. B **51**, 7112 (1995).

[31] P. Echenique *et al.*, Surf. Sci. Rep. **52**, 219 (2004).

[32] P. Saalfrank, Chem. Rev. **106**, 4116 (2006).

[33] E. V. Chulkov *et al.*, Phys. Rev. B **68**, 195422 (2003).

[34] S. Crampin, S. De Rossi, and F. Ciccacci, Phys. Rev. B **53**, 13817 (1996).

[35] A. Nakamura, M. Brandbyge, L. B. Hansen, and K. W. Jacobsen, Phys. Rev. Lett. **82**, 1538 (1999).

[36] Y. J. Lee *et al.*, Phys. Rev. B **69**, 125409 (2004).

[37] P. A. Khomyakov and G. Brocks, Phys. Rev. B **74**, 165416 (2006).

[38] R. N. Barnett and U. Landman, Nature **387**, 788 (1997).

[39] U. Landman, Solid State Commun. **107**, 693 (1998).

[40] H. Häkkinen and M. Manninen, EPL **44**, 80 (1998).

[41] E. Ogando, T. Torsti, N. Zabala, and M. J. Puska, Phys. Rev. B **67**, 075417 (2003).

[42] P. Jelínek, R. Pérez, J. Ortega, and F. Flores, Phys. Rev. B **68**, 085403 (2003).

[43] L. Hui, F. Pederiva, G. H. Wang, and B. L. Wang, J. Chem. Phys. **119**, 9771 (2003).

[44] F. Tavazza, L. E. Levine, and A. M. Chaka, J. Appl. Phys. **106**, 043522 (2009).

[45] F. Tavazza, D. T. Smith, L. E. Levine, J. R. Pratt, and A. M. Chaka, Phys. Rev. Lett. **107**, 126802 (2011).

[46] A. Zugarramurdi, N. Zabala, A. G. Borisov, and E. V. Chulkov, Phys. Rev. Lett. **106**, 249601 (2011).

[47] A. Zugarramurdi, N. Zabala, A. G. Borisov, and E. V. Chulkov, Phys. Rev. B **84**, 115422 (2011).

[48] R. Martin, *Electronic structure: basic theory and practical methods* (Cambridge University Press, Cambridge, 2004).

[49] J. Kohanoff, *Electronic structure calculations for solids and molecules* (Cambridge University Press, 2006).

[50] P. Hohenberg and W. Kohn, Phys. Rev. **136**, B864 (1964).

[51] H. Mera and K. Stokbro, Phys. Rev. B **79**, 125109 (2009).

[52] A. Görling, Phys. Rev. A **54**, 3912 (1996).

[53] D. P. Chong, O. V. Gritsenko, and E. J. Baerends, J. Chem. Phys. **116**, 1760 (2002).

[54] D. M. Ceperley and B. J. Alder, Phys. Rev. Lett. **45**, 566 (1980).

[55] J. P. Perdew and A. Zunger, Phys. Rev. B **23**, 5048 (1981).

[56] A. Liebsch, *Electronic excitations at metal surfaces* (Plenum Press, 1997).

[57] J. P. Perdew, H. Q. Tran, and E. D. Smith, Phys. Rev. B **42**, 11627 (1990).

[58] T. Mahmoodi and M. Payami, Journal of Physics: Condensed Matter **21**, 265002 (2009).

[59] N. W. Ashcroft and N. D. Mermin, *Solid State Physics* (Harcourt, 1976).

[60] M. Koskinen, P. O. Lipas, and M. Manninen, Zeitschrift fr Physik D Atoms, Molecules and Clusters **35**, 285 (1995).

[61] I.-P. Hong *et al.*, Phys. Rev. B **80**, 081409 (2009).

[62] H. Eckardt, L. Fritsche, and J. Noffke, Journal of Physics F: Metal Physics **14**, 97 (1984).

[63] K. Horn *et al.*, Phys. Rev. B **30**, 1711 (1984).

[64] E. Chulkov, V. Silkin, and P. Echenique, Surf. Sci. **437**, 330 (1999).

[65] A. Kiejna, Phys. Rev. B **47**, 7361 (1993).

[66] A. G. Borisov, E. V. Chulkov, and P. M. Echenique, Phys. Rev. B **73**, 073402 (2006).

[67] J. J. Quinn and R. A. Ferrell, Phys. Rev. **112**, 812 (1958).

[68] G. F. Giuliani and G. Vignale, *Quantum theory of electron liquid* (Cambridge University Press, 2005).

[69] E. Runge and E. K. U. Gross, Phys. Rev. Lett. **52**, 997 (1984).

[70] M. Petersilka, U. J. Gossmann, and E. K. U. Gross, Phys. Rev. Lett. **76**, 1212 (1996).

[71] G. Onida, L. Reining, and A. Rubio, Rev. Mod. Phys. **74**, 601 (2002).

[72] F. Aryasetiawan and O. Gunnarsson, Reports on Progress in Physics **61**, 237 (1998).

[73] J. D. Lee, O. Gunnarsson, and L. Hedin, Phys. Rev. B **60**, 8034 (1999).

[74] L. Hedin, Phys. Rev. **139**, A796 (1965).

[75] C. Friedrich and A. Schindlmayr, NIC Series **31**, 335 (2006).

[76] J. M. Pitarke, V. P. Zhukov, R. Keyling, E. V. Chulkov, and P. M. Echenique, ChemPhysChem **5**, 1284 (2004).

[77] E. Chulkov, V. Silkin, and M. Machado, Surf. Sci. **482-485, Part 1**, 693 (2001).

[78] A. G. Eguiluz, Phys. Rev. B **31**, 3303 (1985).

[79] V. M. Silkin, J. M. Pitarke, E. V. Chulkov, and P. M. Echenique, Phys. Rev. B **72**, 115435 (2005).

[80] M. Quijada, A. G. Borisov, I. Nagy, R. D. Muiño, and P. M. Echenique, Phys. Rev. A **75**, 042902 (2007).

[81] G. I. Márk, Eur. J. Phys. **18**, 247 (1997).

[82] M. Abramowitz and I. Stegun, *Handbook of Mathematical Functions*, Fifth ed. (Dover, New York, 1964).

[83] R. Kosloff, *Dynamics of Molecules and Chemical Reactions* (Marcel Dekker, New York, 1996).

[84] R. G. Littlejohn, M. Cargo, T. Carrington, K. A. Mitchell, and B. Poirier, J. Chem. Phys. **116**, 8691 (2002).

[85] D. Kosloff and R. Kosloff, J. Comput. Phys. **52**, 35 (1983).

[86] M. D. Feit, J. A. Fleck, Jr., and A. Steiger, A. J. Comput. Phys. **47**, 412 (1982).

[87] C. Leforestier *et al.*, Journal of Computational Physics **94**, 59 (1991).

[88] W. Schweizer, *Numerical quantum dynamics* (Kluwer Academic Publishers, 2001).

[89] A. Vibok and G. J. Halasz, Phys. Chem. Chem. Phys. **3**, 3048 (2001).

[90] A. Nissen, H. O. Karlsson, and G. Kreiss, J. Chem. Phys. **133**, 054306 (2010).

[91] D. J. Kalita and A. K. Gupta, J. Chem. Phys. **134**, 094301 (2011).

[92] D. Neuhauser and M. Baer, Journal of Chemical Physics **91**, 4651 (1989).

[93] T. Seideman and W. H. Miller, Journal of Chemical Physics **97**, 2499 (1992).

[94] M. A. Van Hove, W. H. Weinberg, and C. M. Chan, *Low Energy Electron Diffraction* (Springer-Verlag: Berlin, 1986).

[95] E. Merzbacher, *Quantum mechanics* (Wiley, 1998).

[96] A. J. F. Siegert, Phys. Rev. **56**, 750 (1939).

[97] G. Breit and E. Wigner, Physical Review **49**, 519 (1936).

[98] V. A. Mandelshtam, T. R. Ravuri, and T. H. S., Phys. Rev. Lett. **70**, 1932 (1993).

[99] V. Ryaboy, N. Moiseyev, V. A. Mandelshtam, and H. S. Taylor, J. Chem. Phys. **101**, 5677 (1994).

[100] M. Wojdyr, J. Appl. Cryst. **43**, 1126 (2010).

[101] M. R. Wall and D. Neuhauser, J. Chem. Phys. **102**, 8011 (1995).

[102] V. A. Mandelshtam and H. S. Taylor, Phys. Rev. Lett. **78**, 3274 (1997).

[103] J. Sjakste, A. G. Borisov, J. P. Gauyacq, and A. K. Kazansky, Journal of Physics B: Atomic, Molecular and Optical Physics **37**, 1593 (2004).

[104] E. Anderson *et al.*, *LAPACK Users' Guide*, Third ed. (Society for Industrial and Applied Mathematics, Philadelphia, PA, 1999).

[105] M. Hankel, G. G. Balint-Kurti, and S. K. Gray, Int. J. Quantum Chem. **92**, 205 (2003).

[106] D. Riedel, R. Delattre, A. G. Borisov, and T. V. Teperik, Nano Letters **10**, 3857 (2010).

[107] M. Frigo and S. Johnson, Proceedings of the IEEE **93**, 216 (2005).

[108] C. E. Shannon, Proceedings of the IEEE **86**, 447 (1998).

[109] R. Bisseling and R. Kosloff, Journal of Computational Physics **59**, 136 (1985).

[110] J. G. Simmons, J. Appl. Phys. **34**, 1793 (1963).

[111] R. Landauer, IBM J. Res. Dev. **1**, 223 (1957).

[112] S. Datta, *Electronic transport in mesoscopic systems* (Cambridge University Press, 1997).

[113] T. Frederiksen, M. Paulsson, M. Brandbyge, and A.-P. Jauho, Phys. Rev. B **75**, 205413 (2007).

[114] D. Ferry and S. Goodnick, *Transport in nanostructures* (Cambridge University Press, 1999).

[115] J. M. Pitarke, F. Flores, and P. M. Echenique, Surf. Sci. **1**, 234 (1990).

[116] A. Hanuschkin, D. Wortmann, and S. Blügel, Phys. Rev. B **76**, 165417 (2007).

[117] R. Tsu and L. Esaki, Appl. Phys. Lett. **22**, 562 (1973).

[118] J. N. Schulman, Appl. Phys. Lett. **72**, 2829 (1998).

[119] K. M. S. V. Bandara and D. D. Coon, J. Appl. Phys. **66**, 693 (1989).

[120] J. I. Pascual *et al.*, Phys. Rev. B **75**, 165326 (2007).

[121] M. Büttiker, Y. Imry, R. Landauer, and S. Pinhas, Phys. Rev. B **31**, 6207 (1985).

[122] S. Davison and M. Stęślicka, *Basic theory of surface states* (Clarendon Press, New York, 1996).

[123] L. Landau and E. Lifshitz, *Quantum mechanics: non-relativistic theory* (Butterworth-Heinemann, 1981).

[124] R. H. Williams, G. P. Srivastava, and I. T. McGovern, Reports on Progress in Physics **43**, 1357 (1980).

[125] A. Mugarza, *Electronic Structure of Low-Dimensional Systems Analyzed by Angle-Resolved Photoemission Spectroscopy*, PhD thesis, University of Basque Country, 2002.

[126] P. M. Echenique and J. B. Pendry, Journal of Physics C: Solid State Physics **11**, 2065 (1978).

[127] M. Ortuño and P. M. Echenique, Phys. Rev. B **34**, 5199 (1986).

[128] P. M. Echenique and J. B. Pendry, Prog. Surf. Sci. **32**, 111 (1989).

[129] J. J. Paggel, T. Miller, and T.-C. Chiang, Science **283**, 1709 (1999).

[130] F. Schiller, A. Leonardo, E. V. Chulkov, P. M. Echenique, and J. E. Ortega, Phys. Rev. B **79**, 033410 (2009).

[131] E. Chulkov, V. Silkin, and P. Echenique, Surf. Sci. **391**, L1217 (1997).

[132] E. G. McRae, Rev. Mod. Phys. **51**, 541 (1979).

[133] J. D. Jackson, *Classical Electrodynamics*, Third ed. (Wiley, 1998).

[134] G. Binnig *et al.*, Phys. Rev. Lett. **55**, 991 (1985).

[135] J. H. Coombs and J. K. Gimzewski, Journal of Microscopy **152**, 841 (1988).

[136] P. Wahl, M. A. Schneider, L. Diekhöner, R. Vogelgesang, and K. Kern, Phys. Rev. Lett. **91**, 106802 (2003).

[137] D. B. Dougherty *et al.*, Phys. Rev. B **76**, 125428 (2007).

[138] J. Gea-Banacloche, Am. J. Phys. **67**, 776 (1999).

[139] O. Vallée, Am. J. Phys. **68**, 672 (2000).

[140] D. M. Goodmanson, Am. J. Phys. **68**, 866 (2000).

[141] A. Davydov, *Quantum mechanics* (Pergamon Press, London, 1969).

[142] S. Stepanow *et al.*, Phys. Rev. B **83**, 115101 (2011).

[143] B. J. Hinch, C. Koziol, J. P. Toennies, and G. Zhang, EPL **10**, 341 (1989).

[144] J. Braun and J. Toennies, Surf. Sci. **384**, L858 (1997).

[145] A. Vázquez de Parga *et al.*, Surf. Sci. **603**, 1389 (2009).

[146] P. Czoschke, H. Hong, L. Basile, and T.-C. Chiang, Phys. Rev. Lett. **93**, 036103 (2004).

[147] O. Pfennigstorf, A. Petkova, H. L. Guenter, and M. Henzler, Phys. Rev. B **65**, 045412 (2002).

[148] Y. Guo *et al.*, Science **306**, 1915 (2004).

[149] M. M. Ozer, J. R. Thompson, and H. H. Weitering, Nat Phys **2**, 173 (2006).

[150] D. Eom, S. Qin, M.-Y. Chou, and C. K. Shih, Phys. Rev. Lett. **96**, 027005 (2006).

[151] C. Brun *et al.*, Phys. Rev. Lett. **102**, 207002 (2009).

[152] S. Qin, J. Kim, Q. Niu, and C.-K. Shih, Science **324**, 1314 (2009).

[153] T. Zhang *et al.*, Nat Phys **6**, 104 (2010).

[154] F. Schulte, Surf. Sci. **55**, 427 (1976).

[155] J. H. Dil, T. U. Kampen, B. Hülsen, T. Seyller, and K. Horn, Phys. Rev. B **75**, 161401 (2007).

[156] L. Aballe, C. Rogero, P. Kratzer, S. Gokhale, and K. Horn, Phys. Rev. Lett. **87**, 156801 (2001).

[157] S. R. Barman, P. Häberle, K. Horn, J. A. Maytorena, and A. Liebsch, Phys. Rev. Lett. **86**, 5108 (2001).

[158] Y. Jia, B. Wu, H. H. Weitering, and Z. Zhang, Phys. Rev. B **74**, 035433 (2006).

[159] J. Kliewer *et al.*, Science **288**, 1399 (2000).

[160] L. Vitali *et al.*, Surf. Sci. **523**, 47 (2003).

[161] H. Petek and S. Ogawa, Progress in Surface Science **56**, 239 (1997).

[162] M. Wolf, E. Knoesel, and T. Hertel, Phys. Rev. B **54**, R5295 (1996).

[163] A. Zugarramurdi, N. Zabala, V. M. Silkin, A. G. Borisov, and E. V. Chulkov, Phys. Rev. B **80**, 115425 (2009).

[164] E. V. Chulkov *et al.*, Eur. Phys. J. B **75**, 37 (2010).

[165] S. Mathias *et al.*, Phys. Rev. B **81**, 155429 (2010).

[166] S. M. Lu *et al.*, J. Appl. Phys. **108**, 083707 (2010).

[167] J. Osma, I. Sarría, E. V. Chulkov, J. M. Pitarke, and P. M. Echenique, Phys. Rev. B **59**, 10591 (1999).

[168] P. M. Echenique, J. M. Pitarke, E. V. Chulkov, and A. Rubio, Chem. Phys **251**, 1 (2000).

[169] B. Hellsing, A. Eiguren, and E. V. Chulkov, Journal of Physics: Condensed Matter **14**, 5959 (2002).

[170] E. V. Chulkov, I. Sarría, V. M. Silkin, J. M. Pitarke, and P. M. Echenique, Phys. Rev. Lett. **80**, 4947 (1998).

[171] S. Crampin, Phys. Rev. Lett. **95**, 046801 (2005).

[172] A. Zugarramurdi, A. G. Borisov, N. Zabala, E. V. Chulkov, and M. J. Puska, Phys. Rev. B **83**, 035402 (2011).

[173] A. Weismann *et al.*, Science **323**, 1190 (2009).

[174] C. Corriol *et al.*, Phys. Rev. Lett. **95**, 176802 (2005).

[175] J. Li, W.-D. Schneider, R. Berndt, O. R. Bryant, and S. Crampin, Phys. Rev. Lett. **81**, 4464 (1998).

[176] M. A. Schneider, L. Vitali, N. Knorr, and K. Kern, Phys. Rev. B **65**, 121406 (2002).

[177] U. Höfer *et al.*, Science **277**, 1480 (1997).

[178] T. Fauster, C. Reuß, I. L. Shumay, and M. Weinelt, Chemical Physics **251**, 111 (2000).

[179] R. S. Becker, J. A. Golovchenko, and B. S. Swartzentruber, Phys. Rev. Lett. **55**, 987 (1985).

[180] R. O. Jones, P. J. Jennings, and O. Jepsen, Phys. Rev. B **29**, 6474 (1984).

[181] S. Ogawa, S. Heike, H. Takahashi, and T. Hashizume, Phys. Rev. B **75**, 115319 (2007).

[182] S. Ogawa, S. Heike, H. Takahashi, and T. Hashizume, J. Appl. Phys. **101**, 09G504 (2007).

[183] J. Jia, D. Shi, B. Wang, and J. Zhao, Phys. Rev. B **74**, 205420 (2006).

[184] C. M. Wei and M. Y. Chou, Phys. Rev. B **75**, 195417 (2007).

[185] D. Yu and M. Scheffler, Phys. Rev. B **70**, 155417 (2004).

[186] K. Jacobi, Phys. Rev. B **38**, 5869 (1988).

[187] C. L. Lin *et al.*, Chin. J. Phys. **48**, 855 (2010).

[188] W. B. Su, S. M. Lu, C. S. Chang, and T. T. Tsong, Phys. Rev. Lett. **106**, 249602 (2011).

[189] A. I. Yanson, I. K. Yanson, and J. M. van Ruitenbeek, Phys. Rev. Lett. **84**, 5832 (2000).

[190] H. Ohnishi, Y. Kondo, and K. Takayanagi, Nature **395**, 780 (1998).

[191] G. Rubio, N. Agraït, and S. Vieira, Phys. Rev. Lett. **76**, 2302 (1996).

[192] J. Krans, J. van Ruitenbeek, and L. de Jongh, Physica B: Condensed Matter **218**, 228 (1996).

[193] W. D. Knight *et al.*, Phys. Rev. Lett. **52**, 2141 (1984).

[194] E. Scheer *et al.*, Nature **394**, 154 (1998).

[195] T. Kizuka, Phys. Rev. Lett. **81**, 4448 (1998).

[196] U. Landman, W. D. Luedtke, B. E. Salisbury, and R. L. Whetten, Phys. Rev. Lett. **77**, 1362 (1996).

[197] T. N. Todorov and A. P. Sutton, Phys. Rev. Lett. **70**, 2138 (1993).

[198] A. M. Bratkovsky, A. P. Sutton, and T. N. Todorov, Phys. Rev. B **52**, 5036 (1995).

[199] M. R. Sørensen, M. Brandbyge, and K. W. Jacobsen, Phys. Rev. B **57**, 3283 (1998).

[200] E. Z. da Silva, A. J. R. da Silva, and A. Fazzio, Phys. Rev. Lett. **87**, 256102 (2001).

[201] P. Z. Coura *et al.*, Nano Letters **4**, 1187 (2004).

[202] D. Wang *et al.*, Nano Lett. **7**, 1208 (2007).

[203] C. Untiedt *et al.*, Phys. Rev. Lett. **98**, 206801 (2007).

[204] A. Marchenkov, Z. Dai, C. Zhang, R. N. Barnett, and U. Landman, Phys. Rev. Lett. **98**, 046802 (2007).

[205] P. Jelínek, R. Pérez, J. Ortega, and F. Flores, Phys. Rev. B **77**, 115447 (2008).

[206] M. Scheffler and C. Stampfl, *Handbook of Surface Science* Vol. 2 (Elsevier, Amsterdam, 2000).

[207] A. Yazdani, D. M. Eigler, and N. D. Lang, Science **272**, 1921 (1996).

[208] N. Zabala, M. J. Puska, and R. M. Nieminen, Phys. Rev. Lett. **80**, 3336 (1998).

[209] C. Yannouleas, E. N. Bogachek, and U. Landman, Phys. Rev. B **57**, 4872 (1998).

[210] J. Bürki, C. A. Stafford, and D. L. Stein, Phys. Rev. Lett. **95**, 090601 (2005).

[211] J. A. Alonso and A. Rubio, *Handbook of Theoretical and Computational Nanotechnology* Vol. 7, Chap. 4 (American Scientific Publishers, Stevenson Ranch, CA, 2006), Edited by M. Rieth andW. Schommers.

[212] M. Di Ventra, S. T. Pantelides, and N. D. Lang, Phys. Rev. Lett. **84**, 979 (2000).

[213] A. Nitzan, Annu. Rev. Phys. Chem. **52**, 681 (2001).

[214] A. Nitzan and M. A. Ratner, Science **300**, 1384 (2003).

[215] Y. Xue and M. A. Ratner, Phys. Rev. B **68**, 115406 (2003).

[216] W. Tian *et al.*, J. Chem. Phys. **109**, 2874 (1998).

[217] F. Chen, J. Hihath, Z. Huang, X. Li, and N. Tao, Annu. Rev. Phys. Chem. **58**, 535 (2007).

[218] M. Tsukada, N. Kobayashi, M. Brandbyge, and S. Nakanishi, Progress in Surface Science **64**, 139 (2000).

[219] J. C. Cuevas, A. L. Yeyati, and A. Martín-Rodero, Phys. Rev. Lett. **80**, 1066 (1998).

[220] H.-W. Lee and C. S. Kim, Phys. Rev. B **63**, 075306 (2001).

[221] A. G. Borisov, F. J. García de Abajo, and S. V. Shabanov, Phys. Rev. B **71**, 075408 (2005).

[222] R. Gutiérrez, F. Grossmann, O. Knospe, and R. Schmidt, Phys. Rev. A **64**, 013202 (2001).

[223] J. Enkovaara *et al.*, Journal of Physics: Condensed Matter **22**, 253202 (2010).

[224] T. Torsti, M. Heiskanen, M. J. Puska, and R. M. Nieminen, Int. J. Quantum Chem. **91**, 171 (2003).

[225] W. H. Press, S. A. Teukolsky, W. T. Vetterling, and B. P. Flannery, *Numerical recipes in FORTRAN (2nd ed.): the art of scientific computing* (Cambridge University Press, New York, NY, USA, 1992).

List of Publications

The articles published (or in process of preparation) during the period of this thesis are listed below:

1. A. Zugarramurdi, N. Zabala, V. M. Silkin, A. G. Borisov, E. V. Chulkov, *Lifetimes of quantum well states and resonances in Pb overlayers on Cu(111)*, Phys. Rev. B **80**, 115425 (2009).

2. E. V. Chulkov, A. Zugarramurdi, S. S. Tsirkin, X. Zubizarreta, I. A. Nechaev, I. Yu. Sklyadneva and S. V. Eremeev, *Electronic structure and excitations on clean and nanostructured metal surfaces*, The European Physical Journal B **75**, 37-47 (2010).

3. A. Zugarramurdi, A. G. Borisov, N. Zabala, E. V. Chulkov and M. J. Puska, *Clustering and conductance in breakage of sodium nanowires*, Phys. Rev. B **83**, 035402 (2011).

4. A. Zugarramurdi, N. Zabala, A. G. Borisov, E. V. Chulkov, *Comment on "Phase Contribution of Image Potential on Empty Quantum Well States in Pb Islands on the Cu(111) Surface"*, Phys. Rev. Lett. **106**, 249601 (2011).

5. A. Zugarramurdi, N. Zabala, A. G. Borisov, E. V. Chulkov, *Theoretical study of constant current scanning tunneling spectroscopy in Pb overlayers*, Phys. Rev. B **84** 115422 (2011).

6. A. Zugarramurdi, N. Zabala, V. M. Silkin, A. G. Borisov, E. V. Chulkov, *Quantum size effects in the lifetimes of quantum well states with image state character*, (To be submitted).